Sheffield Hallam University

A Sheffield Hallam University thesis
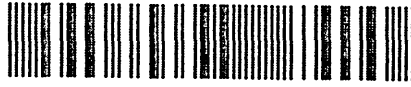
D 46126/83

ProQuest Number: 10701044

ProQuest 10701044

A RE-APPRAISAL OF THE DUSTY GAS MODEL

by

Mariana Henriette Staia

This thesis is submitted in part fulfilment of the
requirements for the Degree of Doctor of Philosophy of
the Council for National Academic Awards. The work was
carried out at Sheffield City Polytechnic, Department
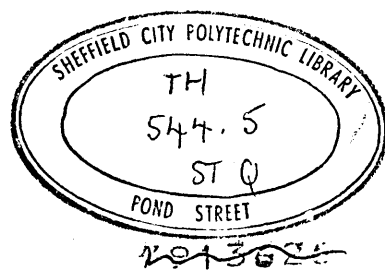of Metallurgy in collaboration with British   Steel
Corporation, Teesside Laboratories.

February 1983

PREFACE

This thesis is submitted in part fulfilment of the
requirements for the Degree of Doctor of Philosophy
of the Council for National Academic Awards. The
research described was carried out during the period
from September 1978 to January 1983 in the Department
of Metallurgy at Sheffield City Polytechnic. No part
of this dissertation has been submitted for a degree
at any other University or College.

During the period of this work the author attended the
following lectures which constituted part of the MSc in
Metallurgical Process Management at Sheffield City Polytechnic:

Module I   Process Metallurgy
                        Mechanical Metallurgy
                        Advanced Thermodynamics

Module II   Computational Methods and Numerical
                        Analysis
                        Accountancy
                        Micro-Economics and Financial Control

Module III   Corrosion Resistance and High Temperature
                        Alloys
                        Oxygen Steelmaking
                        High Strength Steels
                        Refractories
                        Ironmaking
                        Heat treatment and Transformations

Module IV   Case Studies in the subject areas of:

                        Corrosion Resistance and High
                        Temperature Alloys.
                        Heat Treatment and Transformations.
                        Ironmaking. (Appendix 8 of this
                        dissertation)

The Candidate's performance during the above-mentioned
courses has been satisfactorily assessed by means of written
examinations and the continuous assessment of specific
assignments.

ACKNOWLEDGEMENTS

A RE-APPRAISAL OF THE DUSTY GAS MODEL

by: Mariana H. Staia

Abstract

Experimental measurements have been made of gaseous diffusion and flow in porous materials of metallurgical relevance. Hollow spheres of the porous materials, prepared by isostatic compaction, sintering and reaction, have been placed in an apparatus able to maintain gases of known composition and pressure inside and outside the spheres. Two separate types of experiment were carried out. In the first set, the permeation of pure gases across the spheres was determined at a range of different total pressures. In the second set, the counter diffusion of two gases was studied at a single mean pressure but under a range of different pressure gradients. Measurements made with a zero pressure gradient - isobaric experiments - constituted a key component in these binary diffusion experiments. Experiments were conducted at high and low temperatures using helium, argon, carbon dioxide and nitrogen and in porous iron produced by reduction, in sintered porous iron and in lime produced by the decomposition of calcium carbonate.

The experiments were analysed in terms of the Dusty Gas Model, a fresh development of this model being presented to emphasise its phenomenological nature and include a general statement of the influence of mechanically driven gas flows. The standard application of these equations is used to analyse the single gas permeability experiments and thus to determine the Knudsen diffusion coefficient and a parameter quantifying the porous material's resistance to mechanically driven gas flow.

A new unified method of solution is then introduced for binary diffusion, combining a previously obtained solution for isobaric diffusion with a new analysis for non-isobaric diffusion and flow. Using this method, a parameter determining effective binary molecular diffusion coefficients has been obtained from the isobaric experiments and used to predict non-isobaric diffusion rates, these predictions being compared with the corresponding experimental results. Further development of the method has allowed it to be applied to the non-isobaric equi-molar counter diffusion process that occurs during the reduction of hematite and to non-isobaric diffusion during the decomposition of calcium carbonate.

TABLE OF CONTENTS

CONTENTS (CONTINUED)

CHAPTER 4

APPARATUS AND EXPERIMENTAL PROCEDURE

CONTENTS (CONTINUED)

CHAPTER 5

EXPERIMENTAL RESULTS

CONTENTS (CONTINUED)

CONTENTS (CONTINUED)

CONTENTS (CONTINUED)

LIST OF SYMBOLS

Roman Symbols

A_o Area of an orifice, m^2

A_o Phenomenological constant determining the Knudsen diffusion coefficient in a porous solid, $cm^2s^{-1}(g.mol^{-1}K^{-1})^{0.5}$ - equation (3.57)

A_S Cross sectional area of the diffusion shaft, m^2

B_o Phenomenological constant for flow through a porous media, cm^2 - equation (3.19)

C_T Total molar density or concentration, $mol.m^{-1}$

C_D Coefficient of discharge for an orifice

C_o Phenomenological constant - the ratio between the effective and the free gas molecular diffusivities for a gas pair - equation (3.8)

$cond._c$ Conductance for flow along a capillary

$cond._s$ Superficial conductance across a porous structure

C_p The molar density of a reacting particle, $mol.m^{-3}$

$C*$ Mole fraction of suffix species

d Diameter of orifice plate, mm

D_{AB} Molecular diffusion coefficient for suffix gas pair in a free gas, cm^2s^{-1}

$D_{AB,eff}$ Effective binary molecular diffusion coefficient for suffix gas pair, cm^2s^{-1}

$D_{A,eff}$ Effective combined diffusivity for suffix gas, cm^2s^{-1}

∇ Differential operator, m^{-1}

∇_c Differential operator along a capillary, m^{-1}

D_H Hypothetical Knudsen diffusion coefficient used by Hills, cm^2s^{-1}

$D_{K,A}$ Knudsen diffusion coefficient for suffix species, cm^2s^{-1}

f Fraction of molecules reflected diffusely

f Friction factor

F	Driving force for flow along the capillary
G	Molar flow rate in a bulk flow stream, $mol.s^{-1}$
h	Height of manometric fluid, m
k_{eq}	Equilibrium constant for a gas/solid reaction
k_1	Factor related to the aspect ratio of a short Knudsen capillary
L	Length of flow channel, m
M	Relative molecular mass of suffix species, $g.mol^{-1}$
m	Slope of a linear correlation
n	Number of readings
N	Total number of species in a multi-component mixture
$\dot{n}"$	Molar flux density vector, $mol.m^{-2}s^{-1}$
P	Pressure, Atm
r	Radius, m, mm or μm
R	Universal gas constant, 82.03 $cm^3atm.mol^{-1}K^{-1}$ or 8.3145 $J.mol^{-1}K^{-1}$
R	Correlation coefficient for a linear correlation
Re	Reynolds number
r_o	Outer radius of a reacting compact, cm or mm
r*	Dimensionless radius of reaction front in a reacting particle, Defined as $^r/r_o$
S	Shape factor of diffusion tube, m - equation (3.51)
Sc	Schmidt number
$S_e(\quad)$	Standard deviation
Sh	Sherwood number
S_o	Specific surface area of voids per unit volume of actual solid, m^{-1}
T	Temperature, K
t*	Dimensionless reaction time - equation (3.73)

u	Mixing cup velocity, $m.s^{-1}$
u_{eff}	The effective gas velocity transporting stirring momentum, $m.s^{-1}$ - equation (5.4.18)
u_o	Gas velocity through the orifice, $m.s^{-1}$
v_A	Diffusion volume for suffix species
V	Volumetric gas flow, $m^3.s^{-1}$
$\vec{v}_M$	The mechanically driven gas superficial gas velocity across a porous solid, $m.s^{-1}$
x	Co-ordinate in diffusion direction, m
x	Unreacted fraction of a particle
Y_A	Logarithmic driving force for non-equimolar mass transfer - equation (3.64)

Greek Symbols

α_A	Convective mass transfer coefficient for species A, $cm.s^{-1}$
β	Counter current molar flux ratio - equation (3.35)
δ_A	Ratio of effective diffusivity of A to effective molecular diffusivity of the AB pair - equation (3.31)
ϕ	Solid angle, radians
γ	Porosity
Λ	Number of capillaries crossing unit area of a plane, m^{-2}
μ	Viscosity, poise
$\varkappa$	Ratio of Knudsen diffusion coefficient of gas A to that of gas B - equation (3.43)
χ	Geometric factor in distributed size capillary pore model
ς_A	Pressure variable relating friction to Knudsen effects, atm - equation (3.34)
ν	Stoichiometric factor
ψ_A	Driving force for coupled diffusion and flow

process in binary mixtures, atm - equation (3.52)

ρ Density, $kg.m^{-3}$

θ Average angle between capillaries and diffusion direction

τ Tortuosity factor

ω Permeability of gas A through a porous solid, $cm^2.s^{-1}$

Suffices

,1   For position 1

,2   For position 2

A   For gas species A

AB   For binary gas pair A/B

Air   For air

Ar   For argon

B   For gas species B

b   For the bulk gas phase

C   For gas species C

,C   For flow along a capillary

CO   For carbon monoxide

CO_2 For carbon dioxide

d   For the hypothetical dust

dnb   For di-n-butyl phthalate

e   Exit

e   External

F   For mechanically driven flow

f   For friction

G   In the bulk gas phase

He   For helium

He-Ar   For the gas composition in the central cavity of the diffusion cell

H_2	For hydrogen
H_2O	For water vapour
i	For species 'i' in a multicomponent mixture
i	Internal
j	For species 'j' in a multicomponent mixture
ij	For 'ij' species pair in a multicomponent mixture
M	For the mechanically driven flow
N	For naphthalene
obs	Observed value
R	At the reaction front
r	For a capillary of radius r
s	At the surface
s	For the system
T	Totalled for all species present

Superfixes

i	Inside the hollow spherical compact
o	Outside the hollow spherical compact
+	For the fictitious gas plus dust mixture

1. INTRODUCTION

The diffusion of gases in porous materials is of
considerable industrial importance. Catalysis is one area
of great industrial importance although this is only
marginally related to the metallurgical industries. The
diffusion of gases in porous product layers during gas/solid
reactions such as the reduction of oxide ores and the
roasting of sulphides are important metallurgical examples
of gas flow in porous solids as are chemical reactions that
occur during the sintering of metallic powder compacts.

The study of diffusion of gases in porous solids
is complicated by the two diffusion mechanisms involved -
Knudsen diffusion and molecular diffusion. Knudsen
diffusion involves collisions between the molecules of an
individual gas and the walls of the pores in the solid, and
molecular diffusion involves collisions between the
molecules of the different gas species occupying the pore
volume. The two types of diffusion obey different laws so
that their different influences must be separated in any
full treatment of the role that gaseous diffusion plays in
metallurgical processing.

Formal equations had been developed some time ago for the
Knudsen process in long straight capillaries and a number of
different approaches to gaseous diffusion in porous solids
have been based on these equations. These approaches have
generally run in to difficulty since they require the actual

1

structure of the porous solid to be described in terms of
bunches of capillaries. The actual structures of porous
solids are far more complex than bunches of capillaries and
it was for this reason that the Dusty Gas Model was first
proposed. In its original form it attempted to treat the
solid phase as an assemblage of large spherical molecules
and to apply the collision theories of the kinetic theory of
gases to the Knudsen interactions between the actual gas
molecules and the hypothetical 'dust' molecules.

This approach was soon dropped but the model contained
within itself a formalism that allowed both molecular and
Knudsen diffusion to be treated in a coherent manner and it
is this formalism that has become known as the Dusty Gas
Model. This thesis is concerned with the application of
this formalism both to the analysis of diffusion and flow
measurements on porous materials of metallurgical
importance and to the prediction of reaction rates involving
those porous materials.

The second chapter of the thesis contains a survey of the
experimental methods for studying diffusion in porous
solids, both in general and of metallurgical interest, and
a review of the structural models for porous solids
built around Knudsen's treatment for diffusion in a
capillary.

The next chapter presents a restatement of the equations of
the Dusty Gas Model, developed in a way that emphasises the

phenomenological aspects of the model. The style of this restatement is original, as is the incorporation of the effect of mechanically driven flows into the general equations of the model. The chapter then goes on to present an original generalised approach to the solution of the equations for binary gas mixtures diffusing through porous materials. The equation analysing isobaric diffusion measurements developed from this approach in Chapter 3 has been used before by a number of authors, although its use to analysis isobaric diffusion data is by no means universal, some previous authors appearing to equate equi-molar counter diffusion with isobaric diffusion.

The solution method developed for binary diffusion is then further developed to treat non-isobaric diffusion in an original way, including equi-molar counter diffusion in reduction reactions and non-isobaric diffusion in the decomposition of hematite.

The fourth chapter in the thesis describes the experimental techniques that have been developed for preparing porous shells and for measuring rates of gas permeation and diffusion through them. The next chapter presents the experimental results that have been obtained, and the sixth chapter discusses their relevance both to the study of porous materials and to the study of metallurgical processing.

2.1 INTRODUCTION

There are many industrial processes in which gaseous diffusion and flow in porous solids is of considerable importance.

The rates of gas reactions in porous catalysts are limited in many cases by the rate of transport of the reactant and product gases through the catalyst pores to the active catalyst surface. Similarly, the rate of approach to adsorption equilibrium is frequently limited by gas transport through the porous adsorbant. Additional examples are found in cases of non-catalytic gas/solid reactions where the solid reactant or product is a porous solid and the reactant and product gases must be transported into and out of this solid. Frequently, such reactions as, for example, the reduction of iron oxide, the roasting of the sulphide ores, etc involves the formation of solid product layers on the outside of the original solid particles. Gas diffusion is also important in other technical fields such as vapour penetration into foundry sands, outgassing of powder metal compacts, drying etc.

The transport of gases through porous solids is complex and many workers have attempted to establish methods for the correlation and prediction of gas diffusion and flow rates through porous media.

Since the relationships between structure and fluxes are seldom easy to determine, most models for the prediction of gaseous diffusion and flow have been developed from theories for diffusion and flow in capillaries. These have been adapted for use in porous solids through the development of

4

different models for the structure of the solids. Equations
for flow and diffusion through capillaries will be presented
in the following sections and the principal structural models
outlined.

Experimental methods for measuring diffusion coefficients are
then described, particular emphasis being given to materials of
metallurgical interest and the diffusion coefficients obtained
evaluated.

2.2 THE PREDICTION OF GAS DIFFUSION IN POROUS SOLIDS USING STRUCTURAL MODELS

The actual geometry of the pores in a porous material within which a gas is diffusing is important because gas molecules collide with the pore walls as well as with one another. When the diameter of the pores is very much greater than the mean free path of the gas mixture within the pores, collisions between a gas molecule and the walls are relatively rare. Such diffusion is known as molecular diffusion and the solid does little more than restrict the space available for the gas to occupy and constrain the directions in which it can diffuse. When the pore size is very much smaller than the mean free path of the gas mixture, however, almost all the collisions will be between gas molecules and the pore walls. This diffusion process in known as Knudsen diffusion and the actual progress of gas molecules through the porous solid is an amalgamation of the geometry of the pores and the geometry of the random motion of gas molecules. In Knudsen diffusion, it is the microscale of the geometry of the pores that is important. It has proved particularly difficult to develop models for this microscale geometry that are useful on the macroscale normally used for consideration of the diffusion process in mathematical terms. The problems are further intensified because we are seldom concerned with one form of diffusion or the other. In the bulk of the technical processes in which gaseous diffusion in porous solids in important, the diffusion

process is 'mixed', that is it involves both molecule to molecule collisions and molecule to wall collisions, and hence both molecular and Knudsen diffusion are important.

2.2.1 Capillary Pore Model

In order to account for the Knudsen component in the diffusion process, a number of models have been developed to describe the microscale geometry of the pores in terms of average parameters. The basic analysis that is used in the bulk of these structural models is that developed by Knudsen[1] for the behaviour of gases in fine capillaries. Using the kinetic theory of gases, he developed an equation for the diffusion of a gas down the capillary assuming that its molecules only collide with the walls of the capillary and not with one another. Expressing the diffusion process in terms of the equation:-

$$\dot{n}''_{A,C} = [D_{K,A}]_r \cdot \nabla_c C^*_A \qquad (2.1)$$

where ∇_c is the differential operator along the capillary. Knudsen showed that $[D_{K,A}]_r$ is given by:-

$$[D_{K,A}]_r = 2/3 \; r \; \frac{2-f}{f} \left[\frac{8RT}{M_A}\right]^{1/2} \qquad (2.2)$$

where f is the fraction of the molecules that undergo diffuse reflection and is normally taken to be equal to 1.

If two gases occupy the Knudsen capillary together, they will diffuse independently, each obeying equations (2.1) and (2.2).

Thus Knudsen was the first to show that, under isobaric conditions since $C_A + C_B$ is a constant, the fluxes of the two gases are related to their molecular masses by the equations:-

$$\frac{\dot{n}''_{A,C}}{\dot{n}''_{B,C}} = -\left[\frac{M_B}{M_A}\right]^{1/2} \qquad (2.3)$$

When the capillary is very wide, the binary diffusion of a gas down the capillary will obey the normal continuum diffusion equation:-

$$\dot{n}''_{A,C} = -D_{AB} \ \nabla_C C^*_A \ + \ C^*_A \ (\dot{n}''_{A,C} + \dot{n}''_{B,C}) \qquad (2.4)$$

where C^*_A is the mole fraction of gas A in the AB mixture.

For capillaries in which both Knudsen and molecular flow are of comparable importance, Bosanquet[2] argued that the rate at which self diffusion occurs is proportional to the root mean square velocity of gas molecules and inversely proportional to the number of collisions experienced in unit time, ie to the overall frequency of collisions. This overall frequency is equal to the frequency of molecule/wall collisions plus the frequency of molecule/molecule collisions. The rate of Knudsen diffusion on its own is, of course, inversely proportional to the frequency of the

8

molecule/wall collisions and the rate of molecular diffusion is similarly inversely proportional to the frequency of the molecule/molecule collisions. Thus it is possible to define an overall diffusion coefficient, D, given by:-

$$1/D = 1/[D_{K,A}]_r + 1/D_{AA} \qquad (2.5)$$

this equation being called the Bosanquet interpolation formula.

Subsequently, a number of authors[eg 3] have derived this formula using momentum transfer arguments for equimolar counter diffusion in binary gas mixtures of equal molecular masses. For situations involving gases of unequal molecular mass with both molecular and Knudsen diffusion occuring, the momentum transfer argument also gives equation (2.3) and gives the following equation for the flux of gas A in the capillary:-

$$\dot{n}''_{A,C} = \left[\frac{1 - (1-\beta)C_A^*}{D_{AB}} + \frac{1}{[D_{K,A}]_r} \right]^{-1} \nabla_c C_A^* \qquad (2.6)$$

However, if the molecular masses of the two diffusing gases are not equal, the effective diffusion coefficient generated from equation (2.6) becomes a function of composition.

Subsequently Scott and Dullien[4] analysed binary diffusion and flow in a capillary by adding the viscous (Poiseuille) and slip flow transport of each component to its molecular and Knudsen transport.

Just as diffusion in a fine capillary involves a molecular

collision mechanism and a molecular/wall collision

mechanism, so too does the flow of a gas down the capillary

under the action of a total pressure gradient. The

molecular collision mechanism is normal viscous flow - in a

fine capillary, laminar flow - and the molecular/wall

collision mechanism is termed Knudsen flow, being actually

the same as Knudsen diffusion.

The relationship between the flow of gas down a capillary in

laminar flow and the pressure gradient is given by

Poiseuille's equation, this equation indicating that the

flow velocity is proportional to the square of the capillary

radius. Thus, when the capillary is very fine, the viscous

gas flow is reduced sufficiently for the Knudsen flow term,

proportional to the radius, to become significant. Thus the

total gas flow is found to be greater than indicated by the

Poiseuille equation, this phenomena frequently being termed

slip, since the gas velocity can be considered to be non-

zero at the wall. Thus the total flow is given[eg 5] by an

equation that sums the Poiseuille and Knudsen

contributions:-

$$\dot{n}''_{F,C} = \left[\frac{r^2}{8\mu} P + \check{\delta} \, [D_{K,A}]_r \right] \frac{\nabla_c P}{RT} \qquad (2.7)$$

where the factor $\check{\delta}$ varies depending on the proportion of

molecules that are diffusely reflected from the walls of the

capillary. At very low pressures, the value of $\check{\delta}$ is found

to be 1, but there is some evidence[5] that its value falls as the pressure builds up initially from very low values close to zero. This fall explains the initial fall of permeability with increasing pressure that has been reported at very low pressures in capillaries.

Scott and Dulien[4] accounted for the influence on diffusion of flow under the action of a total pressure gradient by adding equation (2.7) multiplied by the mole fraction of A, to equation (2.6). However, in their subsequent manipulations, they assumed the diffusion fluxes to be related by equation (2.3) although, of course, the diffusion conditions are not isobaric. Their treatment, and others developed from it[eg 6], must be considered suspect because of this.

Although Scott and Dullien used the structural model of the single sized capillary, they do not really come into the category of workers under consideration here because they measured diffusion and flow data directly, their only use of a structural model being to deduce structural parameters from their transport measurments. In this respect, they come into the same category as workers such as Carman[5] who used structural models based on assemblies of capillaries to deduce particle and pore sizes in porous media from permeability measurements. The type of model that he used is outlined in the next section.

2.2.2 Random Oriented Single Size Capillary Pore Model

This structural model has been extensively[eg7, 5, 8, 9] used to analyse flow and diffusion in porous materials. Some confusion exists in the literature as to the precise formulation of the model, different authors advocating different expressions for the tortuosity factor. The treatment given here, therefore discusses the geometric nature of the model before showing its applications. The porous material is imagined as being composed of a large number of fine capillaries of radius 'r', Λ of which cross unit area of any given plane in the material in random directions. The model then assumes that an average angle θ can be allotted between these capillaries and the normal to the plane. If then we consider the porous material between the plane and a second parallel plane, distance δx away, the average length of capillaries between the two planes will be $\delta x/\cos\theta$, so that the volume of voids between unit area of the two planes is $\pi\Lambda r^2 \delta x/\cos\theta$. These voids find themselves in a volume of the structure δx, so we can see that the porosity of the structure is given by:-

$$\gamma = \Lambda\pi r^2/\cos\theta \qquad (2.8)$$

If a flux density in the capillaries is $\dot{n}''_{,C}$, the superficial flux crossing unit area of the plane in the structure is given by:-

$$\dot{n}'' = \Lambda\pi r^2 \dot{n}''_{,C} = [\gamma \cos\theta] \dot{n}''_{,C} \qquad (2.9)$$

The value of $\dot{n}''_{,C}$ is to be determined from the relevant flux equation in the capillary which can be generalised in the form:-

$$\dot{n}''_{,C} = \text{cond.}_C \, \nabla_C \, F \qquad (2.10)$$

where F is the driving force for the flow along the capillary.

The capillaries are longer than the direct line across the structure so that the gradient vector along the capillaries is less than the direct gradient vector across the structure. The differential operator across the structure is related to the differential operator along the capillary by the equation:-

$$\nabla_C = \cos(\theta).\nabla \qquad (2.11)$$

Superficial flows through the structure are described in terms of a superficial flux density, $\dot{n}''$, a superficial conductance, cond._S and a superficial driving force gradient, ∇F

$$\dot{n}'' = \text{cond.}_S \, \nabla F \qquad (2.12)$$

The value of cond._S can be evaluated by substituting into equation (2.10), from equation (2.9) for $n''_{,C}$ and from equation (2.11) for ∇_C. This gives:-

$$\dot{n}''/[\, \gamma \cos\theta] = \text{cond.}_C \cos(\theta).\nabla F \qquad (2.13)$$

Comparison between equations (2.13) and (2.12) shows that the conductances across the structure are related to the conductances along the capillaries by the relationship:-

$$\text{cond.}_S = \text{cond}_{,C} \, \gamma \cos^2\theta \qquad (2.14)$$

The terms $[\cos\theta]^{-2}$ is normally called the tortuosity factor and is given the symbol $\mathcal{T}$. Thus equation (2.14) becomes:-

$$\text{cond.}_s = \frac{\mathcal{V}}{\mathcal{T}} \text{cond.}_c \qquad (2.15)$$

For a non-consolidated structure, Wheeler[7] suggested that the capillaries are distributed in random directions so that the average value of θ is 45°, giving a typical value of $\mathcal{T}$ as 2. The value of $\mathcal{V}/\mathcal{T}$ has been measured by some authors using electrical conductivity techniques and values of the order of 2 have been found for $\mathcal{T}$ in many unconsolidated materials. However, confusion has arisen in the literature[eg.10] as to whether $[\cos\theta]^{-1}$ or $[\cos\theta]^{-2}$ is measured by such experiments. The derivation given above shows quite clearly that it is $[\cos\theta]^{-2}$ that is measured, and that this value should apply equally to all fluxes through the porous media.

The capillary conductance for diffusion is given by equation (2.6) and for flow under the action of a pressure gradient by equation (2.7). Although the relationship between the structure conductance and the capillary conductance does not involve the capillary radius, both equations show that the capillary radius is required in the calculations of the capillary conductances, so that methods must be made available for this radius to be determined.

As we have seen, the average length of capillary in a thickness δx of the material is $\delta x/\cos\theta$ so that the surface area of that capillary is $2\pi r \, \delta x/\cos\theta$. Λ capillaries cross unit area of any section through the material, so that the

14

total capillary surface area in a slab of unit area and thickness δx is $\Lambda 2 \pi r \, \delta x/\cos\theta$ and the total void volume is $\pi r^2 \Lambda \delta x/\cos\theta$. Thus the specific surface area of the voids per unit volume of the actual solid material in the structure is given by:-

$$S_0 = \frac{\Lambda 2 \pi r \, \delta x/\cos\theta}{\Lambda \pi r^2 \, \delta x/\cos\theta \ (1-\gamma)/\gamma} \qquad (2.16)$$

Thus the effective capillary radius is given by:-

$$r = \frac{2\gamma}{S_0(1-\gamma)} \qquad (2.17)$$

Values of S_0 can be determined by the B.E.T. method using the surface adsorption of nitrogen.

Thus the random oriented single size capillary pore model gives the following equation for the binary diffusion of a gas through a porous material:-

$$\dot{n}_A'' = \frac{\gamma}{\mathcal{T}} \left[\frac{1 - (1-\beta)C_A^*}{D_{AB}} + \frac{1}{[D_{A,K}]_r} \right]^{-1} \nabla C_A^* \qquad (2.18)$$

in which $[D_{A,K}]_r$ is the Knudsen diffusion coefficient in the capillary of radius r, the value of r being given by equation (2.17). This approach to diffusion in porous media was first used by Wheeler[7] who suggested that the value of $\mathcal{T}$ was 2, because 45° was the average angle at which pores intersected any surface of interest in the medium.

15

The model gives the following equation for the flow of a gas through the porous media under the action of a total pressure gradient as:-

$$\dot{n}''_F = \frac{\gamma}{\tau}\left[\frac{r^2}{8\mu}P + \delta\,[D_{K,A}]_r\right]\frac{\nabla P}{RT} \qquad (2.19)$$

The capillary radius arises in both the molecular flow (viscous) and the Knudsen diffusion terms and is, as with diffusion, normally provided by equation (2.17). Thus we have:-

$$\dot{n}''_F = \left[\frac{\gamma^3}{2\tau(1-\gamma)^2 S_o^2}\frac{P}{\mu} + \frac{\gamma}{\tau}[D_{K,A}]_r\right]\frac{\nabla P}{R\theta} \qquad (2.20)$$

The parameter δ in equation (2.19) has been put equal to 1 in equation (2.20). As stated in Section 2.2.1, experimental evidence for a value of δ smaller than unity is provided by the permeability minimum that is found in fine capillaries at pressures close to zero. In his extensive review of flow in porous media, Carman[5] states that a similar permeability minimum has not been found in porous materials. This means, as discussed in Chapter 3, that permeability will change linearly with pressure so that the Knudsen diffusion term in equation (2.20) which is not a function of pressure will be constant. There is thus no justification for a value of δ other that unity in porous media.

The factor 2τ in the viscous flow term in the equation (2.20) has been found to be about 5 in many unconsolidated porous materials[5] although there is some debate as to

whether this is due to the non-circular shape of the actual flow channels or to departures of the tortuosity factor from its random value of 2. Carman, from his extensive review[5] concludes that the tortuosity factor in unconsolidated porous materials is 2, so that the factor written as $2\mathcal{T}$ in equation (2-20) should properly be taken as $2.5\mathcal{T}$.

Equation (2.20) has had considerable success in correlating the results of flow experiments on unconsolidated porous materials, but less success with consolidated materials, where the tortuosity factor seems to be very much greater/2. than

The random single size pore model has not had so much success in treating diffusion largely because of difficulties in determining the effective capillary radius from which to calculate the Knudsen diffusion coefficient. It is apparent that there is not a single pore size in a porous material. Thus calculations based on surface areas measured by the B.E.T. technique give an average value and there is no reason to suppose that this average is the average value relevant to diffusion. As far as resisting the diffusion of a gas through a porous solid, pores of different sizes will have different effects. Blind pores, for example will provide infinite resistance to diffusion, small pores a great deal of resistance and wide pores very little at all. All these types of pores will, of course, contribute to the B.E.T. surface area but not necessarily in the way that they contribute to diffusion. Thus the mean pore size determined by B.E.T. analysis is not necessarily the mean pore size for diffusion.

B.E.T. analysis is not the only way in which a pore size has

17

been obtained. Mercury porosimetry yields a curve showing
the distribution of pore volume against pore size and some
workers have used this to determine the mean pore size.
Turkdogan[11], in his work on diffusion in iron, for example,
used such a curve to determine the critical radius for
Knudsen diffusion, taking the radius at the point of inflec-
tion on the accumulated distribution curve. It could be
argued that this is likely to over-estimate the diffusion
relevant mean pore diameter because a larger number of pores
will be associated with the smaller diameters, although
Warner[12] argues that porosimetry under-estimates diffu-
sion relative pore sizes because it measures bottle necks in
a pore length. In all events, both methods leave consider-
able uncertainty as to relevance to diffusion of the mean
pore sizes that they generate.

The second criticism refers to the tortuosity value of 2.
This value arises from the assumption that the pores, on
average, intersect any plane through the porous structure at
45°. Perhaps the best illustration of the complexity of the
pore network in consolidated media is presented in papers
by Turkdogan and co-workers[13] on the pore characteristics
of the carbons. Using microscopic techniques in order to
study the structure of their samples, they found that the
structure of the carbons is far from the simple pore
structure suggested by Wheeler. Measured diffusion rates
were compared with values estimated using Wheeler's model.
Differences between the experimental values and the theore-
tical predictions of up to an order of magnitude were noted.

Thus, it is necessary to evaluate an experimental value
of the tortuosity by direct measurement of the diffusion

coefficients themselves. One reason why the tortuosity
must be measured arises from the uncertainties discussed
previously over determination of a diffusion relevant pore
size. The tortuosity, then, remains an adjustable parameter
which can account, amongst other things, for imperfections
in the single size capillary model or in the way in which it
is applied. Problems associated with the choice of the
correct mean pore size for the diffusion process lead to the
next model which accounts for the ranges of pore sizes
actually found in real porous materials.

2.2.3 <u>Random Oriented Distributed Size Capillary Pore Model</u>

Johnson and Stewart[14] and Satterfield and Caddle[15] have
developed the capillary pore model to account for the
distribution of pore sizes that is found in real porous
materials. In the first place, they assumed that the
directions of the pores were randomly orientated and un-
related to their size and this allowed them to sum equation
(2.6) over all pore sizes and thus obtain the expression:-

$$\dot{n}_A'' = \chi \left[\int_0^\infty \left\{ \frac{1 - (1-\beta)C_A^*}{D_{AB}} + \frac{1}{[D_{K,A}]_r} \right\}^{-1} f(r)dr \right] \frac{dC_A^*}{dx} \qquad (2.21)$$

where $f(r)dr$ is the void fraction occupied by pores of radii
between r and $r + dr$ and χ is a geometric factor resulting
from the distribution of pore orientations and was thought
to be 1/3 for an isotropic pore system. The function $f(r)$
can be determined by mercury porosimetry and the integral
then evaluated numerically. The only difference between
the two treatments is that Satterfield & Caddle wrote the
summation in sigma form - a difference of negligible
importance in view of the numerical integration used by

19

Johnson & Stewart. This model has proved fairly successful for unconsolidated porous materials although it is still necessary to regard the geometric factor as a parameter to be adjusted in order to make the equation fit experimentally measured diffusion data. In such materials, values of the geometric factor have been found to vary in the range 1/2 to 1/7[eg14,15,16] although, when such materials are sintered, the value can drop to 1/20. The form of equation (2.21) possesses a further disadvantage since D_{AB} and $[D_{K,A}]$ vary differently with temperature and with pressure, the integral has to be re-evaluated if the temperature or pressure is changed.

Satterfield and Caddle show that a diffusion mean radius can be obtained by equating equation (2.21) integrated along the diffusion path with equation (2.6) written for the capillary of mean radius, multiplied by the overall porosity and similarly integrated along the diffusion path. In both equations, the Knudsen diffusion coefficient is evaluated as a function of the radius using equation (2.2). Satterfield and Caddle point out that this mean radius is a function of operating conditions and this underlines the difficulty discussed in the previous section of using B.E.T. or porosimetry to determine a mean pore radius for the single size pore model. Several authors[eg15,16] report that the distributed pore size model can explain efficiently the variation of diffusion rates with pressure over a wide pressure range.

2.2.4 <u>Bi-modal Pore Size Distribution Model</u>

Wakao and Smith have suggested an ingeneous model to describe diffusion in porous materials[17]. The pores are split

20

into two types, micropores (r < 100A) and macropores (r > 100A) and an effective diffusion coefficient defined for each type of pore.

Diffusion of gas across any plane in the structure is then analysed as occurring either from a macropore into another macropore, or from a micropore into another micropore or from a micropore into a macropore. Since the pores are randomly distributed within the structure, there is a probability of success associated with each of these progressions. For the two macropores, for example, this probability is equal to the square of the macropore void fraction. Incorporation of these probabilities of progression into the model renders the concept of tortuosity unnecessary.

The diffusion process through the structure is given by an equation in which each of these progressions is represented by a separate term, each with its separate diffusion coefficient. These diffusion coefficients are calculated using an equation similar to the Bosanquet interpolation formula except that the molecular diffusion coefficient is weighted by a factor involving the flux ratio and the mole fraction of gas A. The Knudsen diffusion coefficient is calculated from the standard formula using mean pore radii for the macro- and micro-pores. These radii are determined by an integral technique similar to that used in the distributed pore model except that the molecular diffusion coefficient has been omitted. As Satterfield[18] points out, this radius is probably correct in the micro-pores where Knudsen diffusion predominates, but it is not correct in the macro-pores where mixed, or even molecular, diffusion

will occur.

The ability of this model to predict diffusion rates is impressive, especially when it is considered that it contains no adjustable parameters. However, a number of authors[eg 16] have shown that it does not predict the effect of pressure changes on diffusion rates as well as the distributed pore size model does. Indeed, a number of other structural models have also been proposed but none of them has been as successful as the distributed pore size model.

2.2.5   Structural aspects of the early Dusty Gas Model

When the Dusty Gas Model was first proposed[20], it was proposed as a structural model, although its phenomenological aspects have become the more important as it has been developed.

In its early structural form, then, the model approached Knudsen diffusion in a porous solid by suggesting that the solid particles of which the porous solid was composed could be considered as giant gas molecules - one component in a multi-component gas mixture. Maxwell's equations were then written down for the multicomponent gas mixture with all the diffusion coefficients to be determined by standard kinetic theory incorporating, for example, Chapman-Enskog collision integrals[20].

Since Maxwell's equations include one term for each gas to gas interaction, collisions between the giant dust molecules and the normal gas molecules are incorporated into the equations. Gas/dust interdiffusion coefficients and the collision integrals for them were evaluated by assuming that the real gas molecules are scattered after colliding

22

with the dust molecules in a diffuse manner, but with velocities that obey the normal Maxwellian distribution. This treatment gives an expression for the Knudsen diffusion coefficient for each gas as its binary diffusion coefficient with the dust molecules. These expressions demonstrate many of the known characteristics of Knudsen diffusion. However, Evans, Watson and Mason[20] concluded very early on that the dust/gas collision integrals could not be determined theoretically so that the diffusion coefficients had to be determined directly.

Once this conclusion had been reached, the Dusty Gas Model lost its structural aspect since it could do no more than interpret direct diffusion and flow measurements and did not depend upon any structural information. This interpretative facility stemmed from the formalism given by the Maxwell Equations for multi-component gas diffusion which act as the start for the development of the Dusty Gas Model that is presented in Chapter 3.

2.3 EXPERIMENTAL METHODS OF MEASURING EFFECTIVE DIFFUSION COEFFICIENTS IN POROUS MEDIA

Molecular diffusivities can be determined experimentally in a number of ways. A survey of methods for the measurement of binary molecular diffusion coefficients has been carried out by Marrero[21]. The methods included in this survey are somewhat different from the methods used to determine diffusion coefficients in porous media which are the primary concern of the present work.

Relatively few methods have been developed for measuring the effective diffusion coefficients in porous media. Experiments have been performed using open or closed systems under either steady or unsteady state conditions. The closed systems incorporate a closed volume at either end of the diffusion path whereas flowing gas streams are maintained at either end of the diffusion path in the open systems.

Dye and Dallavalle[22] determined effective diffusion coefficients under unsteady flow conditions using a closed system similar to the two bulb method[23] used for determining ordinary binary diffusion coefficients. The diffusion runs were performed for porous specimens of potassium perchlorate with porosities between 20% and 40%. The diffusion cell consisted of a porous plug situated between two closed chambers of equal volume. Each chamber contained a different diffusing gas. Dye and Dallavalle calculated the effective diffusion coefficient from Fick's second law but did not monitor pressure changes across their specimens. They related their results to the structure of the porous media through the porosity γ. Their values can not be considered reliable because, not only does

24

Fick's second law only apply under equi-molar counter diffusion, but it has since been observed by Hoogshagen[25] that pressure gradients can be set up during unsteady state-diffusion measurements and these will affect the measurements made.

Perhaps the most common open system currently in use for the study of diffusion and flow through porous media is that first developed by Wicke and Kallenbach[26]. In this method, a sample of the porous material being investigated is placed in a diffusion cell between gas streams of different composition. For pure diffusion experiments the pressure and temperature are maintained uniform. Pure gas streams are normally fed to either side of the sample, although this is not a necessary restriction. Care must be taken in the design of the diff-usion cell to ensure that boundary layer effects are not present at the cell ends. To achieve this, high gas velocities have to be used and a uniform distribution of gas flow has to be maintained over each end of the plug.

Wicke and Kallenbach determined the steady state diffusion flux by measuring the steady concentration change it produced in one stream only and they calculated diffusion coefficients using Fick's first law. However, as later authors have pointed out[27] equimolar counter diffusion does not occur in isobaric experiments so that Fick's first law is not obeyed. Thus Wicke and Kallenbach's results cannot be compared with later experimental measurements, nor can they be used immediately in developing theories for diffusion through porous media.

Some later authors, using the same technique, measured the

concentration changes in both streams, and obtained the effective diffusion coefficient $D_{AB,eff}$. Experimental investigations using Wicke and Kallenbach's diffusion cell have been performed on catalysts[15][29][30][31], on synthetic porous materials such as porcelain or bohemite pellets[3][17][24][28], on porous graphite[32][33], carbon[8,34] and an array of capillaries[35].

Although very useful, the Wicke-Kallenbach technique has its disadvantages. A single sample of cylindrical shape has to be used and, since it has to be pressed in a conventional die, it will probably display inhomogeneities which could affect the diffusivity measurements. Since the axial flux is measured, the possible influences of anisotropy of the solid and of the dead-end pores cannot be evaluated. Moreover, the temperature and pressure ranges over which this type of apparatus can be conveniently operated are somewhat limited. Thus measurements under conditions close to reaction conditions cannot easily be made.

An unsteady state method which overcomes some of these objections, is the chromatographic peak broadening method which has been put forward by Davis and Scott[36] and used especially for diffusion measurements in adsorbents and catalysts.

The method allows determination of an effective diffusion coefficient for the particular gas solid system involved. A carrier gas is passed continuously through a packed bed of the particles of interest and the response of the system to an injected pulse of test gas is recorded, much as in gas chromatography, although the gases used must be non-

adsorbent. By measuring the height equivalent to a
theoretical plate for the bed as a function of gas velocity
an effective diffusion coefficient may be determined. The
method appears adaptable to a wide range of operating
conditions, gives results reflecting the behaviour of a large
number of particles and, since it is a transient technique,
should reflect the presence of small and dead-end pores.
However, the theory in which the method is based is only
approximate and some difficulties associated with wall
effects and external mass transfer coefficient arise[90].
Improvements to the theory as well as to some experimental
results have been developed by Schneider and Smith[37].
Rosental[38] applied the technique to determine effective
diffusion coefficients in a synthetic bead catalyst and
compared the results obtained with values of an effective
diffusion coefficient calculated using data from N_2
adsorbtion experiments and the structural model proposed
by Wheeler[7]. The discrepancies they obtained confirmed
the necessity to determine the effective diffusion
coefficient experimentally rather than to accept values
predicted theoretically.

Dogu and Smith[39] coupled the dynamic pulse response
technique with a Wicke-Kallenbach type diffusion cell to
measure effective diffusivities in catalyst pellets.
Using their approach both faces of the pellet were exposed to
a flowing reference gas (N_2) and a zero pressure difference
was maintained across the pellet. The passage of a pulse
of diffusing gas (He), introduced at one face of the pellet,
was studied and related to an effective diffusivity. The
method has the advantages of rapidity and the use of small

27

quantities of diffusing component. Furthermore, unsteady state methods in general produce results more relevant to heterogeneous catalysts than steady state methods since dead-end pore effects are not neglected.

Recently Moffat[40] modified the Dogu-Smith dynamic method to allow for operations over a range of total pressures and to facilitate the introduction of pulses of diffusing gas to both faces of the pellet. He evaluated the contributions of Knudsen and molecular diffusion from experimental measurements of the effect of pressure on the time taken for a pulse of test gas to pass through the porous media. Three model systems were used to evaluate this technique: packed beds and pressed pellets of non-porous quartz chips and an array of 100μm capillaries. A straight line relationship between the time taken for the pulse of test gas to pass through the system and the total pressure were obtained in both systems and this relationship was verified for a number of catalysts.

Recently Watanable and co-workers[41] demonstrated that the effective diffusion coefficient measured using unsteady state methods differs from that obtained using a steady state isobaric method. In their experiment, the total pressure response curve arising from stepwise concentration changes at one end of the porous sample, producing unsteady state diffusion through the sample, was observed experimentally using a pressure sensor at the opposite end. The porous material used was a bed of fine glass powder tightly packed giving a porosity of 29%. The flow rates used were set large enough for the flow resistances at the sample surface to be neglected. The gas pair used in the

investigations was N_2-He. The transfer rates of gaseous species in porous media under concentration and total pressure gradients, were considered in terms of the relative contribution of flow and diffusion given by Mason et alia[83]. The unsteady state diffusion equation together with the expressions for the transfer rates of the two species, were solved numerically, using data obtained previously from isobaric flow conditions and diffusional permeability experiments. The theoretical results obtained by using the solution to the nonisobaric rate equations coincided well with the experimental results obtained under various initial conditions for He-N_2 and He-Ar systems. However, assuming an isobaric diffusion condition for this dynamic method, and the pertinent equations solved according to this assumption, the theoretical results obtained differed considerably from the experimental results, indicating that there was the possibility of large errors in obtaining the transport properties by unsteady state diffusion methods without taking into consideration the effect of the total pressure gradients in the system.

Weller and co-workers[27] used the modified two bulb method[23] to measure the effective binary diffusion coefficient of Krypton-85 and Xenon-133 through binary mixtures with He, Ar or Ne permeating a disc of porous graphite at room temperature. The diffusion cell was adapted to permit the continuous counting of a radioactive diffusing gas by a Geiger-Muller tube. One cell compartment was filled with a gas mixture at a definite pressure, the other cell compartment was filled to the same pressure with an identical gas mixture except that it contained a trace of an isotope of one of the component

29

gases. They used Fick's second law to calculate the diffusivities.By examining the variation of the effective diffusion coefficient with pressure and composition they were able to develop a statistical model. The regression model which fitted their experimental results was compared with models proposed by Scott and Dullien[3], Evans[20] and Wheeler[7]. Limited agreement was obtained.

Another technique used to determine diffusivities in porous solids involves measuring the apparent conductivity of a non-conducting porous solid when saturated with a salt solution[3][10]. The apparent specific conductivity of the saturated sample will be less than the true specific conductivity of the liquid. If the pores are distributed at random, the liquid filled cross sectional area available for the passage of current will be a fraction γ of the total cross sectional area, where γ is the porosity of the solid. Furthermore, the current must follow a tortuous path, the length of which is larger than that of the sample so that the apparent conductivity is further reduced. This length ratio is given the symbol τ.[10] Since conductivity and diffusion are closely related processes, effective binary diffusion coefficients were determined from the results by multiplying molecular diffusivities by the ratio γ/τ.

Olsson and McKewan[42] have used a fundamentally different technique for measuring gas diffusivities that is particularly suited for studies in connection with gas-solid reactions. In this method, reactant gas was allowed to diffuse through a porous plug of solid product into a canister that was otherwise sealed. The canister contained loose packed granules of the solid reactant. The

30

diffusivities of the reactant and product gases within the porous solid were deduced from the rate of the reaction, calculated from the rate of change of the weight of the canister.

This method was later used by Turkdogan[13][11] and by Bradshaw[44] to study the diffusion of one gas in the presence of a stagnant gas at room temperature through porous carbon and porous iron, and porous magnetite respectively.

A novel technique has been developed by Hills and co-workers[45] using hollow spheres, obtained by isostatic compression, attached to the end of a hollow diffusion shaft.

Such hollow spheres could easily be held under isothermal conditions during experimental measurements and, due to their geometry, could take advantage of the shrinkage beha-viour of most metallurgically important reactant solids. Such shrinkage, normally taking place during chemical reactions occurring during the formation of the shell, results in the formation of a gas-tight seal around the diffusion shaft. For solids which do not exhibit this shrinkage behaviour the hollow spheres could be sealed to the shaft using a sealing compound. This technique, compared with the conventional diffusion cell, eliminates disadvantages such as inhomogeneity due to conventional pressing methods and difficulties associated with sealing the various components of the cell. For systems that seal without the introduction of sealing compound, the method is unique in that it can allow measurements to be made at high temperature.

31

2.4 DIFFUSIVITY MEASUREMENTS IN POROUS MATERIALS OF METALLURGICAL INTEREST

Two approaches have been adopted to determine diffusivities in porous media of metallurgical interest. Firstly, diffusion coefficients have been obtained directly from measurements of the rate of migration of gaseous species through different porous media. Secondly, values of effective diffusivities have been deduced from kinetic data for the reduction of a porous solid by a reactant gas. Unfortunately this latter technique suffers from two major deficiencies. A model mechanism for the reaction must be assumed and for gas solid reactions in which both molecular and Knudsen diffusion are significant, it is very difficult to deduce separate values for the effective binary diffusion coefficient, D_{ABeff}, and Knudsen diffusion coefficient, $D_{K,A}(D_{K,B})$, without recourse to a structural model involving parameters requiring measurement of the geometry of the pore network. Results obtained by each of these methods will be considered separately in the subsequent sections.

2.4.1 Diffusivity Data from Direct Measurements

Although, as mentioned in the previous section, there have been many investigations into the diffusional characteristics of catalytic reaction systems used in the chemical engineering industries[24,30,34,46,47,48], very little work has been performed on porous material of metallurgical interest. Of the small number of investigations which have been carried out on such systems the majority have involved gas diffusivity determinations at room temperature, very few at higher temperature or under simulated reaction conditions.

32

As already mentioned, McKewan and Olsson[42], in order to improve the understanding of the mechanism of iron ore reduction, measured the rate of molar diffusion of hydrogen and water vapour through discs of reduced iron. Hydrogen was allowed to diffuse through the porous iron disc into a canister which contained loose packed granular wustite. The hydrogen reduced the wustite and the water vapour formed diffused back through the disc into the external gas stream. Since the hydrogen will diffuse through porous medium more rapidly than water vapour, a slight positive pressure was obtained inside the canister. The maximum pressure differential recorded was found to be about 0.04 atm. The rate of diffusion was determined from the recorded weight loss due to reduction of the wustite inside the canister. The effective diffusion coefficient, $D_{H_2-H_2O,eff}$, since a molecular mechanism of diffusion was considered to occur, was found to be 1.46 cm^2/s at 800°C and the ratio $D_{H_2-H_2O,eff}/D_{H_2-H_2O}$ was observed to increase with increasing reduction temperature. Measurements were made at 800, 900 and 1000°C and showed that reduction at these temperatures and atmospheric pressure was limited to a great extent by gaseous diffusion between the bulk phase and the iron-wustite interface.

Hawtin and co-workers[48], investigating the importance of gaseous diffusion in the reaction of gases with graphite, determined the effective diffusion coefficient of the He/N$_2$, He/Ar and CO/CH$_4$ gas pairs through graphite at temperatures between 20 and 600°C. The experimental rig especially designed for this purpose was a variation of the Wicke-Kallenbach method of measuring effective binary diffusion coefficients. The

specimen, in the form of a hollow cylinder of graphite was mounted in a specially designed cell to withstand high temperature. The molecular flow rates of the gases through the graphite cylinder were determined from the total rates of flow of the gases and the compositions of the exit gas streams. The value of the ratio D_{ABeff}/D_{AB} was found to be dependent on the structure of the material used and independent of temperature. The values obtained for this ratio varied between 0.0065-0.0092.

Turkdogan and co-workers[13] also measured effective diffusivities of a range of gas pairs in porous graphite. The experimental technique that they used was similar to that used previously by McKewan[42]. For the CO-CO_2 gas pair at room temperature, conditions were chosen such that CO_2 diffused through stagnant CO, while at elevated temperature, with the CO-CO_2 and H_2-H_2O gas pairs, equimolar counter-current diffusion conditions were employed. For the experiments at room temperature the rate of diffusion of CO_2 through the porous carbon was calculated from the rate of weight change due to the absorbtion of CO_2 by a mixture of ascarite and anhydrone contained in the diffusion cell and connected to a CO-CO_2 atmosphere solely through a plug of the porous carbon. In the experiments at high temperatures, between 500 and 900°C, CO and H_2 diffused through the carbon sample, to react with copper oxide and the reaction products which formed, CO_2 and H_2O respectively, then diffused back through the sample. The diffusion rate was again determined from the rate at which the weight of the total diffusion cell changed, in this case due to the reduction of copper oxide. From the results obtained, Turkdogan concluded that

diffusion in graphite is essentially molecular. The relatively low values for the measured diffusivity ratio indicated that most of the diffusion flux takes place via interconnected large pores.

Paulin[49] determined the effective diffusion coefficient of CO_2-Ar mixtures in porous lime using the technique proposed by Hills[45] described in the previous section. The diffusion coefficient measurements were conducted using a hollow lime sphere prepared from spherical compacts of calcium carbonate formed in a rubber mould using a conventional press. A calcium carbonate sphere, placed on the end of a twin bore, alumina sheath, was introduced into a furnace tube, sintered in CO_2 at 870°C and then decomposed in air at 950°C. This treatment caused the sphere to contract slightly on to the alumina sheath and form a gas tight seal. This arrangement therefore constituted the diffusion cell. One gas could be passed over the outer surface of the sphere while another could be introduced down one of the bores of the alumina shaft into the hollow space within the sphere. The flow rates and compositions of the gas mixtures emerging from the furnace tube and the exit bore of the alumina shaft could be measured. Although the experiments were not performed under isobaric conditions, the maximum measured difference in pressure between the inside and outside of the sphere was only 0.03 atm at 950°C. The values obtained for the effective diffusion coefficient are therefore valid, since it has been shown previously by Truitt and co-workers[32] that small pressure drops across the porous material do not materially affect measured values of the effective diffusion coefficient. The values encountered for the effective diffusivity of an argon-

35

carbon dioxide mixture, $D_{CO_2-Ar,eff}$, at 950°C were between 0.12 to 0.22 cm²/s for lime spheres with porosities varying from 52 to 70%.

Campbell[50] performed measurements on lime spheres using the same technique as Paulin and obtained similar results. Campbell has also measured the permeability of hydrogen through porous lime as a function of the total pressure in the system at room temperature. The results obtained were interpreted using the Dusty Gas Model[20] which predicts the permeability to vary linearly with total pressure in the system, the permeability at zero pressure being equal to the Knudsen diffusion coefficient. Values of the Knudsen diffusion coefficient of H_2 at room temperature were found to vary from 0.208 to 0.256 cm²/s for lime spheres with porosities ranging from 48 to 53.8%. The corresponding values for the Knudsen diffusion coefficient of carbon dioxide gas at 950°C extrapolated from these results were 0.0925 cm²/s to 0.109 cm²/s respectively. Since these values for the Knudsen diffusion coefficient of CO_2 were similar to those obtained for the effective diffusivity $D_{CO_2,eff}$ measured previously, he concluded that the controlling diffusion mechanism in porous lime is Knudsen diffusion.

Two other systems of metallurgical interest were also studied by Campbell: porous iron obtained by reducing ferrous chloride with hydrogen and porous nickel obtained by reducing nickel oxide with H_2. Permeability experiments were performed on both materials and the results interpreted in the same way as for the lime spheres. The values obtained for the Knudsen diffusion coefficient for H_2 in the porous iron of 206 cm²/s at room temperature is excessively high.

Campbell attributed this to the fact that the porosity obtained in this material was extremely high (80%) and the spherical shell obtained after reduction exhibited very low mechanical strength. In porous nickel the value of the Knudsen diffusion coefficient for hydrogen at room temperature varied as a function of the reduction temperature employed in obtaining the porous sample. Values of 3.95 cm^2/s, 5.35 cm^2/s and 10.6 cm^2/s were obtained when the reduction temperature of the nickel oxide was 350°C, 450°C and 250°C respectively.

In order to measure the effective diffusivities of a H_2-Ar gas pair in porous iron and porous nickel, Campbell adopted an isobaric counter-current diffusion technique. The effective diffusion coefficients, $D_{H_2-Ar, eff}$, reported were 0.5 cm^2/s for porous iron and 0.24 cm^2/s for porous nickel, both at 292 K. The average tortuosities obtained were 1.62 and 1.87 for porous iron and nickel respectively.

Partridge and Wall[51] have studied the reaction of iron chloride with hydrogen. They established that the rate of reaction was controlled by the transfer of heat to the reaction interface and by the transfer of hydrogen chloride away from it. In order to check the validity of their model they performed isobaric counter-current diffusion experiments with a helium-nitrogen gas pair at room temperature, using apparatus similar to that used for graphite by Hewitt and Morgan[8]. The value of the diffusivity ratio γ/τ reported was 0.477 corresponding to a tortuosity factor of 1.81 which is in general agreement with Campbell's value[50].

Kim and Smith[52] have measured diffusion rates using an

37

isobaric method in a Wicke-Kallenbach type of diffusion cell, in both sintered and unsintered nickel oxide pellets and reduced porous nickel. Three binary gas systems were used: $He-N_2$, $He-CO_2$ and $CO-CO_2$, at temperatures from 25° to 200°C. The measurements lead to tortuosity factors as high as 100 for highly sintered nickel oxide (γ = 3%) pellets. They reported higher diffusivities and porosities in the porous nickel obtained by reducing highly sintered nickel oxide pellets in hydrogen than were obtained on reducing unsintered nickel oxide.

Ray[53] has employed two different experimental techniques in his work in order to allow the calculation of the effective diffusion coefficient and the tortuosity factor. In one of the methods he measured the flow of a gas under a considerable pressure gradient through a sample of porous reduced cobalt, of porosity 65%, sealed between two glass tubes. One side of the porous sample was maintained at atmospheric pressure, while the other side was connected via a large evacuated flask to a mercury manometer. The build up in pressure over an extended period of time was recorded. By equating the expression for forced flow through a uniform capillary[3] with the rate of accumulation in the flask, and neglecting the diffusional contribution, he obtained plots of pressure versus time from which he calculated the diffusivity ratio. This he found to be equal to 0.65 which is equivalent to a tortuosity factor of 1.

The second method used by Ray[53] was essentially the classical isobaric experiment in which the rate of counter-current diffusion of H_2 and Ar through a porous reduced nickel

sample was measured. A hydrogen concentration cell was
used to measure the concentration of H_2 in the H_2 rich bulk
stream leaving the diffusion cell. The ratio γ/τ was
calculated using the equation for the diffusion flow given
by Mason[20] which requires the value for the Knudsen
diffusion coefficient to be known. This value was calculated
using the value of the pore radius obtained from measurements
involving a nitrogen adsorbtion technique (BET), and by
assuming the porous material to consist of straight round pores.
The diffusivity ratio, γ/τ, was found to be equal to 0.06
which for a porosity of 59% will give a value for the
tortuosity equal to 9.83. Unfortunately Ray did not use
the same sample in order to check the validity of the two
experimental methods proposed. It does seem strange however,
that the tortuosity factor in porous reduced nickel is around
ten times bigger than that in the reduced porous cobalt
sample.

In order to test the theoretical model for the reduction of
Carol Lake hematite pellets to magnetite, proposed by
Matyas and Bradshaw[54], Bradshaw and Unal[44] performed
direct measurements of interparticle diffusivities at room
temperature in hematite and magnetite. The results
obtained were extrapolated to the reaction temperature and
compared favourable with those predicted by the theoretical
model, confirming the dominant influence of gaseous diffusion
in the reduction of Carol Lake pellets to magnetite. The
Knudsen diffusion coefficient was obtained from measurements
of permeability coefficients at various total pressures and
by extrapolating to zero pressure according to the Dusty Gas
Model proposed by Mason et alia[20]. The values obtained

for the Knudsen diffusion coefficient and the 'viscous flow parameter'* B_o/μ, for H_2 in magnetite at 292 K were 2.82 cm²/s and 5.97 cm²/s.atm. respectively.

The effective diffusion coefficient was measured using a technique similar to that developed by Turkdogan[13] and outlined in a previous section. In Unal's work CO_2 was again used as the diffusing species but N_2 was the stagnant gas.[105] The driving force for the diffusion, the CO_2 concentration gradient, was maintained by absorbing the carbon dioxide into soda lime contained within a sealed chamber on one side of the porous material. The diffusion cell incorporating this sealed chamber, was suspended from a load measuring device so that the diffusion flux could be determined by monitoring the change in the cell weight. The conditions developed by this technique are not strictly isobaric, but Bradshaw and Unal showed theoretically that the contribution to the total flux made by viscous flow and Knudsen diffusion was very small for Carol Lake pellets.[44] The value for the effective binary diffusion coefficient of CO_2-N_2 in a reduced magnetite sample at 800°C was 0.24 cm²/s, giving a diffusivity ratio, γ/τ, of 0.15. By extrapolating the results obtained from permeability measurements and diffusion measurements performed at room temperature, the effective diffusivity, $D_{H_2,eff}$, in magnetite was calculated to be 0.122 cm²/s at 600°C and 0.22 cm²/s at 850°C.

Turkdogan and co-workers[11] have measured effective diffusivities in porous iron produced by the reduction of hematite in hydrogen using the experimental technique that

---

* See section 3.1

they used for diffusion measurements on carbons and which has been described earlier in this chapter. The basic features of the technique are that the relationship between the fluxes of the diffusing gases through the porous media is fixed by the stoichiometry of a fast chemical reaction involving one or both of the gases and a solid phase, and that the overall rate of diffusion is experimentally determined from the weight change due to this reaction.

At low temperature they used CO_2 and He as the gas pair, and absorbed the CO_2 in the same 'sink' material as in the experiments on carbon[13]. At higher temperatures, up to 600°C, the canister was filled with a mixture of wustite and iron powder, the wustite being reduced by the hydrogen that diffused counter-currently with water vapour through the porous iron sample previously reduced in situ. The rate of diffusion was determined from the weight loss. The effective diffusivity measured at 20°C and 0.9 atm for the sample of porous iron reduced previously at 800°C was 0.101 cm²/s. At a temperature of 600°C and 1 atm pressure under equimolar flow conditions, the effective diffusivity of hydrogen, $D_{He,eff}$, in the H_2-H_2O mixture through the porous material was 0.124 cm²/s. The results obtained from direct measurements for H_2-H_2O mixtures diffusing through reduced porous iron at 600°C were in excellent agreement with those derived from kinetic reduction data[43].

Szekely and Evans[55], in order to test the structural grain model they proposed for the reduction of nickel oxide pellets with hydrogen, performed isobaric experiments using an experimental arrangement identical to that first used

41

by Mason[20]. The apparatus consisted of a porous plug
of the solid matrix, separating two cavities which were
also connected by a horizontal glass tube containing a
plug of mercury. Hydrogen was passed rapidly through one
cavity and helium through the other. The different
diffusivities of helium and hydrogen caused a net flux
through the porous plug and, as a consequence, the mercury
plug moved along the glass tube thus maintaining equal
pressure on both sides of the porous matrix. The initial
velocity of movement of the mercury plug was determined by
recording pulses from two photoelectric cells, placed under
the glass tube, on a fast strip chart recorder. The net flow
through the porous plug, calculated from velocity measurements,
was equated with the expression for the net flux derived
from the Dusty Gas Model[20]. The Knudsen diffusion co-
efficient has to be known before this expression can be
used to determine an effective diffusivity. Szekely had
not measured the Knudsen diffusion coefficient, however,
and therefore, after determining the grain size, he chose a
structural model which allowed him to estimate the tortuosity
factor. The value that he found was 1.1 and he assumed this
value to be constant throughout his work allowing determina-
tion of the Knudsen diffusion coefficient. He then calculated
the effective diffusivity, $D_{H_2,eff}$, using the Bosanquet inter-
polation formula. The value obtained was compared with values
predicted after he had adjusted three parameters- the tortuos-
ity,the pre-exponential factor and the 'activation energy' for
the chemical rate constant. The behaviour predicted by their
model fitted only a few of their experimental results.
Clearly the assumptions used in developing the model, that
the grains are spherical and uniform in size and reactivity,
are not justified.

2.4.2 Diffusivities deduced from reaction kinetic data

Although it is generally preferable to perform independent measurements of effective diffusivities, many workers have deduced their values from actual kinetic measurements on gas solid reactions. Such deductions can, of course, only be made in the light of a model for the reaction, so that a review of this approach necessarily involves a review of reaction models.

Because of its industrial importance, a great deal of work has been done during the past four decades on the gaseous reduction of iron oxides. Despite the extensive literature, which has been reviewed by Bogdandy[56] and by Szekely[57], only slow progress has been made in understanding the rate controlling process and it is still not possible to produce a generalised model for the reaction mechanism. Difficulties in reconciling the results of different investigations are partly due to the wide variety of different materials studied and partly due to differences in the experimental equipment used, since kinetic measurements can be influenced by factors such as the geometry of the experimental system and the flow pattern of the reacting gases. Early work[58,59,60] on the reduction of hematite with hydrogen suggested the rate controlling mechanism to be the chemical reaction at the interface between the product and reactant solid layers. On the other hand, Kawasaki[61] and Bogdandy[56] proposed from an early date that the rate controlling step was the counter-diffusion of hydrogen and water vapour through the porous iron. Warner[12] showed that both of these steps in the reaction mechanism could jointly control the rate. Work done by Olsson and McKewan[42] on the counter-diffusion of hydrogen

43

and water vapour in porous iron pellets indicated that, with increasing temperature, pore diffusion in the product layer became a dominant factor in controlling the rate of reaction.

Turkdogan[43.] suggested that there are three major limiting rate controlling processes:

(i)   uniform internal reduction

(ii)   limiting mixed   control

(iii)   gaseous diffusion,

depending on temperature and size of the particle.

Numerous mathematical models have been developed in order to elucidate and predict the rate of a heterogeneous gas solid reactions as a function of the degree of the separation between the product and reactant solids. When, on a macroscale examination of a partially reduced pellet, a sharp interface between the unreacted core and the reacted shell is observed, shrinking core behaviour is assumed. When the interface is of definite thickness, however, containing both reduced and unreduced grains, diffuse interface behaviour is assumed. The different models have already been adequately reviewed.[56][57][62]

The shrinking core model has been remarkably successful for the interpretation of experimental results. When it was first proposed, Yagi and Kuni[63] considered that individual rate controlling steps operated. The rate of reaction could be related to the rate of movement of the interface by the mass conservation balance. The relationship derived related the fractional unreduced mass of oxide (1-x) to the reduction time. A chemical control model would predict that $(1-x)^{1/3}$ varied linearly with time.

44

The proportionality constant involves the chemical reaction rate constant so that values of this constant can be determined by measuring the rate at which a dense particle reacts at a known temperature with a gas of a known composition. When plots of $3(1-x)^{2/3} - 2(1-x)$ with time presented a linear relationship, however, the controlling mechanism was considered to be diffusion in the product layer. Finally, mass transfer in the boundary layer was taken to be the controlling step when linear plots of $(1-x)$ against time were obtained.

Hills[62], however, showed that the differences between the patterns of reaction behaviour predicted by the three models are too small for an unequivocal decision to be made. He showed that the evidence which had previously been taken to indicate either chemical control or mixed control could also be predicted and explained in terms of a mass transport control model. This model took account of both mass transfer resistance within the boundary layer and diffusion resistance across the reduced layer. Considering these facts, Hills proposed an improved experimental strategy in which all parameters involved in the transport control model are measured independently and used to predict the rate of reaction on the assumption that it is transport controlled. The other reaction models, he suggested, should only be considered if measured reaction rates are found to be significantly slower than this prediction.

It is not often realistic, however, to think in terms of a single rate controlling step since there may be other factors that have almost equal effect on the overall rate. Rate equations based on a mixed control model which assume

45

shrinking core behaviour have been formulated by many workers[12,64,43,63,65]. The equations describing the fluxes of product and reactant gases were solved simultaneously as a function of reaction stoichiometry. By combination of these equations the overall rate was described in terms of a "driving force" and three sets of resistances, namely:-

(i)   gas phase mass transfer

(ii)   diffusion of reactants and products through the reacted shell

(iii)   chemical reaction occuring at the interface separating the reacted and unreacted regions.

By suitable separation of variables, the above workers have been able to develop functions of the degree of reaction which yield linear plots from which the effective diffusion coefficient and the chemical rate constant can be determined.

We shall focus our attention for the moment on those papers which presented a value for the effective diffusivity from experimental data considered in terms of the shrinking core model.

Kawasaki and co-workers[61], studying the reduction of iron oxide pellets and bars within hydrogen and carbon monoxide at temperatures between 870 and 1200°C, reported that the reduction rate was controlled by the counter-diffusion of reactant and product gases between the reaction zone and the bulk gas. By applying Fick's first law for diffusion, values for the diffusion constants were determined from experimental data. The diffusion constant was defined as $K = 960 \, DZ/RT$, where D is the molecular diffusion coefficient and Z is the diffusivity ratio γ/τ. From

their experimental work the progress of the reduction
process agreed with their theoretical equation only if
improbably high values of γ/τ of 1 for carbon monoxide and
0.7 for hydrogen were used.

Warner[12] has studied the reduction of dense hematite in
hydrogen in order to elucidate the effect of gaseous diff-
usion on the reduction rate. His experimental results were
consistent with a mixed control mechanism involving the
interaction of gaseous diffusion effects with a first
order reversible chemical reaction at the iron wustite
interface. By taking into account the diffusional
resistance offered by the bulk gas phase, he estimated mass
transfer coefficients from a dimensionless correlation based on
experiments at room temperature with the naphthalene-air
system. The transport of hydrogen and water vapour across the
porous reduced iron product layer was consistent with
molecular diffusion, rather than with Knudsen or combined
diffusion, in the light of his study of the nature of the
pores of the reduced material. Although he determined the
pore size for his samples using a mercury porosimetry
technique, obtaining values ranging from $0.4/\text{to } 1.10^{-4}\text{cm}$,
he suggested that the effective pore size for diffusion
would be much larger. His study showed that the structure
contained "bottlenecks" many times smaller than the bulk
pores and the mercury porosimetry technique measures the
minimum constrictions in a pore length[12].

Warner evaluated the effective diffusion coefficient using
a function that related the rate of the reaction at the
interface to the local gas composition and incorporated
a general equation for the transport of hydrogen expressed

in terms of the total driving force and the total transport resistances. Values for the diffusivity ratio γ/τ of 0.33, 0.39, and 0.51 were obtained at temperatures of 750, 850 and 950°C respectively leading to a mean tortuosity factor, τ, of 1.3

Turkdogan and Vinters[43] performed similar experiments with high grade hematite ore. Taking into account the effect of the particle size and the reaction temperature on the time for reduction, they showed the rate controlling mechanism for large hematite pellets to be gaseous diffusion in the product layer. The derived rate of reduction was based on the following assumptions:

(i)   the reduced iron formed a shell around the spherical oxide core

(ii)   a pseudo-steady state was established for the counterflux of H_2O and H_2 through the magnetite, wustite and iron layers and also that the equilibrium compositions were maintained at each interface.

(iii)   the porosity and the effective diffusivity were uniform and independent of reduction time at a given temperature.

The expression obtained by combining the equimolar counter flux of H_2O and H_2 through the reduced iron with the mass balance of oxygen removal, expressed as a function of the relative thickness of the reduced iron, permitted determination of the effective diffusion coefficient from the slope of plots of $[\frac{1}{2} - \frac{x}{3} - \frac{(1-x)^{2/3}}{2}]$ against time.

$D_{H_2,eff}/D_{H_2/H_2O}$ ranging from 0.02 to 0.3 were reported for reduction temperatures ranging from 500 to 1200°C. At 800°C the value of the binary diffusion coefficient was

0.88 cm²/s and the ratio was equal to 0.1 . In their work[43], values for the effective diffusion coefficient were also calculated using reduction data presented by McKewan[91]. The values obtained varied between 0.65 and 1.12 cm²/s, with γ/τ between 0.079 and 0.13, at 800°C, for synthetic hematite ore pellets and sintered hematite ore pellets respectively, indicating that similar values of the effective diffusion coefficient apply in porous iron produced from different types of hematite at the same reduction temperature.

Tien and Turkdogan[65] used the same experimental technique and the same method of interpreting the experimental data in their investigation of gaseous diffusion in wustite formed by partial reduction of the same type of hematite.

For experiments conducted at temperatures of 700°C to 900°C, effective diffusion coefficients of H_2O-H_2 in wustite were found to be within 20% of those in porous iron.[88]

A number of mathematical models[54][65][66] have been proposed to predict reduction rates when a diffuse interface is present. The fundamental equation in these models is based on a mass balance for the reactant gas in a diff- erential volume element of the pellet. Quasi-steady state conditions are assumed since accumulation in the control volume makes a negligible contribution to the equations. The two important parameters which influence the course of reduction are the intrinsic reaction rate of the solid and the effective diffusivity, $D_{H_2,eff}$, the latter being given by the Bosanquet formula. The difference between these models lies in the way the various workers have estimated the reaction rate per unit volume of solid.

Szekely and Evans[66] obtained an expression for the rate of reduction in terms of the rate of advance of the reaction front in individual spherical grains each of which reacted in a shrinking core manner. Although their model, compared with the shrinking core model, does incorporate structural parameters, such as porosity and particle size, it has a limited applicability since the grains are assumed to be identical, spherical and of equal reactivity. Moreover, the effective diffusivity, D_{Aeff}, has to be predicted, using the Bosanquet interpolation formula from grain size measurements, the tortuosity and the rate constant being adjustable parameters.

In order to test the validity of their model relative to actual reaction data, Szekely and Evans performed experiments on NiO using hydrogen[55]. They also measured the grain size and porosity of the porous nickel and the effective diffusivity, $D_{A,eff}$, and evaluated the mass transfer coefficients under the bulk flow conditions. Predictions from their model fitted only a few of their experimental results. The value of the tortuosity factor, τ, that they reported was 1.1. The same model was later[67] applied to the reduction of cylindrical discs of nickel oxide by hydrogen within the temperature range 227-712°C. The experiments were conducted under conditions of diffusion control and the results obtained permitted the evaluation of the effective diffusivity of hydrogen, $D_{H_2 eff}$, from plots of the conversion function versus time. Values between 0.382 and 0.451 cm²/s were encountered for reduction temperatures from 321°C to 361°C respectively. The value of the average tortuosity factor, 2.83, was calculated as a function of a chosen value for

50

the effective grain size which gave the minimum variance in the tortuosity value and the effective diffusivity obtained from kinetic data. Although they claimed to have used the Dusty Gas Model to calculate the Knudsen diffusion coefficient, it is clear from Mason's paper[20] that the model does not enable the Knudsen diffusion coefficient to be predicted; it merely shows how it can be determined from the results of permeability experiments. No such results were reported by Szekely and Evans.

Bradshaw and Matyas[54] attempted to measure a chemical reaction rate for the single particles within Carol Lake pellets by crushing the pellets and screening the product to obtain "micropellets" which possessed all the characteristics of the original pellets. Two criteria governed the size of these particles. Firstly the diffusional resistance between the grains of the micropellets had to be negligible and secondly the specific surface area of the micropellets had to be the same as that of the original macropellet. With these two criteria met, Bradshaw and Matyas maintained that they could measure directly the intrinsic reaction rate that would apply within a reacting pellet.

The value obtained was subsequently used to obtain a solution to the relevant differential equations in order to obtain a value for the effective diffusivity, $D_{CO,eff}$, which they considered as being equal to the effective binary diffusion coefficient since Knudsen effects were not taken into account. For reduction experiments performed on Carol Lake hematite pellets with CO, values of $D_{CO-CO_2,eff}$ equal to 0.12 cm²/s and 0.18 cm²/s at temperatures of 600°C and 800°C respectively, were calculated. These values

51

correspond to a tortuosity factor of 2.6 for a material with an average porosity of 30%. In order to test the validity of this model, Unal and Bradshaw[44] made the independent measurements of the effective diffusion coefficients at room temperature for the N_2-CO_2 gas pair that have already been described.

When the results were extrapolated to the reaction temperature and to CO-CO_2 gas mixtures using the Dusty Gas Model, good agreement was obtained between the two sets of values at 600°C, lesser agreement being obtained at 850°C.

Sadrashemi[69] has studied the reduction of Carol Lake hematite pellets using hydrogen as the reducing gas instead of CO, within a temperature range of 600° to 1000°C. Since a diffuse interface was obtained when reduction was performed at temperatures below 800°C, the experimental results obtained at 750°C were interpreted using the Matyas-Bradshaw model. The average diffusivity calculated from the kinetic data obtained was 0.86 cm^2/s. He reported a value for the tortuosity factor of 2.3 calculated from the Bosanquet interpolation formula and a calculated value for the Knudsen diffusion coefficient in a cylindrical average pore of radius $\bar{r}$ = 2μm measured using the BET technique. The calculated value for the Knudsen diffusion coefficient was 44 cm^2/s at 750°C.

Another system of metallurgical interest was studied by Hills[70]. He elucidated the controlling mechanism of decomposition of calcium carbonate by showing that the rate of decomposition was controlled by the transfer of heat to the reaction interface and by transfer of CO_2 away from it.

52

From the mathematical equations derived, expressed in terms of the total driving force and total resistances for heat and mass transfer, and the extensive experimental data obtained related to the progression of the reaction at various gas temperatures and compositions, the flow relevant transfer coefficients, namely the mass transfer coefficient, the diffusivity, the thermal conductivity and the heat transfer coefficient, were obtained. Good agreement was obtained between the transport parameters measured and values determined from independent experiments reported in the literature. A value for the effective diffusivity of carbon dioxide, $D_{CO_2,eff}$, of 0.0837 cm²/s at a temperature of 850°C was reported.

2.5 FACTORS AFFECTING THE STRENGTH OF SINTERED IRON OXIDE COMPACTS

In order to obtain meaningful measurements of the gaseous diffusion characteristics of a porous medium it must be free from cracks and exhibit a uniform structure. Unfortunately, iron oxide compacts are susceptible to cracking during reduction, primarily due to the crystallographic changes associated with the transition from hematite to magnetite.[71] The tendency for cracking to occur may however be suppressed, if the pre-reduction strength of the iron oxide compact is sufficiently high. Examination of the literature indicates that the principal factors controlling the strength of sintered iron oxide compacts are the original particle size of the ore, the chemical composition and the firing temperature and time.[72,73,74].

It has been demonstrated by a number of workers[75,76] that the compression strength of sintered hematite compacts may be controlled by the degree of grinding of the original ore, and that the best results are achieved when more than 60% of the raw material exhibits a particle size of less than 44µm.

Specific studies of the relationship between the chemical, mineralogical and fired product properties of various types of pellets have also been reported[77,78,79]. The results obtained have demonstrated the importance of the fluxible gangue and ultra fine particle constituents in the development of inter-particle bonding in pellets.

Thomas et alia[74] have shown that with increasing time, temperature and lime concentration more slag phase is formed,

54

thus consolidating the structure. The slag phase performs two major functions during the sintering process. Firstly, it bonds the particles together and secondly, it promotes grain growth by dissolving fine hematite particles and then precipitating hematite on the lower energy surfaces of large particles.

Seth, Ross and Strangway[80,81] have studied the effect of CaO additions, from 2 to 10 mass %, on the reducibility of pure hematite. It was found that the maximum increase in reducibility was obtained with 2 mass % CaO and that this improvement was due neither to a change in the initial porosity, nor to that developed during reduction. The observed improvement in reducibility was attributed to the nature of the reduction mechanism in which wustite is believed to be unstable in the presence of lime, at least in the solid state, and dissociates into metallic iron and dicalcium ferrite. Thus the action of the lime addition on wustite results in the formation of metallic iron and dicalcium ferrite according to the reaction:

$$2CaO + 3FeO = Fe + 2CaO.Fe_2O_3$$
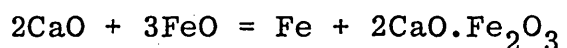
Furthermore, the calcium ferrite so formed will on reduction, give iron and lime directly without producing wustite as an intermediate phase. Edstrom[71] has suggested that this may be an oversimplification since other compounds such as $CaO.2Fe_2O_3$ and $CaO.Fe_2O_3$ may also take part in the reaction, although the basic mechanism is essentially the same. Of the various lime compounds, Edstrom suggests that reduction via $CaO.2Fe_2O_3$ dominates since this is the most important bonding phase in basic sinter.

CHAPTER 3 – <u>THEORETICAL DEVELOPMENT OF THE DUSTY</u>

<u>GAS MODEL</u>

3. PHENOMENOLOGICAL STATEMENT OF EQUATIONS GOVERNING CHEMICALLY AND MECHANICALLY DRIVEN GAS FLOWS THROUGH POROUS SOLIDS

When the Dusty Gas Model was first proposed[82] it contained two new ideas. In the first place, it suggested that interactions between a porous solid and gases diffusing through it could be treated as if the solid were one component in a multi-component gas mixture. It was further suggested[19] that these interactions could be analysed by assuming that the 'dust' particles behaved like large spherical molecules and that standard kinetic theory of gases could be applied to collisions between these giant molecules and the normal gas molecules surrounding them.

Of these two assumptions, the first was phenomenological in nature and the second structural. Evans and his coworkers (20, 83, 84) applied the model extensively, but soon dropped its structural aspect, applying the model purely in its phenomenological form[84]. The basic development that they presented was extremely elaborate in order to include treatments of temperature, forced and pressure diffusion and the gradient of the rate of distortion tensor as well as chemical diffusion. They acknowledged that many of these non-chemical effects were of second order importance, but they had originally thought that the inclusion of the pressure diffusion term in the general formulation would fully account for the effects of variations in the total pressure within the pores. They subsequently found,

56

however, that accurate diffusion fluxes in binary gases under non-isobaric conditions could only be predicted if the binary equations generated from their generalised Dusty Gas equations were augmented by a 'viscous flow term' and that the true pressure diffusion term was also of second order importance. The treatment for the binary gas mixture that they then presented, mirrored their successful treatment for the permeation of a single gas through a porous solid where the Dusty Gas equation was similarly augmented by a 'viscous flow term'.

Although the phenomenological nature of the Dusty Gas Model was emphasised by Mason and Marrero[21] in their review, they used arguments of momentum transfer to develop the general equations governing the diffusion of gases in porous solids. Thus the majority of workers still think of the Dusty Gas Model as a structural model. This is unfortunate since it is the phenomenological nature of the model that is its true strength, dictating the proper experimental strategy to be applied to gaseous diffusion in porous materials.

A straight forward phenomenological development of the Dusty Gas Model is therefore presented here dealing solely with first order effects. Effects due to true pressure diffusion are normally of second order (see Bird, Stewart and Lightfoot pp 567[85]), as are effects due to thermal and forced diffusion, so that none of these effects are

introduced into the general treatment. The treatment
presents an irreversible thermodynamic base for the
diffusion interactions between the actual gases and the solid
as if the gases and the solid formed a single phase treated
as a continuum. This allows adequate treatment of all the
true diffusion effects of normal importance within the
porous media including the Knudsen interactions between each
individual gas species and the surfaces of the pores. In
the presence of an actual pressure gradient through the
porous media, however, the interaction between the flowing
gas mixture as a whole and the pore walls is essentially
heterogeneous in nature in that it involves inertial and
surface friction effects as the gas mixture flows through
the tortuous channels. It is impossible for a
thermodynamic treatment based on the incorporation of the
solid particles as one component in a multi-component
mixture to account for these heterogeneous effects, but their
effect can be 'added on' at a later stage in the treatment.

The treatment starts by describing diffusion phenomena in
gases within the pores of a porous solid in terms of the
Stefan-Maxwell equations for multi-component diffusion.
However, one component in the multi-component mixture to
which the equations are applied is taken as the porous solid
itself, imagined to consist of large dust particles
suspended in the gas mixture and behaving as very large gas
molecules.

These molecules are assumed to behave in the following manner:-

(i)   they reduce the fraction of the total volume available
       for the true gas molecules to occupy to γ , the
       porosity of the porous solid, and lengthen their
       diffusion path by a tortuosity factor τ .

(ii)   they are distributed in space in such a way that the
       'total pressure' of the imagined gas mixture - actual
       gas PLUS dust - is constant.*   For convenience, when
       we are concerned with this total mixture, we will add a
       superfix '+' to the variable concerned.   Thus the
       total pressure of the gas-plus-dust-mixture is p^+, and
       it is this pressure that is assumed to be constant.

(iii) they provide the frame of reference against which to
       analyse the multicomponent diffusion problem.   Their
       net flux relative to this frame of reference is
       obviously zero.

(iv)   they collide with the gas molecules

---

*FOOTNOTE:-   This assumption is slightly different from the
comparable assumption in the treatment of the Dusty Gas
Model proposed by Evans, Watson & Mason.   They assumed the
dust molecules to be uniformly distributed in space so that
their partial pressure gradient would be zero.   Since the
net flux of the dust is zero, Evans, Watson & Mason were
additionally required to assume that the dust molecules
experience an applied force which exactly balances the
summed effect of the partial pressure gradients of the real
gas molecules.   The assumption made here that the total
pressure of the fictitious gas-plus-dust-mixture is constant
amounts to the same thing, is mariginally more in keeping
with the thermodynamics of gas mixtures and is considerably
easier in concept.

(v)   they have molecular masses and diffusion (or

collision) volumes that are effectively infinite (this

was not explicitly stated by Evans, Watson & Mason, but

is implied in their treatment)

3.1   THE FORMULATION OF THE GENERAL EQUATIONS

The Stefan-Maxwell equations for an N component gas mixture

diffusing within a porous solid can then be written down as:-

$$\nabla \overset{\rightarrow}{c_i^*} = \sum_{j=1}^{j=N+1} \frac{1}{c_T^+ D_{ij}^+} \left\{ c_i^{+*} \overset{\rightarrow}{n_j''} - c_j^{+*} \overset{\rightarrow}{n_i''} \right\} \tag{3.1}$$

where $\overset{+}{c_i^*}$ etc refer to mole fractions in the gas-plus-dust-

mixture and the symbols $\overset{\rightarrow}{n_i''}$ and $\overset{\rightarrow}{n_j''}$ refer to the <u>diffusion</u>

fluxes of the gas species 'i' and 'j'. The summation is

made over N+1 species to include the dust as well as the N

true gas species

In starting from the Stefan-Maxwell equation, it is being

assumed that the pressure and temperature gradients are

insufficiently great for pressure and thermal diffusion

effects to be anything but negligible. Massive heat flows

would be necessary to sustain temperature gradients within a

porous solid large enough to invalidate this assumption as

far as thermal diffusion is concerned; the validity of this

assumption has already been discussed from the point of view

of pressure diffusion.

The following relationships apply in the fictitious true-

gas-plus-dust mixture:-

$$\overset{+}{C}\!{}^{*}_{i} = \frac{p_i}{p^{+}_{T}} \quad ; \quad C^{+}_{T} = \frac{p^{+}_{T}}{RT} \tag{3.2}$$

so that, since the net flux of the dust is zero, we can

rewrite equation (3.1) in the following form:-

$$\nabla p_i = \sum_{j=1}^{N} \frac{RT}{p^{+}_{T}D^{+}_{ij}} (p_i \vec{\dot{n}}''_j - p_j \vec{\dot{n}}''_i) - \frac{RTp_d\vec{\dot{n}}''_i}{p^{+}_{T}D^{+}_{id}} \tag{3.3}$$

where p_d is the 'pressure' exerted by the dust molecules.

The complete set of multi-component equations will, of

course, include one equation for the dust molecules:-

$$\nabla p_d = \sum_{j=1}^{N} \frac{RT}{p^{+}_{T}D^{+}_{dj}} p_d\vec{\dot{n}}''_j \tag{3.4}$$

although there are only N independent equations.

Since the fictitious constant total pressure in the gas-

plus-dust-mixture is given by:-

$$p^{+}_{T} = p_d + \sum_{j=1}^{N} p_i \tag{3.5}$$

equation (3.4) becomes:-

$$-\sum_{j=1}^{N} \nabla p_i = \sum_{j=1}^{N} \frac{RT}{p^{+}_{T}D^{+}_{dj}} p_d\vec{\dot{n}}''_j \tag{3.6}$$

This equation is of some importance so the N independent

diffusion equations provided by the Dusty Gas Model are best

regarded as equation (3.6) plus N - 1 equations of the form

of equation (3.3).

The diffusion coefficients appearing in the Stefan-Maxwell

equation, D_{ij}, are the normal binary diffusion coefficients

between the separate gas pairs in the multi-component

mixture. A number of equations have been presented in the literature from which these binary diffusion coefficients can be calculated for true gas pairs. The most accurate is that generated by the Chapman-Enskog treatment for the kinetic theory of gases[86]. Calculation of the collision integrals involved in that equation is somewhat elaborate so that an equation proposed by Fuller et alia[87] is considerably easier to use, especially since it is almost as accurate. We are particularly interested at this juncture in the variation of binary diffusion coefficients with temperature, pressure and gas-pair and the Fuller et alia equation predicts these variations to a high degree of accuracy.

The equation can be written for species in the fictitious dust-plus-gas-mixture in the form:-

$$D_{ij}^{+} = C_o \frac{T_K^{1.75} \times 10^{-3}}{p_T^{+}(v_i^{1/3} + v_j^{1/3})^2} \sqrt{\frac{1}{M_i} + \frac{1}{M_j}} \qquad (3.7)$$

where the factor C_o is phenomenological in nature and is introduced because the dust 'molecules' reduce the volume available for the gas molecules and increase the lengths of their diffusion paths by making them more tortuous.

Multiplying equation (3.7) by p_T^{+} and comparing it with the corresponding equation for the binary diffusion coefficient in a free gas shows that:-

$$p_T^{+} D_{ij}^{+} = C_o \, p_T D_{ij} = p_T D_{ij,eff} \qquad (3.8)$$

where equation (3.8) can be taken as a phenomenological definition of $D_{ij,eff}$, the effective binary molecular

diffusion coefficient of the gas pair i/j within the porous solid.

The coefficient describing the diffusion mechanism involving collisions between the true gas molecules and the 'molecules' of dust cannot be determined using equation (3.7), since effective diffusion volumes or molecular masses have not been determined for the dust 'molecules'. This diffusion process is Knudsen diffusion in the porous solid and is normally described in terms of a Knudsen diffusion coefficient. It is/value of this coefficient that the structural models of porous solids have been designed to predict and the first treatment of the Dusty Gas Model attempted to determine it by use of the Chapman-Enskog theory(19). In the phenomenological statement of the model presented here, we merely regard the Knudsen diffusion coefficient as a phenomenological constant related to the variables used so far in the development by the equation:-

$$D_{i,K} = \frac{p_T^+ D_{id}^+}{p_d} \qquad (3.9)$$

Values of $D_{i,K}$ must then be determined by experiment.

With these definitions, equation (3.3) becomes:

$$\frac{\nabla p_i}{RT} = \sum_{j=1}^{N} \frac{p_i \vec{n}_j'' - p_j \vec{n}_i''}{p_T D_{ij,eff}} - \frac{\vec{n}_i''}{D_{i,K}} \quad : \ i=1 \rightarrow N \qquad (3.10)$$

and equation (3.6) becomes:-

$$-\sum_{j=1}^{N} \frac{\nabla p_j}{RT} = \sum_{j=1}^{N} \frac{\vec{n}_j''}{D_{j,K}} \qquad (3.11)$$

63

These two equations are the basic general equations
describing diffusion interactions experienced by gases
within porous solids; the flux densities appearing in the
equations are the diffusion flux densities.

In the presence of a total pressure gradient across the
pores of the solid, however, there will be an additional
flux of each gas species carried along by the mean fluid motion
of the true gas mixture through the porous solid. This
additional flux is mechanically driven since it is brought
about by the mechanical effect that the pressure
gradient exerts on the gas phase within the pores. If the
mechanically driven superficial gas velocity is $\vec{v}_M$ the
additional mechanically driven flux for each gas species 'i'
will be

$$\vec{n}''_{i,M} = \frac{p_i \vec{v}_M}{RT} \qquad (3.12)$$

The flux densities of 'i' and the other gas species that
have appeared in the Dusty Gas Model equations so far have
been those due to diffusion only. The observed flux of
each gas through the porous media, on the other hand,
comprises this diffusion flux together with the mechanically
driven flux. Thus the total observed flux of 'i' is given
by the equation:-

$$\vec{N}''_i = \vec{n}''_i + \vec{n}''_{i,M} \qquad (3.13)$$

and this equation can be used to eliminate the diffusion
flux from the general equations so far developed, since

equations (3.12) and (3.13) taken together give:-

$$\vec{n}''_i = \vec{N}''_i - \frac{p_i \vec{v}_M}{RT}$$ (3.14)

Equations (3.10) and (3.11) now become:-

$$\frac{\nabla p_i}{RT} = \sum_{j=1}^{N} \frac{p_i \vec{N}''_j - p_j \vec{N}''_i}{p_T D_{ij,eff}} - \frac{\vec{N}''_i - \frac{p_i \vec{v}_M}{RT}}{D_{i,K}} \quad : i=1 \rightarrow N \quad (3.15)$$

and:-

$$-\sum_{j=1}^{N} \frac{\nabla p_j}{RT} = \sum_{j=1}^{N} \frac{\vec{N}''_j - \frac{p_j \vec{v}_M}{RT}}{D_{j,K}}$$ (3.16)

The first set of terms in equation (3.15) are not altered in form because the terms contributed by the mechanically driven flow to the weighted flux difference both involve $p_i p_j$ and therefore do not appear in the difference. This is, of course, what would be expected since equation (3.15) stems from thermodynamics and it is only flows of the separate gas species relative to the mole centre of the entire gas mixture that can have diffusive interactions of a thermodynamic nature.

An equation for the mechanically driven flow through the porous media has been presented as equation (2.20) in Chapter 2. As stated in that chapter, this equation has been particularly successful in describing mechanically driven flows through porous media. Since we have already included in the present treatment the effect of the Knudsen mechanism, we are only interested in the molecular term in equation (2.20). Thus we can write the mechanically driven flow in the capillary as:-

65

$$\vec{n}''_M = \frac{\gamma^3}{2\mathcal{T}(1-\gamma)^2 S_o^2} \frac{P}{\mu} \frac{\nabla P_T}{RT} \tag{3.17}$$

which can be rearranged to give the following equation for the mole centre velocity of the gases across the porous material:-

$$\vec{v}_M = -\frac{\gamma^3}{2\mathcal{T}(1-\gamma)^2 S_o^2} \frac{\nabla p_T}{\mu} \tag{3.18}$$

or

$$\vec{v}_M = -B_o \frac{\nabla p_T}{\mu} \tag{3.19}$$

where B_o is another phenomenological property of the porous media.

Substituting equation (3.19) into equations (3.15) and (3.16) gives:-

$$\frac{\nabla p_i}{RT} = \sum_{j=1}^{N} \frac{p_i \vec{N}''_j - p_j \vec{N}''_i}{p_T D_{ij,eff}} - \frac{\vec{N}''_i + B_o \frac{p_i}{\mu} \frac{\nabla p_T}{RT}}{D_{i,K}} \quad : i=1 \to N$$

$$\ldots\ldots(3.20)$$

and:-

$$-\sum_{j=1}^{N} \frac{\nabla p_j}{RT} = \sum_{j=1}^{N} \frac{\vec{N}''_j + B_o \frac{p_j}{\mu} \frac{\nabla p_T}{RT}}{D_{j,K}} \tag{3.21}$$

We can now use these general equations to analyse some important particular cases.

3.2 PERMEABILITY OF A SINGLE GAS THROUGH A POROUS SOLID.

A single gas will flow through a porous material under the influence of a pressure gradient across the material. The process is called permeability and is described in terms of

a permeability constant, ω_A, defined by the equation:-

$$\vec{N}_A'' = - \frac{\omega_A}{RT} \nabla p_A \qquad (3.22)$$

$\vec{N}_A''$ is the total flux of the gas through the porous media and is brought about by two mechanisms: the mechanically driven bulk flow of the gas under the influence of the pressure gradient opposed by viscous and inertial forces between the gas and the solid; and diffusion, where individual gas molecules follow a labyrinthine path through the porous material, the path being determined by their collisions with the walls of the pores. The relative importance of these two mechanisms is determined by the relationship between the diameter of the pores and the mean free path of the gas molecules.

In terms of the general equations just developed, we can analyse these two interactions in terms of one gas, A, equal to species 'j', and the dusty gas. Thus we have:-

$$- \frac{\nabla p_A}{RT} = \frac{\vec{N}_A'' + B_O \dfrac{p_A}{\mu} \dfrac{\nabla p_A}{RT}}{D_{A,K}} \qquad (3.23)$$

since A is the only true gas species present.

The pressure p_A naturally varies with position, since it is the pressure gradient that causes the gas to flow through the porous media. To an approximation that is not too severe, however, we can replace the local value of p_A with a mean total pressure in the pores (we must of course retain the variable pressure in calculating the pressure gradient).

Thus equation (3.23) can be rearranged to give:-

$$\vec{N}_A'' = - \frac{D_{A,K} + B_o\bar{p}_T/\mu}{RT} \nabla p_A \qquad (3.24)$$

where $\bar{p}_T$ is the mean total pressure.

Equation (3.24) is analogous to equation (2.20) derived for flow through a porous media from the random orientated single size pore model for the structure of a porous solid. It can be seen that it is of the same form except that $D_{A,K}$ and B_o are regarded in equation (3.24) as phenomenological constants that can only be determined by experiment.

Comparison between equations (3.24) and (3.22) shows that the permeability of the porous material is given by the following equation:-

$$\omega_A = D_{A,K} + B_o\bar{p}_T/\mu \qquad (3.25)$$

Thus the permeability increases linearly with the total pressure in the porous media, its value at vanishingly small pressures tending to the Knudsen diffusion coefficient of the gas in the pores. This is in keeping with the dual nature of the flow process through the porous media originally outlined. Reduction of the total pressure in the porous media increases the mean free path of the gas molecules, so that higher and higher proportions of their collisions are with the walls of the flow channels and the mechanism of their flow through the porous media thus becomes that of Knudsen diffusion.

Increasing the mean total gas pressure in the porous media

increases the proportion of collisions occuring between the
gas molecules themselves. The mean free path of the gas
molecules diminishes rapidly, becoming less and less
significant in comparison with the dimensions of the flow
channels. Increasingly, the gas behaves as a continuum
fluid and the the mechanism of its flow through the porous
media is that of viscous flow.

The relative importance of these two mechanisms at any given
pressure can only be determined once the values of $D_{A,K}$ and
B_0 have been determined experimentally. The nature of this
experiment entails measuring the permeability of a given gas
through the porous media at a range of different total
pressures, and plotting the permeability against pressure.
The slope of the resulting experimental line gives the value
of B_0/μ , and the intecept on the ω_A axis at zero pressure
gives the Knudsen diffusion coefficient for the gas in the
medium. The results of experiments of this nature will de
described later in this work.

As we saw in Section 2.2, the Knudsen diffusion coefficient
in a capillary of radius r is given by the equation:

$$[D_{A,K}]_r = 2/3 \, r(8R/\pi)^{1/2} \, (T/M_A)^{1/2} \qquad (3.26)$$

r is the radius of the capillary, and can be regarded as a
specification of the geometry in which the diffusion process
is occuring. Although a specific expression cannot be used
to describe the much more complex geometry of a porous
solid, in principle such an expression could be made

available. Thus we can represent equation (3.26) for a porous solid in the form:-

$$D_{A,K} = A_O \sqrt{\frac{T}{M_A}} \qquad (3.27)$$

where A_O is a phenomenological property of the porous media which can be determined from the experimental measurements. A_O is a dimensional constant which is to be measured in $cm^2.s^{-1}(g.mol^{-1}K^{-1})^{1/2}$ if the diffusion coefficient is to be determined in $cm^2.s^{-1}$.

The form of equation (3.27) is not dependent on a structural model of the porous solid. It does, however, assume that it is the geometric frame provided by the porous solid that determines the length of flight that an individual gas molecule experiences between collisions, all these collisions being, of course, with the pore walls. Thus it is the geometry of the solid that determines the value of A_O but the impossibility of developing an adequate structural model for the shape of the solid means that A_O requires experimental determination. Once A_O is determined, it should apply for all gases, the root mean square velocity being the only factor to vary with the nature of the gas. It is this variation that is represented by the square root term in the equation.

The use of equations (3.25) and (3.27) will be discussed later.

3.3 BINARY DIFFUSION THROUGH POROUS MEDIA

3.3.1 Formulation of the equations

The movement through a porous solid of the two components in a binary gas mixture involves Knudsen interactions between the molecules of each gas and the pore walls; molecular interdiffusion of the two gas species; and bulk flow of the gas mixture as a whole under the action of any total pressure gradient that is set up. These three phenomena can be described in terms of equations (3.20) and (3.21) written for the two component gases A and B. Thus we have:-

$$\frac{\nabla P_A}{RT} = \frac{P_A \vec{N}_B'' + P_B \vec{N}_A''}{P_T D_{AB,eff}} - \frac{\vec{N}_A'' + B_o \dfrac{P_A}{\mu} \dfrac{\nabla P_T}{RT}}{D_{A,K}} \qquad (3.28)$$

and

$$\frac{\nabla P_A + \nabla P_B}{RT} = \frac{\vec{N}_A'' + B_o \dfrac{P_A}{\mu} \dfrac{\nabla P_T}{RT}}{D_{A,K}} + \frac{\vec{N}_B'' + B_o \dfrac{P_B}{\mu} \dfrac{\nabla P_T}{RT}}{D_{B,K}}$$

$$\cdots\cdots\cdots (3.29)$$

Equation (3.29) is of considerable interest and will be considered later. For the moment, however, we will concentrate on equation (3.28), seeking to transform it into a more convenient form.

This transformation is carried out by defining an effective diffusion coefficient for gas species A using the equation:-

$$D_{A,eff} = \left[\frac{1}{D_{A,K}} + \frac{1}{D_{AB,eff}} \right]^{-1} \qquad (3.30)$$

and a parameter δ_A given by:-

$$\delta_A = \frac{D_{A,eff}}{D_{AB,eff}} = \frac{D_{A,K}}{D_{A,K} + D_{AB,eff}} \qquad (3.31)$$

These parameters are actually defined in this way to assist in identifying certain types of limiting behaviour for diffusion in porous solids. The nature of these limits will be discussed later but, for the moment, we will note the following limiting values of the parameters $D_{A,eff}$ and δ_A:-

$$\left[\frac{P_T}{r_e}\right] \rightarrow \infty \quad : D_{AB,eff} \ll D_{A,K} : D_{A,eff} \rightarrow D_{AB,eff} ; \delta_A \rightarrow 1$$

$$\ldots \ldots (3.32)$$

$$\left[\frac{P_T}{r_e}\right] \rightarrow 0 \quad : D_{AB,eff} \gg D_{A,K} : D_{A,eff} \rightarrow D_{A,K} ; \delta_A \rightarrow 0$$

$$\ldots \ldots (3.33)$$

A further parameter can usefully be defined to describe the relative importance of diffusion and friction effects in the porous solid. The parameter has the dimension of pressure and is defined as:

$$\zeta_A = \frac{\mu D_{A,K}}{B_o} \qquad (3.34)$$

We can now use the definitions of these three parameters together with the flux ratio between the flows of A and B to simplify the form of equation (3.28). The flux ratio arises because some external constraint, such as stoichiometry, normally imposes upon the diffusion process a definite relation between the fluxes of the gases A and B. For the moment, we will express this relationship in terms of the equation:-

$$\vec{N}_B'' = -\beta \vec{N}_A'' \qquad (3.35)$$

where β is the flux ratio.

Using these definitions, equation (3.28) becomes:-

$$\vec{N}_A'' = - D_{A,eff} \frac{\nabla P_A}{RT} + \delta_A \frac{P_A}{P_T} \vec{N}_A'' (1-\beta) - B_o \frac{P_A}{\mu} \frac{\nabla P_T}{RT} (1-\delta_A)$$

$$\cdots \cdots (3.36)$$

Further rearrangement gives:-

$$\frac{\vec{N}_A''}{D_{A,eff}} \left[1 - \delta_A \frac{P_A}{P_T} (1-\beta) \right] = - \frac{\nabla P_A}{RT} - \frac{P_A}{\zeta_A} \frac{\nabla P_T}{RT} \qquad (3.37)$$

since $\quad \dfrac{1-\delta_A}{D_{A,eff}} = \dfrac{1}{D_{A,K}}$

Equation (3.37) is one of the two independent equations in this problem. The other equation can either be considered to be the corresponding equation for the flux of gas B:-

$$\frac{\vec{N}_B''}{D_{B,eff}} \left[1 - \delta_B \frac{P_B}{P_T} (1 - 1/\beta) \right] = - \frac{\nabla P_B}{RT} - \frac{P_B}{\zeta_B} \frac{\nabla P_T}{RT} \qquad (3.38)$$

which is identical in form to equation (3.37) except that the suffices for A and B are reversed, or an equation for the total pressure gradient obtained by adding the two equations for the fluxes of the separate gases. Using the facts that

$$P_T = P_A + P_B,$$

and $\quad \delta_A/D_{A,eff} = \delta_B/D_{B,eff}$

and remembering the definitions of β and ζ_A allows this addition to yield:-

$$\vec{N}_A'' \left[\frac{1}{D_{A,K}} - \frac{\beta}{D_{B,K}} \right] = - \left\{ 1 + \frac{B_o}{\mu} \left[\frac{P_A}{D_{A,K}} + \frac{P_B}{D_{B,K}} \right] \right\} \frac{\nabla P_T}{RT} \qquad (3.39)$$

Any two of equations (3.37), (3.38) and (3.39) fully describe the relationships between the fluxes of gas A and B through a porous solid and the total and partial pressure

73

gradients across the solid. Their use to solve any
particular gaseous diffusion problem will depend upon the
way in which boundary conditions are specified at the
borders of the porous solid. Mason et alia concentrated
their work towards problems involving linear fluxes in which
the total and partial pressures were completely specified at
the borders, although they also discussed one specific
experimental case of equi-molar counter flow.

Their treatment, however, cannot be applied to gas/solid
reactions since these involve non-linear fluxes of the
reactant and product gas and a boundary condition at one
border that specifies an equilibrium or similar relationship
between the partial pressures of the two gases, but is
unable to specify either pressure, or indeed the total
pressure at that border.

The treatment presented in the next section but one is
specifically designed for this type of problem. Its
application to entirely pressure determined problems, of the
type considered by Mason et alia, however, involves an
interative technique slightly more direct than the technique
that they used.

However, before methods for the solution of these equations are
discussed, it is useful to consider some limiting forms of the
equations so as to show that they are compatible with more normal
representations of diffusion phenomena, at least under the
limiting conditions where these more normal representations are
valid. 74

3.3.2 Limiting forms of the binary diffusion equations

If the pore size within the porous medium is very fine and the gas is extremely viscous or the Knudsen diffusion coefficient extremely large, the value of the porous media transport parameter, ζ_A, is effectively infinite (see equation 3.34) so that equation (3.37), remembering the definition of β , can be written as:-

$$\vec{N}_A'' = -D_{A,eff} \ \frac{\nabla P_A}{RT} + \frac{P_A}{P_T} \ (\vec{N}_A'' + \vec{N}_B'') \ \zeta_A \qquad (3.40)$$

This equation is closer to the more normal representation of binary diffusion. If the total pressure in the pores is high or the pore diameter large, limiting relationship (3.32) applies so that equation (3.40) can be written as:-

$$\vec{N}_A'' = -D_{AB,eff} \ \frac{\nabla P_A}{RT} + \frac{P_A}{P_T} \ (\vec{N}_A'' + \vec{N}_B'') \qquad (3.41)$$

Under these limiting conditions, any one gas molecule will collide far more frequently with other gas molecules than with the wall of the pore in which it finds itself, so that molecular diffusion will be the dominant diffusion mechanism. This ties in with equation (3.41) which is in the form used for the analysis of binary gaseous molecular diffusion.

The second set of limiting conditions occurs when either the total pressure or the radius of the pores tends to zero. Under these conditions, limiting relationship (3.33) applies, so that equation (3.40) can be written as:-

$$\vec{N}_A'' = -D_{A,eff} \frac{\nabla p_A}{RT} \tag{3.42}$$

These conditions are those under which a gas molecule in a pore will collide far more frequently with the pore wall than with other gas molecules and thus correspond to Knudsen diffusion - in keeping with equation (3-42) which is the equation describing Knudsen diffusion.

Equation (3-40) can thus transform smoothly from the form required for pure Knudsen diffusion to the form required for pure molecular diffusion. Thus equation (3.37) incorporates the more usual representation for binary diffusion but presents a more universally applicable treatment for the movement of gases through porous media.

The next section of this chapter presents a method whereby equation (3.37) can be solved for the general case in which none of the limiting conditions outlined in this section can be said to apply.

3.3.3 Method of solution

For convenience, we define a parameter $\mathcal{K}$ given by:-

$$\mathcal{K} = \frac{D_{A,K}}{D_{B,K}} = \sqrt{\frac{M_B}{M_A}} \tag{3.43}$$

so that equation (3.39) can be multiplied be $D_{A,K}$ to give:-

$$\bar{N}_A'' = -\left[\frac{D_{A,K} + B_o(p_A + \mathcal{K} p_B)/\mu}{1 - \beta \mathcal{K}} \right] \frac{\nabla p_T}{RT} \tag{3.44}$$

Equation (3.37) can be rearranged as:-

$$\vec{N}_A'' = -\frac{D_{A,eff}}{D_{A,K}} \frac{D_{A,K} p_T \nabla p_A + (p_T B_0/\mu) p_A \nabla p_T}{RT\left[p_T - \delta_A(1 - \beta)p_A\right]} \qquad (3.45)$$

Eliminating $\vec{N}_A''$ between equations (3.44) and (3.45) yields, after rearrangement, the following equation for the variation of the total pressure p_T:-

$$\frac{dp_T}{dp_A} =$$

$$\frac{p_T \zeta_A(1 - \beta \varkappa)(1 - \delta_A)}{\left[\zeta_A + p_A + \varkappa(p_T - p_A)\right]\left[p_T - p_A \delta_A(1-\beta)\right] - \left[p_A p_T(1-\delta_A)(1-\beta\varkappa)\right]}$$

$$\ldots \ldots \ldots (3.46)$$

where, for convenience, we have defined a transport parameter of the porous media, ζ_A, following the equation:-

$$\zeta_A = \frac{\mu D_{A,K}}{B_0} \qquad (3.47)$$

ζ_A has the units of pressure.

Equation (3.46) can now be used to eliminate dp_T/dp_A from equation (3.44) or (3.45) to give:-

$$\vec{N}_A'' = \frac{-D_{A,eff}/RT \; \nabla p_A}{1 - \dfrac{p_A \delta_A(1-\beta)}{p_T} - \dfrac{(1-\delta_A)(1-\beta\varkappa)p_A}{\zeta_A + p_A + \varkappa(p_T - p_A)}} \qquad (3.48)$$

In essence, equations (3.46) and (3.48) allow us to solve directly any diffusion problem in which β is known, without recourse to the type of iterative techniques used by Mason et alia. It is not immediately apparent, however, how this can be done, since the flux at any point in the porous solid is a function of the total pressure and the partial pressure of gas A as well as the gradient of that partial pressure. A possible approach would be to combine a

77

differential conservation equation with equation (3.48) and thus determine the spatial variation of the total and partial pressures through reference to equation (3.46). A more direct method of solution is available, however, using the shape factor concept developed to treat steady state heat transfer problems.

To use this concept we consider 'b' to be the coordinate along the direction of the vector ∇p_A, and take A as the total area available for flow at any given value of 'b'. Under these conditions:-

$$\nabla p_A = \frac{dp_A}{db} \quad \text{and} \quad \vec{N}_A'' = \frac{\dot{N}_A}{A}$$

and we can separate the variables of equation (3.48) to give:

$$\frac{db}{A} \frac{\dot{N}_A RT}{D_{A,eff}} = \left[1 - \frac{p_A \delta_A (1-\beta)}{p_T} - \frac{(1-\delta_A)(1-\beta \varkappa) p_A}{\zeta_A + p_A + \varkappa(p_T - p_A)} \right]^{-1} dp_A$$

$$\cdots \cdots \cdots (3.49)$$

Integration of this equation between borders '1' and '2' of the region of porous solid followed by rearrangement gives:-

$$\dot{N}_A = S \frac{D_{A,eff}}{RT} \left\{ [\psi_A]_1 - [\psi_A]_2 \right\} \qquad (3.50)$$

where S is the shape factor - dependent only upon the shape and extent of the porous solid region and defined as:-

$$S = \left[\int_1^2 \frac{db}{A} \right]^{-1} \qquad (3.51)$$

and ψ_A is the driving force for the diffusive flow process,

having the units of pressure and being defined by the
differential equation:-

$$\frac{d \psi_A}{dp_A} = \left[1 - \frac{p_A \delta_A (1-\beta)}{p_T} - \frac{(1-\delta_A)(1-\beta \mathcal{K})p_A}{\zeta_A + p_A + \mathcal{K}(p_T - p_A)}\right]^{-1} \qquad (3.52)$$

The difference in ψ_A across the diffusion region,

$[\psi_A]_1 - [\psi_A]_2$ may be evaluated by integrating equations
(3.52) and (3.46) as a pair of simultaneous ordinary non-
linear equations from the pressure conditions at one
boundary to the pressure conditions at the other boundary.
This integration is carried out over a range of p_A as the
independent variable and is thus not affected by the
geometry of the diffusion region.   The value of the result
of the integration thus depends only upon the properties of
the porous solid and the partial and total pressure
conditions at the borders of the porous solid region: it is
independent of the diffusion path.   The formulation
presented here, then, has a considerable advantage over
Mason et alia's original formulation, since the iterative
process involved in their determination of the mean gas
viscosity along the diffusion path is avoided.   The use of
these equations will now be considered by application to a
range of special cases.

3.3.4 Isobaric diffusive flow in a binary gas mixture.

Isobaric conditions can be regarded as being defined by the
identities $\nabla p_T = 0$, or $dp_T/dp_A = 0$.   Thus either
equation (3.44) or (3.46), respectively, shows that the
necessary condition for isobaric diffusion is:-

$$\beta \mathcal{K} = 1, \quad \text{or} \quad \mathcal{K} = 1/\beta \tag{3.53}$$

and that this relation applies whatever diffusion or flow regime is operating. Substituting for β from equation (3.35) and for $\mathcal{K}$ from equation (3.43) and then from equation (3.27) allows this relationship to be expressed in the form:-

$$\frac{\vec{N}''_A}{\vec{N}''_B} = -\frac{D_{A,K}}{D_{B,K}} = -\sqrt{\frac{M_A}{M_B}} \tag{3.53A}$$

Experimental measurements have long been known to show that this relationship exists between the molecular masses of two gases and their fluxes within a porous solid under isobaric conditions and that this relationship applies not only under conditions where Knudsen diffusion occurs, but under all diffusion and flow regimes. It is a considerable achievement of the Dusty Gas Model that it is able to predict this universal applicability of the relationship.

Substitution of equation (3.53) into equation (3.52), followed by rearrangement, gives:-

$$\frac{d\psi}{dp_A} = -\frac{\mathcal{K} p_T}{\mathcal{K} p_T - \delta_A(\mathcal{K}-1)p_A} \tag{3.54}$$

which has to be integrated across the porous solid region from boundary 1 to boundary 2. Thus we have:-

$$[\psi_A]_1 - [\psi_A]_2 = \frac{\mathcal{K} p_T}{\delta_A(\mathcal{K}-1)} Ln\left\{\frac{\mathcal{K} p_T - \delta_A(\mathcal{K}-1)[p_A]_2}{\mathcal{K} p_T - \delta_A(\mathcal{K}-1)[p_A]_1}\right\} \tag{3.55}$$

Substitution into equation (3.50) and remembering the definition of δ_A gives:-

$$\dot{N}_A = \frac{\mathcal{K} S D_{AB,eff}\, p_T}{RT(\mathcal{K}-1)} Ln\left\{\frac{\mathcal{K} p_T - \delta_A(\mathcal{K}-1)[p_A]_2}{\mathcal{K} p_T - \delta_A(\mathcal{K}-1)[p_A]_1}\right\} \qquad (3.56)$$

Equation (3.56) confirms that the fluxes of A and B under
isobaric conditions are independent of the viscous flow par-
ameters.   The equation is not important for its technical
application since isobaric diffusion occurs extremely seldom
in technical problems.   The importance of equation (3.56)
stems from the experimental measurements that can be based
upon it.   These measurements, together with the
permeability measurements for a pure gas, allow the complete
characterisation of the diffusion behaviour of a porous
solid in terms of three phenomenological parameters, as
discussed in the next section.

3.3.5 Phenomenological diffusion properties of a porous solid

As has been stated previously, the main advantage of the
Dusty Gas Model over other treatments for gaseous diffusion
in porous solids lies in its phenomenological nature.
This allows a complete description of the diffusion
properties of a porous solid to be expressed in terms of
three phenomenological constants which are properties of the
solid.   The values of these constants for any given porous
solid are of course determined by the structure of the
solid, but their experimental evaluation does not require
any knowledge of the structure to be available.   The
development of equation (3.56) signals a convenient stage in
the theoretical development of the Dusty Gas Model for these
phenomenological constants to be defined and their

81

experimental evaluation outlined.

The three phenomenological constants are designated here as A_O, B_O and C_O. The constant A_O is a Knudsen diffusion parameter defined by the equation:-

$$D_{A,K} = A_O \sqrt{\frac{T}{M_A}} \qquad (3.57)$$

The constant B_O is the bulk flow parameter already defined in equation (3.19). It relates the bulk flow velocity of a gas through a porous solid to the total pressure gradient vector through the solid and the bulk viscosity of the gas:-

$$\vec{V}_M = -B_O \frac{\nabla P_T}{\mu} \qquad (3.58)$$

The final constant C_O is a molecular diffusion parameter defined as:-

$$D_{AB,eff} = C_O D_{AB} \qquad (3.59)$$

The three constants can be determined, for any given porous solid, from the results of permeability measurements carried out on a pure gas at a range of different mean total pressures, and from one binary diffusion coefficient measurement under isobaric conditions. Constants A_O and B_O are determined from the permeability measurements as already outlined in equation (3.25) In the present context, that equation becomes:-

$$\omega_A = A_O \sqrt{\frac{T}{M_A}} + B_O \frac{\bar{P}_T}{\mu} \qquad (3.60)$$

The determination of ω_A for any given pure gas of known viscosity at a range of different values of p_T and linear

82

analysis of the experimental results along the lines of equation (3.60) allows the values of the two constants to be determined.

The value of C_O can be determined from one diffusion measurement under isobaric conditions using equation (3.56) to analyse the results. Rearranging the equation shows that the value of C_O can be determined from an experimental determination of the diffusion flux under isobaric conditions with a known composition difference between the gas phases at either end of the diffusion path:-

$$C_O = \frac{\dot{N}_A RT(\mathcal{K} - 1)}{\mathcal{K}\, D_{AB} S \bar{p}_T Ln\left\{\dfrac{\mathcal{K}\bar{p}_T - \delta_A(\mathcal{K}-1)\,[p_A]_2}{\mathcal{K}\bar{p}_T - \delta_A(\mathcal{K}-1)\,[p_A]_1}\right\}}$$

(3.61)

Contrary to a cursory glance, equation (3.61) is not explicit in C_O because $\overset{\curvearrowright}{\delta}_A$ depends upon C_O. Indeed, equation (3.31) can be rewritten to yield:-

$$\overset{\curvearrowright}{\delta}_A = \left[1 + C_O \frac{D_{AB}}{D_{A,K}}\right]^{-1}$$

(3.62)

which shows that the value of A_O must already be available from permeability measurments to enable $D_{A,K}$ to be determined as an essential step in the evaluation of C_O.

Equation (3.61), after substitution from equation (3.62), could be solved by the Newton Raphson method, but a much simpler approach involves an iterative procedure in which a value of C_O is first estimated to allow a value of $\overset{\curvearrowright}{\delta}_A$ to be determined and then used in equation (3.61) to determine a

better estimate of C_O. This procedure may then be continued to obtain any desired degree of accuracy. A suitable value from which to start this procedure is C_O = 0.4.

3.4 BINARY NON-ISOBARIC DIFFUSION

Non-isobaric diffusion occurs when the pressure along the diffusion path is not maintained at a uniform value. This will occur whenever the value of β departs from the square root of the molecular mass ratio shown in equation (3.53). Thus all chemical reactions, either catalytic or non-catalytic, taking place in porous solids will do so under non-isobaric conditions, but the effect will only be important when the molecular masses of the gases differ significantly. In effect in technical processes, this means whenever hydrogen is involved. In the laboratory, the importance of the non-isobaric nature of the diffusion process will be most manifest when hydrogen or helium are involved.

Obviously, allowing the pressure to vary along the diffusion path introduces a further degree of freedom into the problem and this is represented in the mathematical description by the emergence of an additional unknown quantity. In problems where the pressures are fully specified at both ends of the diffusion path, this additional unknown is the value of β . In problems where the value of β is specified, normally by the stoichiometry of a chemical reaction, the unknown will be a pressure at one end of the

diffusion path.

The method of solution outlined in Section 3.3.3 has been developed for problems involving chemical reactions, that is for problems in which the value of β is known. Application of the method of solution to the relatively rare problems in which the pressures are completely specified involves iteration. A value of β must first be estimated and used in the equations to calculate the total and partial pressure at one end of the diffusion path - equation (3.46) gives the total pressure. These pressure values are then to be compared with the known pressures so that a better estimate can be made of β and the iterative process repeated and continued until the desired level of accuracy has been reached.

In general, however, even when the value of β is known, solution of the equations will involve some element of trial and error. In non-catalytic gas-solid reactions, equilibrium conditions can often be assumed to exist at the reaction front. Thus one boundary condition for the solution of equation (3.46) is provided by a relationship linking the partial pressures at that boundary. Conditions at the other boundary must specify both pressures, for this boundary provides the starting point for the numerical solution of equation (3.46). The numerical solution must then approach the second boundary on a trial and error basis in order to determine the values of p_A and p_T that satisfy

the equilibrium condition there. The reduction of hematite is an example of this type of problem and is discussed in the next section but one.

Sometimes, equilibrium conditions cannot be assumed to exist at the reaction front in a non-catalytic gas-solid reaction, the boundary conditions for the solution of the diffusion equations involving kinetic relationships that link partial pressures at the boundaries to the diffusion flux. Analysis of the non-isobaric experiments carried out in this work provides an example of this type of problem. The method of solution is described in the next section.

3.4.1 Analysis of the non-isobaric diffusion experiments

As a check on the Dusty Gas Model, the diffusion fluxes of two gases were measured experimentally under different isobaric conditions. Gases of known composition were maintained at known pressures either side of a diffusion cell and the diffusion fluxes through the cell were determined. The measured fluxes were compared with predictions of the Dusty Gas Model using values of the three phenomenological diffusion properties determined for the diffusion cell as outlined in the previous section. This section outlines how the equations of the Dusty Gas model were used to make the predictions.

The fluxes of both gases and the compositions and total pressures either side of the diffusion cell were determined in the experiments so that the check on the Dusty Gas Model

involved the prediction of some of this data from the remainder. Which data was predicted and which used as the basis for the prediction was immaterial so that a procedure was adopted to mirror, as closely as possible, the procedure described above for the analysis of gas-solid reactions.

Thus the values of β , $[p_T]_1$, $[p_{He}]_{b,1}$ and $[p_{He}]_{b,2}$ taken from the experimental results were used as the input data from which to predict the flux of Helium, $\dot{N}_{He}$, and the total pressure in the centre of the sphere, $[p_T]_2$. The diffusion cell used was in the form of a hollow sphere, the outside of the spherical shell being taken as border 1 and the inside as border 2. Pure helium was fed to the inside of the sphere but the outside, border 1, was taken as the origin so that the integration of equations (3.46) and (3.52) was carried out over positive increments of p_{He}, ie against the direction of the He flux.

Although the bulk gas compositions inside and outside the sphere were known from the experimental results, the surface concentrations were not known. Mass transfer coefficients either side of the shell had been determined so that relations between the measured bulk compositions and the unknown surface compositions were available of the form:-

$$\dot{N}_A = A_o \propto_A C_T \left\{ [Y_A]_b - [Y_A]_s \right\} \tag{3.63}$$

where Y_A is the non-linear driving force for non-equimolar mass transfer defined by:-

$$Y_A = - \frac{Ln[1 - (1-\beta)^{p_A}/p_T]}{1 - \beta} \tag{3.64}$$

87

and C_T is the total molar density in the gas phase.

Since these equations are non-linear, and anyway involve the fluxes of the diffusing gases, their use as boundary conditions for the numerical solution of equations (3.46) and (3.52) involves an iterative procedure. Thus the latter equations were first integrated from $[p_{He}]_{b,1}$ to $[p_{He}]_{b,2}$ using the values of A_O B_O and C_O determined in previous permeability and isobaric experiments on the diffusion cell*. The value of $[\psi_{He}]_2 - [\psi_{He}]_1$ determined in this way was then used in equation (3.50) to determine the flux of helium, the shape factor having been determined from the geometry of the hollow sphere. This first estimate of the flux of helium was then used with equations (3.63) and (3.64), written for the inside and for the outside of the spherical shell, to determine first estimates of the surface partial pressure of helium. The equation generated for the helium partial pressure at the outer surface, for example, is:-

$$[p_{He}]_{s,1} = \frac{[p_T]_1}{(1-\beta)} \left\{ 1 - \left[1 - \frac{(1-\beta)[p_{He}]_{b,1}}{[p_T]_1} \right] \exp\left[\frac{\dot{N}_{He}(\beta-1)RT}{[p_T]_1 \alpha_1 A_1} \right] \right.$$

$$\cdots \cdots (3.65)$$

with a similar equation for the inner surface helium pressure in which the suffix '1' is replaced by '2'.

---

* A mean value was used for the viscosity of the gas mixture within the solid, the viscosities of argon and helium being relatively close (see Section 5.4.3.2)

88

Once better estimates of the surface helium pressures had been obtained in this way, the integration was repeated and the iteration continued until two consequent values of the diffusion flux differed by less than 0.1%.

The mass transfer coefficients used at the inner and outer surfaces of the spherical shell were determined as outlined in Section 5.4.3.2 and 5.4.3.3 . The FORTRAN programme that carried out the calculations is listed in Appendix 4 , the programme being operated on a 'Shelton sig/net' microcomputer. Results of the computations are presented and compared with the experimentally measured values in Section 6.4 .

3.4.2 Diffusion in gas-solid reactions

By far the most important metallurgical application of the Dusty Gas Model is analysing the role played by gaseous diffusion in reactions between gases and solids that result in the formation of a porous product layer. The flux ratio is determined by the stoichiometry of the reaction and gas compositions are known at the outer surface of the porous layer but not in the reaction region between the product and reactant solids. Although not essential to the application of the Dusty Gas Model, it is more convenient if we consider a narrow reaction region or front at which we can assume that equilibrium conditions apply between the reactant and product gases and solids.

The formula for the reaction can be represented as:

89

$$S1 \; + \; A \; \longrightarrow \; S2 \; + \; \beta \; B \qquad\qquad (3.66)$$

where S1 and S2 are the reactant and product solids respectively.

If we designate the outer boundary as border 1 and the reaction front as border 2, we know the values of $[p_A]_1$ and $[p_T]_1$. Since equation (3.50) only involves differences in ψ , we can allot any value we choose to $[\psi_A]_1$, zero being the most convenient. Thus we can start the integration of equations (3.46) and (3.52) from border 1. We do not, however, know a priori when to stop the integration, since p_A is the independent variable and its value at the reaction front is not known. We do, however, know the equilibrium relationship at the reaction front which, in terms of p_A and p_T, can be expressed as:-

$$\left\{ [p_T]_2 \; - \; [p_A]_2 \right\}^{\beta} \; = \; K_{eq} \; [p_A]_2 \qquad (3.67)$$

Thus we can only discover the actual pressure of gas A at the reaction front by a trial and error procedure in which equation (3.46) is integrated in a step-wise manner, for example using a Runge-Kutta technique. This integration is started at border 1 from the known values of p_A and p_T, carried out using negative increments of p_A and stopped when equation (3.67) is satisfied. This will require a test after each integration step, integration only being continued if the current value of p_T is less than the value predicted by equation (3.67) from the current value of P_A.

If the current value of p_T is greater, the last numerical integration must be repeated over a smaller increment in p_A, the value of the increment being adjusted by trial and error until equation (3.67) is satisfied to whatever degree of accuracy is required.

Equation (3.52) will be integrated simultaneously to generate the value of $\left[\psi_A\right]_1 - \left[\psi_A\right]_2$ to be used in equation (3.50) to generate the flux of A and hence the rate of the reaction. In a reaction in which gaseous diffusion in the porous solid is the sole rate determining processes, the integration described above need only be carried out once since the values of $\left[\psi_A\right]_2$, $\left[p_A\right]_2$ and $\left[p_T\right]_2$ determined by the integration will apply whatever the geometry of the porous product layer - thus the single integration will apply throughout the entire reaction. Examples of the application of the equations in this way are given in subsequent sections and then used in the discussion chapter to examine the influences of Knudsen diffusion and bulk flow.

The relative ease with which this solution is obtained is of limited utility, however, since most gas-solid reactions appear to occur by a mixed control mechanism in which gas phase mass transfer and or chemical reaction rates at the reaction front play a part in controlling the reaction rate. In this case, an iterative procedure, similar to that outlined in 3.5.1, must be adopted for treating the boundary

conditions.

The next two sections of the chapter outline simple applications of the method proposed.

3.4.3 Application to the hydrogen reduction of hematite

The reduction of hematite in hydrogen has been studied extensively. The hematite is reduced to magnetite, then to wustite and finally to iron and it is now generally concluded that the counter diffusion of hydrogen and water vapour through the outer porous layer of iron plays a major role in determining the rate of the reduction reaction. However, the treatments that have been presented for the diffusion process have involved a number of simplifying assumptions. Only the treatments recently published[eg.11] have considered the role of Knudsen diffusion and no treatment has been presented to examine the effect of pressure driven flow.

As discussed in Section 3.5, diffusion through the iron layer must take place under non-isobaric conditions so that a bulk pressure difference will be built up across the iron layer. Thus the gas mixture will be driven across the porous iron layer and this flow will have some role to play in the mechanism of the reaction. The methods developed in this chapter allow the importance of this role to be examined. This is best done if relative reaction rates or reaction times are calculated for hypothetical reduction processes controlled solely by diffusion in the porous iron

layer, calculations being performed including and then excluding the role played by the mechanically driven flow.

The shrinking core model has often been used to analyse the rate at which a spherical pellet of hematite will be reduced. In this model, the reaction front at any reaction time t is regarded as a spherical surface of radius r within a spherical particle of radius r_o. The diffusion process thus takes place between these two spherical surfaces, the shape factor for this diffusion path being:-

$$S \quad = \quad 4\pi \left[\frac{1}{r} - \frac{1}{r_o} \right]^{-1} \tag{3.68}$$

As the reaction proceeds, the reaction interface retreats toward the centre of the particle at a rate given by the following mass balance equation at the reaction front:-

$$C_p V \, 4\pi r^2 \frac{dr}{dt} \quad = \quad - \dot{N}_{H_2} \tag{3.69}$$

in which C_p is the molar density of the particle, and V is the appropriate stoichiometic factor.

Although the reduction reaction takes place in a series of steps, the intermediate oxide phases occupy very narrow spherical shells around the inner hematite core, at least when reduction takes place in pure hydrogen. Thus the

overall reaction is:-

$$Fe_2O_3 \quad + \quad 3H_2 \quad \rightarrow \quad 2Fe \quad + \quad 3H_2O \tag{3.70}$$
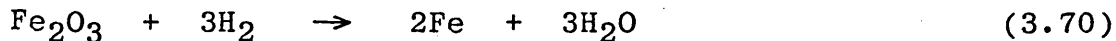
so that the stoichiometric factor in the mass balance

equation is 3.

Although the overall reaction is represented by equation (3.70), the equilibrium conditions at the reaction front as seen by the diffusion process are those for the reduction of wustite:-

$$FeO + H_2 = Fe + H_2O \qquad (3.71)$$
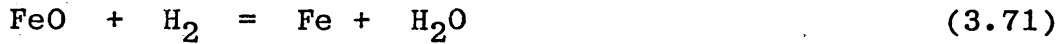
and it is the equilibrium constant for this reaction that is to be used in equation (3.67) defining the limit of the numerical integration.

Substituting into equation (3.69) from equation (3.50) for $\dot{N}_{H_2}$ and from equation (3.68) for S gives, after rearrangement:

$$\frac{dr^*}{dt^*} = -\frac{\delta_{H_2} C_o \left\{ \left[\psi_{H_2} \right]_1 - \left[\psi_{H_2} \right]_2 \right\}}{3\, RT\, C_p\, r^*(1-r^*)} \qquad (3.72)$$

where r^* is the fractional reaction front radius ($= {}^r/r_o$) and t^* is a dimensionless time defined as:-

$$t^* = \frac{t \cdot D_{H_2/H_2O}}{r_o^2} \qquad (3.73)$$

Integration of equation (3.72) yields, after rearrangement:-

$$1 - 3r^{*2} + 2r^{*3} = \frac{2\, \delta_{H_2} C_o \left\{ \left[\psi_{H_2} \right]_1 - \left[\psi_{H_2} \right]_2 \right\}}{RT\, C_p} t^* \qquad (3.74)$$

Thus a total dimensionless reaction time can be calculated

for the condition $r^* = 0$ as:-

$$t^* = \frac{RT\, C_p}{2\delta_{H_2} C_o \left\{ \left[\psi_{H_2} \right]_1 - \left[\psi_{H_2} \right]_2 \right\}} \qquad (3.75)$$

Since $\left[\psi_{H_2} \right]$ has the units of pressure, this equation can be rendered dimensionless by multiplying both sides by p_T and rearranging to give:-

94

$$t^* \frac{p_T}{RT\, C_P} = \frac{p_T}{2\delta_{H_2}\, C_o\left\{\left[\psi_{H_2}\right]_1 - \left[\psi_{H_2}\right]_2\right\}} \qquad (3.76)$$

Values of the right hand side of this equation have been calculated for a range of different conditions as set out in Table 6.7. The computer programme that was written to carry out the necessary integrations is described in Appendix 7. The programme was very similar to that used for the calculations described in Section 3.5.1 analysing the non-isobaric diffusion experiments. Iteration was not necessary, however, since the boundary conditions did not involve fluxes. However, the viscosities of hydrogen and water vapour differ considerable so that a variable viscosity was used in integrating equations (3.46) and (3.52). A linear interpolation proportional to mole fractions was used between the viscosities of the pure species. The reduction times calculated under different conditions are discussed in Section 6.6.

3.4.4 Diffusion in the decomposition of calcium carbonate.

Hills[70] has investigated the decomposition of calcium carbonate and formed the view that it is controlled by heat and mass transfer. He showed that the temperature of the reacting particle was changing continuously throughout the time of the reaction and that the instantaneous reaction rate was related to the changing partial pressure difference in a way that was compatible with control of the reaction by diffusion through the porous layer of lime on the outside of

the unreacted central sphere of calcium carbonate. By
analysing this relationship he was able to elucidate values
for the effective diffusion coefficient, the values that he
found being compatible with values of the Knudsen diffusion
coefficient estimated by inserting published data for
specific surface areas of limes into the single size
capillary pore model.

However, a more comprehensive study of diffusion in porous
lime has been undertaken in this work and it is necessary
to ask whether this study invalidates the conclusions that
Hills has drawn as to the reaction mechanism. To this end,
the theoretical methods developed in this section have been
used to determine relative dimensionless times for the
decomposition of calcium carbonate. These times have then
been used to estimate a pseudo Knudsen diffusion coefficient
of the type used by Hills so that this value can be compared
with the values he determined. In addition, the importance
of mechnically driven flows in the kinetics of calcium
carbonate decomposition will also be examined.

The decomposition of calcium carbonate is easier to treat
than the reduction of hematite because the equilibrium
condition at the reaction front gives the partial pressure
of carbon dioxide directly. Thus integration of equations
(3.46) and (3.52) can start at the outer surface and proceed
to the equilibrium partial pressure of carbon dioxide, this
gas being taken as the gas species A with air the other
species. No trial and error procedure is involved.

The calculations and equations are virtually identical to those for the reduction of hematite, except that the value of beta is zero. Dimensionless decomposition times for a spherical pellet can be calculated in the same way using equation (3.74) except that differences between the stoichiometries of the reduction of hematite and the decomposition of calcium carbonate change the '2' in equation (3.74) to '6'. Values of dimensionless times calculated in this way are shown and discussed in Section 6.6. In addition, pseudo Knudsen diffusion coefficients are calculated of the type used by Hills who analysed the diffusion process in the porous lime using the equation:-

$$\dot{N}''_{CO} = \frac{4\pi D_H r_o \left[p_{CO_2} \right]_R}{RT_G(^1/_{r*} - 1)} \qquad (3.77)$$

where D_H is the pseudo Knudsen coefficient, $\left[p_{CO_2} \right]_R$ is the partial pressure of CO_2 at the reaction front and the gas phase surrounding the decomposing particle contains no CO_2.

Thus the equation from Hills' treatment that corresponds to equation (3.76) for $t*$ would be:-

$$t* \frac{p_T}{RTC_p} = \frac{p_T}{6 \ D_H/D_{CO_2,Air} \left[p_{CO_2} \right]_R} \qquad (3.78)$$

Equation (3.76) does not really apply during the decomposition of calcium carbonate because the temperature of the reacting particle is changing all the time. However, taking the reaction front temperature and pressure as constant during the entire reaction, although a major approximation, will not invalidate conclusions drawn about

the relative importance of different aspects of the
diffusion and flow processes - the changing temperature
arises solely from the interaction between the heat transfer
and diffusion processes.

Comparison between equation (3.78) and (3.76) shows that the
pseudo Knudsen diffusion coefficient is given by:-

$$D_H = \frac{D_{CO_2,eff}\left\{\left[\psi_{CO_2}\right]_1 - \left[\psi_{CO_2}\right]_2\right\}}{\left[p_{CO_2}\right]_R} \qquad (3.79)$$

Values of D_H calculated using this equation are also
discussed in section 6.6.

3.5 <u>OUTLINE FOR TREATMENT OF MULTI-COMPONENT PROBLEMS</u>

The Dusty Gas Model provides a coherent framework of
analysis for gas solid reactions independent of the number
of gaseous components involved. Thus parameters evaluated
in experients involving single gases and binary gas mixtures
can be used without modification in the analysis of multi-
component problems. The ease with which such complex
problems can be approached is indicated here, although the
solution of such a problem is beyond the scope of this
thesis.

The direct reduction of iron ores in reformed natural gas
provides an important multi-component application of the
Dusty Gas Model in that four gases are involved, hydrogen,
water vapour, carbon monoxide and carbon dioxide. The
complete statement of the diffusion and flow problem in the
porous product layers of an iron ore particle will involve

98

four equations of the form of equation (3.15), one for each

gas. As an example, the equation for hydrogen is:-

$$\frac{\nabla p_{H_2}}{RT} = \frac{p_{H_2} \vec{\tilde{N}''}_{H_2O} - p_{H_2O} \vec{\tilde{N}''}_{H_2}}{p_T \ D_{H_2/H_2O,eff}} + \frac{p_{H_2} \vec{\tilde{N}''}_{CO} - p_{CO} \vec{\tilde{N}''}_{H_2}}{p_T \ D_{H_2/CO,eff}}$$

$$+ \frac{p_{H_2} \vec{\tilde{N}''}_{CO_2} - p_{CO_2} \vec{\tilde{N}''}_{H_2}}{p_T \ D_{H_2/CO_2,eff}} + \frac{\vec{\tilde{N}''}_{H_2} + B_o \dfrac{p_{H_2}}{\mu} \dfrac{\nabla p_T}{RT}}{D_{H_2,K}} \qquad (3.80)$$

Since the parameters A_o and C_o determined in the

permeability and binary diffusion experiments are properties

of the porous solid only, the effective binary diffusion

coefficients in the above equation and the Knudsen diffusion

coefficient are given by equations (3.57) and (3.59) which,

for example, become:-

$$D_{H_2,K} = A_o \sqrt{\frac{T}{M_{H_2}}} \qquad (3.81)$$

and:-

$$D_{H_2/H_2O,eff} = C_o \ D_{H_2/H_2O} \qquad (3.82)$$

Thus the values of A_o and C_o measured in the single gas

permeability experiment and in the isobaric diffusion

experiment can be clearly seen to be relevant to the multi-

component problem. Although the solution of the equation

(3.80) and the other three equations for the other gases is

beyond the scope of this thesis, a method of solution has

been developed[104] in which equation (3.80) is simplified by

applying to it the stoichiometric relationships for each

reacting gas pair and then by linking the effective binary

molecular diffusion coefficients within two bands for gas

99

pairs involving hydrogen, and not involving hydrogen.
Although this approach obviously involves some degree of
approximation, its existence illustrates the utility of the
Dusty Gas Model for very complex diffusion problems.

CHAPTER 4 – <u>APPARATUS AND EXPERIMENTAL PROCEDURE</u>

4.1 INTRODUCTION

The total effective diffusion coefficient of a gas migrating through a porous solid is made up of two components:

a) The Knudsen diffusion coefficient, D_{KG}

b) The effective binary diffusion coefficient $D_{AB,eff}$.

As a consequence, the experimental work has been divided into two parts aimed at evaluating each of these components. The Dusty Gas Model for a single component gas system allows the Knudsen diffusion coefficient in a porous solid to be related to the permeability. The permeability can be determined from measurements of the volumetric flow rate of a pure gas through the porous solid under the influence of a pressure gradient. In this particular work Knudsen diffusion coefficients have been evaluated using this approach for spherical shells of porous lime, porous reduced iron and porous sintered iron at both room temperature and elevated temperature.

The effective binary diffusion coefficient, $D_{AB,eff}$, may be obtained from determinations of the volumetric flow rates and compositions of multicomponent countercurrent gas flows through the porous solid. Once the Knudsen diffusion coefficient of a gas, D_{KG}, and the effective binary diffusion coefficient, D_{ABeff}, are known the total effective diffusion coefficient, $D_{G,eff}$, may be calculated. The experimental technique used involved the preparation of porous hollow spheres which had to be sealed on to the end of a hollow shaft. The shaft contained separate passages to allow gas to be introduced into the central cavity of the sphere and then removed from it. The

assembly was sealed inside of a furnace tube so that a gas could be passed outside the sphere.

The initial permeability measurements were performed using lime spheres. Lime was chosen as a convenient medium to develop the initial experimental technique and, since diffusional data[50] exists for porous lime compacts, this served to provide a check on the validity of the results. The basic technique developed for the permeability measurements in porous lime is described in Section 4.2.

Having established the basic technique, the work was then extended to permeability measurements in porous, reduced, iron spheres. This is described in Section 4.3.

In the final part of this work, described in Section 4.4, countercurrent gaseous diffusion through porous lime and porous reduced iron was investigated for both isobaric and non-isobaric flow conditions. The results of the isobaric flow experiments were used to calculate the effective binary diffusion coefficient, D_{ABeff}, which together with the results of permeability experiments, could be used to quantify certain parameters which characterise the diffusion of the gases through the porous medium.

The non-isobaric experiments were used to provide data for comparison with the prediction obtained from the Dusty Gas Model.

4.2 PERMEABILITY MEASUREMENTS ON POROUS LIME SPHERES

4.2.1 THE PRODUCTION OF THE LIME SPHERES

The production of the lime spheres was carried out in three main steps:

1) Compaction of analar calcium carbonate powder around a Wood's metal sphere and the subsequent removal of the Wood's metal.

2) Sintering of the hollow spheres in an atmosphere of pure CO_2 at $870^{O}C$.

3) Calcination in air of the hollow calcium carbonate spheres at $950^{O}C$.

4.2.1.1 COMPACTION

Analar grade precipitated $CaCO_3$ powder with a maximum impurity content of 0.166% was obtained from Hopkins and William Ltd. The powder was placed in a three part plastic mould, made of Gelflex Hot Melt Compound, a castable material based on vinyl resin, which behaves as a liquid under high pressures thus allowing isostatic pressing conditions to be established and therefore achieving uniform compaction of spherical shapes. The three part Gelflex mould, shown in Figure 4.1, was produced in a die using a top and a funnel, previously heated at $150^{O}C$, to feed molten plastic to compensate for contraction into the die during solidification.

Wood's metal, having a composition of 15% Bi, 26.7% Pb, 13.3% Sn and 10.0% Cd and with a melting temperature of $70^{O}C$[102] was used to produce the metallic core inside the compacted sample spheres. Wood's metal spheres were produced by pouring the liquid alloy into a two part steel

103

Figure 4·1 : The geometry of the Gelflex mould and the steel die used to produce it.

Gelflex Mould
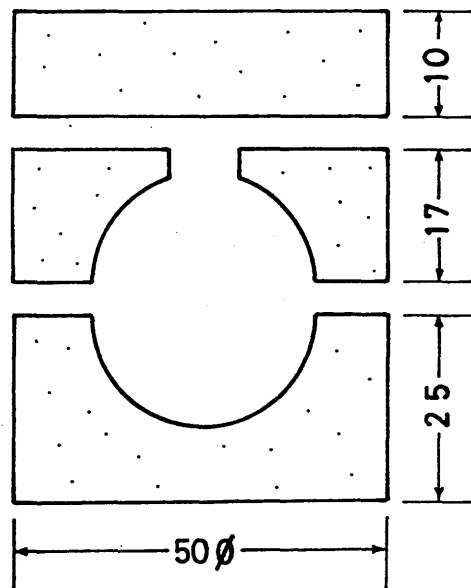
Steel Die
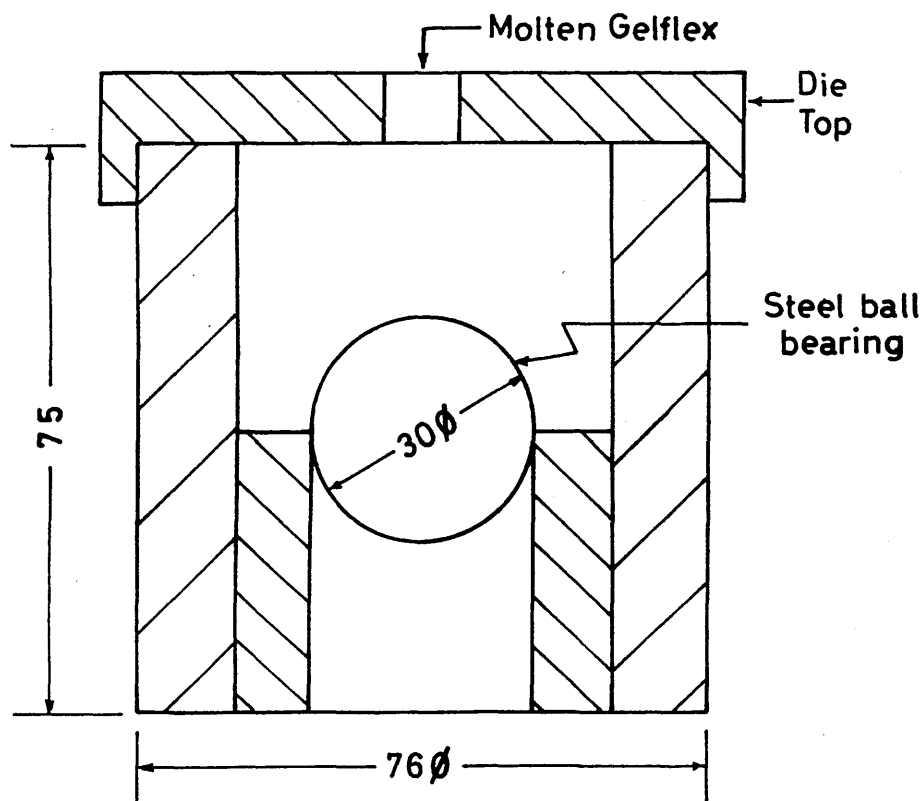
All dimensions in mm.

die containing a spherical cavity of 0.625 cm radius shown in Figure 4.2.

In order to make the hollow sphere from $CaCO_3$ powder the bottom part of the plastic mould was filled and the Wood's metal sphere centered in this powder. The upper part of the plastic mould was then placed over the bottom part and filled with an equal quantity of powder. A circular disc of Gelflex,1.5 cm high,was finally placed on top of the mould to produce a uniform distribution of Gelflex around the sphere. The mould and its contents were introduced into the bore of the die.

A rubber composite disc was placed at either end of the plastic mould in order to prevent leakage of the Gelflex between the bore and plungers during pressing. Compacting pressures varying from 150 to 250 MN/m^2 were applied to the plunger for three minutes. Almost perfect spheres of $CaCO_3$ were obtained. By varying the compaction pressure the porosity of the calcium carbonate spheres produced could be varied as shown in Table 4.1.

Figure 4·2 : The two-piece steel mould used to produce the Woods
metal spheres.

Section XX'

Molten Woods metal

Locating
pins

Parting
line →

6·25 mm diameter
cavity
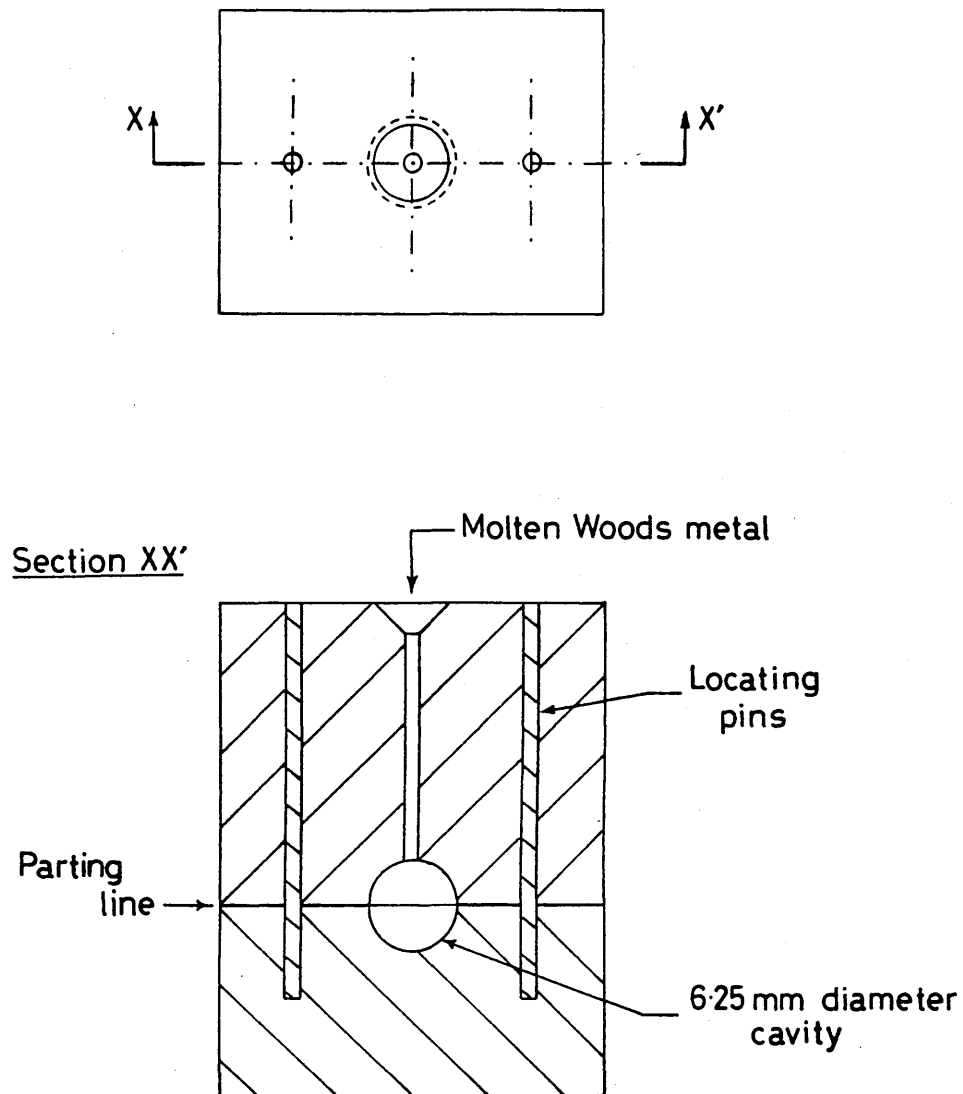
Table 4.1   The effect of compaction   pressure on the porosity of the calcium carbonate spheres

Sphere No.	Force /(kN)	Weight of Wood's Metal (B)/(g)	d /(mm)	Weight CaCO$_3$ sphere Containing Wood's Metal (A)/(g)	W$_1$/ (g)	W/ (g)	W$_s$ = (A-B)/ (g)	W-B/ (g)	W$_2$=W-W$_1$/ (g)	V$_a$ = $\frac{W_2+W_s}{\rho_{Hg}}$ /(cm^3)	ρ_a =$\frac{W_s}{V_a}$ /(g cm^{-3})	γ= 1- $\frac{\rho_a}{\rho_{true}}$	Pressu /kN.m^{-2}
69	510	10.8753	23.85	20.5076	2.9	65.22	9.6323	54.3447	51.4447	4.5305	2.1355	0.2149	259.7
68	400	10.9747	23.67	20.8012	2.9	71.0	9.8265	60.0253	57.125	4.9440	1.9874	0.2693	203.7
65	300	10.7343	27.17	20.5632	2.9	71.30	9.8289	60.5957	58.0257	4.9800	1.9719	0.2750	152.7
66	300	10.9360	23.80	20.7050	2.9	71.2	9.7690	60.094	57.364	4.9578	1.9704	0.2750	152.7
63	200	10.8330	24.34	20.4197	2.9	71.7	9.5867	60.86	57.967	4.9888	1.9216	0.2935	101.8

Cross-sectional area of mould   =   19.635 cm^2

ρ_{Hg} =   13.541 g/cm^3

ρ_{true}CaCO$_3$ =   2.72 g/cm^3

See Section 4.3.5 for nomenclature and method.

4.2.1.2 POWDER COMPACTION DIE

The die used initially was constructed from two concentric
rings of steel with an interference fit between the two.
The outer sleeve was made from EN 25, while the inner
sleeve and also the plunger were made from H 11. The die
performed satisfactorily for a short period of time but then
problems were encountered with its use, until finally,
the inner sleeve cracked. It was therefore found necessary
to design and manufacture a suitable replacement die which
would better stand the operating conditions imposed upon
it.

The performance of isostatic pressing tools is in general
governed by a number of factors, including proper design
and method of manufacture, correct heat treatment, degree
of care in the assembly and so on. Perhaps the most important
consideration is the choice of the tool material and
deficiencies with respect to this proved to be the reason
for the failure of the original die which had been designed
prior to the current project. The hardness of the heat
treated material used for the inner sleeve and plunger was
found to be too low (37 HRC) to sustain the loads imposed.
The history of the problems associated with this die are
summarised below.

After the compaction of a limited number of spheres it was
discovered that the bore and the plunger had bulged
slightly, necessitating the application of pressure to
separate them.   This operation produced scoring of the
bore surface. After almost every successive pressing the
bore and the plunger had to be reground, which meant that
the close fit between the bore and the plunger no longer

existed. Eventually the fit became so poor that a new

plunger had to be manufactured to fill the bore. This

rectified the problem for a short period of time, but on

the application of greater pressure to obtain a less porous

sphere, the inner sleeve cracked due to stress concentra-

tion in an area of the bore where scoring was most

noticeable. The design of the new die became inevitable.

4.2.1.2a   THE DESIGN OF THE IMPROVED POWDER COMPACTING DIE

To withstand the stresses set up during compaction, and

taking into account that the dimensions and mass of the

isostatic tool have to be such to permit ease of handling,

it is a current practice to surround the compaction container

liner with one or more appropriate rings. The support rings

are designed to have an interference fit between mating

diameters of adjacent rings and between the inner ring and

the die insert. The interference imposes a compressive hoop

stress on the inner rings and on the die insert. The

compressive hoop stresses imposed by all the support rings

has a cumulative effect at the surface of the bore of the die

insert and consequently, the resultant tensile hoop stress on

this bore is reduced. This enables the maximum stress

difference between the radial compressive and hoop tensile

stresses, particularly at the surface of the bore of the

die insert, to be reduced and allows larger loads to be

sustained before any one material reaches its yield

condition.

Frequently the concentric rings are machined with a 1°

taper[95] to predetermined lines and forced into one another

by a hydraulic press to obtain higher interference than

can usually be obtained by shrinking.

Several methods[96,97,98,99] for calculating the diameters of the rings and the degree of interference have been described in the literature. A procedure for determining the appropriate radii, interference fits and resultant stress for a multi-ring die has been developed by Becker and Molick[99] which assumed a von Mises criteria of yielding and a state of plane stress in the liner and rings. The maximum pressure, $P_{o,max}$, that the bore can withstand before yielding occurs, is given by:

$$P_{o,max} = \tfrac{1}{2} \sum_{r=1}^{n} y_n - \frac{n}{2} \left(\frac{y_1 y_2 \ldots y_n}{k^2}\right)^{1/n} \tag{4.1}$$

where:

n = number of rings

y_n = the yield strength in uniaxial tension for ring n

k = the overall radius ratio = $k_1 . k_2 \ldots k_n = \dfrac{r_{e,n}}{r_{i,o}}$

k_n = the external-internal radii ratio for ring n

$r_{e,n}$ = the outer radius of the container

$r_{i,o}$ = the inner radius of the container.

The material to be used in the construction of the die had the following characteristics:

Material	Yield Strength	Use
EN 25	$y_1 = 112.5$ kg/m²	outer ring
H 13	$y_2 = 150.4$ kg/m²	intermediate ring
KE 970	$y_3 = 175.8$ kg/m²	inner ring

Using formulae (4.1) the value of the maximum pressure is

$$P_{o,max} = \tfrac{1}{2}(175.8 + 150.4 + 112.5) - \frac{3}{2}\left(\frac{175.8 \times 150.4 \times 112.5}{3^2}\right)^{1/3}$$

$$= 119.95 \text{ kg/m}^2$$

110

The value of k = 3 was imposed by the necessity to have an internal radius, $r_{i,o}$ = 2.54 cm, in order to coincide with the dimensions of the plastic mould and an outer radius $r_{e,n}$ = 7.62 cm, which was determined by the outer radius of the outer ring of the original die, which was reused in order to reduce machining and heat treatment time. If r_1 is the external radius of the inner ring and r_2 is the external radius of the intermediate ring, then r_1 and r_2 are defined by the relationship:

$$y_1 \left(\frac{r_{i,o}}{r_1}\right)^2 = y_2 \left(\frac{r_1}{r_2}\right)^2 = y_3 \left(\frac{r_2}{r_{e3}}\right)^2 \qquad (4.2)$$

Substitution into equation 4.2 of the appropriate values leads to the result that:

r_1 = 4.049 cm

r_2 = 5.974 cm

A schematic diagram of the new die is shown in Figure 4.3 and photographs of the actual die are shown in Plates 4.1a and 4.1b.

4.2.1.2b CALCULATION OF THE RELATIVE INTERFERENCE BETWEEN THE INTERMEDIATE AND OUTER RINGS

It is difficult to obtain data on the modulus of elasticity, Poisson's ratio and yield strength of the steel used for the bore and rings. Values which have been quoted[95] for steels in general indicate that at room temperature the modulus of elasticity, E, may vary from 17,700 - 19,950 kg/m^3 and Poisson's ratio, ν, from 0.25 - 0.33. The values of the elastic modulus and Poisson's ratio of the intermediate and outer ring materials were chosen as E = 18,985 kg/m^2 and ν = 0.27 respectively. The relative interference, S, between the two rings is given by

Figure 4·3 :   Sectional view of the powder compaction die and mould.

Plunger
    : KE 970 steel.

15·24 cm

11·95 cm

8·10 cm

5·08 cm

17·50 cm

Barrel :

KE 970 steel.

H 13 steel.

EN 25 steel.

Gelflex disc.

Gelflex mould.

KE 970 steel
    cylinder.
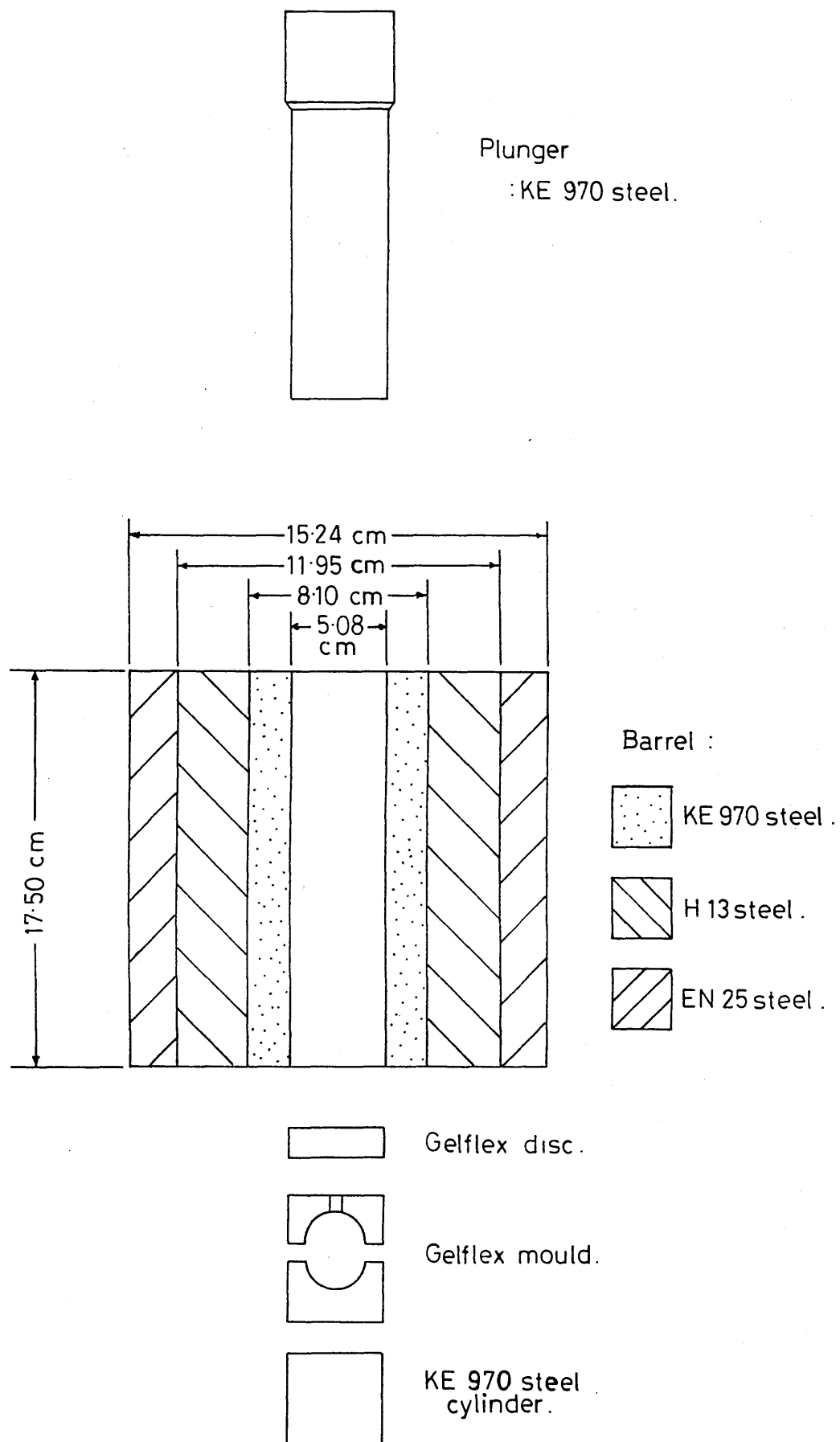
Plate 4.1:

    (a)   The powder compaction die and the Gelfex
           mould.

    (b)   The barrel of the powder compaction die
           showing the three ring construction.

(a)

(b)

113a
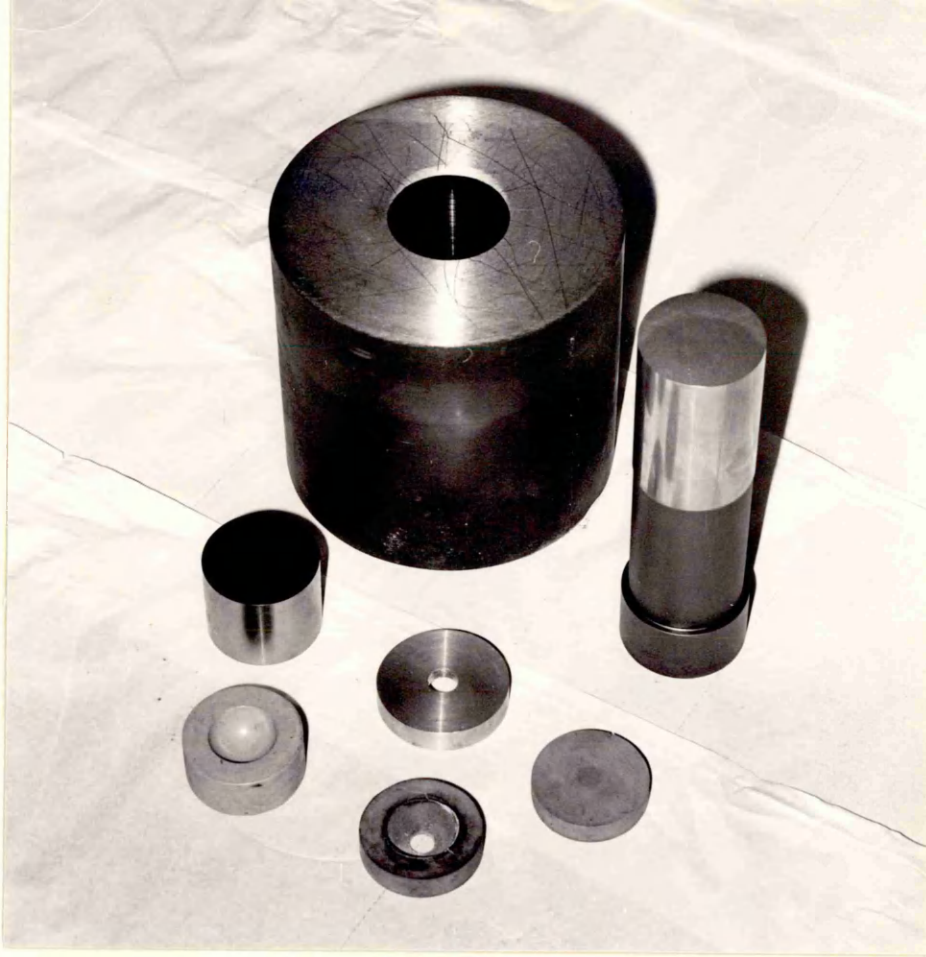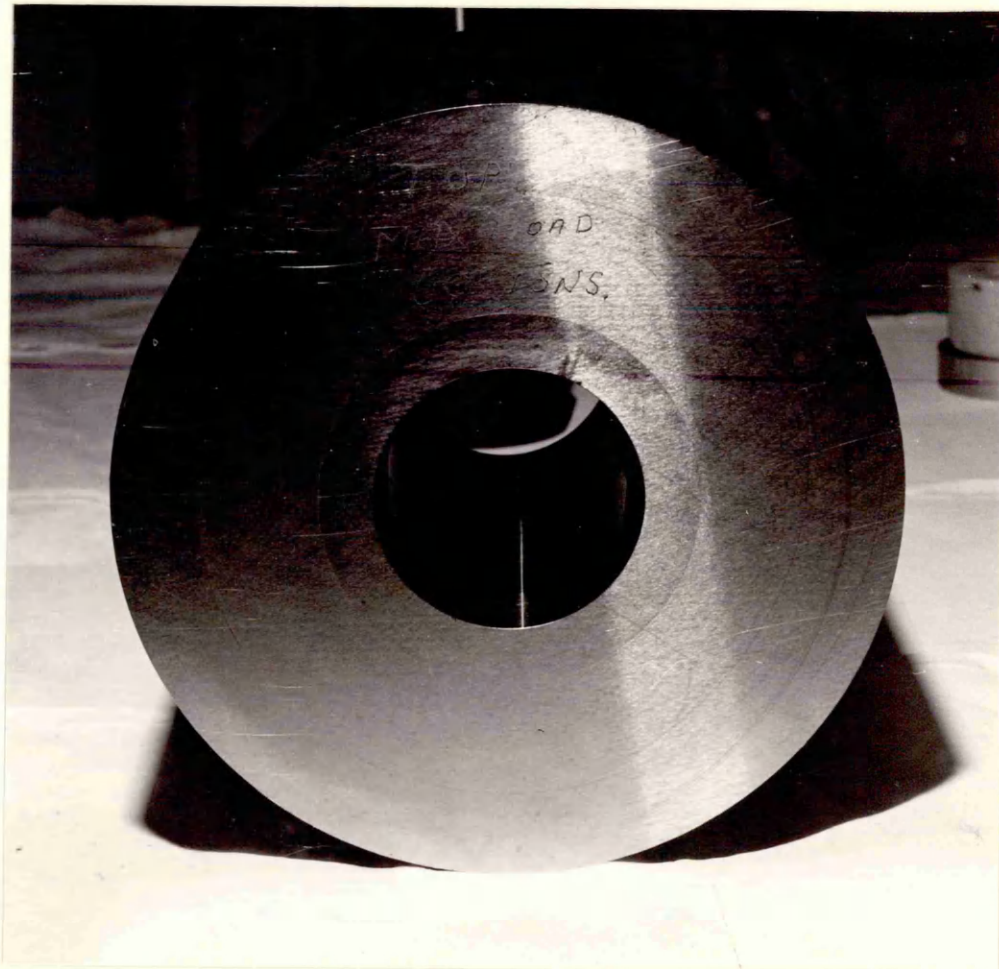
the general formula.

$$\frac{S}{y_3} = \alpha\left(\frac{1-\nu_2{}^2}{E_2}\right) + \beta\left(\frac{1-\nu_3{}^3}{E_3}\right) - \gamma_c \qquad (4.3)$$

where:

$$c = \frac{\nu_2(1+\nu_2)}{E_2} + \frac{\nu_3(1+\nu_3)}{E_3} \qquad (4.4)$$

$$\alpha = \frac{1}{2}\left(1 - \frac{3_a}{k^1}\right) \qquad (4.5)$$

$$k^1 = \left(\frac{r_{e.3}}{r_1}\right) \qquad (4.6)$$

$$\beta = \frac{1}{2}\left(1 + \frac{a}{k^1}\right) \qquad (4.7)$$

$$\gamma = \frac{1}{2}\left(1 - \frac{a}{k^1}\right) \qquad (4.8)$$

$$a = \left(\frac{y_2}{y_3}\right)^{1/2} \qquad (4.9)$$

when: $E_2 = E_3 = E$ and $\nu_2 = \nu_3 = \nu$ and under conditions of plane stress the equation 4.3 reduces to:

$$2\gamma = \frac{SE}{y_3(1 - \nu^2)} \qquad (4.10)$$

where $A = 2\gamma$ = constant.

Typical values of the constant A have been determined as a function of the value of k_1 and the ratio of y_2/y_3 and are tabulated in NEL Report No. 197[95].

For k_1 = 1.882 and y_1/y_2 = 1.35 the value for A = 0.42 by interpolation, in which case the interference fit for intermediate and outer ring using equation 4.10 is equal to 0.0368 cm. It should be remembered that this solution only applies for a two ring die. For a three ring die the relationship is rather more complex and no analytical solution is available.[100]

The degree of interference between inner and intermediate ring has been arbitrarily taken as 0.0294 cm which represents a 20% decrease compared with that previously

114

calculated. The satisfactory performance of the die over a long period of time would appear to suggest that this assumption has been reasonable.

4.2.1.2c <u>THE MANUFACTURE OF THE DIE</u>

The die components were machined by workshop staff within the Department of Metallurgy of the Sheffield City Polytechnic. The individual components had to be machined very precisely and the mating angles had to match exactly. The taper bore of the outer ring, made from the already existing EN 25 outer sleeve from the original die, was remachined in its hardened state, first by turning using a tungsten carbide tool and finally by internal cylindrical grinding.

The intermediate sleeve made from H 13 and the inner sleeve made from D2 KE 970 were first rough turned both externally and internally leaving approximately 1.5 mm of material on both faces. Machining stresses were removed at this stage by thermal stress relieving treatment in order to avoid distortion during the subsequent hardening treatment. Both items were then turned to within 0.2 mm of their final dimensions. The components were then hardened and tempered in order to develop their maximum hardness. After hardening and tempering, the intermediate and inner sleeves were precisely ground to give the correct interference and mating angle. A 2 mm radius was ground on the leading outer edge of both the intermediate and inner sleeves in order to reduce the chance of tearing when the components were pressed together.

The intermediate sleeve was pressed into the outer one and then finally the inner sleeve pressed into position.

4.2.2   PREPARATION OF THE CALCIUM CARBONATE SPHERES FOR PERMEABILITY MEASUREMENTS

After compaction and porosity measurements of the $CaCO_3$ spheres, the Wood's metal had to be removed. At first this was achieved by carefully drilling by hand a 4.3 mm diameter hole, this diameter coinciding with the external diameter of the alumina support tube (see Figure 4.4). The sphere was gently heated while being held on a cylindrical support. The Wood's metal melted and ran out leaving a perfectly clean internal surface.

Whilst this technique proved satisfactory for the removal of the Wood's metal, later problems were encountered:

a) Drilling by hand produced a hole which was insufficiently precise to produce a good shrink fit on the end of the alumina tube.

b) The sphere had a tendency to crack during the drilling operation.

To overcome these problems, the technique had to be modified. The Wood's metal was removed by hand drilling a 2 mm diameter hole, which is half of the diameter of the hole required for the alumina tube, and after allowing the molten Wood's metal to run out through this hole, the diameter of the hole was then increased to that of the alumina support. In order to prevent the spheres cracking during this operation a slight compressive stress was imposed on the sphere using the box shown in Figure 4.5.

Within the metal box the sphere was centrally positioned and packed in sand. A piece of foam rubber was placed over the sphere and the metal lid of the box screwed down, thus compressing the sphere.

116

Figure 4·4 : Sectional view of the lime sphere and twin-bore alumina support tube .

Flowmeter

Manometer
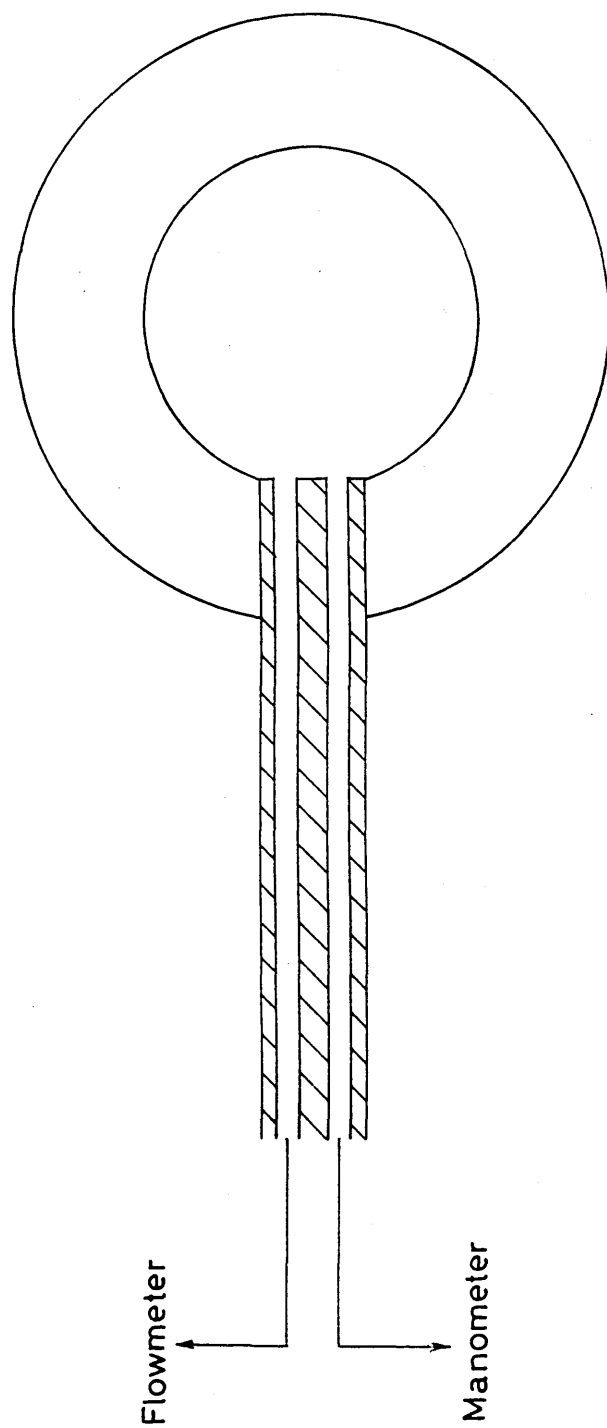
gure 4·5 : A cut-away view of the box used to support the hollow calcium carbonate sphere while drilling the hole for the diffusion shaft.
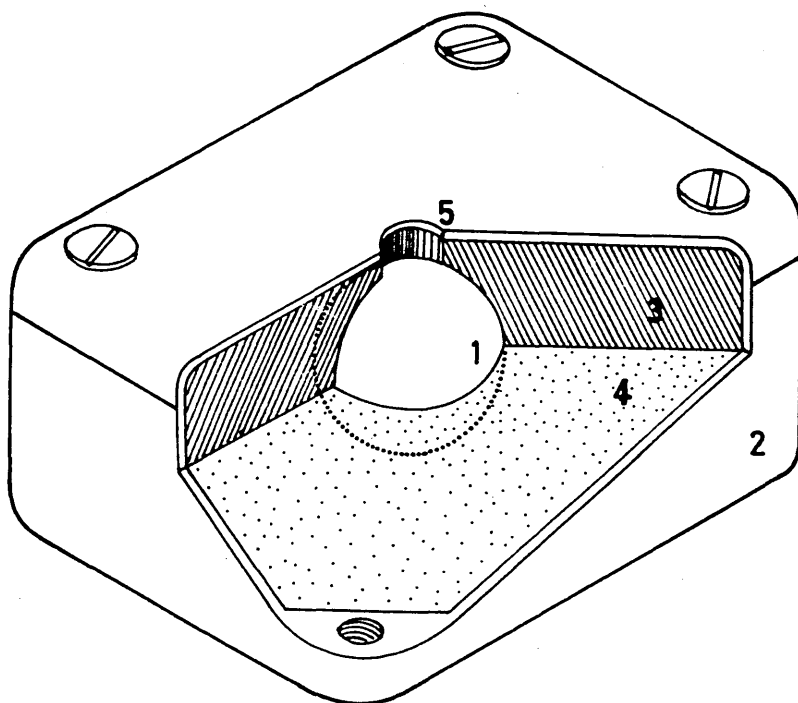
Key to the diagram :

1. Calcium carbonate sphere.
2. Metal box.
3. Compressed foam rubber.
4. Fine sand.
5. Hole through box lid for drill.

A hole in the lid of the box coincided with the hole drilled to remove the Wood's metal, provided that the sphere had been correctly positioned. The sphere could be then effectively drilled without cracking, using a vertical drilling machine.

4.2.3 SINTERING AND CALCINATION OF CaCO₃ SPHERES

Permeability measurements were made on lime spheres
produced by sintering and calcination of the compacted
calcium carbonate spheres, the measurements, the sintering
and the calcining being carried out in the same furnace.
The furnace was a horizontal tube heated by 8 silicon
carbide elements and for which the temperature profile,
indicating a hot zone of 4 cm, had been determined. The
furnace tube was made of aluminous porcelain, 50 cm long
with an external diameter of 5 cm.

The furnace temperature was controlled using a Eurotherm
controller. The ends of the tube were sealed by water
cooled aluminium end assemblies using copper cooling coils.
Details of these assemblies are presented in Figure 4.6. A
drilled CaCO₃ sphere was positioned on the end of the alumina
support shaft taking care to ensure that the end of the
tube did not protrude beyond the inner wall of the sphere.
The sphere being treated was held in position at the end of
the support rod (Plate 4.2) and was then carefully introduced
into the horizontal tube of the furnace. A shaped block of
sintered alumina cement supported the shaft inside the tube
and enabled the sphere to be positioned in the hot zone without
touching the walls. After positioning the sphere the end
plate with the O ring in place was tightened to produce a
gas tight seal. The furnace tube was purged for one hour,
by passing CO₂ at a rate of 200 cm³/min. Using the same
CO₂ flow rate, the sphere was then heated to the sintering
temperature of 870°C and held at this temperature for one and
a half hours.

Calcination of the sphere was achieved by increasing the
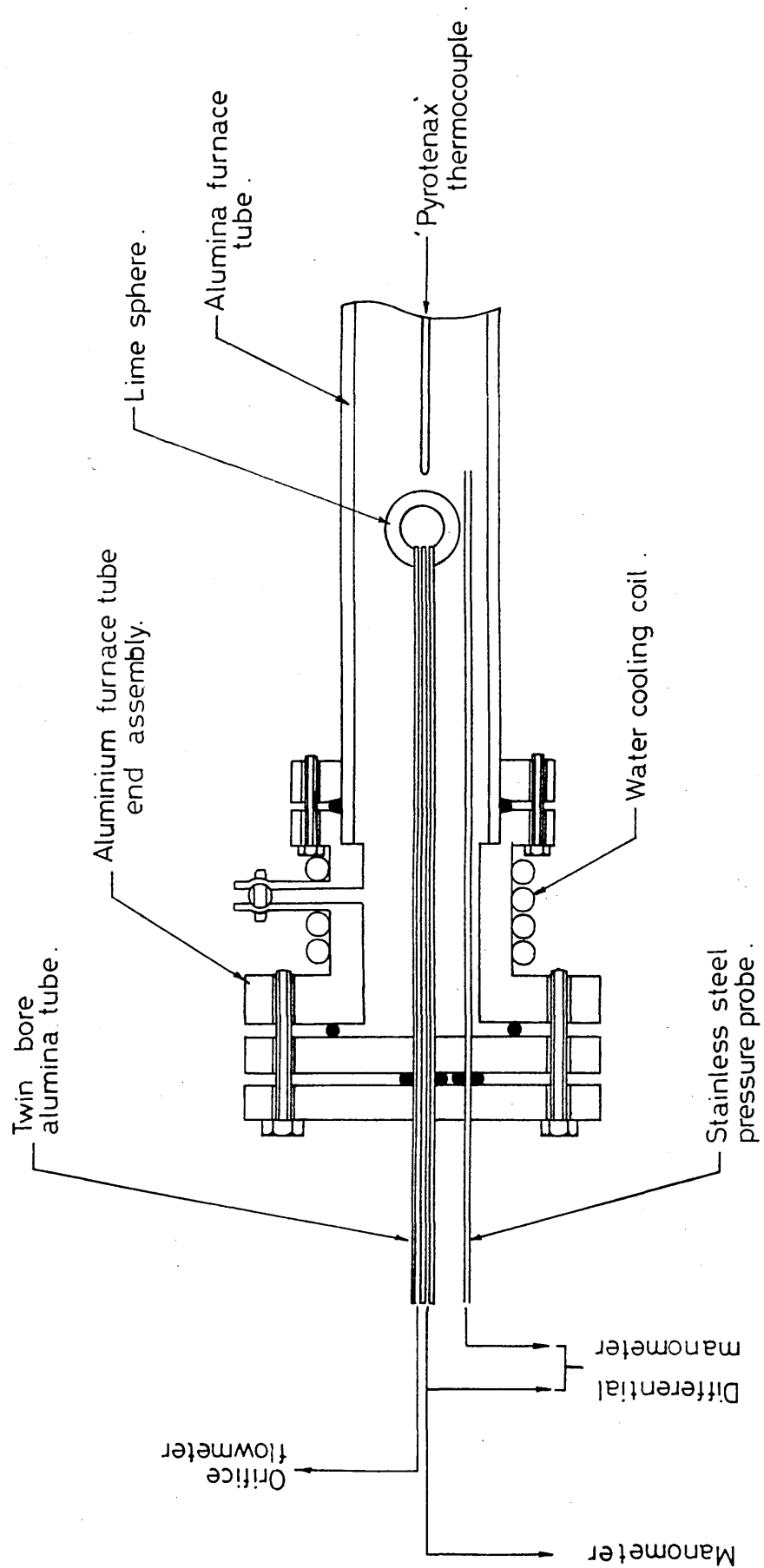
Figure 4.6 : Detail of the furnace tube for the measurement of gas permeability through porous lime spheres.

121

Plate 4.2:   A lime sphere on the end of the twin-bore
              alumina support tube.
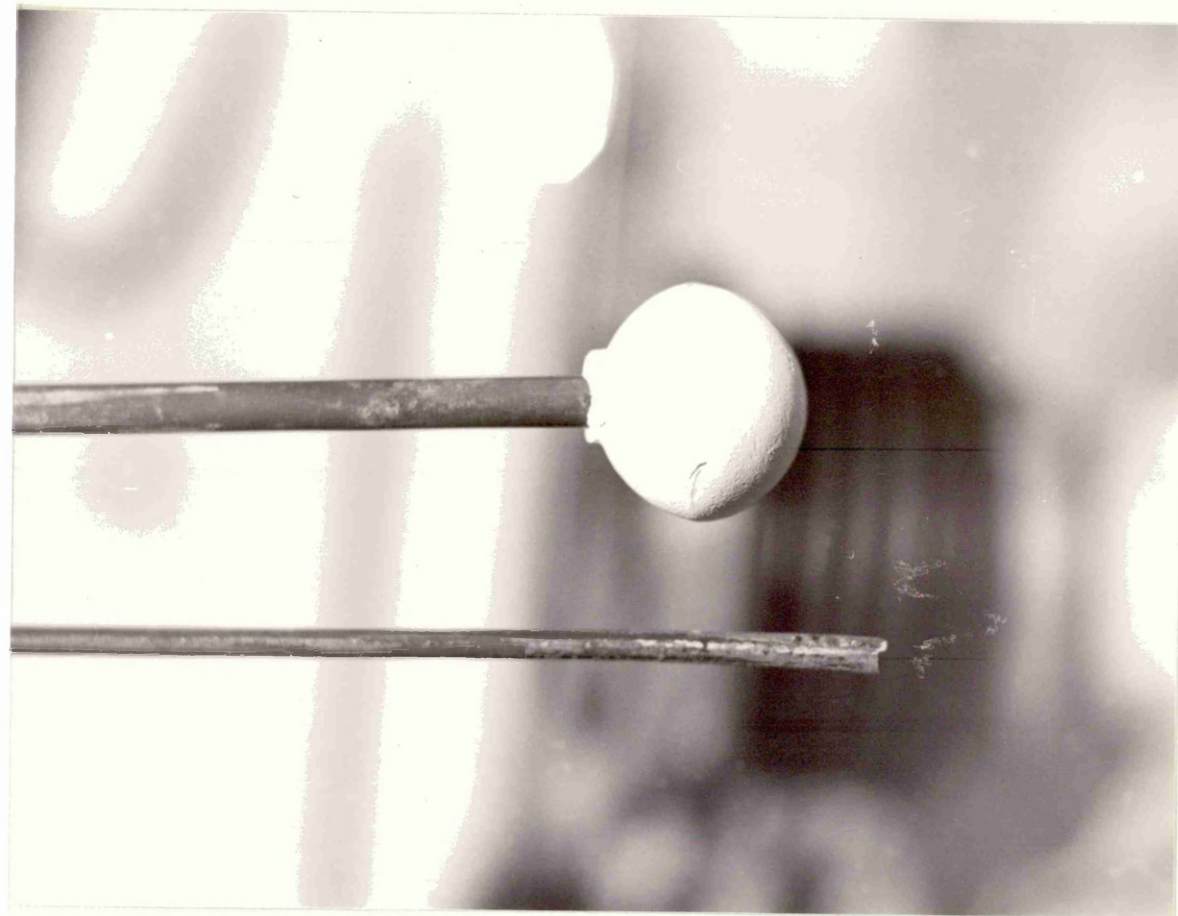
temperature to 950°C and, when this temperature was
reached, introducing a flow of air into the system and
maintaining it during one and a half hours before any
permeability experiments were initiated.

The supply of an adequate flow of air was found to be
critical in achieving complete decomposition of the car-
bonate. It was found that an air flow rate of at least
300 cm^3/min. had to be maintained throughout the calcination
period. After purging with the appropriate inert gas the
sphere was in a condition suitable for permeability measure-
ments to begin.

4.2.4 FLOW SYSTEM FOR PERMEABILITY MEASUREMENTS

The permeability of the CaO sphere was determined at various total system pressures by monitoring the volumetric gas flow rate through the porous shell. A schematic diagram of the full apparatus used in this work for the permeability measurements is shown in Figure 4.7.

The gas to be used for the permeability measurements was supplied from gas cylinders obtained from BOC. The flow rate of the gas into the system was controlled by means of the combined needle valve and orificemeter No.1 shown in Figure 4.7.

For permeability measurements close to atmospheric pressure, valve B was fully opened and valve A partially but not fully closed.

To achieve pressures greater than 1 atm. within the furnace tube, valves A and B were partially closed by different amounts so as to maintain a pressure drop across the lime shell sufficient to produce a measurable flow at orificemeter No.2.

For experiments with a system pressure less than one atmosphere the exhaust gas bottle,which served to minimise fluctuations in pressure in the system,was connected to the rotary vacuum pump, valve B being fully opened and valve A was partially closed. The rotary pump could be controlled in order to maintain different pressures within the system.

The lime sphere was supported within the furnace on the end of the twin bore alumina support shaft. One of the bores of

Figure 4·7 : Schematic diagram of the flow system for the measurement of gas permeability through porous lime spheres.
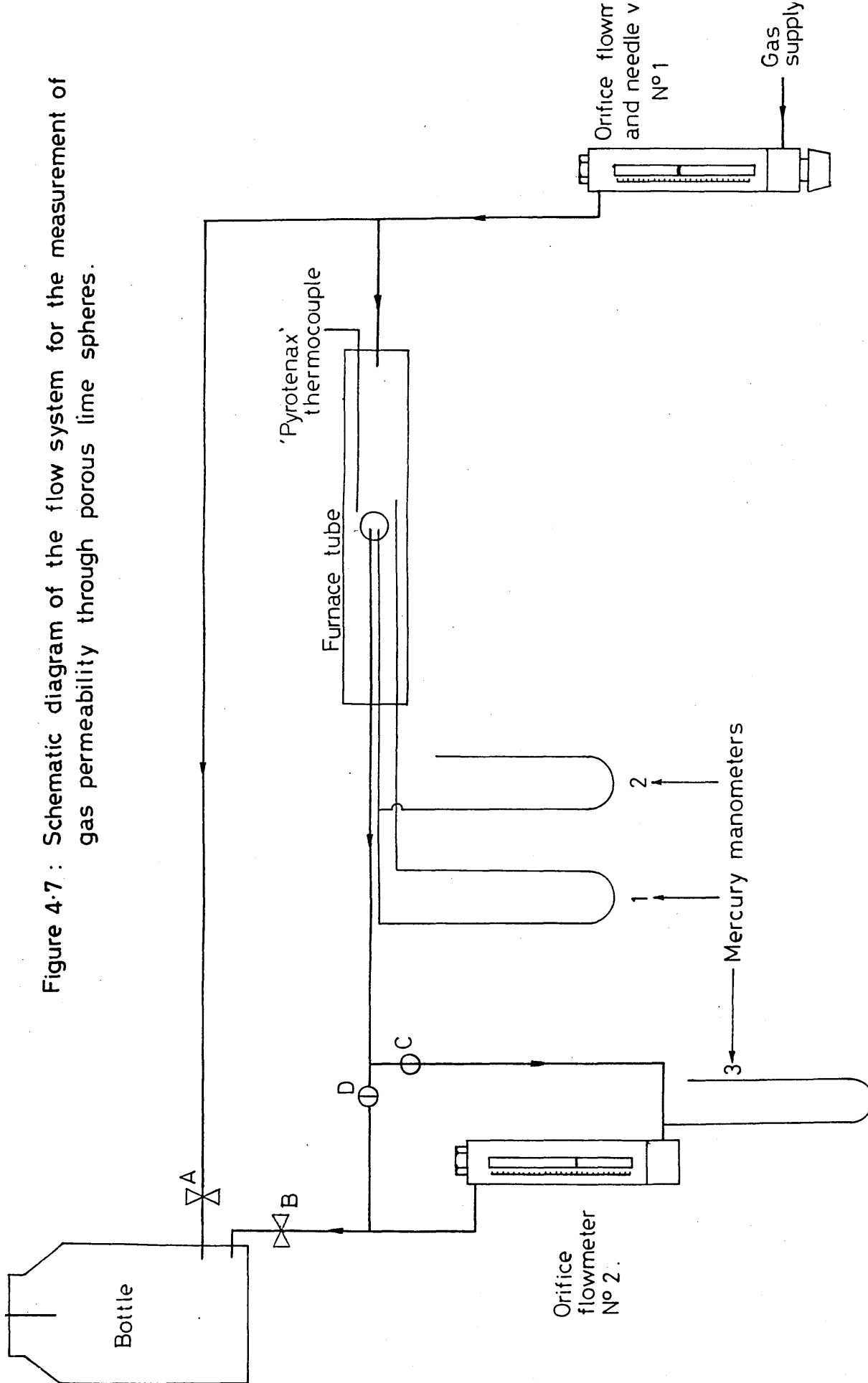
the shaft was connected to orifice flowmeter No.2 which
thus measured the rate at which the gas permeated through
the porous lime. The other bore was used to measure the
total pressure within the sphere by means of the mercury
manometer No.2. The same bore was also connected to one
side of a second mercury manometer,No.1,the other side of
which was connected to a hollow stainless steel probe. The
end of this probe was positioned close to and slightly in
front of the lime sphere within the furnace tube. Manometer
No.1 therefore measured the pressure difference across the
porous lime shell.

4.2.5   THE MEASUREMENTS OF GAS FLOW RATES

Gallenkamp orificemeters, using di-n-butyl phthalate as the manometric fluid were used to monitor gas flow rates (see Figure 4.7). The gas flow rate leaving the lime sphere via the ceramic support tube was very small and as a consequence was especially difficult to measure. Since there was no commercially available orifice plate which would adequately permit the measurement of the flow rates produced, a special orifice plate with a 0.1 mm diameter hole was fabricated out of 0.01 mm thick aluminium foil. Especially thin aluminium foil was chosen in order to minimise the pressure drop due to frictional losses during passage of the gas through the orifice. The 0.1 mm diameter hole was produced by sandwiching the aluminium between thin aluminium plates and drilling through the "sandwich" with a micro-drill of the required diameter. The piece of perforated foil was then mounted over the hole of a standard, normal diameter, Gallenkamp orifice plate (see Figure 4.8 and Plate 4.3) and sealed in position using Araldite epoxy resin.

Figure 4·8 : Sectional view of the 0·1mm diameter, foil orifice plate.

Aluminium foil

Araldite seal

0·1mm⌀

Standard Gallenkamp 'orifice'.
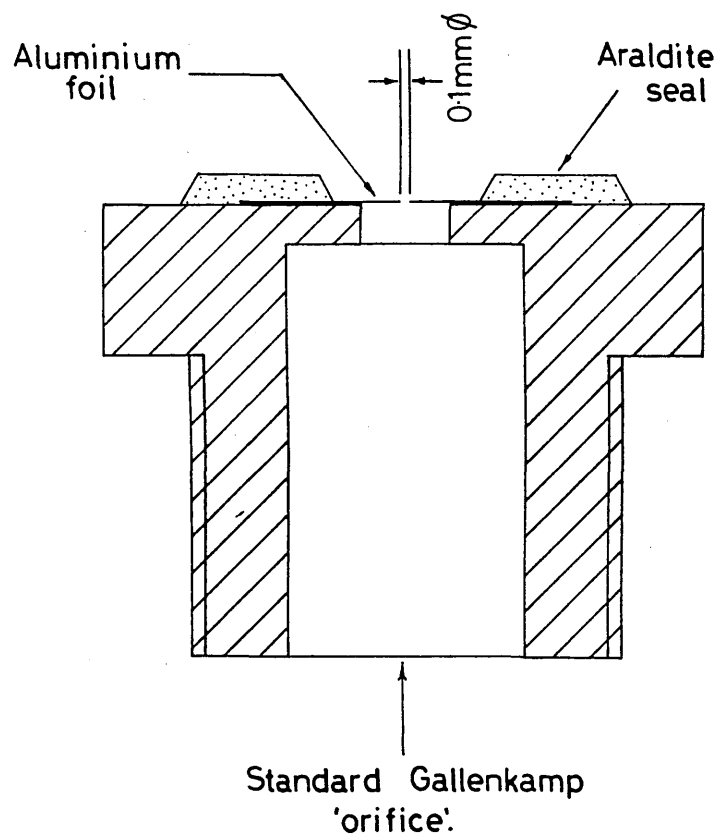
Plate 4.3:   The 0.1 mm diameter, foil orifice plate.

4.2.6 EXPERIMENTAL PROCEDURE

Prior to initiating the permeability experiments, the whole system was purged using the appropriate gas for which measurements were to be made.

Before actually making any permeability measurements, the pressure within the entire flow system was increased to about 1.5 atm. and all seals and joints were tested for leaks using soap solution. Only when this had been done was the apparatus ready for actual permeability determinations.

The volumetric flow rate of the gas leaving the sphere via the alumina support tube was monitored by orificemeter No.2 for various total pressures within the system, this being varied using the technique described in the previous section. When changing the pressure, valve C was always kept closed and valve D open, in order to prevent any surge of pressure in the system forcing manometer fluid out of the flowmeter. Once the desired pressure had been reached, valve C was opened and valve D closed. Conditions were allowed to stabilise for 20 minutes, before the head of fluid within the flowmeter No.2 and the pressure indicated by manometer No.1 and 2 were simultaneously noted.

Permeability experiments were carried out using helium and argon. The high temperature experiments were performed at the same temperature used for the decomposition of $CaCO_3$ spheres (1230K).

After the high temperature experiments had been completed, the sphere was slowly cooled over a period of several hours to lower temperatures and permeability determinations were

repeated. The sphere was then cooled to room temperature and removed from the furnace so its dimensions and porosity could be measured.

After cooling to room temperature, and before removing from the alumina support shaft, several diameters of the lime sphere were measured in different directions, using a standard micrometer, and the mean value calculated. The individual measurements rarely varied by more than ±0.6 mm. The sphere was then removed from the support shaft, a procedure which inevitably resulted in the fracture of the sphere into several fragments. Several measurements of the thickness of the shell fragments, these rarely varying by more than ±0.9 mm, were made, using a point micrometer, and again the mean value was calculated. The largest fragments of the lime sphere were used to determine its porosity.

4.2.7 DETERMINATION OF THE POROSITY OF LIME SPHERES

The evacuation method as described in British Standard 1902, part: 1A: 1966, was used to determine porosity.

A large fragment of the broken sphere was weighed (W_a) in air as soon as possible after its removal from the furnace. It was placed in a beaker inside a vacuum desiccator and the pressure reduced to less than 650 Pascals for a period of 20 minutes. While still applying the vacuum, a quantity of di-n-butyl phthalate was introduced into the beaker from a reservoir fitted to the lid of the vacuum desiccator. (See Plate No.4.4). A few more minutes were allowed to elapse before the pump was switched off and air admitted to the desiccator. The sample was removed and reweighed (W_b) whilst suspended in a balance bridge of di-n-butyl phthalate. Finally the fragment was weighed in air after the careful removal of any excess of the immersion liquid from its surface (W_c).

The apparent porosity of the sample is defined as:

$$P_a = \frac{W_c - W_a}{W_c - W_b} \times 100 = 100(1 - \frac{D_b}{D_{as}}) \qquad (4.10A)$$

where D_b = bulk density = $\dfrac{W_a}{W_c - W_b} D_1$

D_1 = density of the immersion liquid

D_{as} = apparent solid density = $\dfrac{W_a}{W_a - W_b} \times D_1$

The results of the porosity measurements are presented in the results section 5.3.2.

Plate 4.4:   The apparatus for the evacuation method
             (B.S. 1902, part 1A : 1966) used to
             determine the porosity of lime spheres.
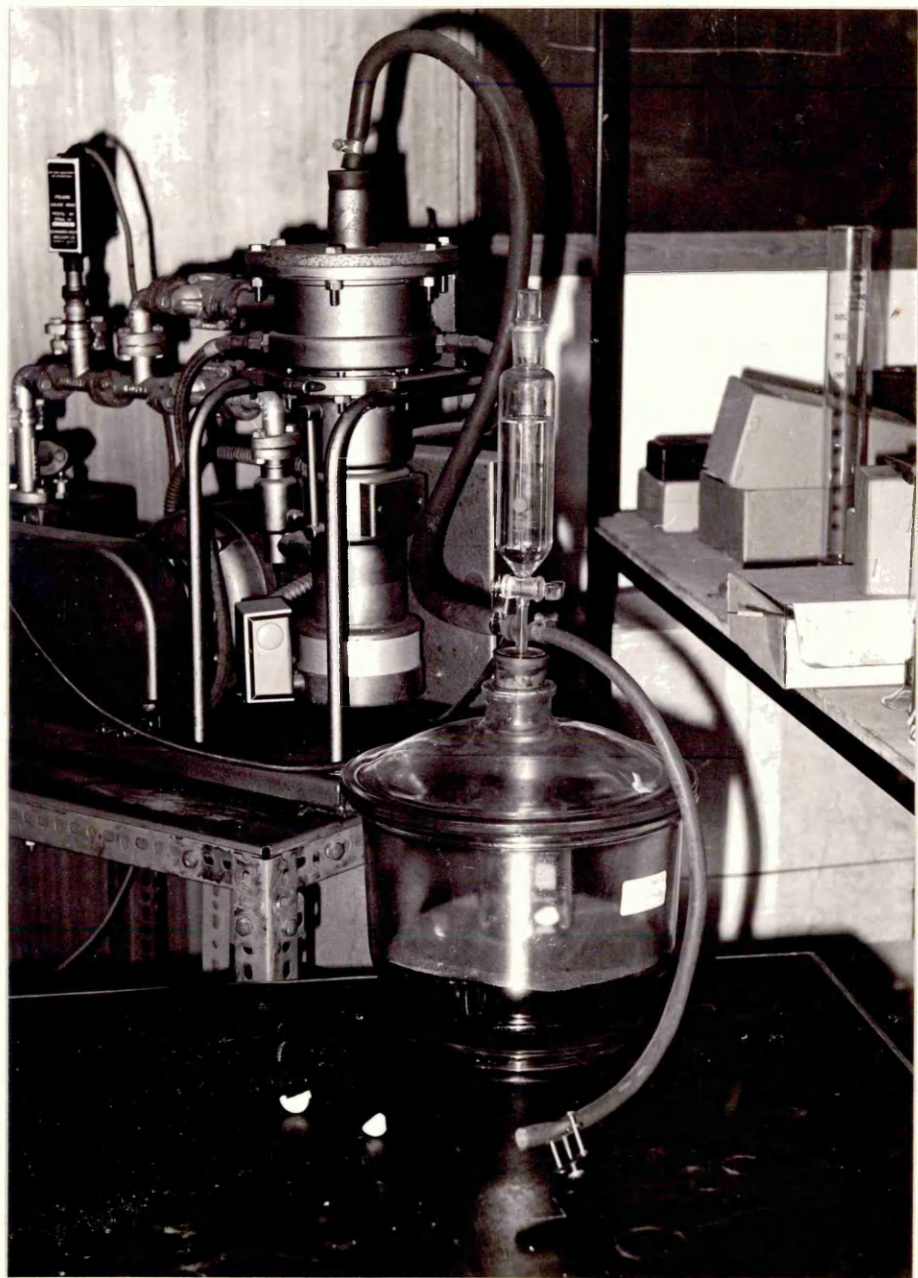
4.3 PERMEABILITY MEASUREMENTS ON REDUCED IRON SPHERES

4.3.1 MATERIALS USED FOR THE PRODUCTION OF IRON OXIDE SPHERES

The iron oxide starting material used in this work was iron ore provided by Teesside Laboratory, BSC. This was essentially almost a pure hematite ore with only 0.226% (SiO_2+ Al_2O_3), having a particle size analysis of:

    44.01% > 75 μm

    32.93% > 53 μm

    23.06% < 53 μm

In order to improve the green strength of the compact it is normal to add 8-14% of moisture[106]. Addition of 5% was found to be adequate.

At the outset of the work it had been anticipated that strong reduceable pellets could be obtained from the above mixture. Subsequent experimental work demonstrated that a much finer particle size was required for the iron ore. The original iron ore was ground for 4 hours producing material with a particle size distribution of:

     6.52% > 75 μm

    10.13% > 63 μm

    12.25% > 53 μm

     2.85% > 45 μm

    68.25% < 45 μm

In addition it was found that it was necessary to introduce 2% of CaO to the mixture. Analar grade CaO was used for this addition.

The development work which was undertaken to arrive at this mixture in order to produce a strong highly reduceable compact, free from cracks in the reduced state will be described in more detail in Section 4.3.3.

4.3.2 COMPACTION OF THE IRON OXIDE SPHERES

The technique used to compact the hematite spheres was essentially the same as that used to produce the $CaCO_3$ spheres described in Section 4.2.1.1, the Fe_2O_3 mixture being isostatically pressed around a Wood's metal sphere in a Gelflex mould using the die described in Section 4.2.1.2.

A compaction pressure of 25.4 MN/m^2 was used for 3 minutes. This value was determined by trial and error and appeared to be the optimum. Lower pressures were insufficient to bring about compaction, whilst higher pressure appeared to produce so great an elastic deformation in the Wood's metal sphere that, on release of the pressure from the die, the sphere's expansion induced tensile stresses in the Fe_2O_3 shell causing it to crack. After compaction a small hole was drilled in the position ultimately to be occupied by the diffusion shaft, using the method described in 4.2.1.4.

The Wood's metal was then removed by heating the inverted sphere supported by a small crucible, to 100°C. Whilst the majority of the Wood's metal could be removed in this way, a very small film tended to adhere at the inner surface of the sphere. This was removed by introducing a small amount of mercury into the cavity and allowing it to stand over night in a fume cupboard at room temperature. The mercury could then be decanted leaving a hollow Fe_2O_3 sphere with the inner surface free of any contamination.

4.3.3 DEVELOPMENT OF THE TECHNIQUES FOR THE SINTERING AND SUBSEQUENT REDUCTION OF THE IRON OXIDE SPHERES

The objective of this part of the work was to produce a strong hollow iron sphere, highly reducible, free from cracking and with a uniform porosity which would permit permeability and diffusion measurements to be made. It was originally hoped that the green iron oxide compacts could be directly reduced in order to achieve these properties. Unfortunately, when their reduction was attempted they disintegrated. The 'as compacted' spheres were clearly insufficiently strong to withstand the stresses induced as a result of the volumetric changes occurring during reduction. It was therefore necessary to sinter the green compacts in order to enhance their strength prior to reduction. Sintering was carried out in a muffle furnace which was open to the atmosphere and reduction studies were performed using pure H_2 in a vertical tube furnace.

4.3.3.1 SINTERING OF THE HOLLOW IRON OXIDE SPHERES

In the initial experiments the reduction strengths of the compacts were very low. Attempts were made to improve this strength by creating a diffusional bond between the hematite particles. To this end the compacted hollow spheres were heated in the muffle furnace in air for a period of 5 hours at a temperature of 1250°C.

No significant improvement in the behaviour of the spheres during reduction was obtained since they still exhibited extensive cracking.

As a consequence of the study of the literature described in Section 2.7 it was decided to introduce 2% CaO into the

hematite powder prior to compaction. Sintering of the compacted sphere was carried out for 20 hours at 1370°C in air. The resultant pellet on reduction exhibited no cracking demonstrating that the lime addition had been effective in increasing the reduction strength of the sintered compact. The addition of 2·0% lime was therefore adopted as standard practice in the manufacture of all the iron oxide spheres.

The effect of the lime addition on the structure of the material was investigated by scanning electron microscopy. Typical microstructures from various positions within a partially reduced sphere are shown in Plate 4.5 to illustrate the type of structure encountered. Within the unreduced sintered iron oxide layer, X-ray diffraction produced evidence for the existence of $CaO.2Fe_2O_3$ in the eutectic region indicated in Plate 4.5f.

Edax analysis confirmed that $CaO.2Fe_2O_3$ was a component phase constituent in the eutectic present. The actual composition of the phase obtained by analysis is shown in Table 4.2 together with its stoichiometric composition.

Table 4.2

	Ca(%)	O (%)	Fe(%)
Stoichiometric Composition	10.60	29.78	59.62
Edax Analysis	10.080	28.56	61.36
	10.484	29.07	60.746
	11.02	29.56	59.419

Plates 4.5 a-f

a. An optical photomicrograph of the unreduced sinter showing the presence of Fe_2O_3 grains and Fe_2O_3-CaO.2 eutectic (x 400).

b. An optical photomicrograph showing the boundary betw the unreduced and partially reduced sinter (x 400).

c. An optical photomicrograph within the partially redu sinter showing the presence of Fe_2O_3-CaO.2Fe_2O_3 eute (x 400).

d. An optical photomicrograph of an area close to the boundary between the partially and fully reduced zon the specimen (x 400).

e. An optical photomicrograph of the reduced iron struc close to the outer surface of the sphere. The mater is almost fully reduced, only a small amount of FeO persisting (x 400).

f. A scanning electron micrograph of an area of the unr sinter. Edax analysis was performed on the area ind and the results obtained, which are presented in Tab 4.2, confirmed the presence of CaO.2Fe_2O_3 phase.

Key to Symbols

H	:	Hematite; Fe_2O_3
M	:	Magnetite; Fe_3O_4
W	:	Wustite; FeO
Fe	:	Reduced iron
E	:	Eutectic; Fe_2O_3 - CaO.2Fe_2O_3
E_r	:	Partially reduced eutectic; FeO - CaO.2FeO

(a)

(b)

(c)

(d)

141

(e)

(f)

142
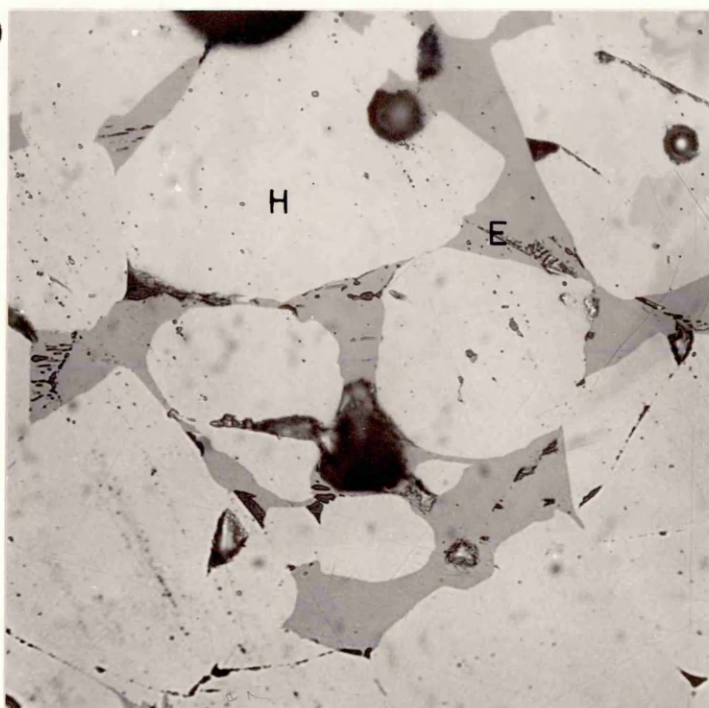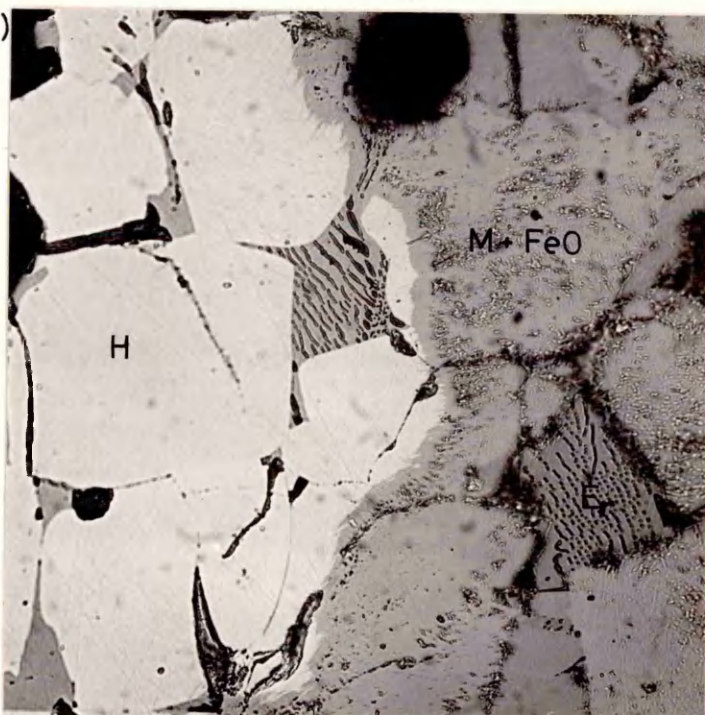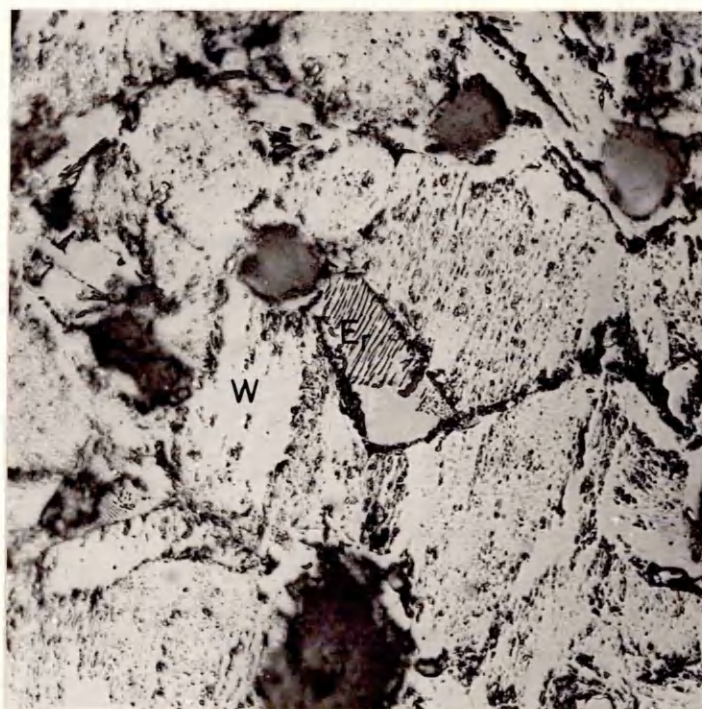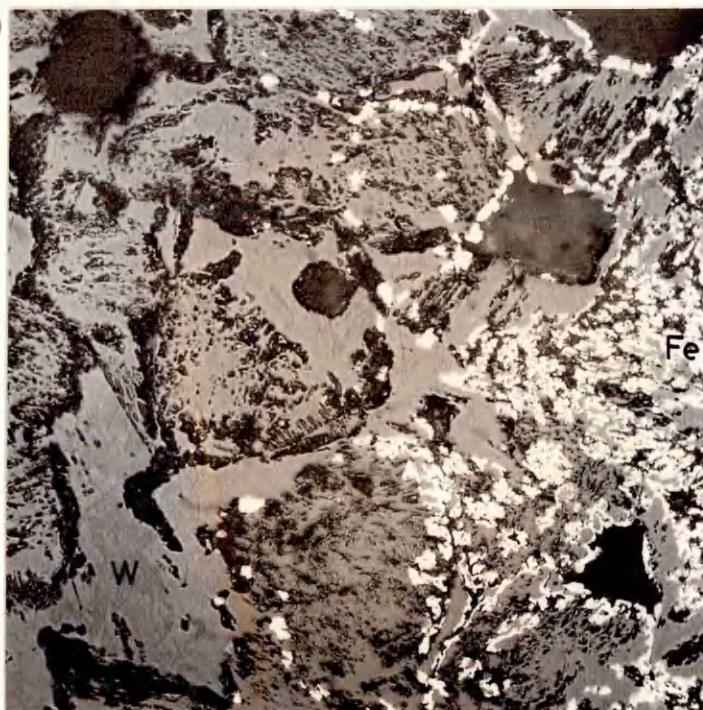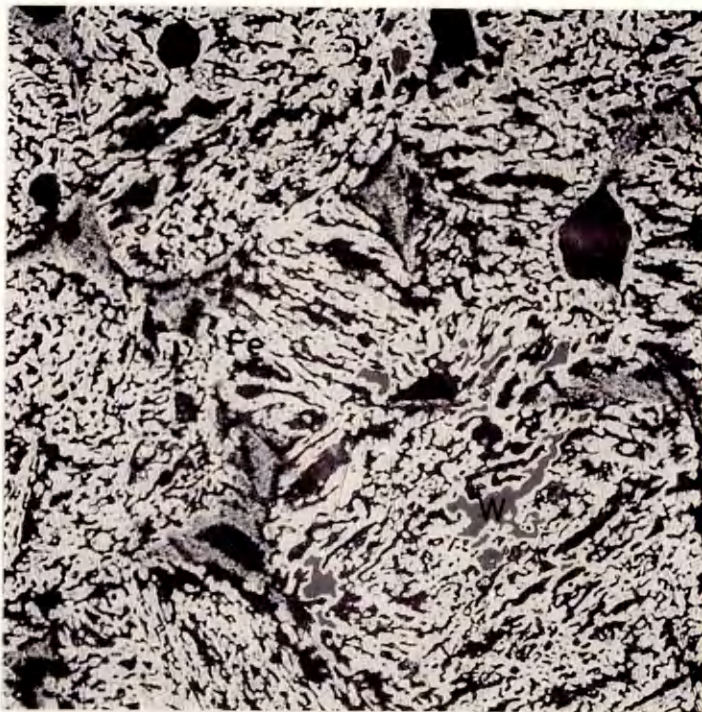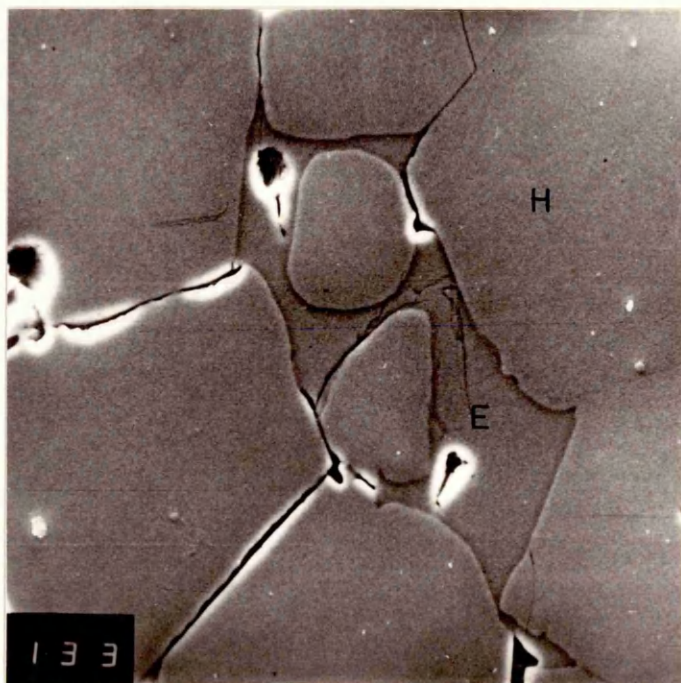
4.3.3.2 REDUCTION

Experiments were carried out in order to determine the optimum conditions necessary to achieve a high degree of metallisation as a consequence of the reduction process at 825°C. It was essential to reduce the iron oxide as completely as possible to iron, since incomplete topographic reduction would result in a rim of iron oxide with different transport characteristics.

A reduction temperature of 825°C was arbitrarily chosen as the optimum temperature, since it represents a compromise between the opposing requirements for a fast reduction rate whilst limiting the extent to which sintering of the reduced iron could occur.

The degree of metallisation was calculated from the mass loss occurring during reduction in H_2 for a fixed period of time. Reduction could not be monitored with the sphere attached to the diffusion shaft in the horizontal tube furnace. This was because, due to shrinkage during reduction, the spheres had to be cut before they could be removed from the shaft making a meaningful mass after reduction impossible to obtain. Separate reduction experiments were therefore carried out in a vertical tube furnace, the dimensions of the tube being identical to those of the horizontal tube used for permeability measurements. The hole in the sphere, where the diffusion shaft would ultimately be located was plugged with a small rod of mild steel to ensure similarity between the reduction process in these spheres and in the spheres in the horizontal furnace after their attachment to the diffusion shaft.

The spheres in the reduction experiments were suspended in the hot zone of the vertical furnace in a wire mesh basket with the plug positioned downstream in the reducing gas flow.

Experiments were conducted by reducing the spheres for a period of 60 minutes at various flow rates from 0.45 l/min hydrogen to 14 l/min, in order to establish the critical flow rate sufficient to ensure that starvation did not occur.[12][101]

The results are summarised in Table 4.3 in which the degree of reduction, %R, is expressed as:- $\frac{OXYGEN\ LOST}{INITIAL\ OXYGEN} \times 100$. The relationship between the degree of reduction and the volumetric flow rate of the reducing gas is illustrated in Figure 4.9. On the basis of the results shown in Figure 4.9 it was decided to use a flow rate of 5.612 lH_2/min in the subsequent experiments in which the degree of reduction as a function of time was determined. The results are also presented in Table 4.3 and graphically in Figure 4.10. From Figure 4.10 a minimum time of 2 hours and 30 minutes is necessary to achieve 99.3% reduction.

It was therefore decided that for the permeability experiments, the iron oxide spheres would be reduced at a temperature of 825°C for a period of 2.5 hours and using a flow rate of hydrogen of 5.612 l/min.

The average porosity of the partially reduced spheres was also determined, the results being shown in Figure 4.11

Iron Oxide Sphere	Weight before reduction (g)	Weight after reduction (g)	Flow of H_2 (l/min)	Time (min)	%R	γ
B	26.1164	23.8199	0.450	60	30.0	–
C	26.0594	22.2327	0.935	60	50.1	–
E	26.8204	21.3264	1.870	60	68.83	0.5297
F	27.9153	21.6821	5.612	60	76.12	–
G	25.9741	20.1153	5.612	60	77.0	0.5400
H	25.5708	19.7650	9.350	60	76.5	0.5410
I	27.4995	21.5308	14.071	60	74.0	0.5413
J	28.6480	23.8402	5.612	30	57.3	0.4529
K	32.0064	23.0212	5.612	90	95.79	0.5921
L	25.6373	18.225	5.612	120	98.57	0.6009
M	28.2177	20.0033	5.612	150	99.24	0.5967
N	25.7218	18.2443	5.612	150	99.10	0.6024
O	26.2349	18.6018	5.612	150	99.20	0.6001
P	25.1491	17.8386	5.612	150	99.10	0.5983

Figure 4·9 : The reduction of hematite spheres containing 2% CaO and sintered at 1370°C, by hydrogen at 825°C for one hour.
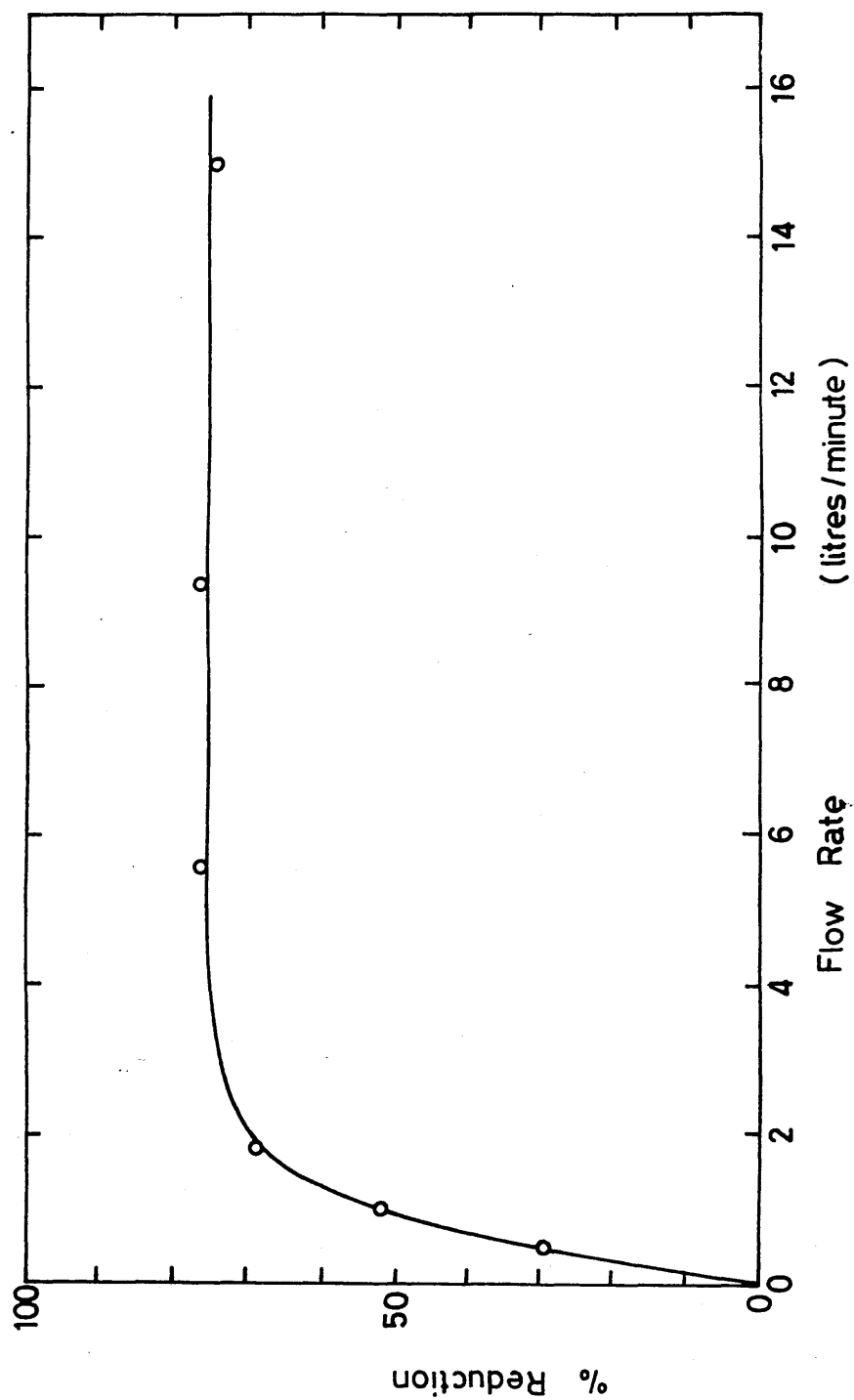
Figure 4·10 : The reduction of hematite spheres containing 2% CaO and sintered at 1370°C , in hydrogen at a flow rate of 5·612 l./min. at 825°C.

147
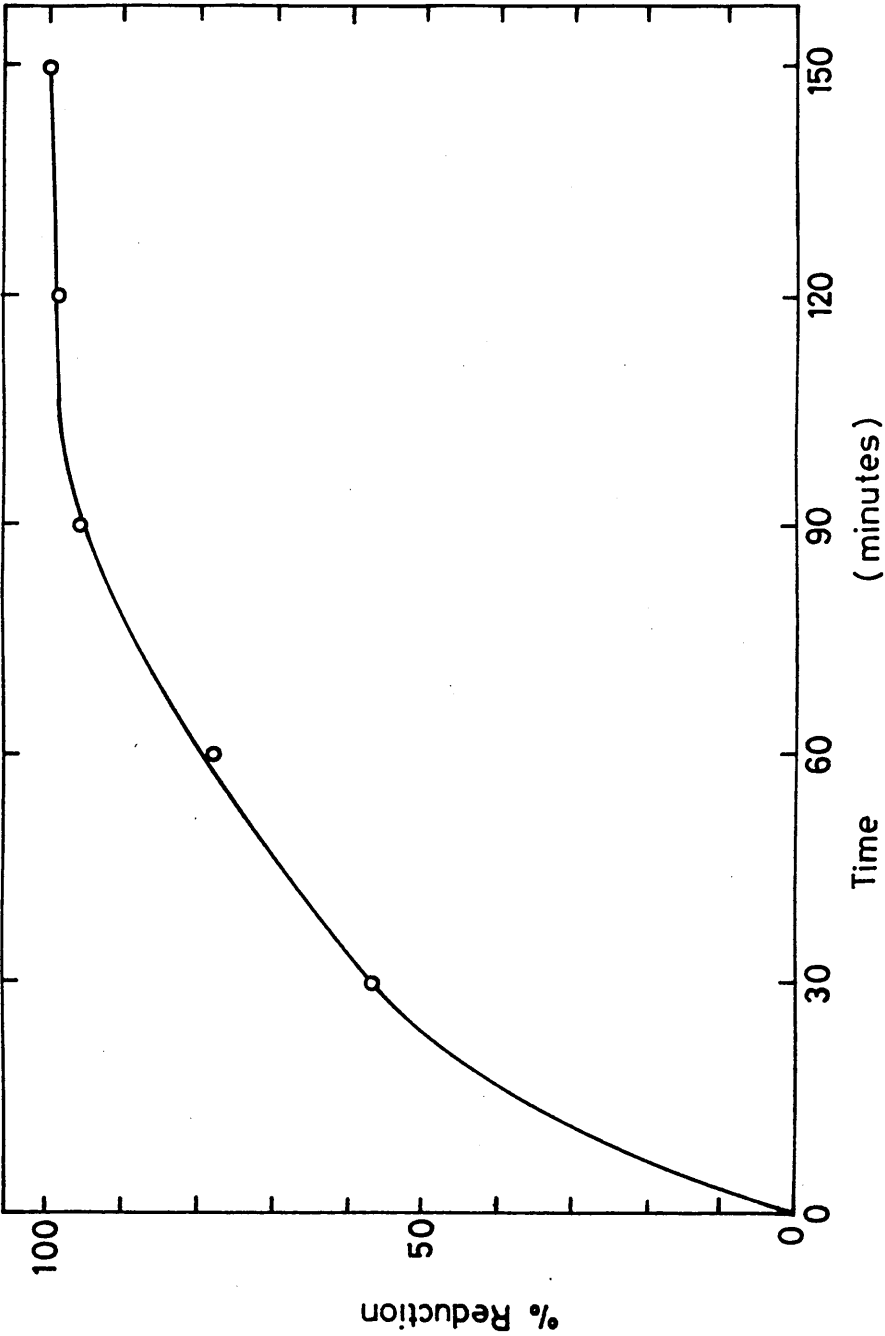
2% CaO, sintered at 1370°C and reduced in hydrogen at a flow rate of 5·612 l./min. at 825°C.

Porosity (%)

Degree of Reduction (%)

100

50

0

45

50

55

60

148
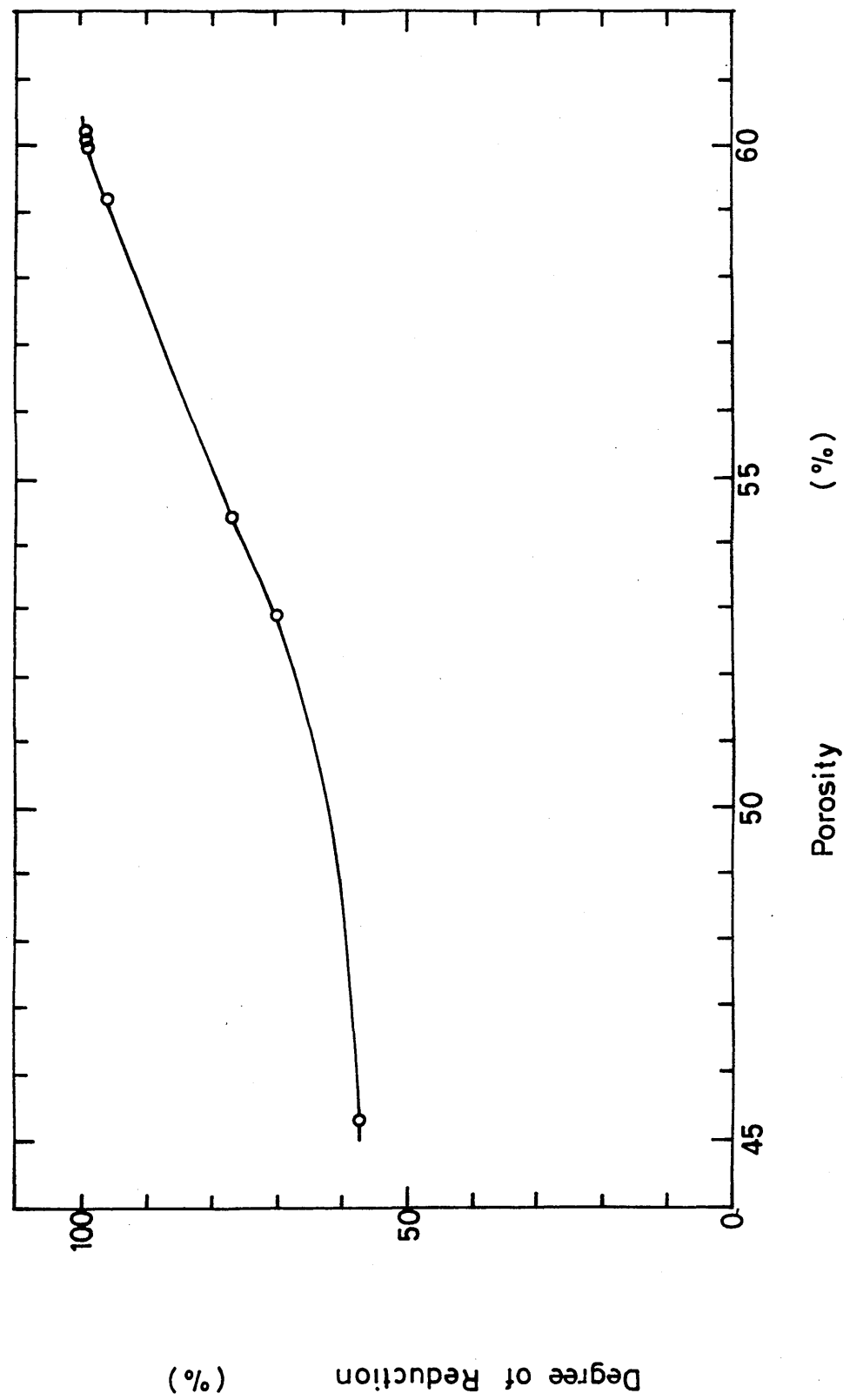
4.3.4 EXPERIMENTAL PROCEDURE FOR THE PERMEABILITY MEASUREMENTS USING REDUCED IRON SPHERES

The compaction, sintering and reduction techniques developed,as described in the previous sections,resulted in the production of hollow iron spheres suitable for the measurements of permeability.

The technique adopted was identical to that described in Section 4.2.6 for the hollow lime spheres using the horizontal tube furnace and the gas flow system shown in Figure 4.7. Only one modification to the apparatus was required. The alumina diffusion shaft used for the lime permeability measurements had to be replaced by a stainless steel shaft, since alumina readily reacts with iron oxide at elevated temperatures. The new diffusion shaft, shown in Figure 4.12, simply consisted of two concentric tubes of austenitic stainless steel, the external diameter of the outer tube being of 0.678 cm. The inner tube was connected to manometers 1 and 2 in Figure 4.7 in order to measure the pressure inside the sphere and the pressure drop across the wall of the sphere, while the annular space between the inner and outer tube was connected to the orifice flowmeter No.2 in Figure 4.7. The inner stainless steel tube was maintained in a central position inside the outer tube by means of a series of small welded protrusions on its outer surface.

For the purpose of permeability measurements the iron oxide spheres were actually reduced in H_2 at 825°C inside the horizontal tube furnace while supported on the end of the diffusion shaft, a hole of the same diameter as the outer tube of the diffusion shaft having been drilled in the

Figure 4·12 : The stainless steel tube diffusion shaft used for the permeability measurements on porous iron spheres , also showing detail of the end seals.

Porous iron sphere

Welded protrusions to centralise inner tube

Stainless steel tubes

To manometer

Machined brass end assembly

Rubber O-ring seals

To orifice flowmeter
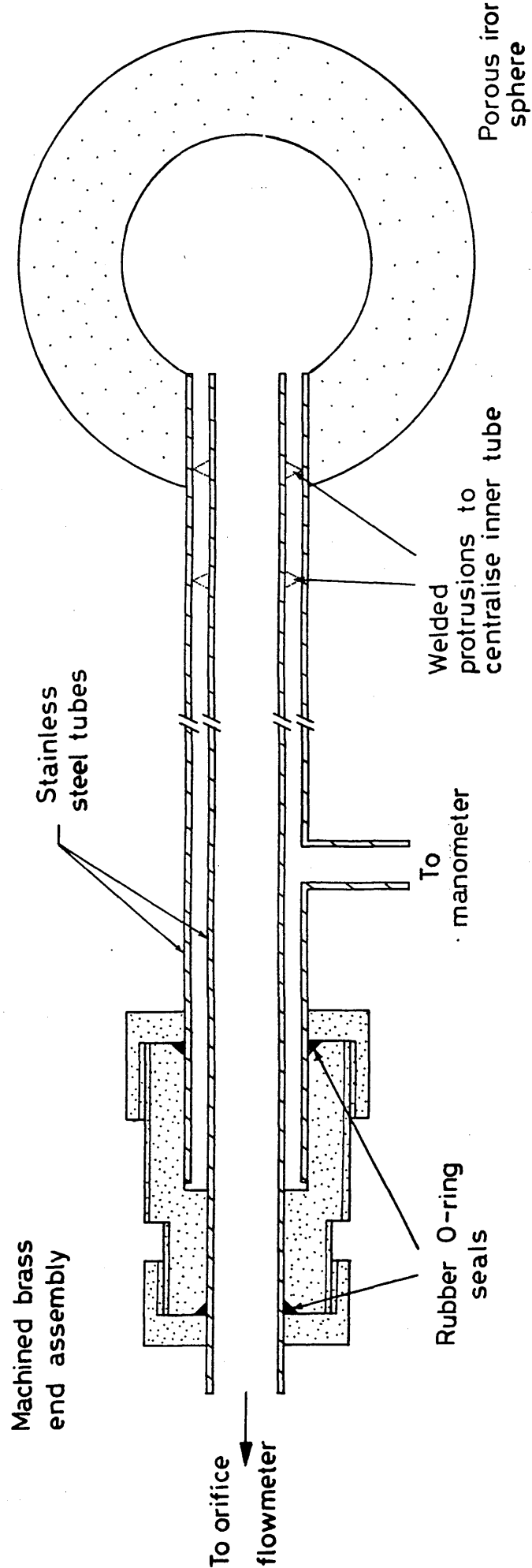
sintered iron ore spheres using a diamond drill.

During reduction, a small volumetric contraction takes place ensuring a gas tight seal between the sphere and the diffusion shaft. After the permeability measurements had been carried out the reduced iron sphere was so tightly fastened to the diffusion shaft that it could only be removed by cutting it with a hack saw. The thickness of the iron shell and the diameter of the sphere were measured using a micrometer and its porosity determined using the mercury balance as described in Section 4.3.5. Permeability measurements were carried out at 898 K and room temperature using helium and argon.

The flow rate of gas through the iron shell was somewhat larger than that through the lime sphere. A Gallenkamp orifice size 1 was therefore used. The orifice meter was calibrated for flow rate as a function of pressure drop, using a total gas volume meter and the results are presented in Tables 5.1 and Figure 5.4 in Section 5.2.2.

In addition to permeability measurements carried out on iron oxide spheres immediately after reduction, measurements were also made on a small number of spheres which had been sintered at 1100°C for 5 hours in hydrogen after the normal reduction procedure at 825°C, 1100°C being the maximum operating temperature of the horizontal tube furnace.

The results of the permeability experiments are presented in Section 5.3.3.

4.3.5 DETERMINATION OF THE POROSITY OF REDUCED IRON SPHERES

The mercury balance technique, as described in British Standard BS1302 Part 1A: 1966, was used to measure the porosity of the reduced and sintered iron spheres. The samples obtained from the iron spheres were larger than those obtained with lime and, since the mercury balance method is more suited for larger sample sizes, this technique was adopted.

The mercury balance technique operates on the principle of a hydrometer but, since mercury is denser than the aluminium of which the instrument is made, it is necessary to add weight at a position below the centre of buoyancy so that the instrument will float in a vertical position. This is achieved by placing the vessel containing the mercury on a bridge and providing a scale pan below the level of the support. The specimen holder is immersed in the mercury and weights are added, W_1, to the scale pan to sink the apparatus to the mark (see Figure 4.13). The specimen holder is raised above the surface of the mercury and the holder placed over an iron sample of a known weight. Additional weights, W_2, are added to overcome the increased upthrust and sink the instrument to the mark.

The apparent bulk volume is calculated as follows:

$$V_a = \frac{W + W_2}{\rho_{Hg}} \qquad (4.11)$$

where ρ_{Hg} = density of mercury

$\quad$ W $\quad$ = weight of the sample

$\quad$ W_2 $\quad$ = additional weight (the difference between the total weight on the scale pan and the weight W_1)

152

Figure 4·13
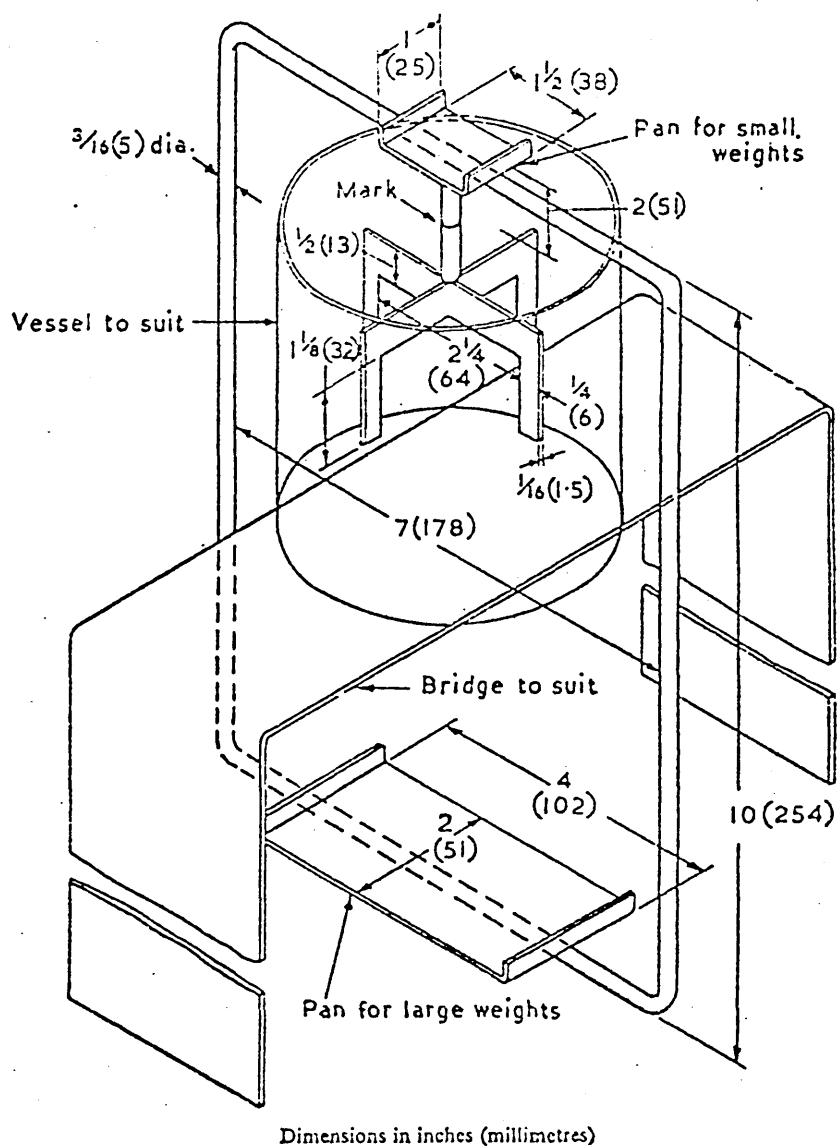
The mercury balance (B.S. 1302 Part 1A : 1966).

153

The apparent density, ρ_{ap}, is the ratio between the volume of the sample and the apparent volume and hence the porosity is defined by

$$\gamma = (1 - \frac{\rho_{ap}}{\rho_{true}}) \times 100 \qquad\qquad (4.12)$$

where ρ_{true} is the density of iron = 7.8 g/cm^3

4.4   COUNTER-CURRENT GASEOUS DIFFUSION THROUGH LIME AND POROUS IRON

The final part of the work involved the measurement of the counter current rates of gaseous diffusion of helium and argon through porous spherical shells of lime and iron. Helium was introduced into the cavity inside the hollow shell whilst a stream of argon was allowed to flow over the outer surface of the sphere which was sealed inside the furnace tube.

Counter diffusion of argon and helium occurred causing the stream of gas leaving the furnace tube to be diluted with helium and the stream of gas leaving the inner cavity of the sphere to be mixed with argon.

The experimental technique developed involved the careful measurement of the volumetric flow rates of pure gases entering and the gas mixtures leaving the system, the determination of the compositions of the exit gas streams and the control of the pressure distribution within the system.

4.4.1 DEVELOPMENT OF THE MODIFIED DIFFUSION SHAFT

The support shaft used in the iron sphere permeability measurements had to be modified in two ways in order for it to be used satisfactorily for the diffusion measurements. After these modifications it was designated as 'the diffusion shaft'. This diffusion shaft had to be capable of supplying pure gas to the cavity within the shell, of removing the resultant gas mixture and also of providing the means for controlling and monitoring the pressure inside the sphere. The ideal design required the use of a shaft comprising three concentric tubes. At the outset of this work, however, the size range of tubes commercially available only permitted the use of two concentric tubes and therefore a pressure monitoring probe had to to be introduced as an independent tube entering the shell cavity diametrically opposite the diffusion shaft itself, as shown in Figure 4.14.

The second modification involved redesigning the end of the diffusion shaft so that the gas stream entering the central cavity of the sphere via the annular passage between the inner and outer tubes,would mix the gas volume within the central cavity as completely as possible,whilst maintaining a uniform distribution of local mass transfer coefficient values over the inner surface of the cavity. These two requirements can be met if the gas leaves the diffusion shaft annulus at high velocity but with a profile that matches as nearly as possible the shape of the central cavity.

156

Figure 4.14: The diffusion shaft used for the diffusion measurements on porous iron spheres.

Porous iron sphere

Stainless steel tubes

Helium in

Argon/helium mixture out

To manometer

157
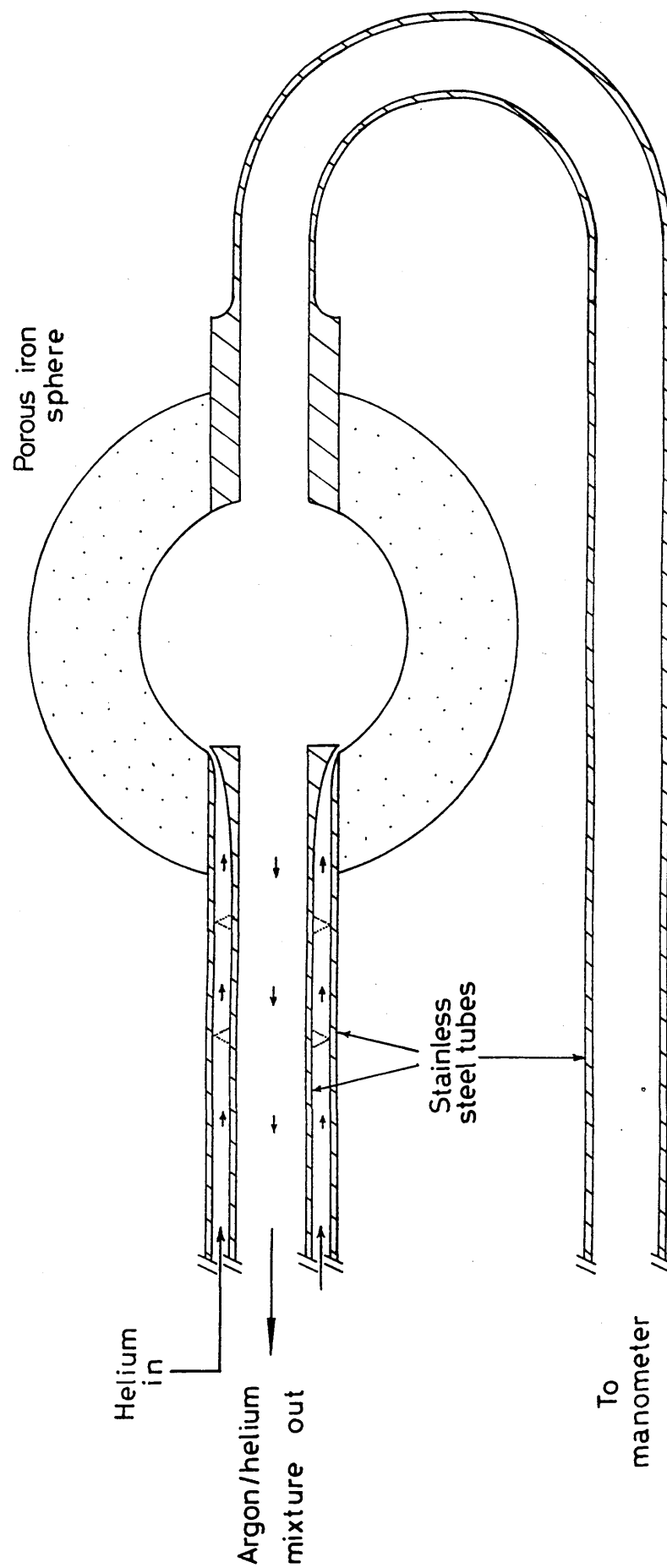
This is achieved by flaring the end of the inner tube as shown in Figure 4.14. In order to obtain the correct profile for this flaring and hence for the flow of gas into the inner cavity, water was passed through the diffusion shaft and the position of the inner tube adjusted until an optimum jet profile was achieved. Plate 4.6 shows the water jet produced in this way, illustrating both the profile of the flow and its high velocity. Once a satisfactory water jet was achieved, the inner tube was fixed in position, relative to the outer tube, by means of the locking nuts on the O ring seal assembly at the outer end of the diffusion shaft, as illustrated in Figure 4.12.

The diffusion shaft and pressure probe described above were used in the diffusion experiments for iron spheres. However, when this arrangement was used in conjunction with porous lime difficulties arose. The calcium carbonate hollow spheres were so fragile that any misalignment or vibration during the course of inserting the diffusion shaft and the pressure probe into the sphere and then introducing the assembly into the furnace tube resulted in the fracture of the sphere.

Fortunately a supply of stainless steel hypodermic needle tubing was discovered at about this time and this permitted a diffusion shaft of the original intended design, comprising three concentric tubes, to be constructed as shown in Figure 4.15. By using the innermost tube to control the internal pressure within the sphere, the independent pressure probe as used in conjunction with the iron spheres was discarded. The end of the intermediate tube was flared as

158

Plate 4.6: The profile of a water jet emerging from the annular exit of the stainless steel diffusion shaft.
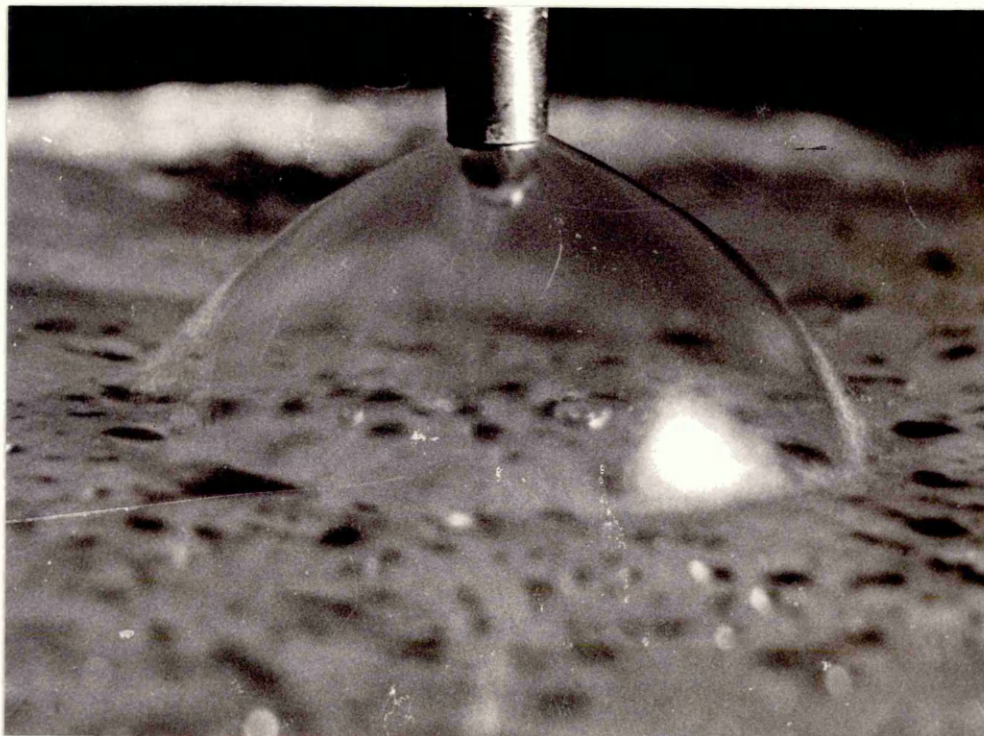
Figure 4·15 : The improved stainless steel tube diffusion shaft.

Helium
in

To manometer

Argon/helium
mixture out
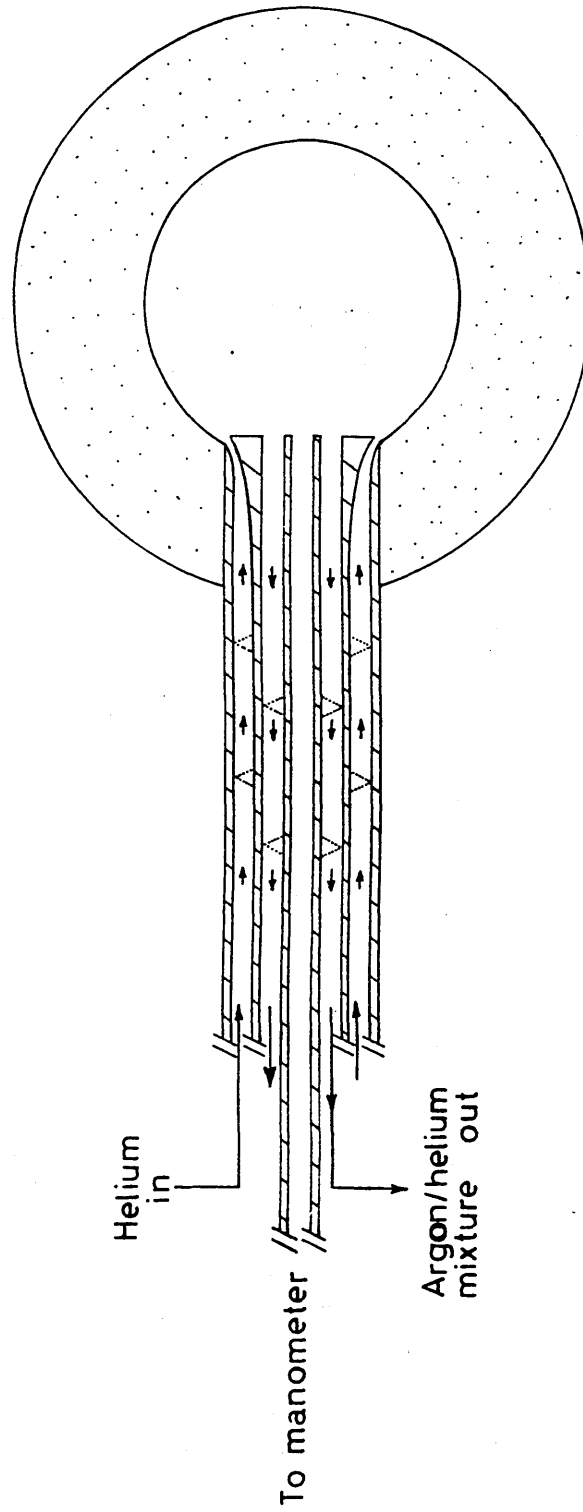
before so that, once again, the optimum gas flow conditions entering the inner cavity of the sphere could be obtained.

4.4.2 EXPERIMENTAL APPARATUS AND FLOW SYSTEM FOR THE DIFFUSION EXPERIMENTS

A schematic diagram of the apparatus used in the diffusion experiments on porous reduced iron spheres is shown in Figure 4.16. For lime spheres, the apparatus only differed due to the positioning of the internal pressure probe, as already described in the previous section. The furnace used for the permeability experiments was also used in this part of the work.

Referring to Figure 4.16, argon was introduced at a controlled rate into the furnace tube via orificemeter A, while orificemeter B was used to control the flow of helium entering the sphere via the outer annular passage of the diffusion shaft.

The flow rates of the gas mixtures leaving the furnace tube and leaving the spherical shell via the inner or intermediate passage of the diffusion shaft, were measured by means of orificemeters C and D respectively.

U tube manometers were again used to monitor the pressure inside the sphere, the pressure inside the tube and the pressure drop across the wall of the spherical shell. Due to the pressure drop along the exit passage of the diffusion shaft, a fourth manometer was used to monitor the pressure at which the gases entered orificemeter D.

In order to control the gas pressures within the system, the gas flows leaving orificemeters C and D were bubbled through two separate tubes inserted into two separate columns of mercury. The pressure inside the sphere and the pressure drop across it were controlled by varying the depth of

162
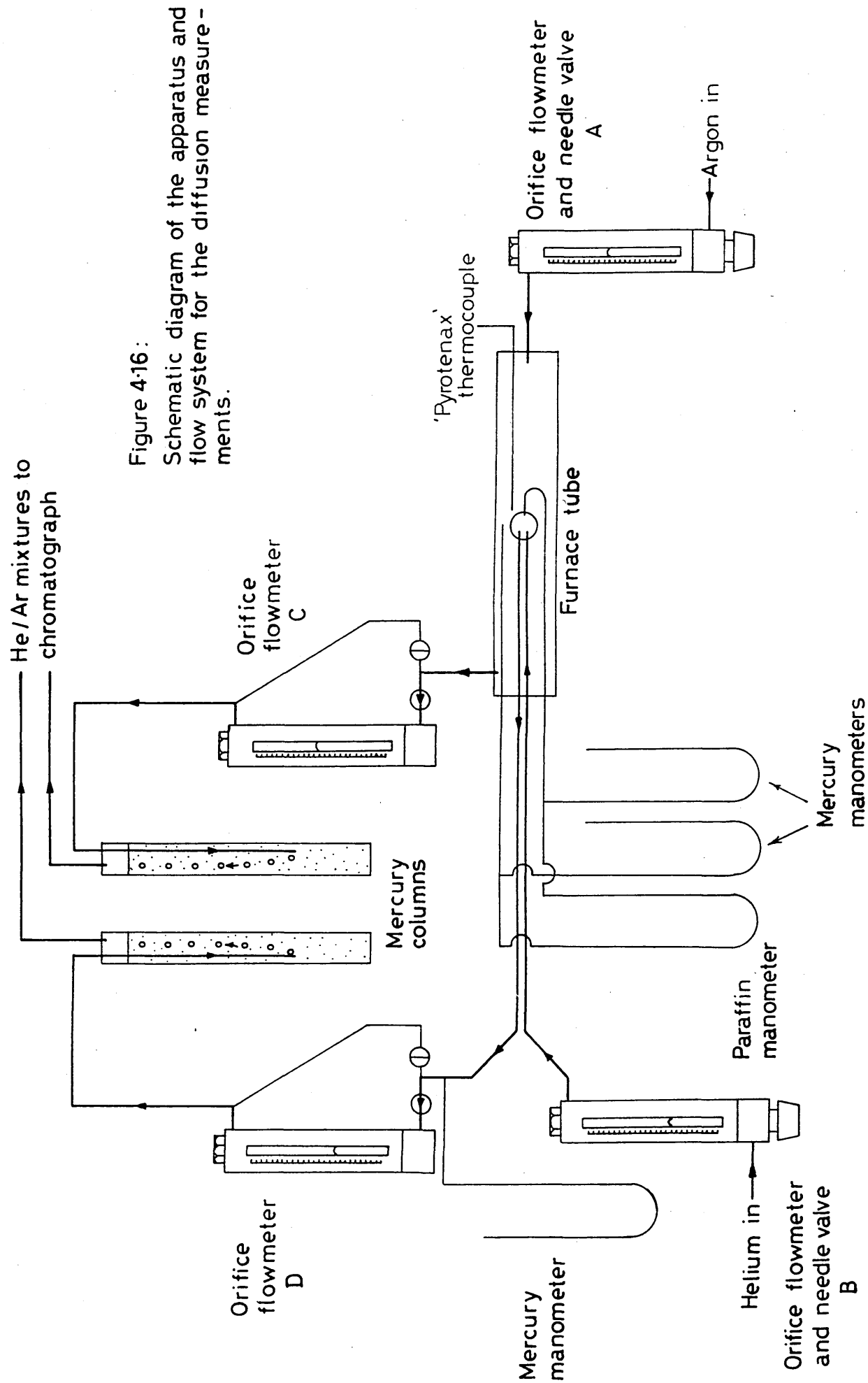
Figure 4·16: Schematic diagram of the apparatus and flow system for the diffusion measurements.

163

immersion of the two tubes. The gas streams leaving
the Hg columns were transported to a chromatograph for
analysis as described in the next section.

4.4.3 GAS ANALYSIS

The gas mixtures leaving the furnace and the diffusion shaft during the diffusion experiments, were analysed with the aid of a Sigma II Chromatograph manufactured by Perkin Elmer Ltd and fitted with an automatic sampling valve. This instrument is a versatile multicolumn temperature programmable instrument. Nitrogen was used as a carrier gas in the analysis of helium-argon mixtures.

The standard operating conditions for this chromatograph in the present work are summarised in Table 4.4. The apparatus was connected to a single pen recorder used with a chart speed of 1 cm/min and a sensitivity of 1 mV.

The chromatograph was calibrated with a Wosthoff gas mixing pump that produced argon-helium mixtures of a desired composition to an accuracy of ±0.1 %. Since the chromatograph is pressure sensitive, a by-pass system was used in order to ensure a constant inlet pressure for the gas mixture of approximately 2 cm H_2O.

Provided that good separation of the peaks and a steady base line were obtained, the results from the calibration were processed by measuring the peak height as that between the base line for the peak and peak apex.

The calibration curves for helium and argon in helium-argon mixtures from 0-100% are presented in the Results section. The instrument was calibrated frequently and the results compared with the initial calibration curve. No significant changes were observed over the period of time for which the diffusion experiments were performed.

165

TABLE 4.4 OPERATING CONDITIONS FOR SIGMA II GAS
         CHROMATOGRAPH

CARRIER GAS USED : NITROGEN

INLET PRESSURE CARRIER GAS : 517 kN/m^2

FILAMENT CURRENT : 65 mA

MAXIMUM OPERATING TEMPERATURE : 100°C

OVEN TEMPERATURE : 50°C

CARRIER GAS FLOW RATE THROUGH
COLUMNS : 35 cm^3/min

COLUMNS : PORAPAK Q (50/80 mesh)
          (1.5 m length)

: MOLECULAR SIEVE type
  13x (60/85 mesh)
  (1.15 m length)

ATTENUATION : helium * 16

: argon * 8

TIME   PEAK$_{He}$: 1.8 min

TIME   PEAK$_{Ar}$: 2.6 min

POLARITY :NORMAL FOR HELIUM

:REVERSE FOR ARGON

The gas supply system for analysis of the exit gases

during the diffusion measurements was the same as that used

for calibration. Care was taken to ensure that steady state

conditions were achieved before each final measurement was

made for each particular set of experimental conditions. A

gas analysis was only accepted as valid when three pairs

of peaks of the same height had been observed. The time

taken for the steady state to be achieved and the final

gas analysis obtained was usually about one hour.

4.4.4 EXPERIMENTAL PROCEDURE

After assembling the apparatus, before diffusion measurements could be carried out, the iron oxide spheres had to be reduced or the $CaCO_3$ sintered and calcined. These operations were performed as described in Section 4.3.3.2 and 4.2.3 respectively.

Argon was introduced into the furnace tube and helium into the cavity of the sphere at flow rates which had been previously determined by trial and error to give gas mixtures which could easily be analysed by the chromatograph.

For diffusion measurements under isobaric conditions,the depths to which the tubes in the exit gas stream were immersed into the Hg columns was adjusted in order to achieve zero pressure drop across the wall of the shell whilst maintaining the total pressure within the system at a fixed arbitrary value. Having achieved this condition, flow was allowed to stabilise and accurate measurements were made of the flow rate through orificemeters A, B, C and D. The compositions of the gases leaving the furnace tube and leaving the diffusion shaft were determined using the chromatograph. Measurements were made for various total pressures and various input flow rates of argon and helium. For measurements under non isobaric conditions,the depth of immersion of the tubes inside the mercury columns was adjusted in order to produce different values for the pressure drop, Δp, across the spherical shell whilst maintaining the total pressure in the system constant.

Experiments were conducted with iron spheres at room temperature and 625°C and for CaO spheres at room

temperature and 950°C. After completing the experimental measurements, each sphere was removed from the furnace, and its diameter measured using a standard micrometer, the mean of several readings being taken. The sphere was then cut from the diffusion shaft, the mean shell thickness measured using a point micrometer and its porosity determined as described in Section 4.3.5.

As in the case of the porosity measurements, the contraction experienced during the reduction of the iron oxide spheres was sufficient to seal them effectively to the end of the diffusion shaft. Unfortunately an effective seal could not be achieved in the case of lime, this being attributed to the large difference between the coefficients of thermal expansion of lime and of stainless steel since an effective seal had been obtained for the permeability experiments on lime in which an alumina shaft had been used. Room temperature measurements for lime could, however, be made using the stainless steel shaft by cementing the calcined sphere on to the end of the shaft using araldite.

4.4.5 INTERNAL MASS TRANSFER COEFFICIENT MEASUREMENTS

Mass transfer coefficientsto the surface of the inner cavity of the diffusion sphere during the diffusion experiments at high or room temperature had to be determined and this was done using a dimensionless correlation based on experiments on a room temperature analogue.

This technique, used for the first time by Winding and Cheyney[103] has been extensively used by Warner[12], Campbell[50] and more recently by Sadrehashemi[69].

The analogue system studied in the present work was the vaporisation of cast naphthalene spheres of the same size as the spheres used in the diffusion experiments.

In order to prevent evaporation of naphthalene from the outer surface of the spheres, it was necessary to cover them with an impermeable medium: Campbell[50], in his experiments painted the naphthalene spheres with an epoxy resin. He expressed doubts, however, about the effectiveness of this method and attributed certain spurious results to the incomplete coating of the surface.

In this work it was decided to enclose the naphthalene spheres in a thick shell of epoxy resin. The shell was made in two halves,using the die previously used to produce the Gelflex mould as described in Section 4.2.1.1,and is shown in Figure 4.17. The two halves of the shell were held in place by two bolts. Adhesive tape was wound around the joint during the experiment to eliminate the possibility of any naphthalene evaporation from the joint. A hole was drilled centrally through one half of the epoxy shell into the inner cavity, this hole having the same diameter as the diffusion

Figure 4·17 : The naphthalene shell used in the determination of the internal convective mass transfer coefficient.

Hollow naphthalene sphere

Adhesive plastic tape to seal the joint between the two halves of the outer shell.

Plasticene seal

Air in

Air + naphthalene vapour out

Stainless steel diffusion shaft

Epoxy resin outer shell

Pictorial View
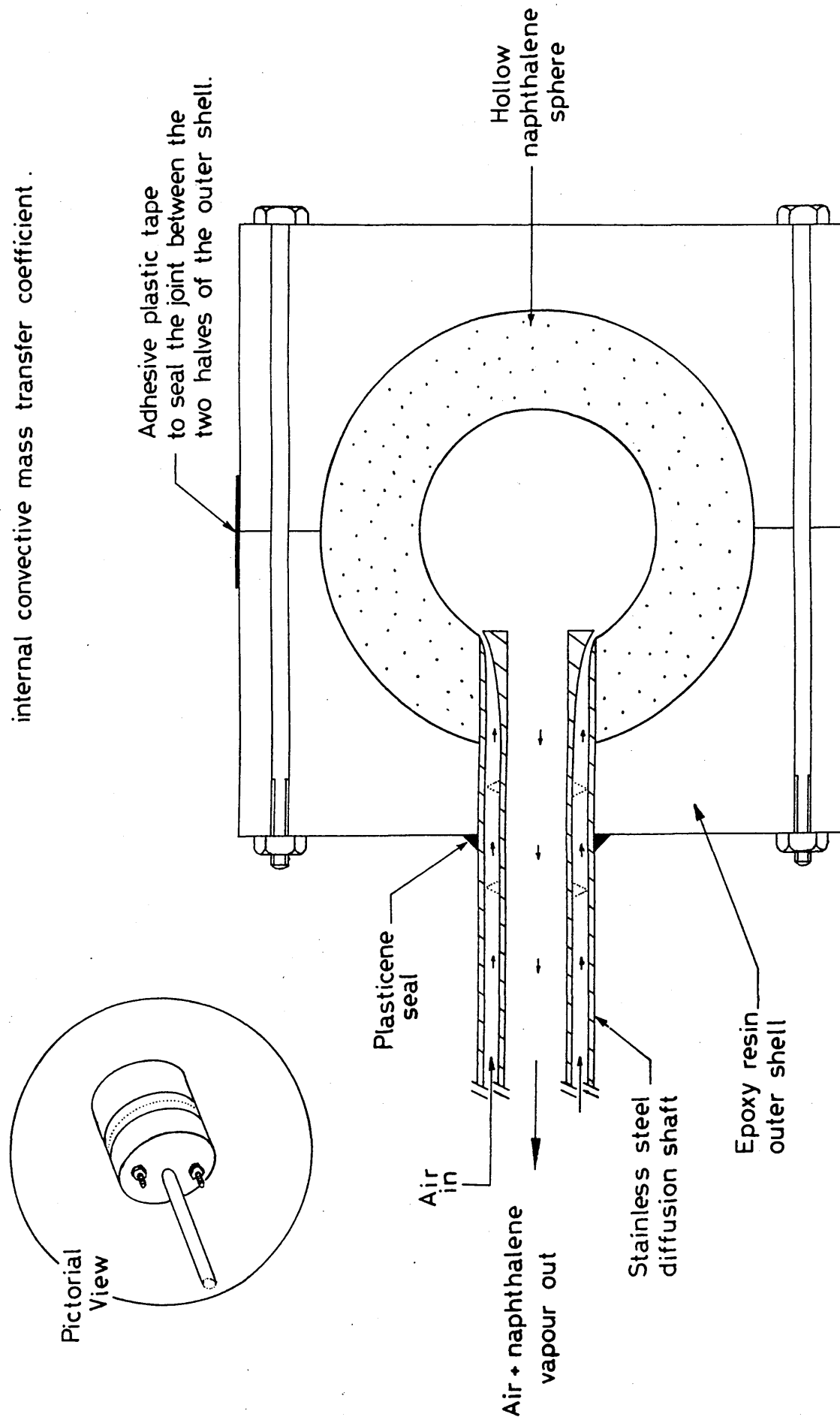
shaft.

Hollow naphthalene spheres were cast inside the epoxy resin shells using the following procedure: tin (II) chloride spheres were produced using the mould previously employed to produce the Wood's metal sphere (see Figure 4.2), tin (II) chloride being melted at 220°C and cast into the mould. These spheres were attached to a length of wire using Araldite so that they could be held rigidly in the centre of the cavity formed when the epoxy resin shells were bolted together, the wire entering the cavity along the hole drilled for the diffusion shaft. Molten naphthalene was then poured around the tin (II) chloride spheres and solidified in situ. The melting point of the naphthalene is 82.5°C and a casting temperature of 90°C was used. This was regarded as the minimum degree of superheat which would permit the liquid naphthalene to completely fill the annular space inside the shell and still ensure the optimum grain size for the mass transfer determination.

A total of ten epoxy resin shells were prepared, the naphthalene being cast from the same batch,with the same degree of superheat,in order to achieve as nearly as possible identical solidification and grain size conditions for all the samples. After allowing sufficient time for the naphthalene to cool to room temperature, the piece of wire was pulled out. The hole in the shell, having become blocked by the naphthalene was reopened by drilling down to the surface of the tin (II) chloride sphere. The tin (II) chloride was removed by dissolving it in warm water. The surplus of water was shaken out of the hole and the inner surface dried carefully using cotton wool.

172

The entire shell was then placed on the diffusion shaft
and positioned so that the end of the shaft coincided with
the inner surface of the cavity,as shown in Figure 4.17.
The thickness of the shell wall tended to vary slightly
and hence great care was taken in the positioning of the
diffusion shaft. The thickness of the shell was measured
using a steel rod by inserting it into the hole drilled for
the diffusion shaft. The required depth of the insertion
of the diffusion shaft could therefore easily be obtained
from a mark made on the probe rod. Although a good fit
existed between the hole through the shell and the diffusion
shaft, as an added precaution, the joint between the two
was sealed using plasticine. Air was blown through the
inner annulus of the diffusion shaft and the flow rate was
recorded using a rotameter. The temperature of the air,
both entering and leaving the diffusion shaft was recorded,
although no difference between the two was observed.

Air was allowed to flow for a period of time varying from
1 to 3 hours. The entire shell and its contents were weighed
before and after each experiment and from the total mass
of the naphthalene which was evaporated and the vapour pressure
of the naphthalene for the mean air temperature recorded,
the mean convective mass transfer coefficient was calculated
from these measurements, as will be described later in
Section 5.4.2b.

5.1   INTRODUCTION

The experimental results will be presented in three sections. Since the method of measurement of the volumetric flow rates was common to all the experiments, the calibration data for the orifice flow meters and the accuracy of this data will be considered first.

The results of the permeability measurements will then be presented followed by the results of the diffusion measurements.

5.2   CALIBRATION OF ORIFICE FLOWMETERS

5.2.1   METHOD OF CALIBRATION

By applying Bernoulli's equation to flow through an orifice and assuming that the gas velocity through the orifice is very much greater than the upstream gas velocity it can be shown that:-

$$u_o = C_D \cdot \sqrt{\frac{2 . \Delta p}{\rho}} \qquad (5.2.1)$$

where, u_o = gas velocity through the orifice

C_D = discharge coefficient for the orifice

Δp = pressure difference across the orifice

and ρ = the density of the gas

For an ideal gas,

$$u_o = \frac{\dot{V}}{A_o} = \frac{\dot{n} RT}{P A_o} \qquad (5.2.2)$$

and,

$$\rho = \frac{M \dot{n}}{\dot{V}} = \frac{MP}{RT} \qquad (5.2.3)$$

where, $\dot{V}$ and $\dot{n}$ are the volumetric and molar flow rates

through the orifice.

A_O is the cross sectional area of the orifice

M is the molecular mass of the gas

R is the Universal Gas Constant

P and T are the pressure and temperature in

the system, respectively

Substituting equation (5.2.2) and (5.2.3) in equation

(5.2.1) and rearranging yields:

$$\dot{n} = A_O C_D \sqrt{\frac{2}{R}} \sqrt{\frac{\Delta p\ P}{MT}} \qquad (5.2.4)$$

and,

$$\dot{n} = A_O C_D \sqrt{\frac{2\rho_{dnb}}{R}} \sqrt{\frac{\Delta h\ P}{MT}} \qquad (5.2.5)$$

where Δh is the manometer head of di-n-butyl phthalate

with density ρ_{dnb}.

By plotting the molar flow rate of gas in the calibration

experiment against $\sqrt{\dfrac{\Delta hP}{MT}}$ a straight line relationship

should be obtained.

Rearranging equation (5.2.5) gives:

$$\dot{n} \sqrt{M} = A C_D \sqrt{\frac{2}{R}} \sqrt{\frac{\Delta hP}{T}} \qquad (5.2.6)$$

and hence a plot of $\dot{n}\sqrt{M}$ vs $\sqrt{\dfrac{\Delta hP}{T}}$ should yield a straight line relationship which is valid for all gases for a particular orifice.

5.2.2   CALIBRATION RESULTS FOR THE ORIFICE FLOWMETERS

Throughout this work the volumetric flow rates of the gases used were measured by means of Galenkamp orifice meters using di-n-butyl phthalate as the manometric fluid. In the case of standard orifices size 2 and size 3 calibration data was supplied by Gallenkamp for air at one atmosphere pressure and 15°C.

For standard orifice size 1 no calibration data was supplied and hence a calibration curve was obtained for each gas used with the aid of an Alexander-Wright total volume meter. The calibration data for this orifice is presented in Table 5.1 and Figures 5.1, 5.2 and 5.3 and as a plot of $\dot{n}\sqrt{M}$ versus $\sqrt{\dfrac{\Delta hP}{T}}$ in Figure 5.4 which permits the orifice to be used in conjunction with any gas of known molecular mass M.

In the experiments to determine the counter diffusion fluxes of two gases, the flowmeters were used to measure the flow rate of binary gas mixtures. The molecular mass in these cases was taken as the mean molecular mass of the gas mixture which was obtained from its composition as indicated by chromatographic data.

For flow measurements in conjuction with the permeability measurements in porous lime, orifice size 1 proved to be too

Table 5.1   Calibration data for orifice number 1

Δh	$\dot{V}_{Ar}$ (cm³/s)	$\dot{V}_{He}$ (cm³/s)	$\dot{V}_{N_2}$ (cm³/s)	$\dot{n}_{Ar}$ (mol/s)	$\dot{n}_{He}$ (mol/s)	$\dot{n}_{N_2}$ (mol/s)	$\dot{n}_{Ar}\sqrt{M_{Ar}}$	$\dot{n}_{He}\sqrt{M_{He}}$	$\dot{n}_{N_2}\sqrt{M_{N_2}}$	$10^2 \times \sqrt{\dfrac{\Delta h P}{T}}$
1.4	1.03	3.25	1.23	43.64	137.92	52.09	275.81	275.84	275.64	6.930
2.2	1.46	4.61	1.74	61.88	195.56	73.90	391.08	391.12	391.04	8.751
3.0	1.68	5.31	2.00	71.25	225.15	85.06	450.31	450.30	450.09	10.219
4.0	2.00	6.33	2.39	85.02	268.64	101.52	537.33	537.28	537.19	11.800
5.1	2.35	7.41	2.80	99.50	314.46	118.83	628.85	628.92	628.79	13.320
6.2	2.67	8.43	3.18	113.10	357.43	135.08	714.80	714.86	714.78	14.690
7.6	2.92	9.24	3.49	124.01	391.84	148.10	783.75	783.68	783.67	16.260

P = 1.013 (atm)
T = 18°C

177

Figure 5·1 : Calibration curve for orifice number 1 using argon.
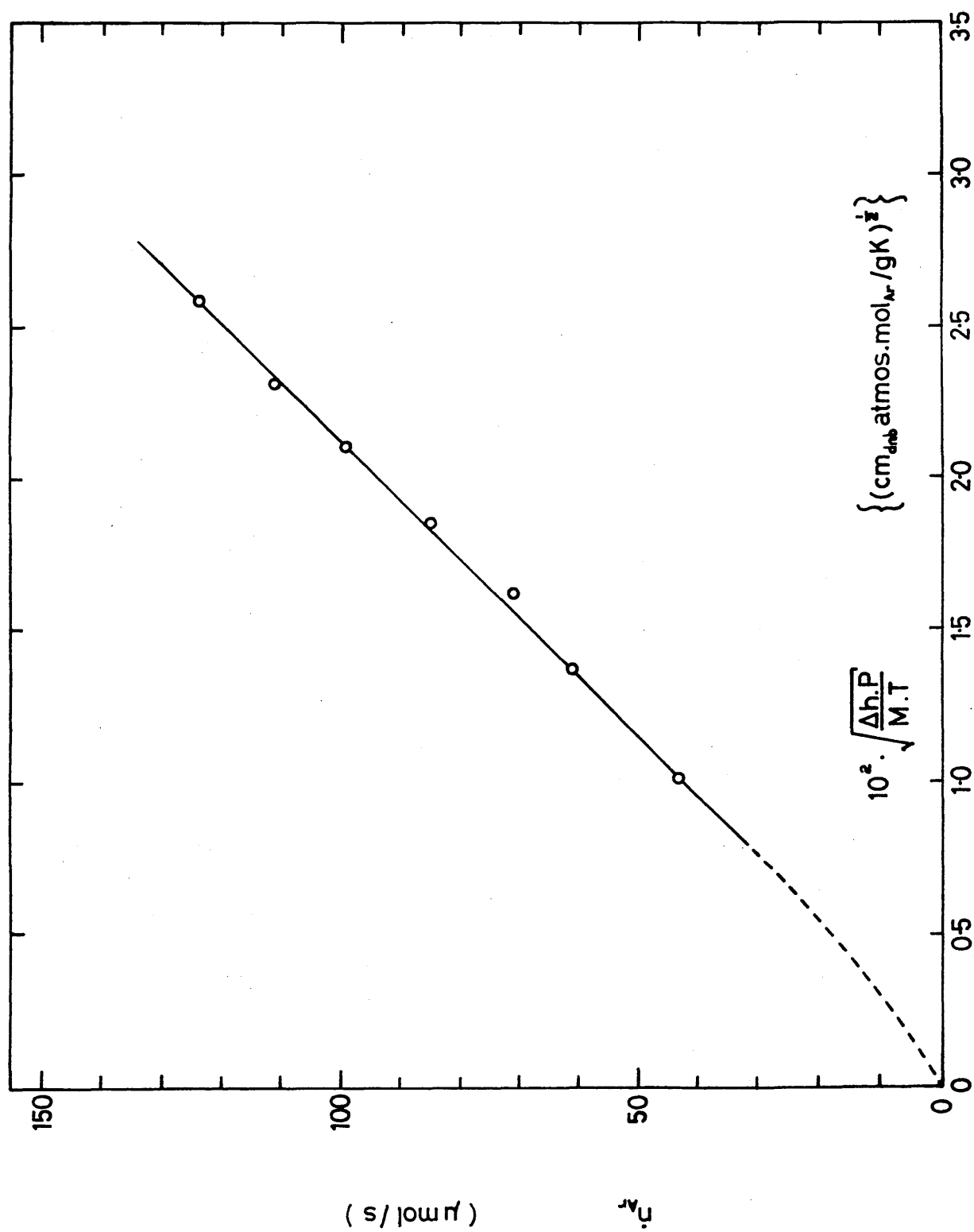
Figure 5·2 : Calibration curve for orifice number 1 using helium.

$$10^2 \cdot \sqrt{\frac{\Delta h . P}{M . T}} \quad \left\{ \left(cm_{dnb} . atmos . mol_{He} / g K \right)^{\frac{1}{2}} \right\}$$

$\dot{n}_{He}$ (μ mol / s)

179
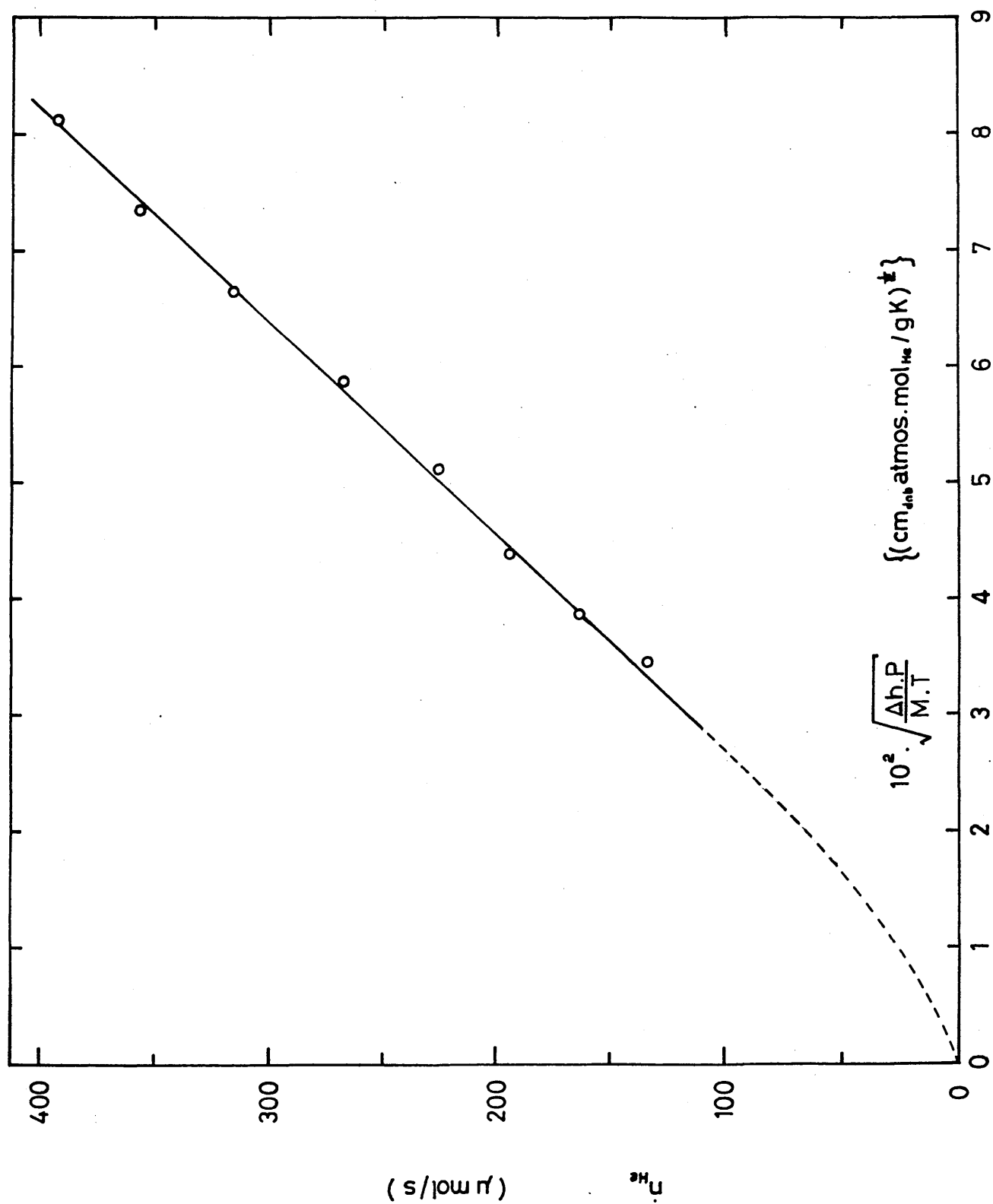
Figure 5·3 : Calibration curve for orifice number 1 using nitrogen.

$$10^2 . \sqrt{\frac{\Delta h . P}{M.T}} \quad \left\{ (cm_{dnb} . atmos . mol_{N_2} / gK)^{\frac{1}{2}} \right\}$$

$\dot{n}_{N_2}$ ($\mu mol/s$)
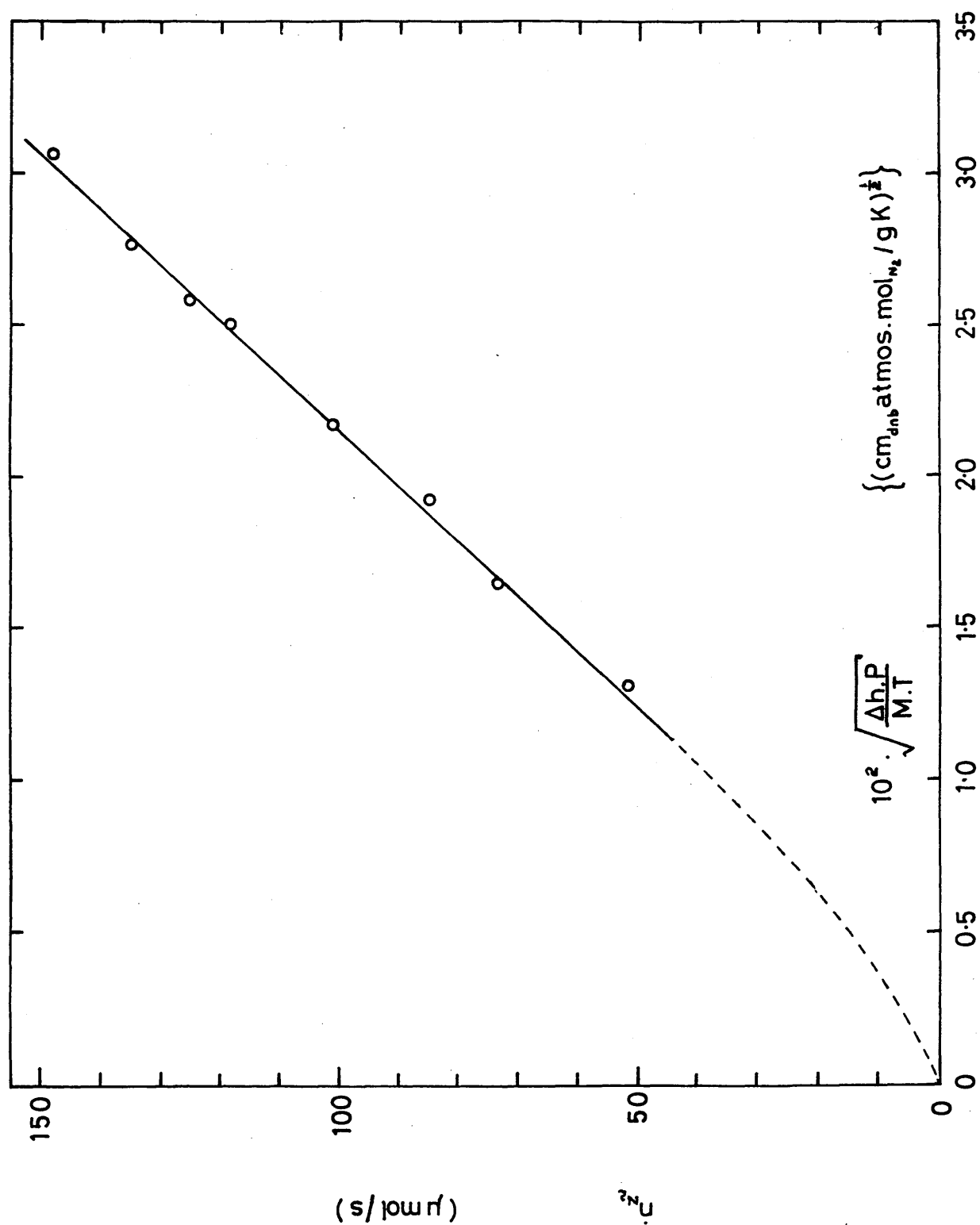
Figure 5·4 : Calibration curve for orifice number 1.

$$10^2 \sqrt{\frac{\Delta h.P}{T}} \qquad \left\{ (cm_{dnb}.atmos./K)^{\frac{1}{2}} \right\}$$

y-axis: $\dot{n}.\sqrt{M} \qquad \left\{ \mu(mol.g)^{\frac{1}{2}}/s \right\}$
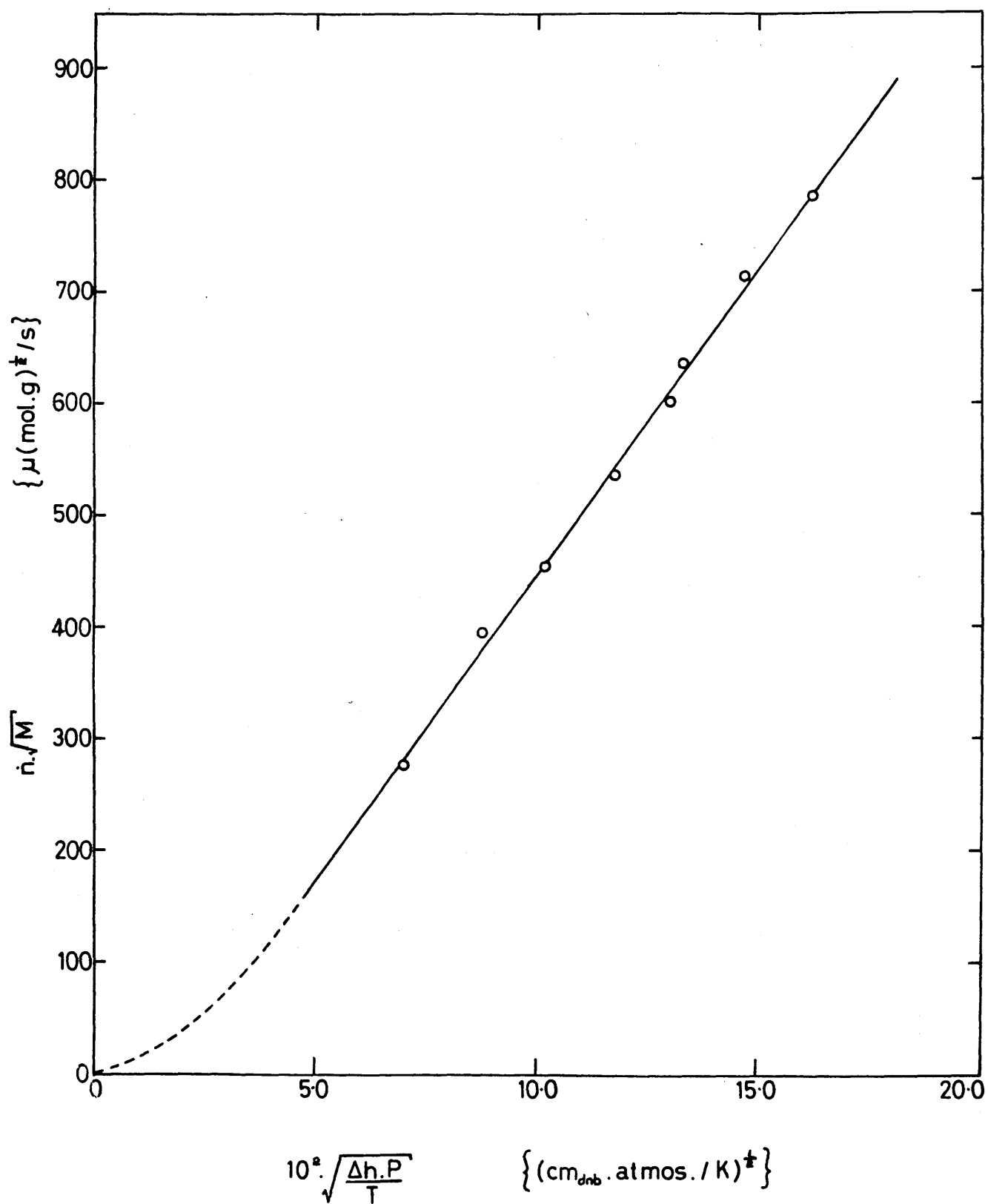
large and therefore the 0.1 mm diameter foil orifice meter described in Section 4.2.5 was used. This was calibrated for argon and helium using a bubble flowmeter. The calibration data is presented in Table 5.2 and 5.3 and as plots of $\dot{n}$ versus $\sqrt{\dfrac{\Delta hP}{MT}}$ in Figures 5.5 and 5.6. When the data for argon and helium were presented in the form of a plot of $n\sqrt{M}$ versus $\sqrt{\dfrac{\Delta hP}{T}}$ as shown in Figure 5.7 it can be seen that the results for the two gases do not lie on a common line as was the case for the calibration data for orifice sizes 1, 2 and 3.

In deriving equation (5.2.4) it was assumed that the contribution to the observed pressure drop due to frictional interactions between the flowing gas and the inner surface of the orifice would be negligible. With decreasing orifice diameter it is to be expected that wall frictional effects should increase. In the case of the foil orificemeter, it would appear that the attempt to minimise this effect by using thin aluminium foil in order to produce as short a flow channel as possible has not been entirely successful and it is this that explains the slight discrepancy, approximately 6%, between the argon and helium calibration data shown in Figure 5.7.

Figure 5·5 : Calibration curve for the 0·1 mm diameter, foil orifice using argon.

$\dot{n}_{Ar}$ (μmol / s)

$10^2 \cdot \sqrt{\dfrac{\Delta h \cdot P}{M \cdot T}}$

$\left\{ \left(\dfrac{cm_{dnb} \cdot atmos \cdot mol_{Ar}}{g \cdot K} \right)^{\frac{1}{2}} \right\}$

183
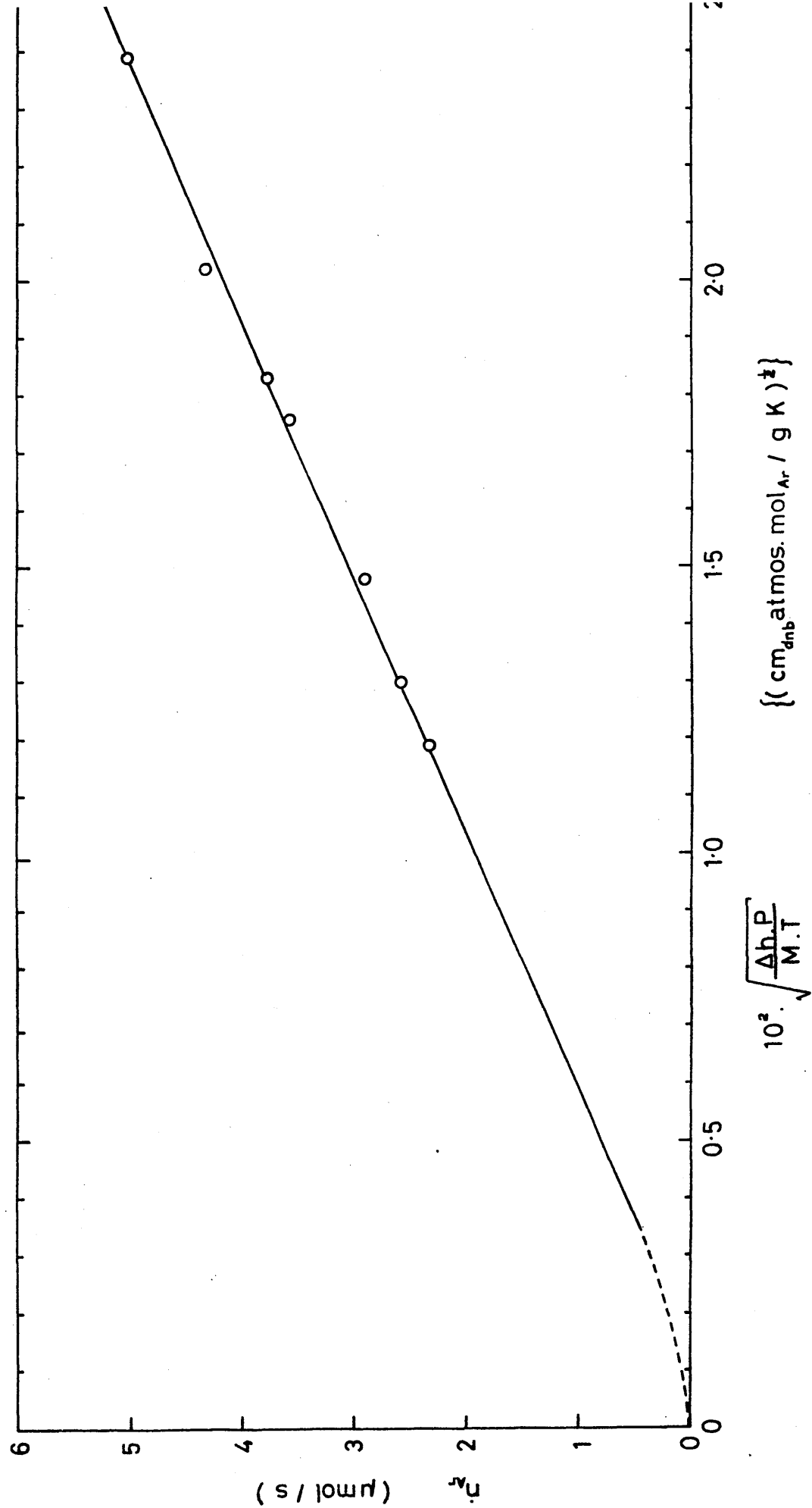
Table 5.2   The calibration of the foil orifice meter using argon at T = 296 K and P = 0.993 atm.

Δh (cm di-n-bt)	$\dot{V}$ (ml/s)	$\dot{n}$ (mol/s)	$\frac{\Delta h\ P}{MT}$	$\sqrt{\frac{\Delta h\ P}{MT}}$
1.7	0.0560	2.3143	$1.4278\ 10^{-4}$	$1.1949\ 10^{-2}$
2.0	0.0630	2.5768	$1.6798\ 10^{-4}$	$1.2961\ 10^{-2}$
2.6	0.0707	2.8929	$2.1837\ 10^{-4}$	$1.4777\ 10^{-2}$
3.7	0.0898	3.6724	$3.1076\ 10^{-4}$	$1.7628\ 10^{-2}$
4.0	0.0932	3.8093	$3.3596\ 10^{-4}$	$1.8329\ 10^{-2}$
5.2	0.1071	4.3788	$4.3674\ 10^{-4}$	$2.0898\ 10^{-2}$
6.8	0.1229	5.0270	$5.7110\ 10^{-4}$	$2.3898\ 10^{-2}$

M = 39.944 (g/mol)

$$\dot{n} = \frac{\dot{V}}{22.4\ 10^3\ (ml/mol)} \cdot \frac{0.993\ (atm)}{1\ (atm)} \cdot \frac{273\ (K)}{296\ (K)} = 40.886\ 10^{-6}\ \dot{V}$$

$$\frac{\Delta h P}{MT} = \Delta h\ \frac{0.993}{39.944 \cdot 296} = 8.399 \cdot 10^{-5}\ \Delta h\ \left\{ \frac{cm\ d-n-bt\ \cdot\ atm\ \cdot\ mol}{g\ \cdot\ K} \right\}$$

Figure 5·6 : Calibration curve for the 0·1mm diameter, foil orifice using helium.
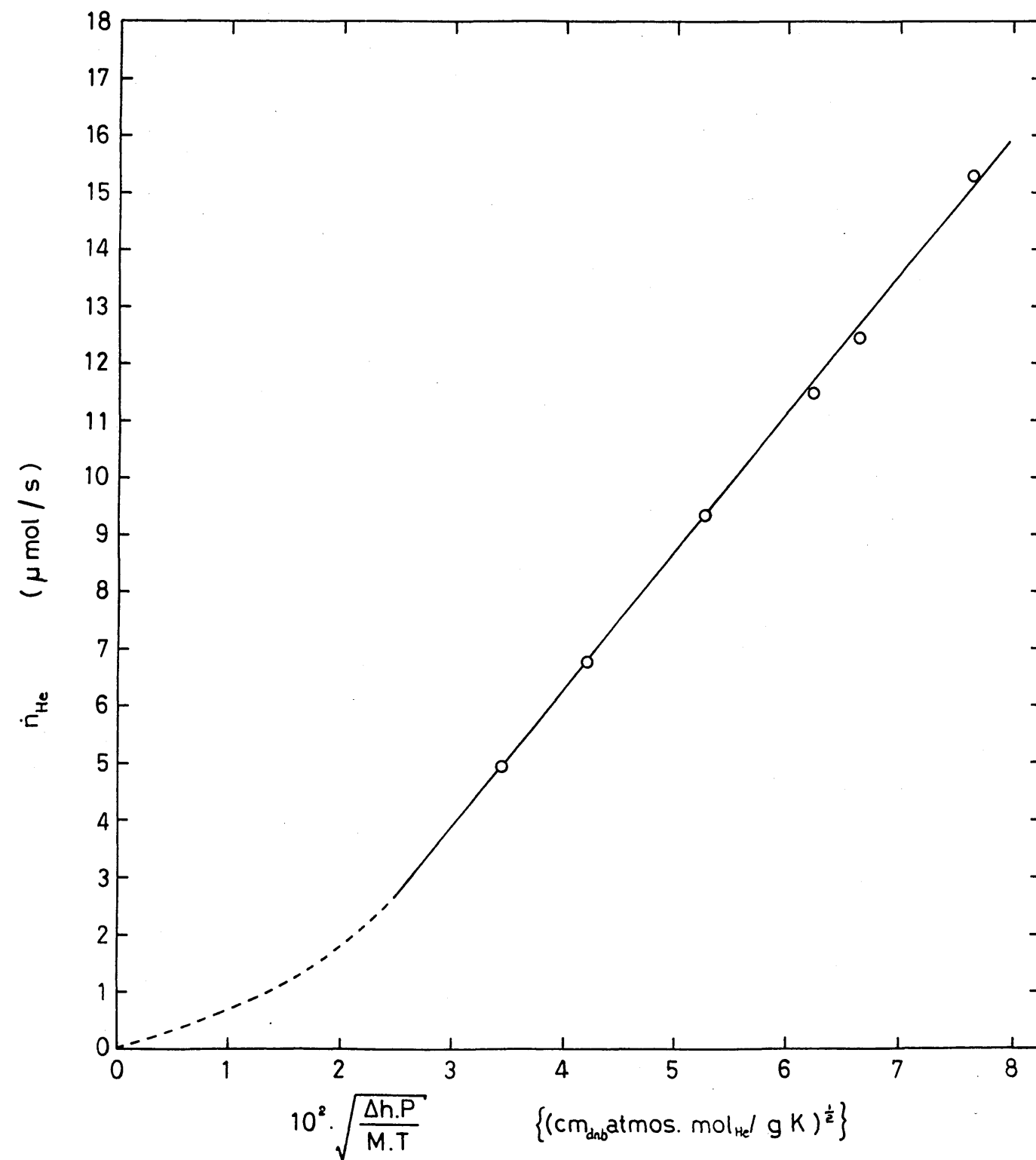
Table 5.3   The calibration of the foil orifice meter using
             helium at T = 297 K and P = 0.99 atm.

Δh (cm di-n-bt)	$\dot{V}$ (ml/s)	$\dot{n}$ (mol/s)	$\dfrac{\Delta h\ P}{MT}$	$\sqrt{\dfrac{\Delta h\ P}{MT}}$
1.4	0.1212	4.9516	$11.662\ 10^{-4}$	$3.4150\ 10^{-2}$
2.1	0.1666	6.7673	$17.493\ 10^{-4}$	$4.1825\ 10^{-2}$
3.3	0.2307	9.3710	$27.489\ 10^{-4}$	$5.2430\ 10^{-2}$
4.7	0.2830	11.4955	$39.151\ 10^{-4}$	$6.2571\ 10^{-2}$
5.3	0.3061	12.4338	$44.149\ 10^{-4}$	$6.6445\ 10^{-2}$
7.0	0.3658	14.8587	$58.310\ 10^{-4}$	$7.6361\ 10^{-2}$

M = 4.0 (g/mol)

$$\dot{n} = \frac{\dot{V}\ (ml/s)}{22.4\ 10^3\ (ml/mol)} \cdot \frac{0.99\ (atm)}{1\ (atm)} \cdot \frac{273\ (K)}{297\ (K)} = \dot{V} *40.62\ 10^{-6}(mol/s)$$

$$\frac{\Delta hP}{MT} = \frac{\Delta h\ (cm\ d\text{-}n\text{-}\ bt) \cdot 0.99\ (atm)}{4\ (g/mol) \qquad \cdot\ 297\ (K)} = 8.33 \cdot 10^{-4}\ \Delta h \left\{ \frac{cm\ d\text{-}n\text{-}bt\ \cdot\ atm\ \cdot mol}{g\ \cdot\ K} \right\}$$

186

Figure 5·7 : A comparison of the calibration curves for the 0·1mm diameter, foil orifice using argon and helium.
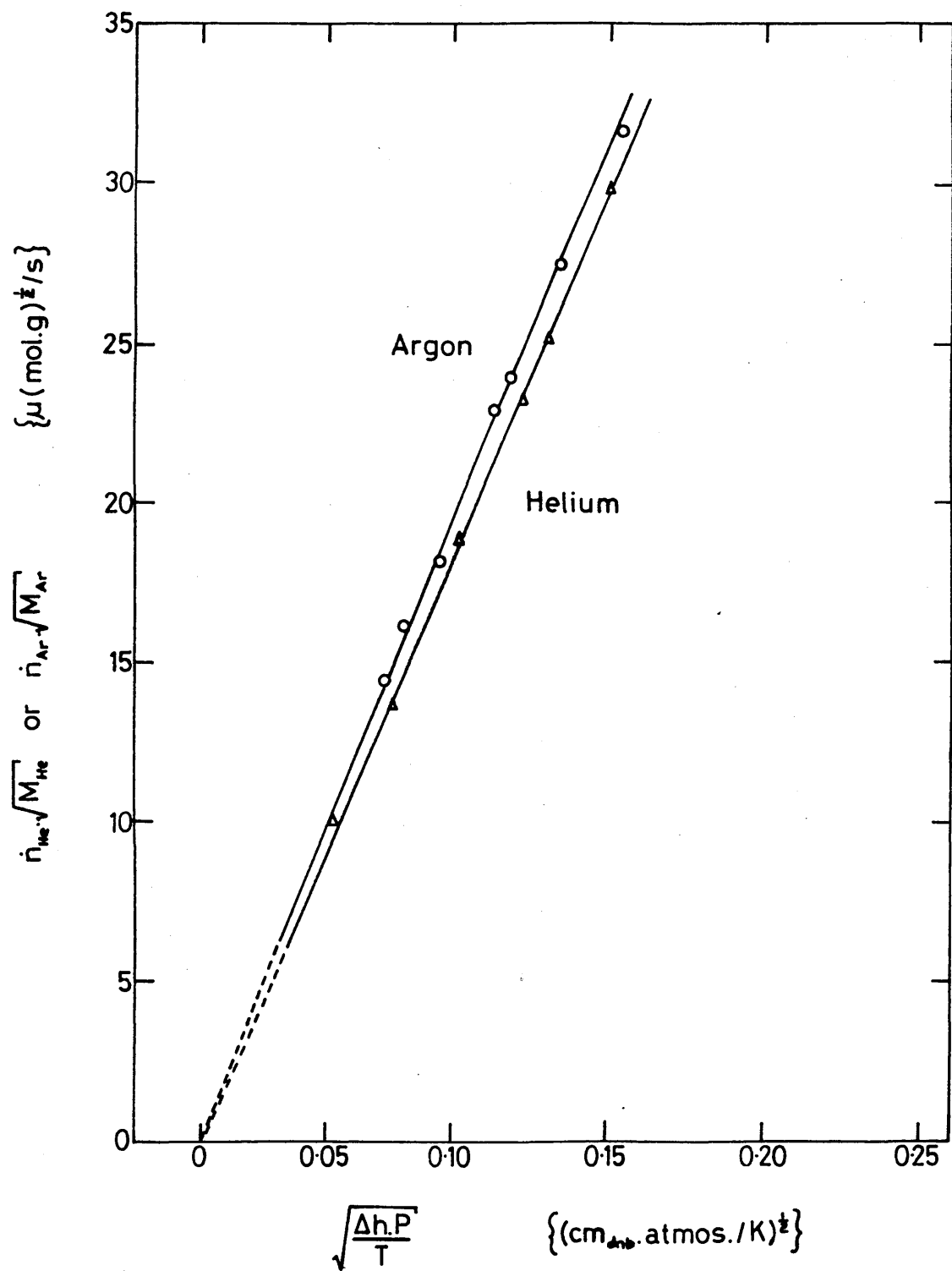
The observed pressure drop (Δp_{obs}) experienced by a gas flowing through a particular orifice is therefore made up of two components:

(a)   A pressure drop arising from the conservation of the momentum of the gas as it flows through the constriction (Δp) and which may be defined by rearranging equation (5.2.4):

$$\Delta p = \frac{RMT}{2} \left\{ \frac{\dot{n}}{AC_D} \right\}^2 \frac{1}{P} \qquad (5.2.7)$$

(b)   A pressure drop arising from the frictional interaction of the gas with the internal surface of the orifice (Δp_f). Hence,

$$\Delta p_{obs} = \Delta p + \Delta p_f \qquad (5.2.8)$$

The frictional pressure drop, Δp_f, may be estimated from the Fanning equation:

$$\Delta p_f = 2f \frac{L}{d} \rho u^2 \qquad (5.2.9)$$

where,

f   is the frictional factor and which at low values of the Reynold's number is equal to 16/Re.

L and d   are the length and diameter of the orifice respectively.

ρ is the density of the gas at the temperature and pressure pertaining.

and u   is the mixing cup velocity of

               the gas through the orifice

               which may be obtained by

               dividing the volumetric

               flow rate by the cross sectional

               area of the orifice, the

               volumetric flow rate being related to

               the molar gas flow rate via the Gas

               Laws.

Hence, $\Delta p_f = \dfrac{40.7\,\mu\,L\,\dot{n}\,R\,T}{d^4}\,\dfrac{1}{P}$ (5.2.10)

The foil orifice meter used in this work, was calibrated by

means of a bubble flowmeter at room temperature and atmospheric

pressure.The calibration data for the foil orifice meter using

helium is summarised in Table 5.4 and at each flow rate the

contribution of Δp_f to the observed pressure drop has been

calculated using the Fanning equation. It can be seen that over

the range of helium flow rates for which the flowmeter was

suitable, wall friction accounted on average for only 5.4% of

the total observed pressure drop. For the same foil

orifice meter used in conjunction with argon, the proportional

contribution of wall friction to the total pressure drop is only

about 1.90%, since the range of argon volumetric flow rates for

which the foil orifice could be used were so much lower than the

helium volumetric flow rates.

Table 5.4   The pressure drop arising from frictional effects in the calibration of the foil orifice meter using helium

Δh (cm di-n-bt)	$\dot{V}$ (mL/s)	u (m/s)	Re	f	ΔP_f (Pa)	Δh_f (cm di-n-bt)	$\left|\dfrac{\Delta h_f}{\Delta h}\right| \times 100$ (%)
1.4	0.1219	15.52	13.10	1.22	9.90	0.096	6.9
2.1	0.1666	21.21	17.90	0.89	13.50	0.131	6.2
3.3	0.2307	29.37	27.80	0.65	19.00	0.184	5.6
4.7	0.2830	36.03	30.40	0.53	23.30	0.226	4.8
5.3	0.3061	38.97	32.90	0.49	25.20	0.245	4.6
7.0	0.3658	46.57	39.40	0.41	30.10	0.292	4.2
						Mean %	5.4

For the orifice : $d = 10^{-4}$ m   and $L = 10^{-5}$ m

$\rho_{He} = 0.169$ kg/m^2 $\mu = 2.10^{-5}$ Pa.s

Since the foil orifice meter was calibrated at one atmosphere pressure but used in the permeability experiments at pressures ranging from 0.5 - 1.5 atmospheres, the effect of the total pressure range in the system on the contribution of Δp_f to the overall pressure drop must also be considered. Examination of equations (5.2.7) and (5.2.10) shows the pressure drop across the orifice, Δp_{obs}, to be inversely proportional to the total pressure in the system:-

$$\Delta p_{obs} = \left\{ \frac{RMT}{2} \left[\frac{\dot{n}}{AC_D}\right]^2 + \frac{40.7\,\mu\,L\,\dot{n}\,R\,T}{d^4} \right\} \frac{1}{P} \qquad (5.2.11)$$

Any change in the total pressure in the system will therefore result in a proportionately similar change in Δp and Δp_f and therefore Δp_f will always be approximately 5.4% of the observed pressure drop for helium through the foil orifice. It may be concluded that, in view of the small error incurred, and the constancy of this error with pressure variations, that the graphical presentation of the calibration data in the form of independent plots of $\sqrt{\dot{n}}$ vs $\sqrt{\frac{\Delta p P}{MT}}$, thereby neglecting the frictional effects for argon and helium, is reasonable for the foil orifice meter. The effect of the error was further minimised by using the calibration curve for argon for permeability measurements involving argon and the calibration curve for helium for permeability measurements involving helium.

191

5.3 GAS PERMEABILITY MEASUREMENTS

5.3.1 METHOD OF CALCULATION

The gas permeability through a porous solid at a constant total pressure, is calculated from the following relationship:-

$$\omega = \frac{\dot{n} \, R \, T}{S \, \Delta p} \qquad (5.3.1)$$

where, $\dot{n}$ = molar flow of gas

ω = gas permeability

Δp = pressure difference across the porous solid

R = Universal Gas Constant

T = absolute temperature

S = shape factor for the porous media, which in the case of this work was effectively a hollow spherical shell and is defined by:

$$S = \frac{\emptyset \pi r_e r_i}{r_e - r_i}$$

where, r_i and r_e represent the internal and external radii respectively.

and, $\emptyset$ is the solid angle subtended by the internal surface of the sphere neglecting the area cut off by the alumina support tube.

Values of the molar flow rate, n, have been obtained from the results of the experimental technique described in Sections 4.2 and 4.3, using the calibration curves for each gas through the

relevant orifice meter (see Section 5.2.3).

Experiments were carried out at different total system pressures, the system pressure P_S, being calculated as:-

$$P_S = \frac{\Delta p + 2p_i}{2} + B.P. \quad (5.3.2)$$

where, Δp = pressure difference across the porous shell

   p_i = internal pressure (relative to atmospheric pressure)

   B.P. = barometric pressure

Permeability values were determined following equation (5.3.1) and then plotted against the system pressure. The Knudsen diffusivity was obtained by extrapolating the resulting straight line to zero pressure according to the equation (3.25):-

$$\omega = D_{K,A} + \frac{B_0}{\mu} P_S \quad (3.25)$$

The value of B_0/μ was obtained as the slope of the line.

5.3.2 PERMEABILITY RESULTS FOR POROUS LIME

Permeability measurements were performed on a total of five different lime spheres, the spheres having been produced by decomposition of $CaCO_3$ spheres which had been compacted at two different pressures in order to produce different degrees of porosity.

Spheres 58, 59 and 60 were compacted at a pressure of $250MN/m^2$ producing lime porosities of 46.18%, 45.72% and 47.93% respectively. Spheres 62 and 71 were compacted at a pressure of producing lime porosites of 56.80% and 58.77% respectively. For each sphere, the permeability, ω , was determined for various values of the total pressure in the system, P_s, at temperatures of 292K, 413K, 443K and 1230K using argon and/or helium. The results obtained are presented in Tables 5.5 to 5.15 and Figures 5.8 to 5.15. The line of best fit was obtained using the least squares method for each set of results. The intercepts, slopes and correlation factors obtained are presented in the Tables and Figures as relevant.

5.3.3 PERMEABILITY RESULTS FOR REDUCED IRON SPHERES

Permeability measurements were performed on a total of six reduced iron spheres produced as described in Section 4.3.3.

Experiments were conducted using both argon and helium at temperatures of 292 and 898 K. Results obtained are presented in Tables 5.16 to 5.33 and shown graphically in Figures 5.16 to 5.33.

As for the lime experiments the line of best fit was obtained by using the least squares method. The intercept, slope and correlation factor are presented in each Table and Figure.

5.3.4 PERMEABILITY RESULTS FOR SINTERED IRON SPHERES

Three reduced iron spheres were sintered at 1373 K for five hours in H_2 prior to permeability measurements being carried out at 291 K and 898 K using Ar and N_2. The results are presented in Tables 5.34 to 5.42 and Figures 5.34 to 5.42 .

Figure 5·8 : The permeability of helium through sphere 58 at 441 K.

$S = 14·02$ cm ; $\gamma_{CaO} = 46·18\%$

Lime sphere 58

$D_{K,He,441} = 0·639$ cm²/s

Slope = 0·789 cm²/atmos.s

Correlation factor = 0·998

Helium

P_S 196   (atmospheres)
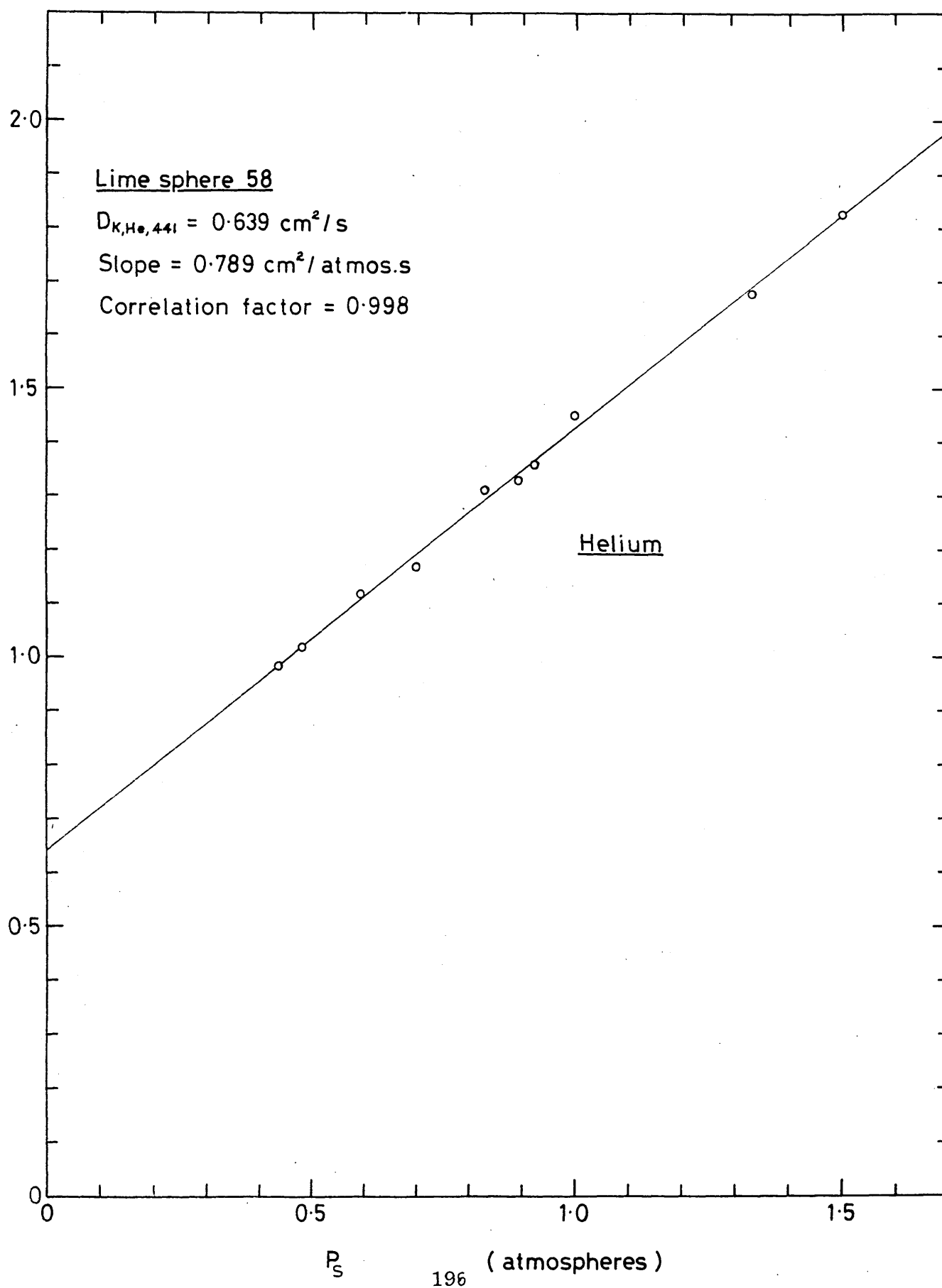
TABLE No.5.5   Permeability Data for Helium through
                Calcium Oxide sphere 58 at 441 K

Barometric pressure = 0.990 (atm)
Shape factor   = 14.02 (cm)

No Reading	Δp/ (atm)	p_i/ (atm)	p_s/ (atm)	$\dot{n}$/ ($\mu mol.s^{-1}$)	ω/ ($cm^2.s^{-1}$)
1.	0.0205	0.996	1.06	11.60	1.45
2.	0.0080	1.324	1.33	5.20	1.68
3.	0.0080	0.920	0.92	4.21	1.36
4.	0.0080	0.890	0.89	4.15	1.34
5.	0.0100	0.826	0.83	5.07	1.31
6.	0.0200	0.700	0.71	9.14	1.17
7.	0.0134	0.587	0.58	5.81	1.12
8.	0.0134	0.471	0.48	5.29	1.02
9.	0.0167	0.429	0.44	6.34	0.98

$D_{He,K}$ = 0.639 $(cm^2.s^{-1})$

Slope = B_o/μ_{He} = 0.789 $(cm^2.s^{-1}.atm^{-1})$

Correlation factor = 0.998

Figure 5·9 : The permeability of Ar and He through sphere 58 at 1230 K.

S = 14·02 cm ; γ_{CaO} = 46·18 %

Lime sphere 58

$D_{K,He,1230}$ = 1·091 cm²/s

Slope = 0·413 cm²/atmos.s

Correlation factor = 0·942

Helium

Argon

Lime sphere 58

$D_{K,Ar,1230}$ = 0·340 cm²/s

Slope = 0·330 cm²/atmos.s

Correlation factor = 0·960

ω (cm²/s)

P_S (atmospheres)

198

TABLE No. 5.6   Permeability Data for Argon through
                 Calcium Oxide sphere 58 at 1230 K

Barometric pressure = 0.975 (atm)
Shape factor   = 14.02 (cm)

No Reading	Δp/ (atm)	p_i/ (atm)	p_s/ (atm)	$\dot{n}$/ (μmol.s^{-1})	ω/ (cm^2.s^{-1})
1.	0.0360	1.0240	1.042	3.35	0.669
2.	0.0550	1.0725	1.100	4.96	0.650
3.	0.0300	1.1840	1.990	3.29	0.790
4.	0.0400	1.3000	1.320	4.33	0.781
5.	0.0334	1.4008	1.417	3.57	0.770
6.	0.0300	1.5450	1.560	3.70	0.890
7.	0.0360	0.7820	0.800	3.20	0.640
8.	0.0467	0.7450	0.769	3.58	0.552
9.	0.0267	0.5510	0.565	1.92	0.520
10.	0.0300	0.3360	0.351	2.00	0.480

$D_{Ar,K}$ = 0.3397 (cm^2.s^{-1})

Slope = B_o/μ_{Ar} = 0.3302 (cm^2.atm^{-1}.s^{-1})

Correlation factor = 0.960

TABLE No. 5.7   Permeability Data for Helium through
                 Calcium Oxide sphere 58 at 1230 K

Barometric pressure = 1.007 (atm)
Shape factor   = 14.02 (cm)

No Reading	$\Delta p/$ (atm)	$p_i/$ (atm)	$p_s/$ (atm)	$\dot{n}/$ (μmol.s^{-1})	$\omega/$ (cm^2.s^{-1})
1.	0.0180	0.993	1.022	3.72	1.49
2.	0.0670	0.996	1.030	14.33	1.54
3.	0.0230	0.993	1.004	4.89	1.53
4.	0.0568	1.160	1.180	11.99	1.52
5.	0.0702	1.327	1.362	16.57	1.70
6.	0.0200	1.489	1.500	4.58	1.65
7.	0.0361	1.591	1.610	9.03	1.80
8.	0.0267	0.790	0.800	5.11	1.38
9.	0.0495	0.724	0.749	9.28	1.35
10.	0.0314	0.669	0.685	6.49	1.49
11.	0.0250	0.500	0.513	4.34	1.25
12.	0.0450	0.397	0.420	8.43	1.35
13.	0.0212	0.289	0.300	3.44	1.17

$D_{He,K}$ = 1.091 (cm^2.s^{-1})

Slope = B_o/μ_{He} = 0.413 (cm^2.atm^{-1}.s^{-1})

Correlation factor = 0.942

Figure 5·10 :   The permeability of Ar and He through sphere 59 at 1231 K.

S = 13·88 cm ; γ_{c_aO} = 45·72%

Lime sphere 59

$D_{K,He,1231}$ = 1·264 cm²/ s

Slope = 0·328 cm²/atmos.s

Correlation factor = 0·989

Helium

Argon

Lime sphere 59

$D_{K,Ar,1231}$ = 0·396 cm²/ s

Slope = 0·249 cm²/atmos.s

Correlation factor = 0·921

, cm / s ,

P_s 201   (atmospheres)
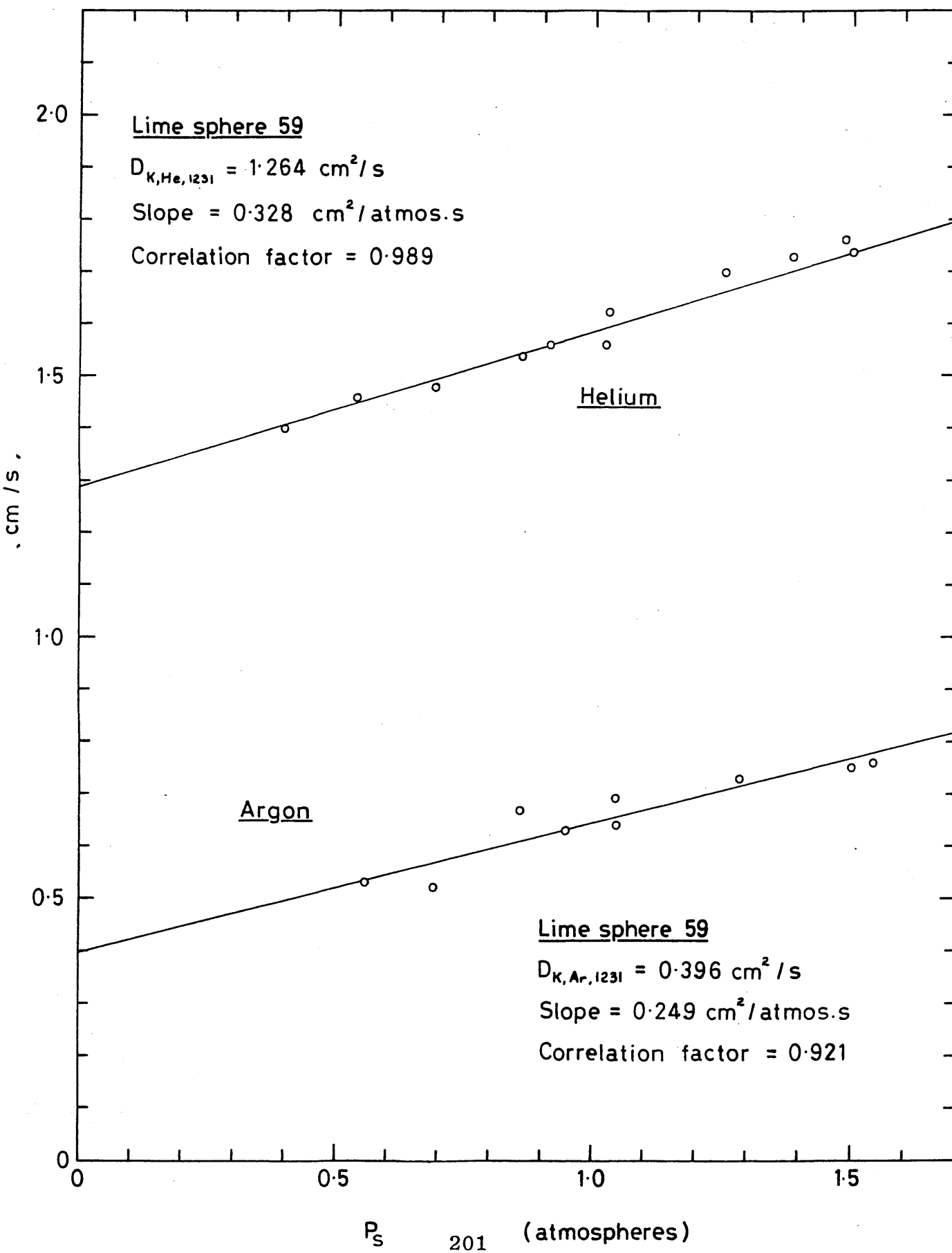
TABLE No. 5.8   <u>Permeability Data for Argon through</u>
                                       <u>Calcium Oxide sphere 59 at 1231 K</u>

Barometric pressure = 1.022 (atm)
Shape factor   = 13.88 (cm)

No Reading	$\Delta p/$ (atm)	$p_i/$ (atm)	$p_s/$ (atm)	$\dot{n}/$ (μmol.s^{-1})	$\omega/$ (cm^2.s^{-1})
1.	0.0260	1.0253	1.083	2.46	0.590
2.	0.0300	1.2685	1.284	3.00	0.730
3.	0.0167	1.1273	1.136	1.53	0.670
4.	0.0200	1.5370	1.547	2.09	0.760
5.	0.0250	1.0300	1.043	2.19	0.640
6.	0.0138	0.9420	0.940	1.20	0.630
7.	0.0250	0.8540	0.866	2.30	0.671
8.	0.0214	0.6810	0.690	1.53	0.520
9.	0.0317	0.5370	0.552	2.31	0.530

$D_{Ar,K}$ = 0.3962 (cm$\cdot^2$s^{-1})

Slope = 0.249 (cm^2.atm^{-1}.s^{-1}) = B_0/μ_{Ar}

Correlation factor = 0.921

TABLE No. 5.9   Permeability Data for Helium through
                  Calcium Oxide sphere 59 at 1231 K

Barometric pressure = 1.022 (atm)
Shape factor   = 13.88 (cm)

No Reading	Δp/ (atm)	p_i/ (atm)	p_s/ (atm)	$\dot{n}$/ (μmol.s^{-1})	ω / (cm^2.s^{-1})
1.	0.0133	1.022	1.028	2.96	1.62
2.	0.0434	1.256	1.277	10.14	1.70
3.	0.0468	1.381	1.404	11.12	1.73
4.	0.0442	1.483	1.505	10.73	1.76
5.	0.0300	1.005	1.020	6.43	1.56
6.	0.0300	0.905	0.920	6.43	1.56
7.	0.0351	0.843	0.860	7.42	1.54
8.	0.0367	0.674	0.692	7.46	1.48
9.	0.0300	0.524	0.539	6.01	1.46
10.	0.0267	0.387	0.400	5.13	1.40

$D_{He,K}$ = 1.2639 (cm^2.s^{-1})

Slope = B_0/μ_{He} = 0.328 (cm^2.s^{-1}.atm^{-1})

Correlation factor = 0.989

Figure 5·11 : The permeability of helium through sphere 60 at 413 K.

$S = 16·92$ cm ; $\gamma_{c\infty} = 47·93$ %

Helium

Lime sphere 60

$D_{K,He,413} = 0·769$ cm^2/s

Slope = $0·780$ cm^2/atmos. s

Correlation factor = $0·947$

ω

(cm^2/s)

P_s (atmospheres)

<u>TABLE No. 5.10</u>   <u>Permeability Data for Helium through</u>
    <u>Calcium Oxide sphere 60 at 413 K</u>

Barometric pressure = 1.006 (atm)
Shape factor   = 16.92 (cm)

No Reading	$\Delta p/$ (atm)	$p_i/$ (atm)	$p_s/$ (atm)	$\dot{n}/$ ($\mu mol.s^{-1}$)	$\omega/$ ($cm^2.s^{-1}$)
1.	0.0142	1.0180	1.03	10.20	1.431
2.	0.0186	1.4220	1.43	11.35	1.916
3.	0.0089	1.2180	1.22	7.95	1.785
4.	0.0103	1.0835	1.09	8.10	1.567
5.	0.0133	0.9560	0.96	10.30	1.541
6.	0.0133	0.8710	0.88	9.85	1.474
7.	0.0186	0.8770	0.88	8.65	1.460
8.	0.0163	0.7710	0.78	11.60	1.423
9.	0.0149	0.6640	0.67	9.75	1.310
10.	0.0148	0.5220	0.53	8.75	1.182

$D_{He,K}$ = 0.7695 ($cm^2.s^{-1}$)

Slope = B_o/μ_{He} = 0.780 ($cm^2 \cdot s^{-1}.atm^{-1}$)

Correlation factor = 0.947

S = 16.92 cm ; γ_{CaO} = 47.93 %

Lime sphere 60

$D_{K,He,1230}$ = 1.347 cm²/s

Slope = 0.353 cm²/atmos.s

Correlation factor = 0.965

Helium

Argon

Lime sphere 60

$D_{K,Ar,1230}$ = 0.382 cm²/s

Slope = 0.238 cm²/atmos.s

Correlation factor = 0.992

P_S (atmospheres)
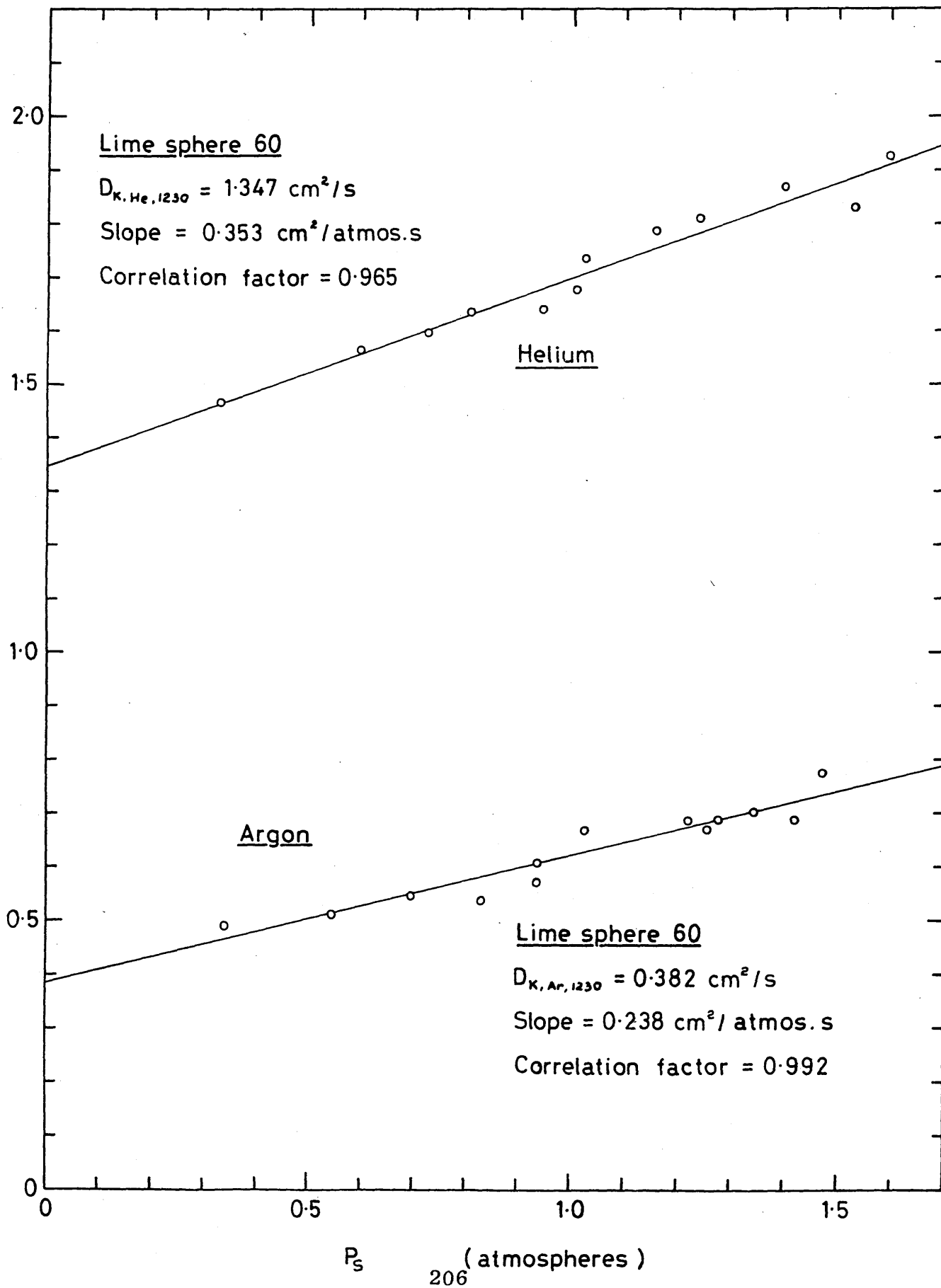
TABLE No. 5.11   Permeability Data for Argon through
                  Calcium Oxide sphere 60 at 1230 K

Barometric pressure = 1.009 (atm)
Shape factor   = 16.92 (cm)

No Reading	$\Delta p/$ (atm)	$p_i/$ (atm)	$p_s/$ (atm)	$\dot{n}/$ (μmol.s^{-1})	$\omega/$ (cm^2.s^{-1})
1.	0.0200	1.2130	1.22	2.30	0.685
2.	0.0267	1.2380	1.25	3.00	0.669
3.	0.0334	1.2590	1.27	3.85	0.687
4.	0.3680	1.4000	1.42	4.25	0.688
5.	0.3510	1.3240	1.34	4.10	0.696
6.	0.0307	1.4530	1.47	4.00	0.776
7.	0.0267	1.0120	1.03	3.00	0.669
8.	0.0340	0.9180	0.93	3.40	0.607
9.	0.0384	0.9180	0.93	3.67	0.569
10.	0.0234	0.8180	0.83	2.10	0.534
11.	0.0307	0.6780	0.69	2.80	0.543
12.	0.0368	0.5240	0.54	3.15	0.510
13.	0.0334	0.3200	0.33	2.75	0.490

$D_{Ar,K} = 0.382$ (cm^2.s^{-1})

Slope $= B_o/\mu_{Ar} = 0.2377$ (cm^2.s^{-1}.atm^{-1})

Correlation factor = 0.9920

TABLE No. 5.12   Permeability Data for Helium through
                  Calcium Oxide sphere 60 at 1230 K

Barometric pressure = 1.006 (atm)
Shape factor   = 16.92 (cm)

No Reading	$\Delta p/$ (atm)	$p_i/$ (atm)	$p_s/$ (atm)	$\dot{n}/$ (μmol.s^{-1})	$\omega/$ (cm^2.s^{-1})
1.	0.0434	1.010	1.03	12.2	1.676
2.	0.0524	1.570	1.59	16.9	1.923
3.	0.0434	1.215	1.24	13.2	1.814
4.	0.0210	1.390	1.40	6.8	1.868
5.	0.0340	1.144	1.16	10.2	1.790
6.	0.0247	1.013	1.02	7.2	1.738
7.	0.0535	1.497	1.52	16.4	1.829
8.	0.0200	0.934	0.94	5.5	1.639
9.	0.0400	0.782	0.80	10.9	1.625
10.	0.0410	0.705	0.73	11.0	1.598
11.	0.0300	0.578	0.59	7.9	1.569
12.	0.0300	0.315	0.33	7.3	1.463

$D_{He,K} = 1.3469$ (cm^2.s^{-1})

Slope $= B_0/\mu_{He} = 0.3531$ (cm^2.s^{-1}.atm^{-1})

Correlation factor = 0.9648

Figure 5·13 : The permeability of helium through lime sphere number 62 at 1230 K.

$$S = 19·48 \, cm \; ; \; \gamma = 56·80 \, \%$$

Helium

Lime sphere 62

$D_{K,He,1230} = 1·419 \, cm^2/s$

Slope $= 0·585 \, cm^2/atmos.s$

Correlation factor $= 0·989$
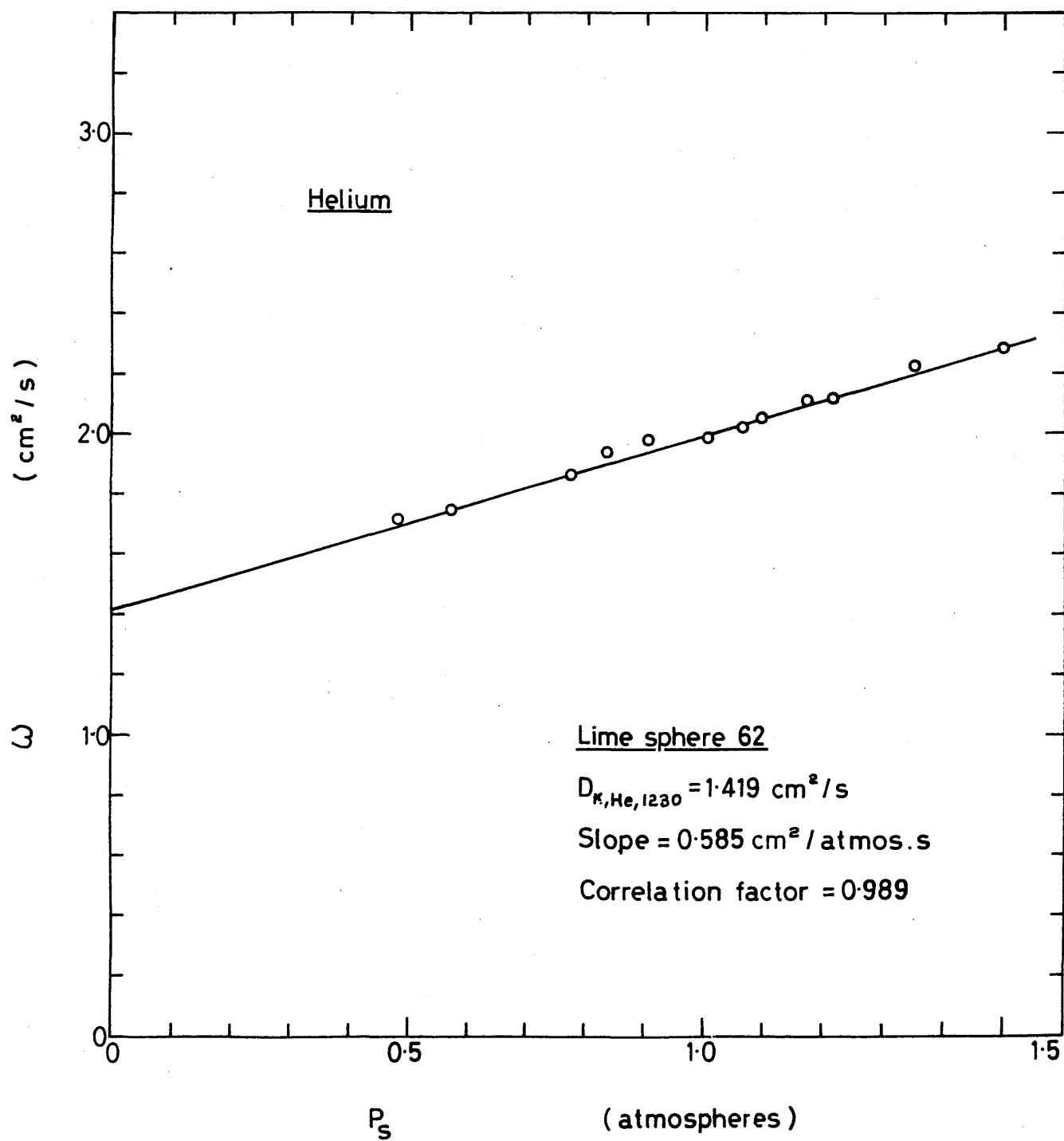
Table No.5.13   Permeability data for Helium through
                     Calcium Oxide sphere No. 62 at 1230 K

Barometric pressure =   0.997 (atm)
Shape factor   =   19.48 (cm)

No Reading	$\Delta p/$ (atm)	$p_i/$ (atm)	$p_s/$ (atm)	$\dot{n}/$ ($\mu mol.s^{-1}$)	$\omega/$ ($cm^2.s^{-1}$)
1.	0.0200	1.000	1.010	7.6	1.96
2.	0.0117	1.056	1.062	4.6	2.03
3.	0.0190	1.085	1.094	7.5	2.05
4.	0.0117	1.164	1.169	4.8	2.11
5.	0.0150	1.206	1.213	6.2	2.13
6.	0.0217	1.338	1.349	9.3	2.22
7.	0.0217	0.895	0.905	8.3	1.99
8.	0.0200	0.833	0.843	7.5	1.94
9.	0.0300	0.761	0.776	10.8	1.86
10.	0.0184	0.560	0.569	6.2	1.74
11.	0.0133	0.479	0.486	4.4	1.71

$D_{K,He}$ = 1.419 ($cm^2.s^{-1}$)

Slope B_o/μ_{He} = 0.585 ($cm^2.atm^{-1}.s^{-1}$)

Correlation factor = 0.989

Figure 5·14 : The permeability of argon through sphere number 62 at 1230 K.

$S = 19.48\,cm$; $\delta = 56.80\%$

Argon

Lime sphere 62

$D_{K,Ar,1230} = 0.442\ cm^2/s$

Slope $= 0.434\ cm^2/atmos.s$

Correlation factor $= 0.986$

y-axis: ω (cm^2/s)

x-axis: $\dfrac{P}{S}$ (atmospheres)
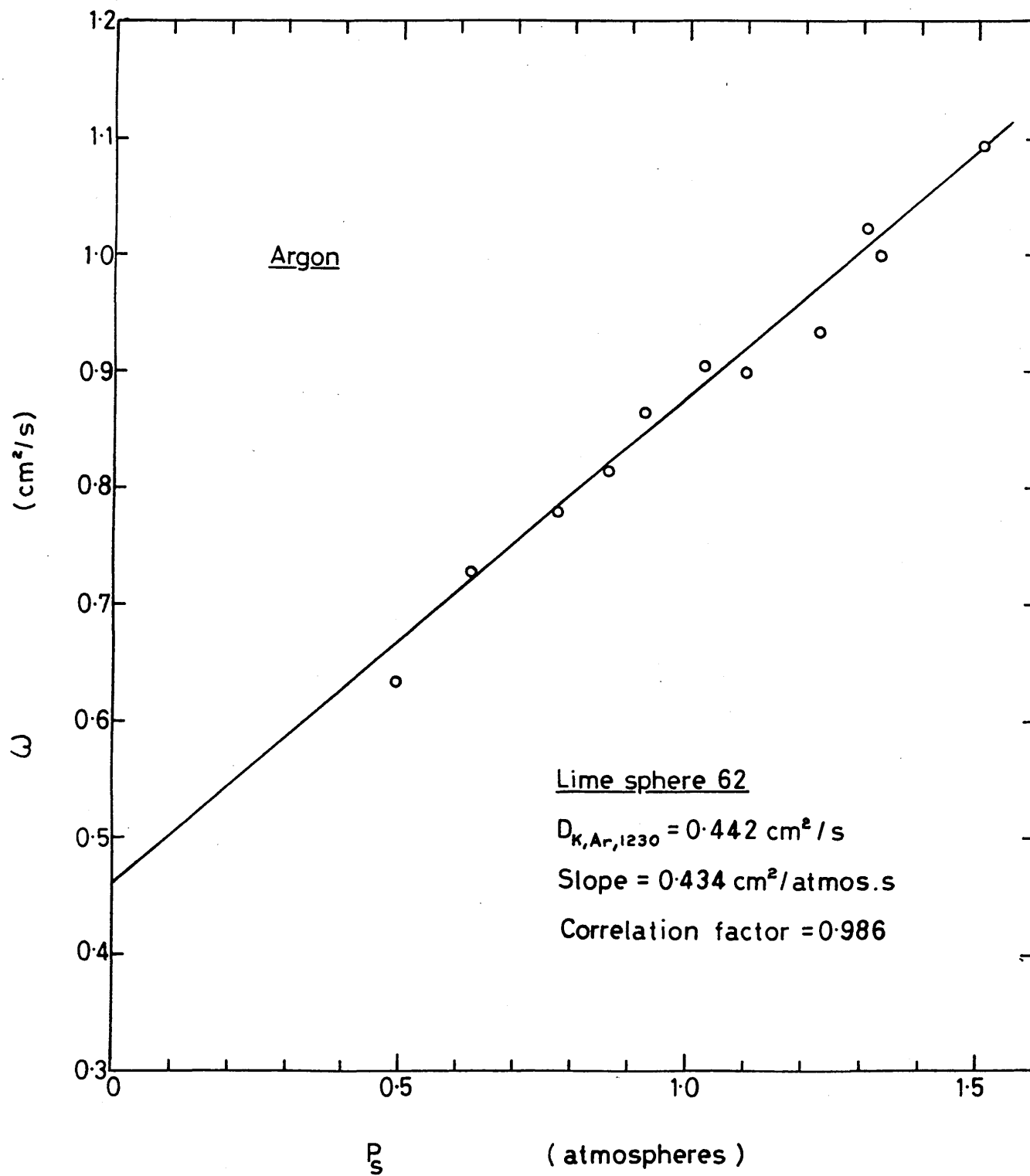
Table No.5.14   Permeability data for Argon through
                  Calcium Oxide sphere 62 at 1230 K

Barometric pressure = 1.005 (atm)
Shape factor   = 19.48 (cm)

No Reading	$\Delta p/$ (atm)	$p_i/$ (atm)	$p_s/$ (atm)	$\dot{n}/$ ($\mu mol.s^{-1}$)	$\omega/$ ($cm^2.s^{-1}$)
1.	0.0217	1.008	1.023	3.80	0.906
2.	0.0200	1.213	1.223	3.60	0.932
3.	0.0267	1.292	1.306	5.30	1.025
4.	0.0307	1.312	1.327	6.00	1.010
5.	0.0217	0.915	0.925	3.60	0.865
6.	0.0247	0.846	0.861	4.45	0.820
7.	0.0290	0.767	0.776	4.40	0.780
8.	0.0274	0.614	0.626	3.80	0.728
9.	0.0217	0.488	0.497	2.65	0.630

$D_{K,Ar} = 0.442$ ($cm^2.s^{-1}$)

Slope $B_o/\mu_{Ar} = 0.434$ ($cm^2.s^{-1}.atm^{-1}$)

Correlation factor = 0.986

Figure 5·15 : The permeability of argon through sphere number 71
at 292 K.

S=18·10 cm ; ४=58·77%

Argon

Lime sphere 71

$D_{K,Ar,298} = 0.231$ cm²/s

Slope = 1·58 cm²/atmos.s

Correlation factor = 0·991

P_S (atmospheres)

213
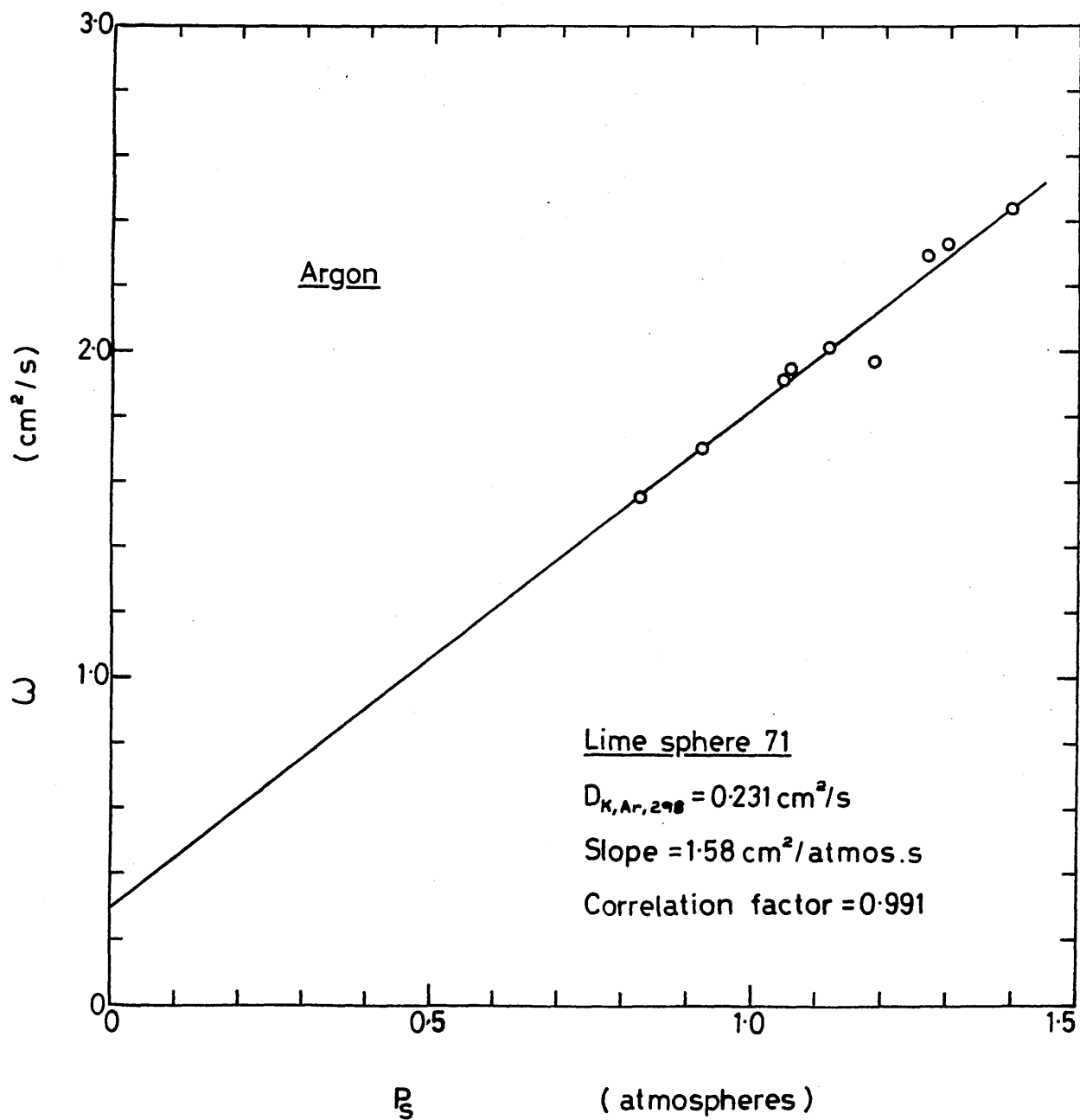
Permeability data for Argon through
                                Calcium Oxide sphere 71 at 292 K

Barometric pressure = 1.01 (atm)
Shape factor   = 18.1 (cm)

No Reading	$\Delta p/$ (atm)	$p_i/$ (atm)	$p_s/$ (atm)	$\dot{n}/$ (μmol.s^{-1})	$\omega/$ (cm^2.s^{-1})
1.	0.0447	1.0258	1.0480	63.60	1.92
2.	0.0324	1.1350	1.1510	78.25	2.02
3.	0.0473	1.1610	1.1850	58.80	1.97
4.	0.0416	1.2480	1.2680	71.20	2.30
5.	0.0369	1.2810	1.2990	63.80	2.32
6.	0.0469	1.0330	1.0570	81.48	1.95

$D_{K,Ar}$ = 0.2308 (cm^2.s^{-1})

Slope B_o/μ_{Ar} = 1.58 (cm^2.s^{-1}.atm^{-1})

Correlation factor = 0.991

Figure 5.16   : The permeability of argon through sphere Q at 291 K.

$S = 15.87 cm$; $\gamma = 59.88\%$

Argon

(cm²/s)

Iron sphere Q

$D_{K,Ar,291} = 0.892$ cm²/s

Slope = 4.67 cm²/atmos.s

Correlation factor = 0.998

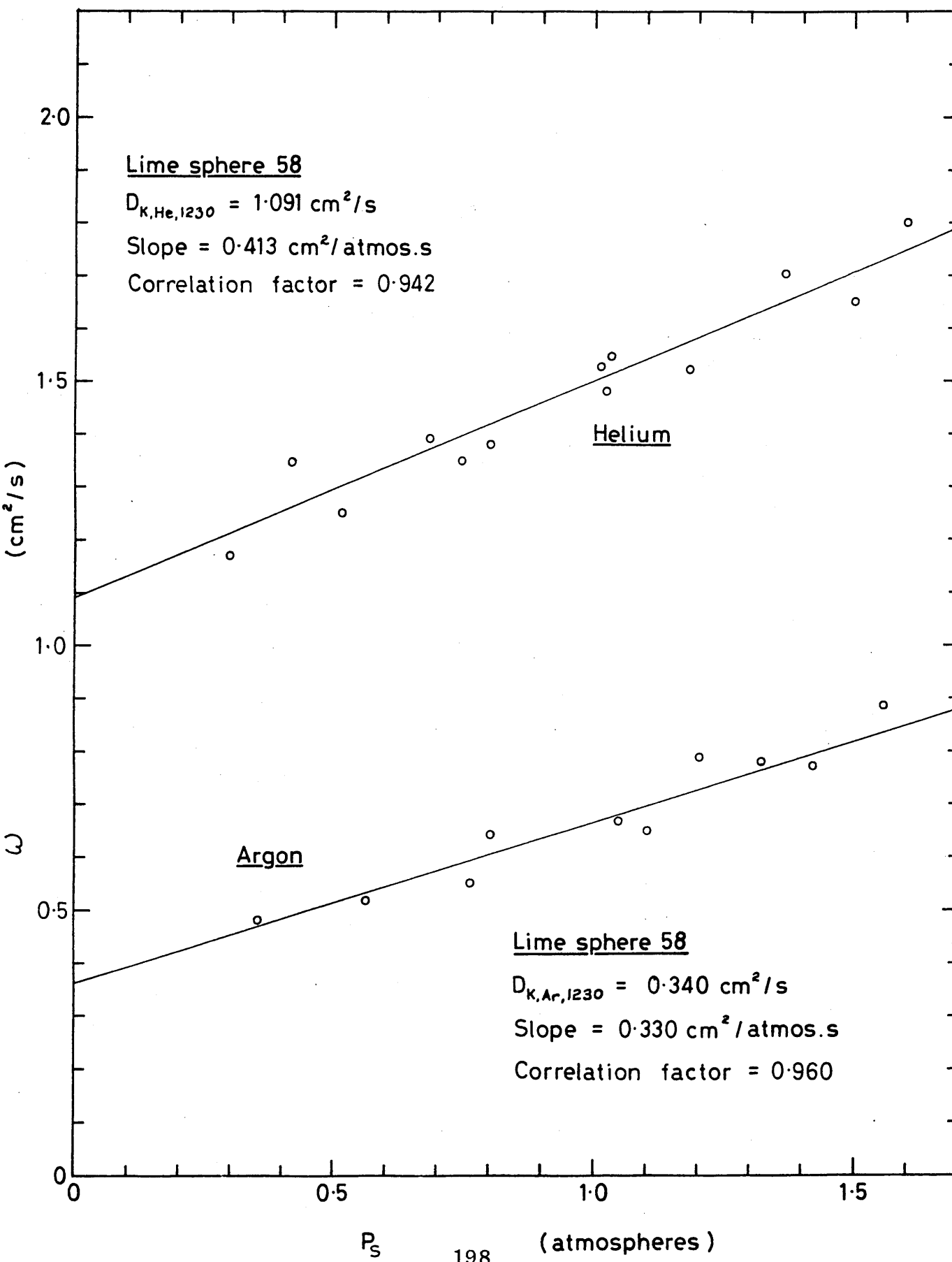P_S (atmospheres)

TABLE No.5.16   Permeability Data for Argon through
Iron reduced sphere Q at 291 K

Barometric pressure = 1.027 (atm)
Shape factor   = 15.87 (cm)

No Reading	Δp/ (atm)	$p_{orifice}$ /(atm)	p_i/ (atm)	p_s/ (atm)	$\dot{n}$/ (μmol.s^{-1})	ω / (cm^2.s^{-1})
1.	0.0150	1.027	1.090	1.098	60.0	6.01
2.	0.0133	1.115	1.184	1.191	57.0	6.44
3.	0.0167	1.141	1.231	1.240	73.5	6.62
4.	0.0200	1.222	1.300	1.310	96.5	7.26
5.	0.0167	1.275	1.362	1.371	80.5	7.25
6.	0.0200	1.340	1.446	1.456	101.5	7.64
7.	0.0167	1.439	1.521	1.530	89.5	8.06
8.	0.0133	0.774	0.869	0.876	42.5	4.81
9.	0.0234	0.669	0.781	0.793	71.5	4.60
10.	0.0267	0.626	0.729	0.743	76.6	4.32
11.	0.0200	0.763	0.556	0.566	48.5	3.65
12.	0.0234	0.372	0.499	0.511	51.5	3.31

$D_{Ar,K} = 0.892$ (cm^2.s^{-1})

Slope = B_o/μ_{Ar} = 4.67 (cm^2.s^{-1}.atm^{-1})

Correlation factor = 0.998

Figure 5·17 : The permeability of argon through sphere Q at 898 K.

S = 15·87 cm ; γ = 59·88 %

Argon

Iron sphere Q

$D_{K,Ar,898}$ = 1·34 cm^2/s

Slope = 1·83 cm^2/atmos.s

Correlation factor = 0·982

P_S (atmospheres)

TABLE No.5.17   Permeability Data for Argon through
                   Iron reduced sphere Q at 898 K

Barometric pressure = 1.016 atm
Shape factor   = 15.87 cm

No Reading	$\Delta p/$ (atm)	$p_{orifice}/$ (atm)	$p_i/$ (atm)	$p_s/$ (atm)	$\dot{n}/$ (μmol.s^{-1})	$\omega/$ (cm^2.s^{-1})
1.	0.0870	1.035	1.046	1.090	62.0	3.31
2.	0.1270	1.065	1.076	1.140	93.0	3.40
3.	0.0870	1.196	1.205	1.270	64.0	3.42
4.	0.1170	1.264	1.275	1.334	97.5	3.87
5.	0.1136	1.367	1.373	1.430	101.5	4.14
6.	0.0800	0.926	0.945	2.985	53.5	3.11
7.	0.1270	0.799	0.820	0.884	83.0	3.03
8.	0.1136	0.715	0.738	0.795	64.0	2.62
9.	0.1270	0.538	0.564	0.628	71.5	2.55
10.	0.1540	0.377	0.408	0.485	70.0	2.11
11.	0.1660	0.314	0.246	0.408	66.5	2.14
12.	0.1170	0.300	0.333	0.392	55.5	2.20

$D_{Ar,K}$ = 1.34 (cm^2.s^{-1})

Slope = B_o/μ_{Ar} = 1.83 (cm.atm^{-1}.s^{-1})

Correlation factor = 0.9817

Figure 5·18 : The permeability of helium through sphere Q at 291 K .

$S = 15·87$ cm ; $\gamma = 59·88$ %

Helium

Iron sphere Q

$D_{K,He,291} = 2·96$ cm^2/ s

Slope = 5·32 cm^2/atmos.s

Correlation factor = 0·995

Permeability Data for Helium through
                         Iron reduced sphere Q at 291 K

Barometric pressure = 1.026 (atm)
Shape factor   = 15.87 (cm)

No Reading	Δp/ (atm)	$P_{orifice}$/ (atm)	p_i/ (atm)	p_s/ (atm)	$\dot{n}$/ (μmol.s^{-1})	ω/ (cm^2.s^{-1})
1.	0.0401	1.041	1.063	1.084	228.0	8.56
2.	0.0434	1.083	1.106	1.128	256.0	8.86
3.	0.0434	1.089	1.112	1.134	261.0	9.06
4.	0.0367	1.197	1.220	1.239	226.0	9.26
5.	0.0337	1.302	1.326	1.343	226.0	10.09
6.	0.0336	1.404	1.432	1.479	246.0	11.00
7.	0.0300	1.682	1.506	1.522	220.0	11.02
8.	0.0467	0.925	0.956	0.978	254.0	8.17
9.	0.0467	0.835	0.863	0.887	244.0	7.87
10.	0.0437	0.713	0.741	0.763	213.0	7.35
11.	0.0501	0.618	0.646	0.671	217.0	6.52
12.	0.0501	0.536	0.563	0.588	202.0	6.06
13.	0.0601	0.441	0.467	0.498	218.0	5.45

$D_{He,K}$ = 2.96 (cm^2.s^{-1})

Slope = B_o/μ_{He} = 5.32(cm.s^{-1}.atm^{-1}.)

Correlation factor = 0.995

Figure 5·19 : The permeability of helium through sphere Q at 898 K.

$S = 15·87$ cm ; $\delta = 59·88 \%$

Helium

Iron sphere Q

$D_{K,He,898} = 4·81$ cm^2/s

Slope = 2·75 cm^2/atmos.s

Correlation factor = 0·991

ω (cm^2/s)

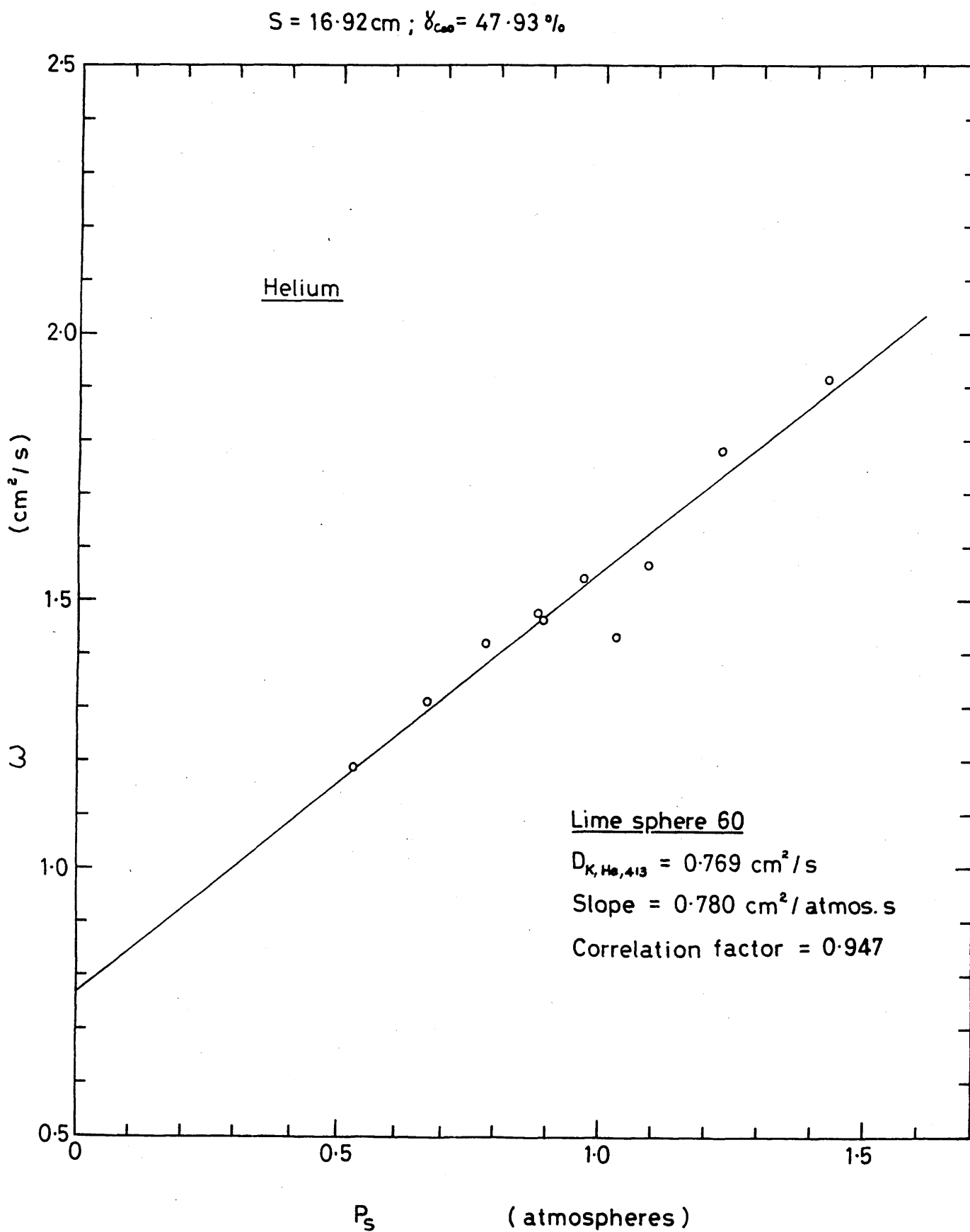$\frac{P}{S}$ (atmospheres)

TABLE No. 5.19   Permeability Data for Helium through
                  Iron reduced sphere Q at 898 K

Barometric pressure = 1.016 (atm)
Shape factor   = 15.87 (cm)

No Reading	$\Delta p/$ (atm)	$P_{orifice}/$ (atm)	$P_i/$ (atm)	$P_s/$ (atm)	$\dot{n}/$ ($\mu mol.s^{-1}$)	$\omega/$ ($cm^2.s^{-1}$)
1.	0.1069	1.010	1.038	1.092	183.0	7.95
2.	0.1270	1.043	1.071	1.134	215.0	7.86
3.	0.1270	1.196	1.218	1.288	235.7	8.62
4.	0.1102	1.292	1.311	1.367	203.5	8.57
5.	0.1270	1.377	1.396	1.458	237.0	8.66
6.	0.1236	1.433	1.448	1.510	236.0	8.87
7.	0.1069	0.822	0.869	0.923	169.0	7.34
8.	0.1270	0.697	0.747	0.811	197.0	7.20
9.	0.1571	0.628	0.679	0.758	230.0	6.80
10.	0.1738	0.481	0.536	0.623	243.0	6.49
11.	0.1571	0.436	0.497	0.571	217.5	6.43
12.	0.1270	0.360	0.418	0.482	165.0	6.03

$D_{He,K} = 4.81$ ($cm^2.s^{-1}$)

Slope $= B_o/\mu_{He} = 2.75$ ($cm^2.s^{-1}.atm^{-1}$)

Correlation factor = 0.991

Figure 5·20 : The permeability of argon through sphere R at 292 K.

S = 13·24 cm ; γ = 60·34 %

Argon

Iron sphere R

$D_{K,Ar,291}$ = 0·954 cm^2/s

Slope = 4·84 cm^2/atmos.s

Correlation factor = 0·996

ω (cm^2/s)

P_S (atmospheres)

TABLE No.5.20   Permeability Data for Argon through
                 Iron reduced sphere R at 292 K

Barometric pressure =   1.020 (atm)
Shape factor   = 13.24 (cm)

No Reading	$\Delta P/$ (atm)	$P_{orifice}/$ (atm)	$P_i/$ (atm)	$P_s/$ (atm)	$\dot{n}/$ (μmol.s^{-1})	$\omega/$ (cm^2.s^{-1})
1.	0.0240	1.034	1.041	1.053	82.5	5.20
2.	0.0340	1.088	1.097	1.114	119.5	6.34
3.	0.0210	1.188	1.198	1.209	80.0	6.86
4.	0.0310	1.234	1.246	1.261	124.0	7.21
5.	0.0240	1.300	1.313	1.325	96.5	7.25
6.	0.0210	1.401	1.417	1.427	93.5	8.03
7.	0.0210	1.437	1.453	1.467	91.5	7.85
8.	0.0340	0.915	0.908	0.925	99.0	5.25
9.	0.0340	0.781	0.782	0.799	90.5	4.80
10.	0.0310	0.599	0.610	0.626	66.5	3.87
11.	0.0310	0.487	0.483	0.498	60.0	3.49

$D_{Ar,K} = 0.954$ (cm^2.s^{-1})

Slope $= {}^{Bo}/\mu_{Ar} = 4.84$ (cm^2.atm^{-1}.s^{-1})

Correlation factor = 0.996

Figure 5·21 : The permeability of argon through sphere R at 898 K.

$S = 13·24$ cm ; $\gamma = 60·34\%$

Argon

Iron sphere R

$D_{K, Ar, 898} = 1·397$ cm^2/s

Slope = $1·915$ cm^2/atmos.s

Correlation factor = $0·992$

P_S (atmospheres)

225

TABLE No. 5.21   Permeability Data for Argon through
                  Iron reduced sphere R at 898 K

Barometric pressure = 1.020 (atm)
Shape factor   = 13.24 (cm)

No Reading	$\Delta p/$ (atm)	$p_{orifice}/$ (atm)	$p_i/$ (atm)	$p_s/$ (atm)	$\dot{n}/$ (μmol.s^{-1})	$\omega/$ (cm^2.s^{-1})
1.	0.0935	1.030	1.042	1.089	88.5	3.48
2.	0.0902	1.101	1.111	1.157	60.0	3.70
3.	0.0952	1.181	1.190	1.238	65.5	3.82
4.	0.1036	1.292	1.299	1.351	75.5	4.06
5.	0.0802	1.407	1.412	1.453	60.5	4.20
6.	0.0735	1.480	1.487	1.521	55.0	4.16
7.	0.1136	0.902	0.912	0.978	66.0	3.23
8.	0.1069	0.746	0.768	0.822	55.0	2.87
9.	0.1136	0.636	0.661	0.718	56.5	2.77
10.	0.1169	0.603	0.628	0.687	55.5	2.67
11.	0.1169	0.472	0.500	0.599	53.0	2.52

$D_{Ar,K}$ = 1.397 (cm^2.s^{-1})

Slope = B_o/μ_{Ar} = 1.915 (cm^2.s^{-1}.atm^{-1})

Correlation factor = 0.992

Figure 5·22 : The permeability of helium through sphere R at 291 K.

$S = 13·24$ cm ; $\gamma = 60·34$ %

Helium

Iron sphere R

$D_{K,He,291} = 2·94$ cm^2/s

Slope = 5·79 cm^2/atmos.s

Correlation factor = 0·9927

ω (cm^2/s)

P_s (atmospheres)

TABLE No. 5.22.   Permeability Data for Helium through
                    Iron reduced sphere R at 291 K

Barometric pressure = 1.020 (atm)
Shape factor   = 13.24 (atm)

No Reading	$\Delta p/$ (atm)	$p_{orifice}$ /(atm)	$p_i/$ (atm)	$p_s/$ (atm)	$\dot{n}/$ $(\mu mol.s^{-1})$	$\omega /$ $(cm^2.s^{-1})$
1.	0.0401	1.035	1.057	1.078	208.0	9.38
2.	0.0467	1.093	1.116	1.139	245.0	9.47
3.	0.0436	1.197	1.221	1.243	250.0	10.34
4.	0.0434	1.264	1.288	1.310	253.0	10.51
5.	0.0401	1.314	1.338	1.358	239.5	10.77
6.	0.0434	1.354	1.378	1.400	263.5	10.95
7.	0.0401	1.389	1.414	1.434	257.0	11.55
8.	0.0367	1.467	1.491	1.510	244.0	11.97
9.	0.0401	0.919	0.967	0.968	183.0	8.23
10.	0.0434	0.782	0.810	0.832	175.5	7.29
11.	0.0417	0.663	0.691	0.712	166.5	7.20
12.	0.0667	0.572	0.599	0.623	247.0	6.67
13.	0.0401	0.473	0.500	0.521	129.0	5.81
14.	0.0401	0.397	0.623	0.444	133.0	5.99

$D_{He,K} = 2.94$ $(cm^2.s^{-1})$

Slope $^{B}o/\mu_{He} = 5.79$ $(cm^2.s^{-1}.atm^{-1})$

Correlation factor = 0.9927

Figure 5·23 : The permeability of helium through sphere R at 898 K.

S = 13·24 cm ; ४ = 60·34%

Helium

Iron sphere R

$D_{K,He,898}$ = 4·93 cm²/s

Slope = 2·89 cm² /atmos.s

Correlation factor = 0·996

TABLE No. 5.23   Permeability Data for Helium through Iron reduced sphere R at 898 K

Barometric pressure = 0.998 (atm)
Shape factor   = 13.24 (cm)

No Reading	$\Delta p/$ (atm)	$p_{orifice}/$ (atm)	$p_i/$ (atm)	$p_s/$ (atm)	$\dot{n}/$ (μmol.s^{-1})	$\omega/$ (cm^2.s^{-1})
1.	0.1270	1.002	1.035	1.094	185.0	8.11
2.	0.1236	1.025	1.053	1.115	181.0	8.15
3.	0.1337	1.107	1.220	1.287	207.5	8.64
4.	0.1303	1.262	1.282	1.348	208.8	8.88
5.	0.1270	1.343	1.360	1.424	207.0	9.07
6.	0.1303	1.410	1.424	1.500	217.5	9.29
7.	0.1270	0.869	0.915	0.078	172.5	7.56
8.	0.1270	1.745	0.793	0.857	170.0	7.45
9.	0.1471	0.526	0.580	0.654	182.5	6.90
10.	0.1404	0.431	0.487	0.558	162.5	6.44
11.	0.1404	0.369	0.426	0.497	161.5	6.40

$D_{He,K}$ = 4.93 (cm^2.s^{-1})

Slope = B_o/μ_{He} = 2.89 (cm^2.s^{-1}.atm^{-1})

Correlation factor = 0.996

Figure 5.24 : The permeability of argon through sphere T at 291 K.

$S = 12.53$ cm ; $\delta = 60.26\%$

Argon

Iron sphere T

$D_{K,Ar,291} = 0.91$ cm^2/s

Slope $= 4.78$ cm^2/atmos.s

Correlation factor $= 0.997$

ω (cm^2/s)

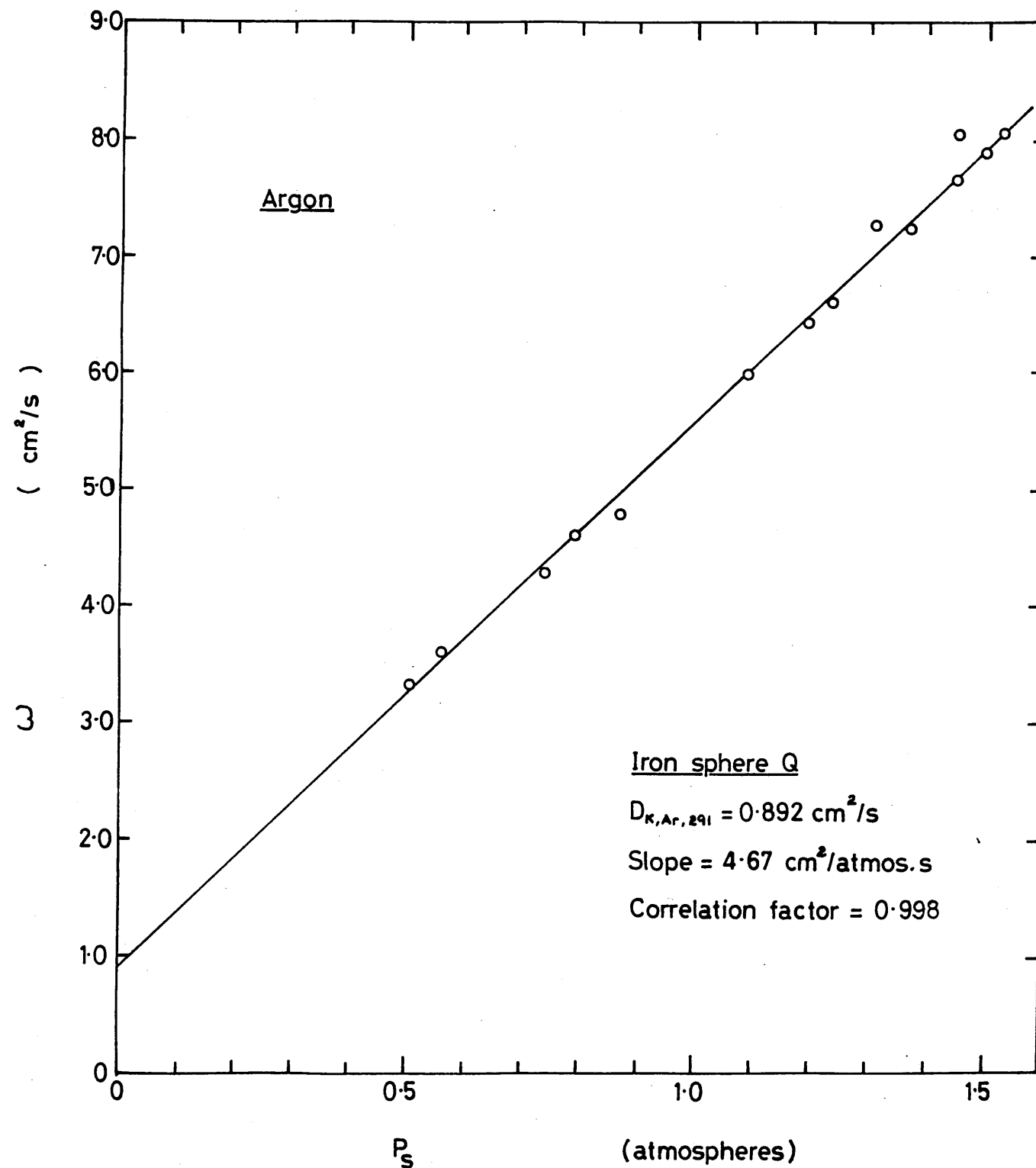P_s (atmospheres)
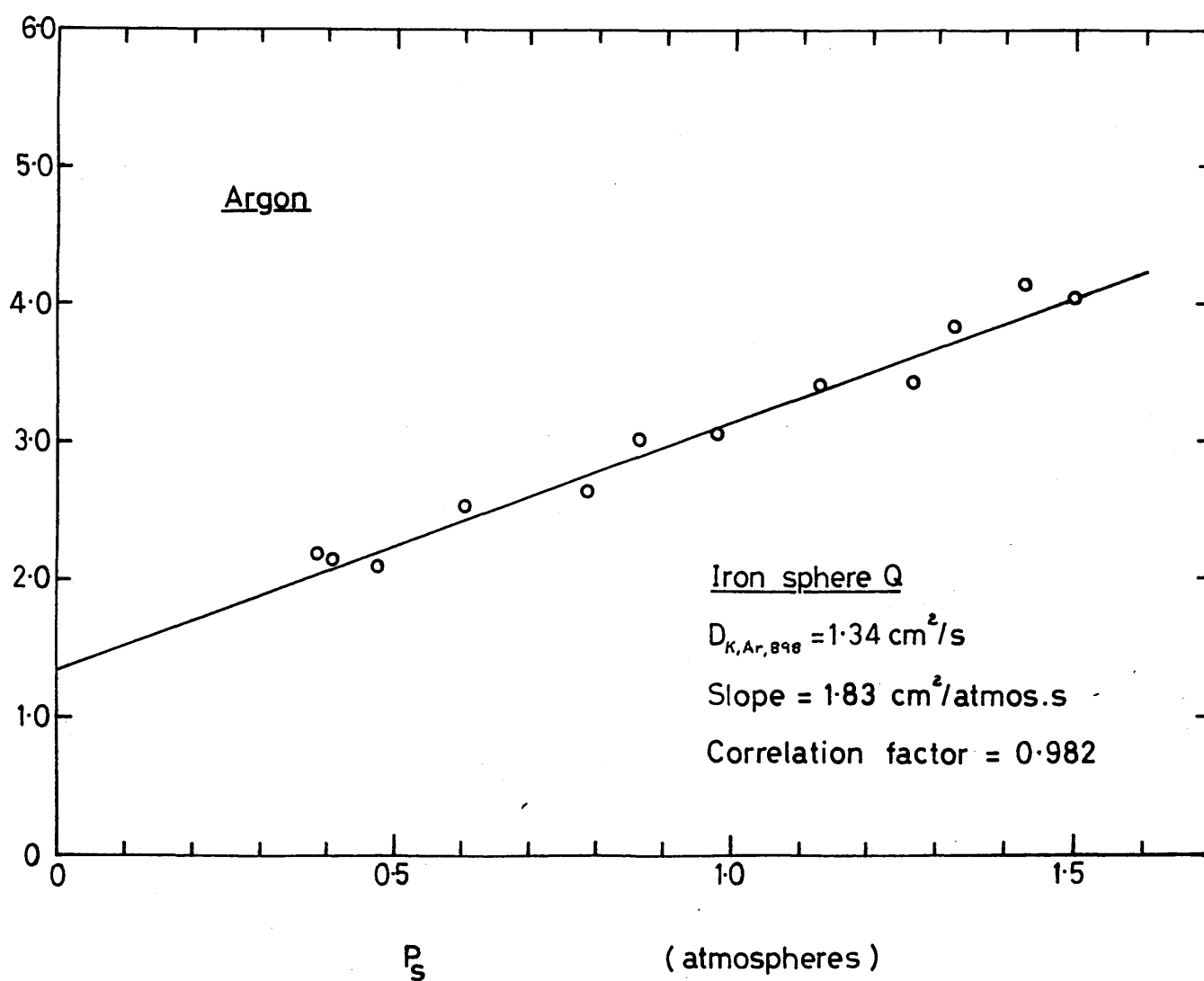
TABLE No. 5.24   Permeability Data for Argon through
                  Iron reduced sphere T at 291 K

Barometric pressure = 1.010 (atm)
Shape factor   = 12.53 (cm)

No Reading	Δp/ (atm)	$p_{orifice}$/ (atm)	p_i/ (atm)	p_s/ (atm)	$\dot{n}$/ ($\mu mol.s^{-1}$)	ω/ ($cm^2.s^{-1}$)
1.	0.0167	1.013	1.020	1.028	52.0	5.93
2.	0.0217	1.171	1.180	1.191	77.0	6.76
3.	0.0267	1.239	1.240	1.254	98.0	6.99
4.	0.0200	1.318	1.300	1.310	75.0	7.14
5.	0.0217	1.376	1.380	1.390	84.0	7.37
6.	0.0217	1.416	1.420	1.430	87.5	7.68
7.	0.0367	0.943	0.987	1.005	113.0	5.87
8.	0.0234	0.780	0.792	0.804	56.0	4.56
9.	0.0334	0.669	0.689	0.706	75.0	4.28
10.	0.0267	0.576	0.595	0.609	56.0	3.99
11.	0.0334	0.681	0.502	0.518	59.0	3.36
12.	0.0384	0.353	0.375	0.394	54.0	2.68

$D_{Ar,K}$ = 0.91 ($cm^2.s^{-1}$)

Slope = B_0/μ_{Ar} = 4.78 ($cm^2.atm^{-1}.s^{-1}$)

Correlation factor = 0.997

Figure 5·25 : The permeability of argon through sphere T at 898 K.

S = 12·53 cm ; γ = 60·26 %

Argon

Iron sphere T

$D_{K,Ar,898}$ = 1·15 cm²/s

Slope = 2·08 cm²/atmos.s

Correlation factor = 0·996

P_S (atmospheres)

ω (cm²/s)

233

TABLE No.5.25   Permeability Data for Argon through
                       Iron reduced sphere T at 898 K

Barometric pressure =   0.999 (atm)
Shape factor   =   12.53 (cm)

No Reading	Δp/ (atm)	$p_{orifice}$/ (atm)	p_i/ (atm)	p_s/ (atm)	$\dot{n}$/ (μmol.s^{-1})	ω / (cm^2.s^{-1})
1.	0.0969	1.002	1.012	1.059	55.0	3.33
2.	0.1069	1.016	1.029	1.082	61.5	3.38
3.	0.1036	1.042	1.054	1.106	61.0	3.45
4.	0.1270	1.061	1.074	1.137	74.5	3.44
5.	0.0802	1.178	1.186	1.226	52.0	3.80
6.	0.0935	1.229	1.236	1.283	62.0	3.90
7.	0.1036	1.325	1.333	1.385	72.0	4.02
8.	0.1136	1.373	1.380	1.437	79.0	4.09
9.	0.1203	0.847	0.865	0.925	64.0	3.12
10.	0.1203	0.716	0.738	0.798	58.0	2.83
11.	0.1537	0.608	0.638	0.715	69.0	2.64
12.	0.1103	0.696	0.521	0.576	45.0	2.40
13.	0.1170	0.385	0.416	0.472	41.5	2.08

$D_{Ar,K}$ =   1.15 (cm^2.s^{-1})

Slope = ^{B}o / μ_{Ar} = 2.08 (cm^2.s^{-1}.atm^{-1})

Correlation factor = 0.996

Figure 5·26 : The permeability of helium through sphere T at 291 K.

$S = 12.53\,cm$; $\gamma = 60.26\,\%$

Helium

Iron sphere T

$D_{K,He,291} = 2.97\ cm^2/s$

Slope $= 6.79\ cm^2/atmos.s$

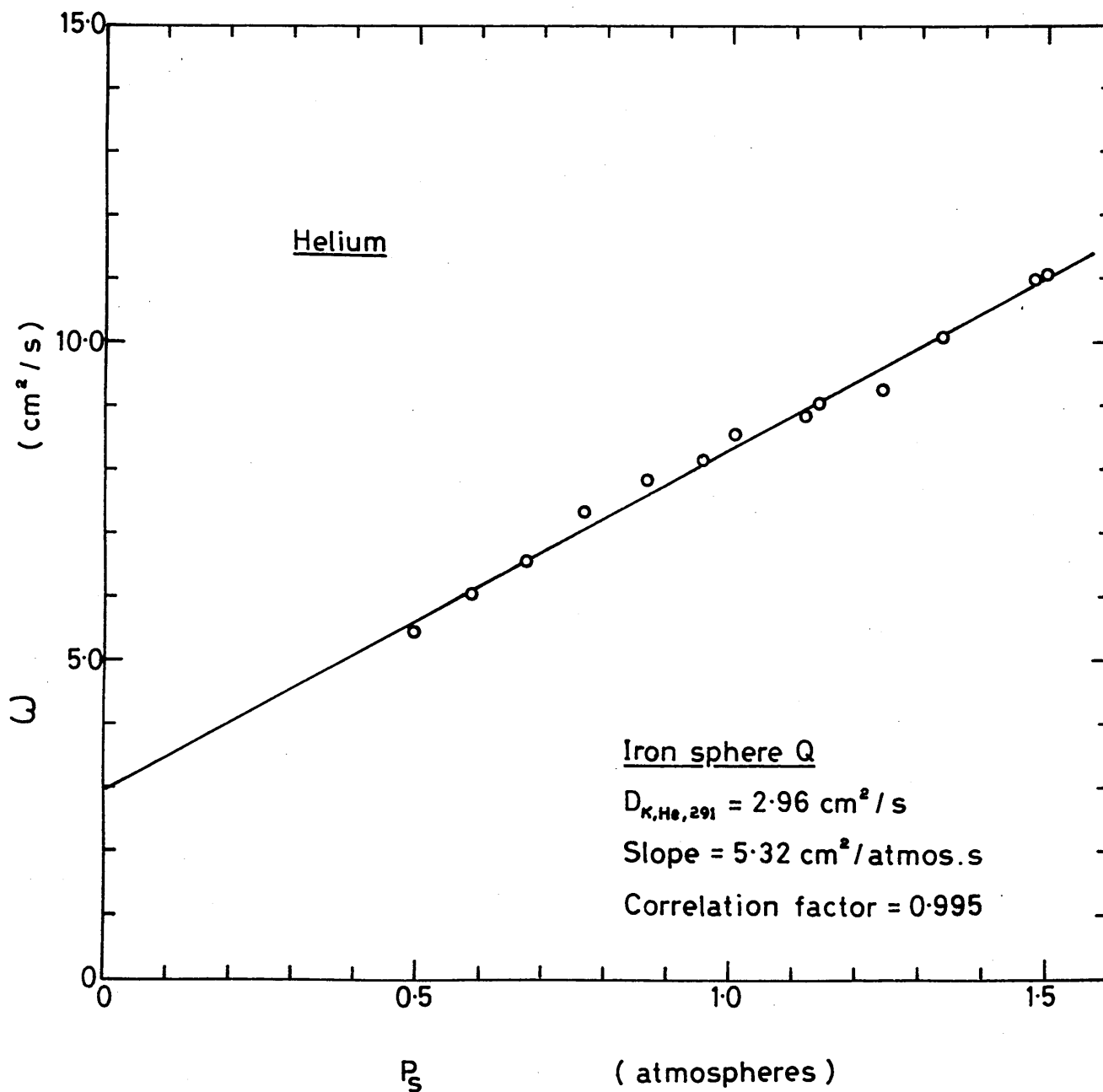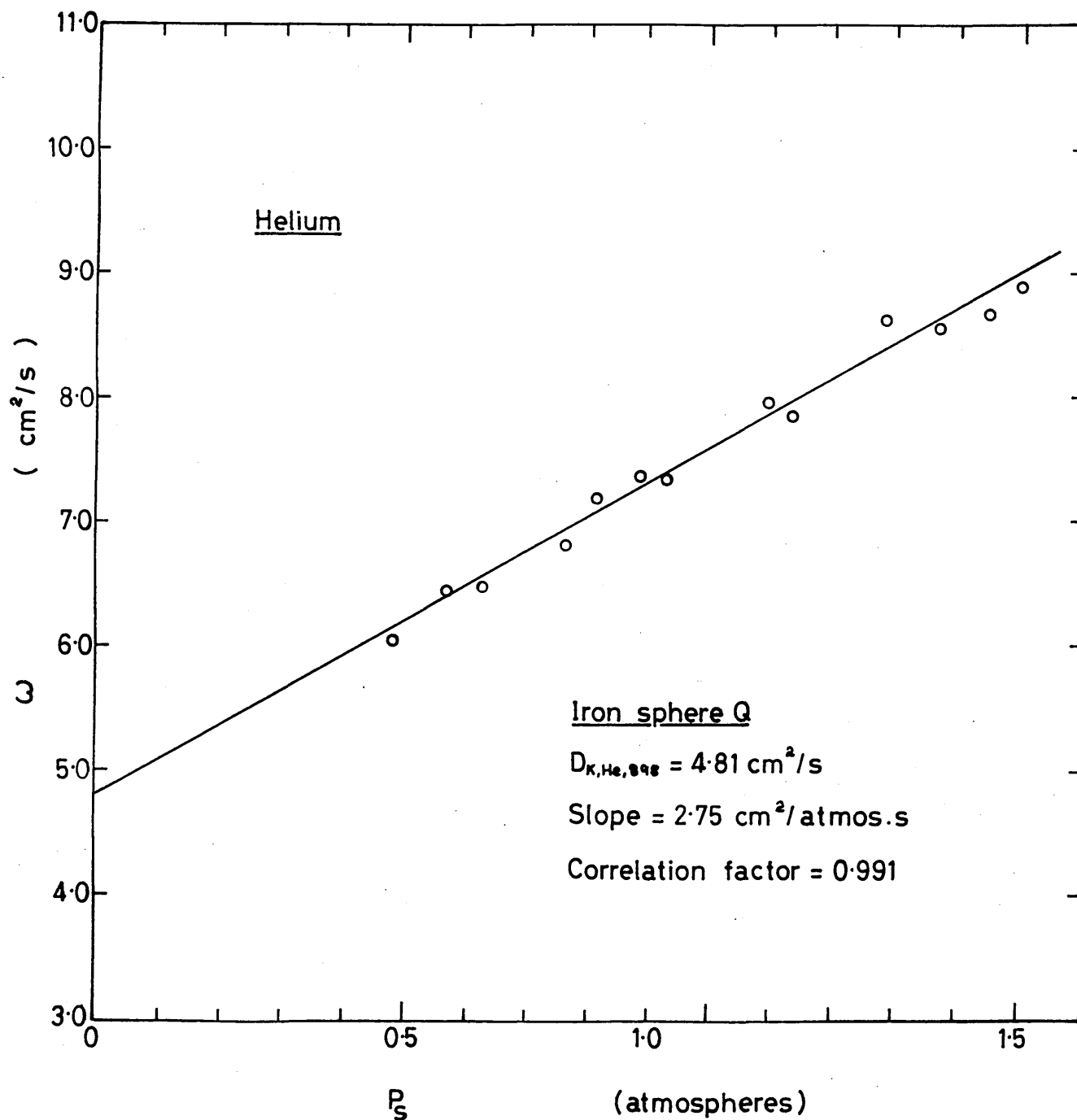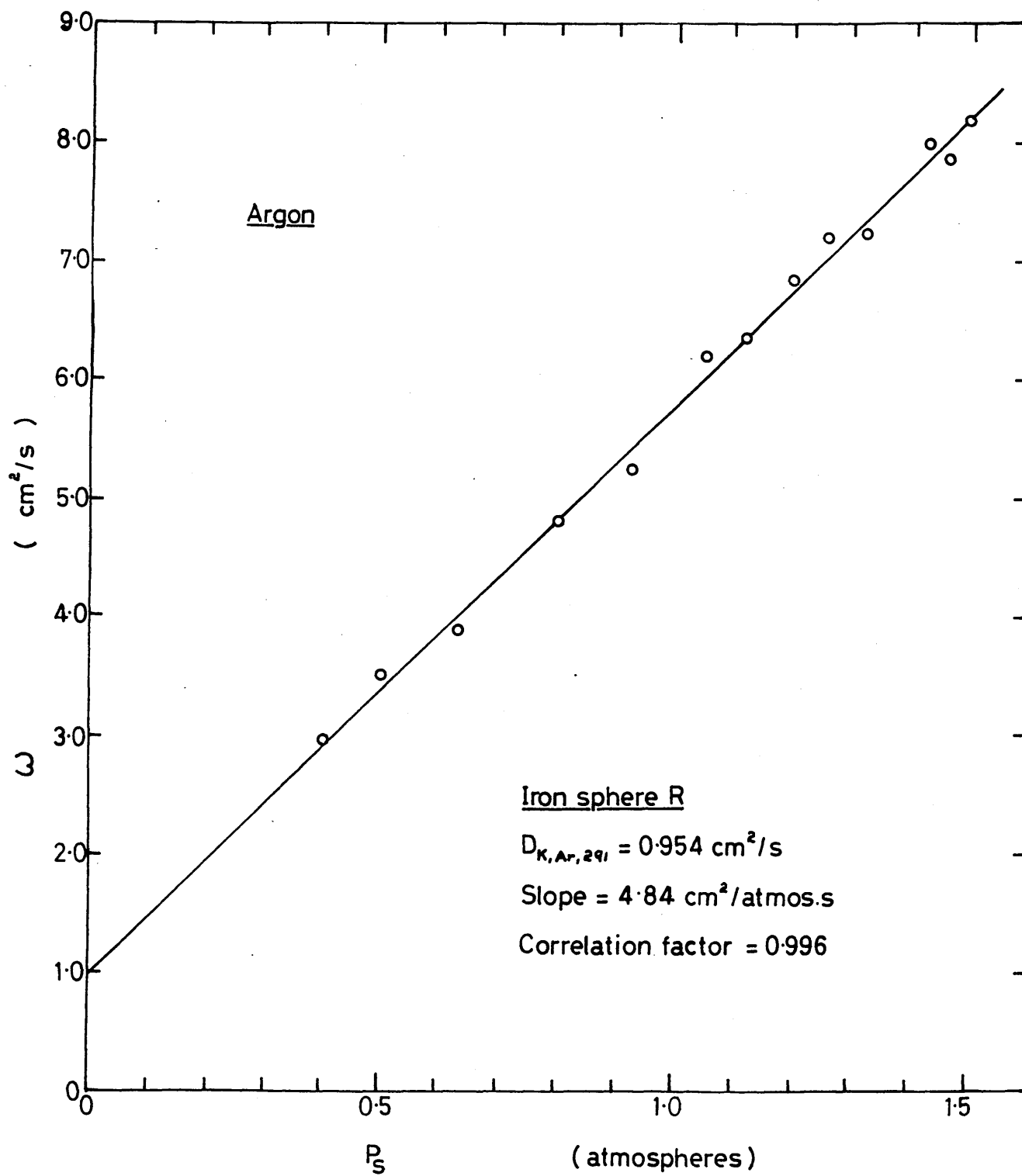Correlation factor $= 0.9937$

TABLE No.5.26   Permeability Data for Helium through
                 Iron reduced sphere T at 291 K

Barometric pressure = 1.010 (atm)
Shape factor   = 12.53 (cm)

No Reading	$\Delta P/$ (atm)	$P_{orifice}/$ (atm)	$P_i/$ (atm)	$P_s/$ (atm)	$\dot{n}/$ (μmol.s^{-1})	$\omega/$ (cm^2.s^{-1})
1.	0.0401	1.087	1.107	1.120	216.3	10.28
2.	0.0367	1.156	1.167	1.185	220.5	11.45
3.	0.0317	1.214	1.220	1.236	189.6	11.40
4.	0.0351	1.278	1.287	1.305	217.3	11.80
5.	0.0418	1.371	1.357	1.378	265.4	12.10
6.	0.0401	0.854	0.872	0.893	191.9	9.12
7.	0.0434	0.741	0.769	0.791	191.0	8.39
8.	0.0367	0.671	0.669	0.687	150.0	7.79
9.	0.0451	0.760	0.788	0.511	146.7	6.20

$D_{He,K}$ = 2.97 (cm^2.s^{-1})

Slope = $^{Bo}/_{\mu He}$ = 6.79 (cm^2.atm^{-1}.s^{-1})

Correlation factor = 0.9937

Figure 5·27 : The permeability of helium through sphere T at 898 K.

$S = 12·53$ cm ; $\gamma = 60·26\%$

Helium

Iron sphere T

$D_{K,He,898} = 5·14$ cm^2/s

Slope $= 3·020$ cm^2/atmos. s

Correlation factor $= 0·967$

ω (cm^2/s)

P_s (atmospheres)
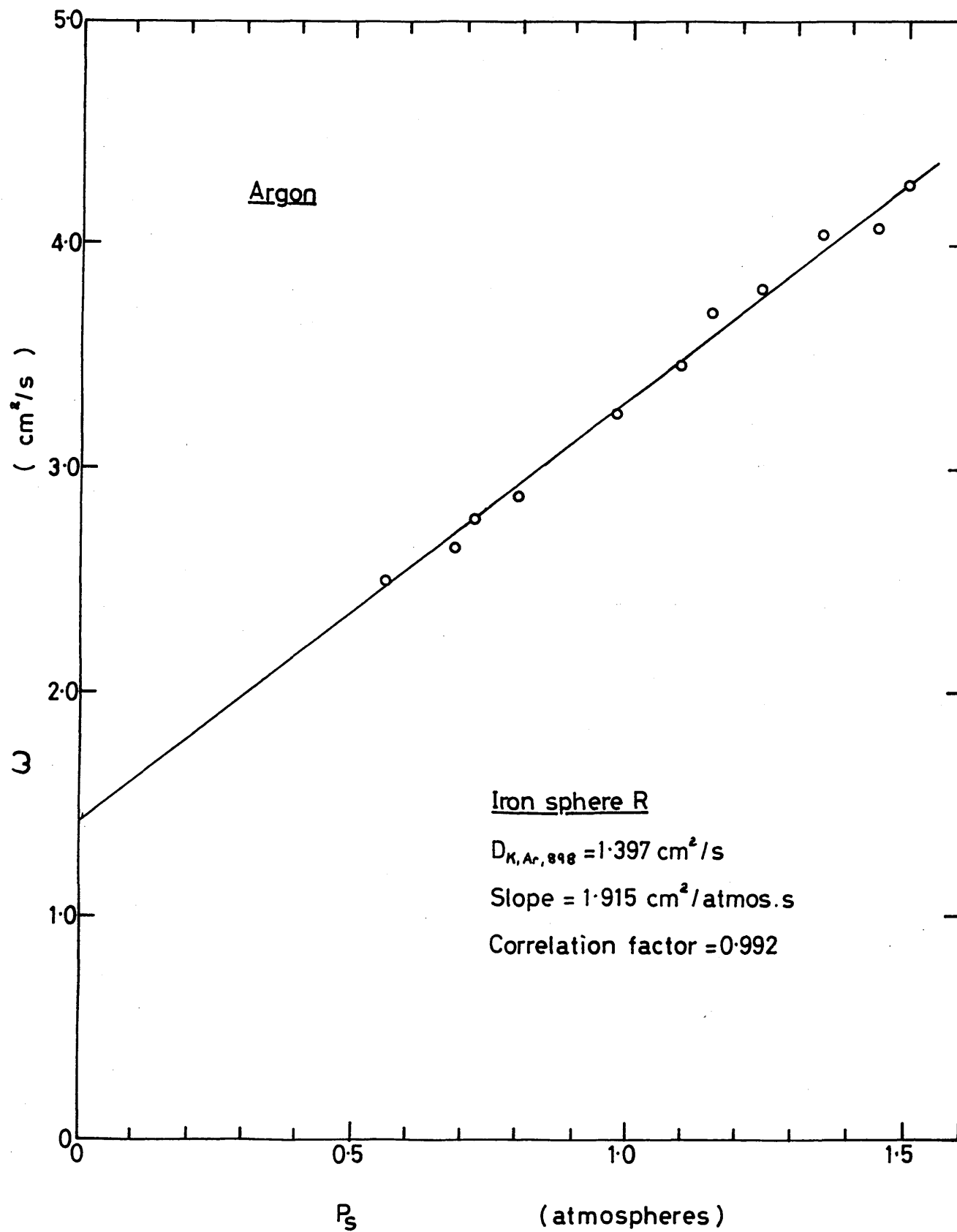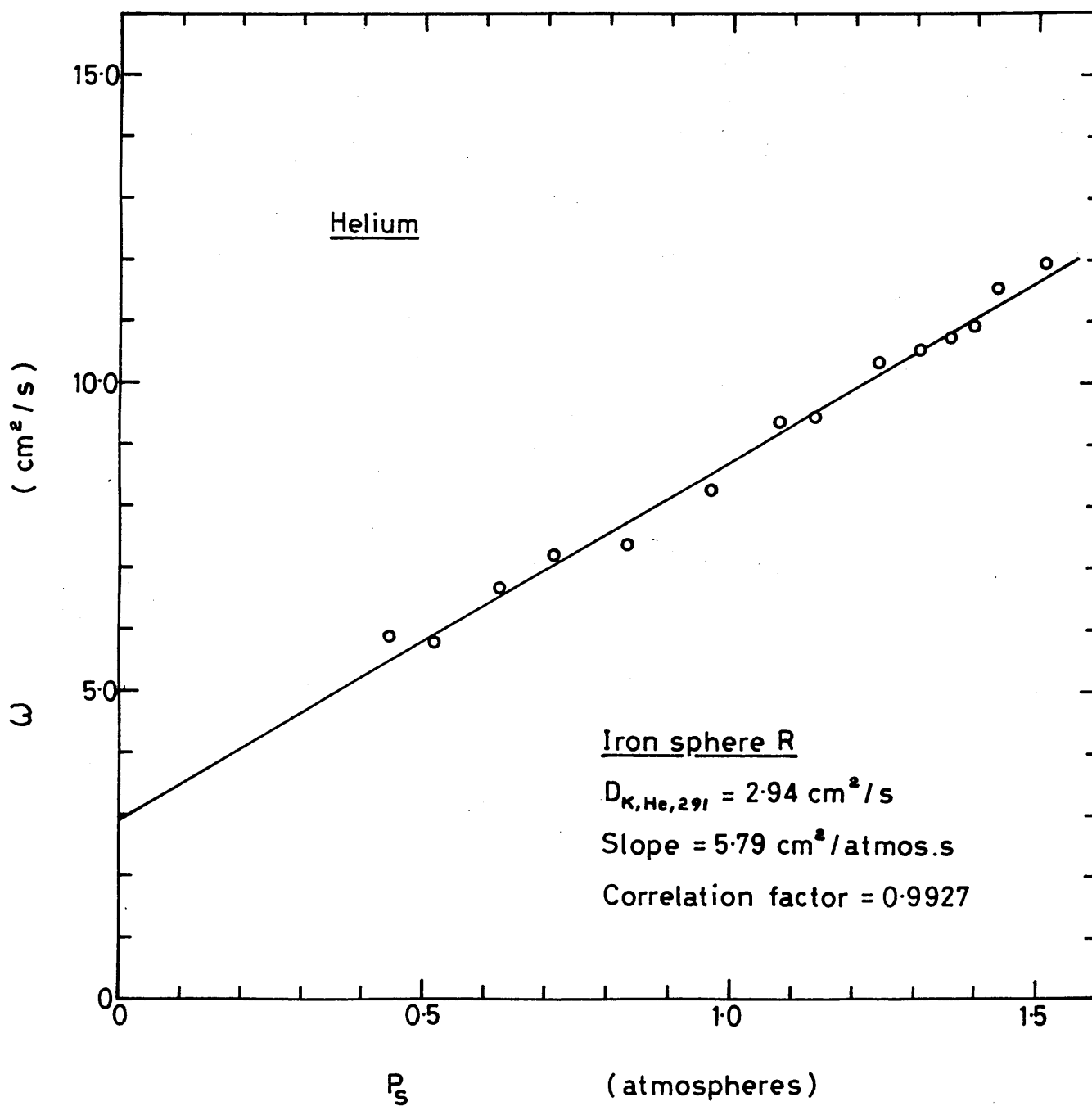
TABLE No. 5.27.   Permeability Data for Helium through
                   Iron reduced sphere T at 898 K

Barometric pressure = 1.005 (atm)
Shape factor   = 12.53 (cm)

No Reading	$\Delta p/$ (atm)	$p_{orifice}/$ (atm)	$p_i/$ (atm)	$p_s/$ (atm)	$\dot{n}/$ (μmol.s^{-1})	$\omega/$ (cm^2.s^{-1})
1.	0.1102	1.011	1.029	1.084	167.5	8.79
2.	0.1102	1.051	1.094	1.150	159.3	8.50
3.	0.1270	1.154	1.188	1.252	195.0	8.89
4.	0.1470	1.214	1.238	1.312	230.0	9.05
5.	0.1670	1.263	1.292	1.375	262.5	9.09
6.	0.2038	1.323	1.355	1.457	325.0	9.23
7.	0.1236	1.429	1.449	1.571	200.0	9.36
8.	0.1871	0.816	0.864	0.957	257.5	7.96
9.	0.1571	0.698	0.747	0.825	207.5	7.67
10.	0.1821	0.535	0.600	0.691	220.0	6.99
11.	0.1738	0.414	0.486	0.513	197.5	6.57
12.	0.1069	1.141	1.121	1.195	168.0	9.09

$D_{He,K}$ = 5.14 (cm^2.s^{-1})

Slope = B_o/μ_{He} = 3.020 (cm.atm^{-1}.s^{-1})

Correlation factor = 0.967

Figure 5·28 :   The permeability of argon through sphere V at 291 K.

$$S = 12·73 \text{ cm} ; \, \gamma = 60·04\%$$

Argon

Iron sphere V

$D_{K,Ar,291} = 0·81 \text{ cm}^2/\text{s}$

Slope = 4·45 cm²/atmos.s

Correlation factor = 0·992

ω

(cm²/s)

P_s (atmospheres)

TABLE No.5.28   Permeability Data for Argon through Iron reduced sphere V at 291 K

Barometric pressure = 1.010 (atm)
Shape factor   = 12.73 (cm)

No Reading	$p/$ (atm)	$p_{orifice}/$ (atm)	$p_i/$ (atm)	$p_s/$ (atm)	$\dot{n}/$ (μmol.s^{-1})	$\omega /$ (cm^2.s^{-1})
1.	0.0240	1.013	1.023	1.040	69.0	5.39
2.	0.0340	1.169	1.181	1.200	111.5	6.15
3.	0.0210	1.249	1.257	1.270	75.0	6.69
4.	0.0240	1.299	1.319	1.330	85.5	6.68
5.	0.0240	1.357	1.367	1.380	87.5	6.83
6.	0.0240	1.415	1.429	1.440	95.0	7.42
7.	0.0240	1.096	1.096	1.110	68.0	5.31
8.	0.0240	0.847	0.858	0.870	61.8	4.83
9.	0.0240	0.792	0.773	0.780	57.0	4.45
10.	0.0340	0.680	0.694	0.710	72.0	3.97
11.	0.0340	0.604	0.611	0.630	69.0	3.80
12.	0.0310	0.450	0.467	0.480	50.0	3.02
13.	0.0310	0.339	0.371	0.380	38.0	2.29

$D_{Ar,K}$ = 0.81 (cm^2.s^{-1})

Slope $= B_o/\mu_{Ar}$ = 4.45 (cm^2.s^{-1}.atm^{-1})

Correlation factor = 0.992

Figure 5·29 : The permeability of argon through sphere V at 898 K.

S = 12·73 cm ; δ = 60·04 %

Argon

Iron sphere V

$D_{K,Ar,898}$ = 1·25 cm²/s

Slope = 1·603 cm²/atmos.s

Correlation factor = 0·992

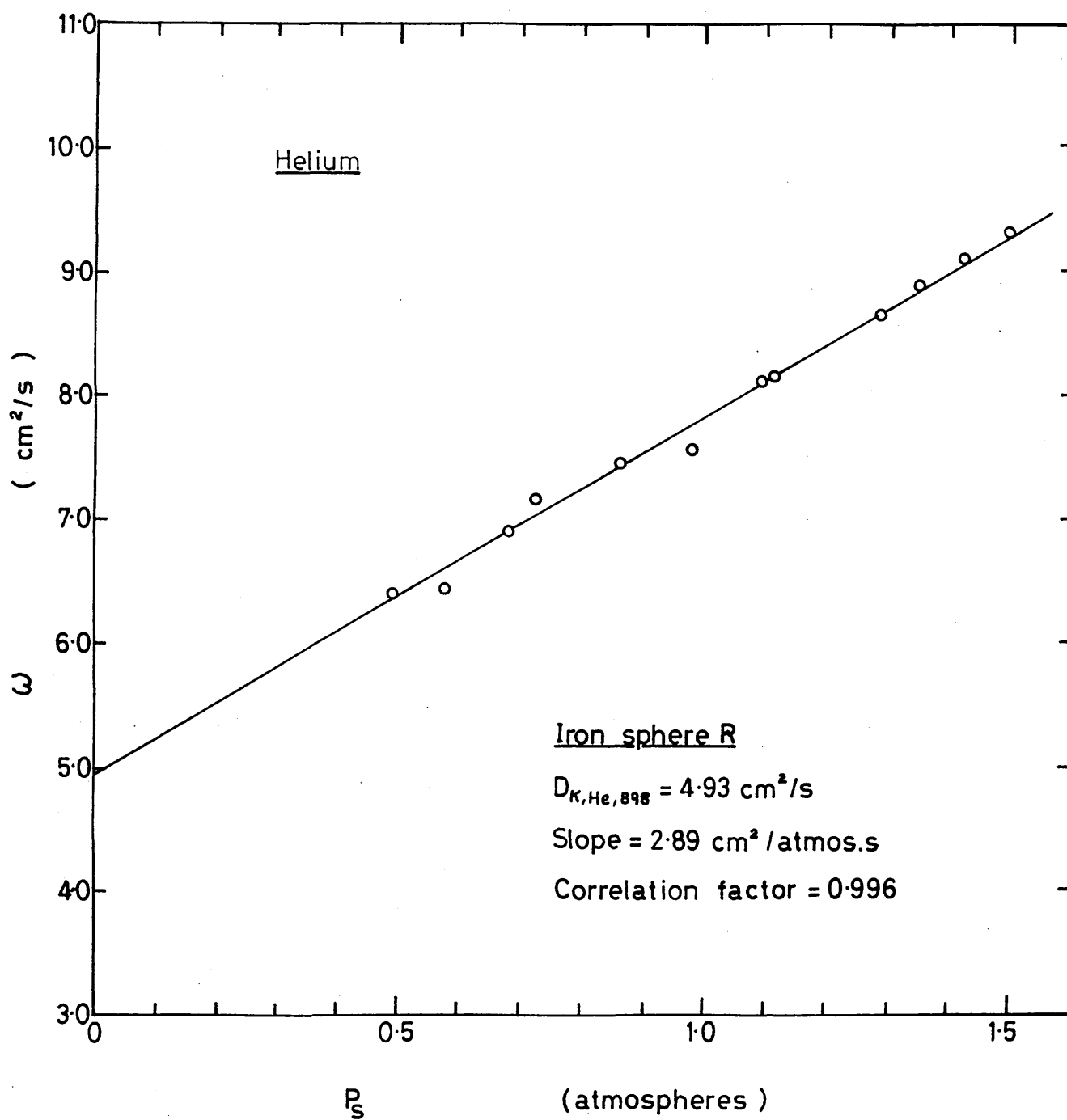P_s (atmospheres)
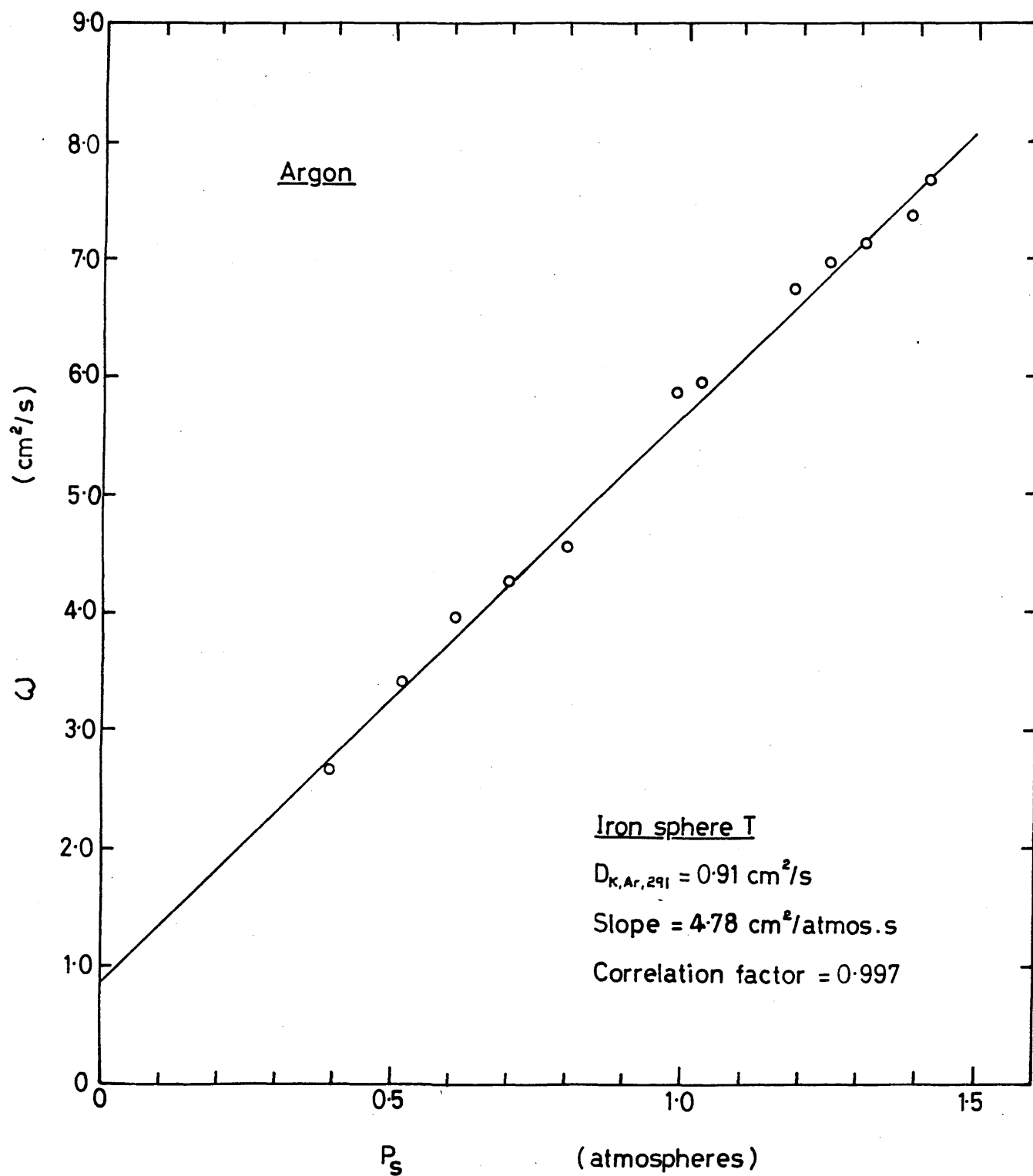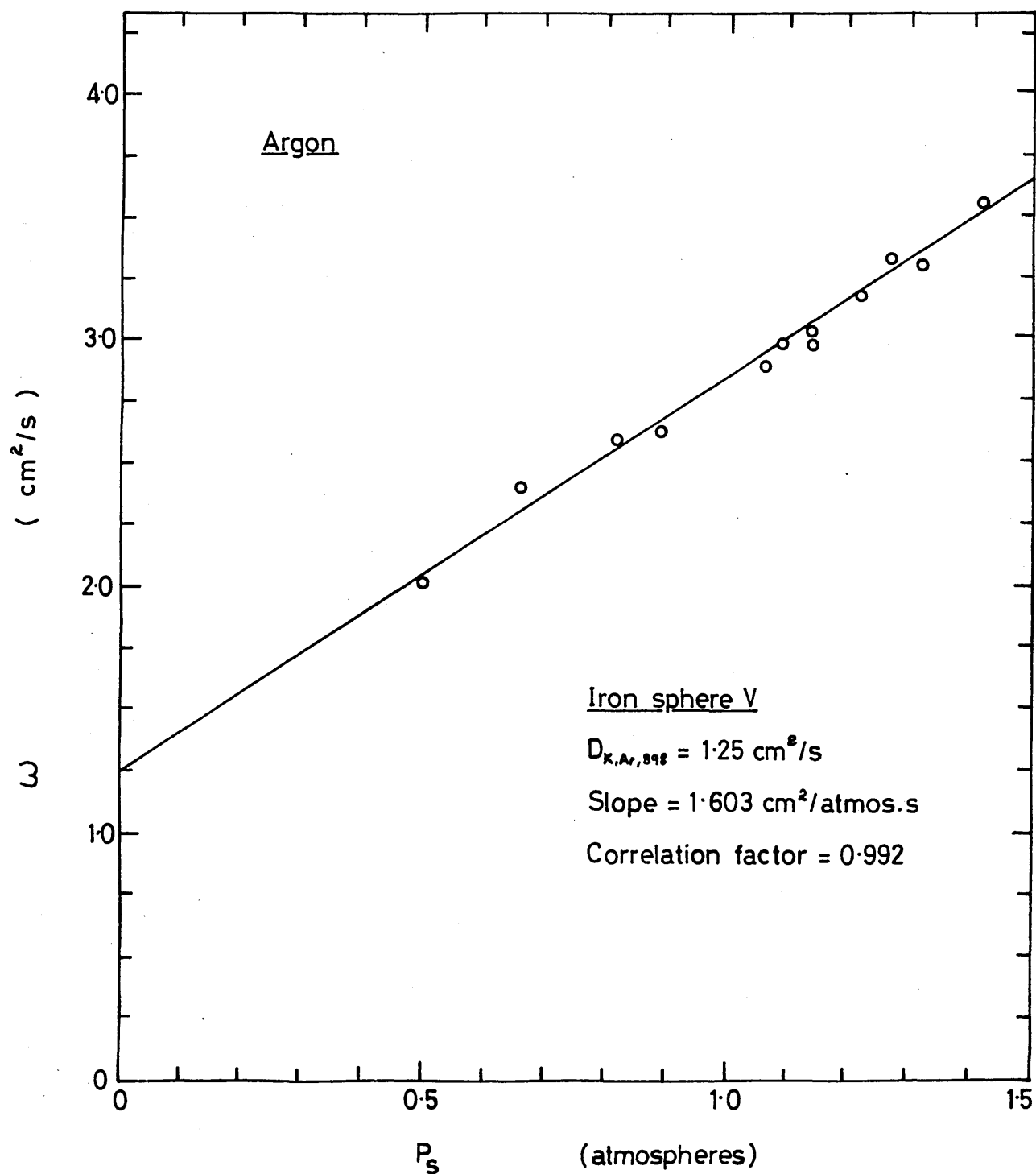
TABLE No.5.29   Permeability Data for Argon through
                  Iron reduced sphere V at 898 K

Barometric pressure = 1.008 (atm)
Shape factor   = 12.73 (cm)

No Reading	$\Delta p/$ (atm)	$P_{orifice}/$ (atm)	$p_i/$ (atm)	$p_s/$ (atm)	$\dot{n}/$ (μmol.s^{-1})	$\omega/$ (cm^2.s^{-1})
1.	0.127	1.014	1.021	1.090	65.5	2.98
2.	0.127	1.064	1.072	1.140	65.5	2.98
3.	0.140	1.070	1.078	1.140	73.0	3.01
4.	0.130	1.146	1.155	1.220	71.5	3.18
5.	0.103	1.210	1.221	1.270	59.0	2.32
6.	0.117	1.248	1.260	1.320	66.5	3.29
7.	0.067	1.371	1.385	1.420	41.0	3.54
8.	0.070	1.407	1.422	1.460	44.5	3.68
9.	0.080	1.465	1.482	1.520	52.0	3.76
10.	0.087	1.010	1.018	1.060	43.5	2.89
11.	0.130	0.829	0.827	0.890	59.0	2.62
12.	0.154	0.744	0.747	0.820	69.0	2.59
13.	0.170	0.559	0.573	0.660	70.0	2.38
14.	0.144	0.404	0.426	0.500	52.0	2.09

$D_{Ar,K}$ = 1.250 (cm^2.s^{-1})

Slope = B_o/μ_{Ar} = 1.603 (cm^2.s^{-1}.atm^{-1})

Correlation factor = 0.992

Figure 5·30 : The permeability of helium through sphere V at 898K.

$$S = 12.73 \text{ cm} ; \; \forall = 60.04\%$$

Helium

Iron sphere V

$D_{K,He,898} = 5.28 \text{ cm}^2/\text{s}$

Slope = 2·47 cm^2/atmos.s

Correlation factor = 0·987

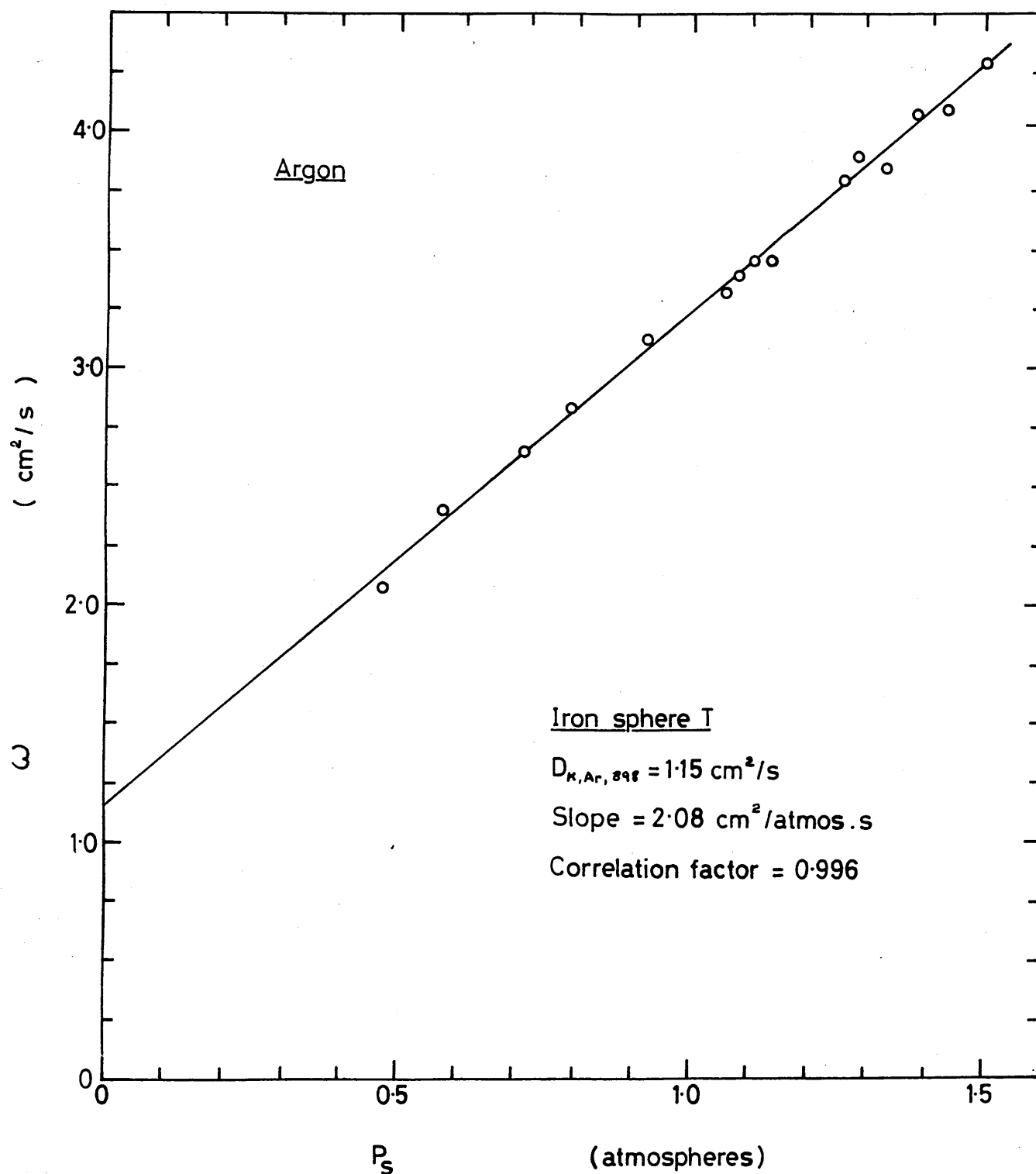ω (cm /s)

P_S (atmospheres)
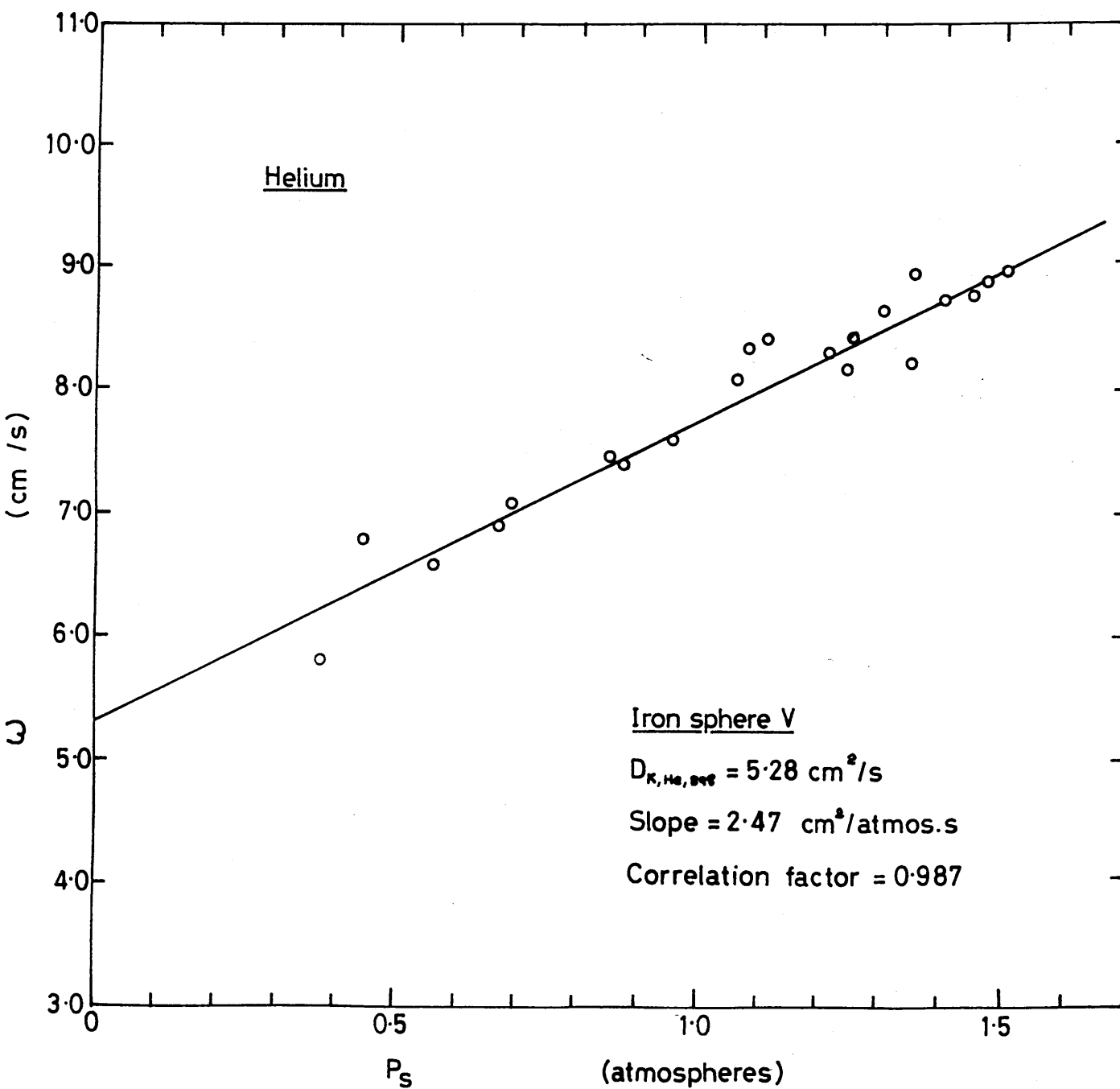
TABLE No.5.30   Permeability Data for Helium through
Iron reduced sphere V at 898 K

Barometric pressure = 0.994 (atm)
Shape factor   = 12.73 (cm)

No Reading	$\Delta P/$ (atm)	$P_{orifice}/$(atm)	$p_i/$ (atm)	$p_s/$ (atm)	$\dot{n}/$ (μmol/s)	$\omega/$ (cm^2.s^{-1})
1.	0.0902	0.985	1.0140	1.075	130.0	8.34
2.	0.0902	1.032	1.0600	1.105	137.5	8.82
3.	0.1236	1.076	1.1020	1.163	180.0	8.43
4.	0.1457	1.119	1.1770	1.217	207.5	8.26
5.	0.1069	1.167	1.1910	1.244	157.5	8.42
6.	0.1303	1.219	1.2410	1.306	195.0	8.66
7.	0.1337	1.276	1.2940	1.360	207.5	8.98
8.	0.1457	1.309	1.3280	1.399	217.5	8.76
9.	0.1537	1.350	1.3680	1.475	233.5	8.80
10.	0.1303	1.378	1.3950	1.460	202.5	8.99
11.	0.1571	0.830	0.8770	0.955	207.5	7.67
12.	0.1607	0.737	0.7860	0.866	205.0	7.40
13.	0.1607	0.696	0.7460	0.826	205.0	7.40
14.	0.1570	0.538	0.5920	0.670	192.5	7.09
15.	0.1471	0.456	0.5720	0.585	175.0	6.88
16.	0.1404	0.313	0.3720	0.762	165.0	6.80
17.	0.1404	0.244	0.3050	0.375	140.0	5.77

$D_{He,K}$ = 5.28 (cm^2.s^{-1})

Slope = B_0/μ_{He} = 2.47 (cm^2.s^{-1}.atm^{-1})

Correlation factor = 0.987

Figure 5·31 : The permeability of argon through sphere X at 291 K.

S =10·63 cm ; ४ =58·94%

Argon

Iron sphere X

$D_{K,Ar,292} = 0·886$ cm^2/s

Slope = 4·26 cm^2/atmos.s

Correlation factor = 0·986
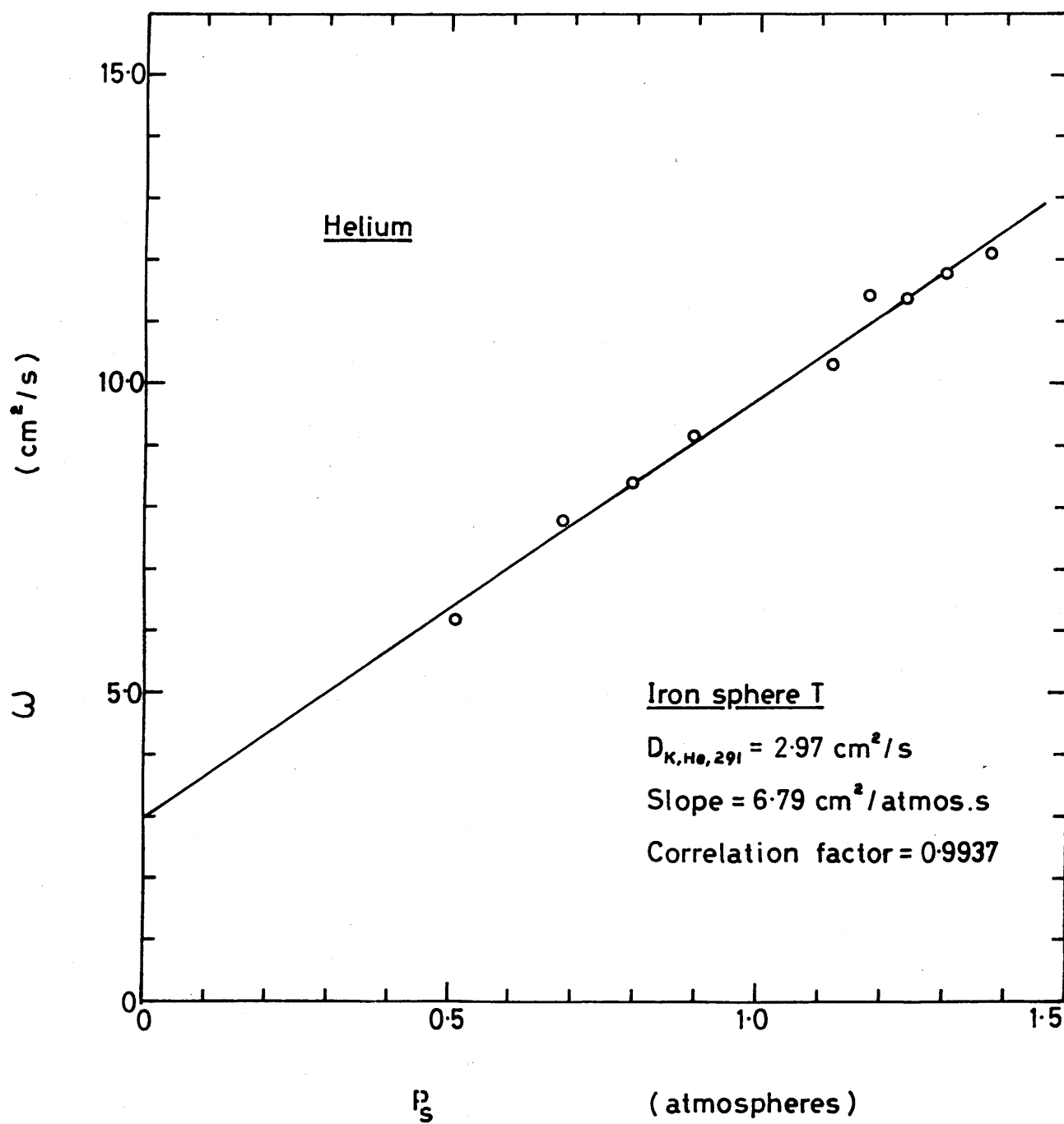
245
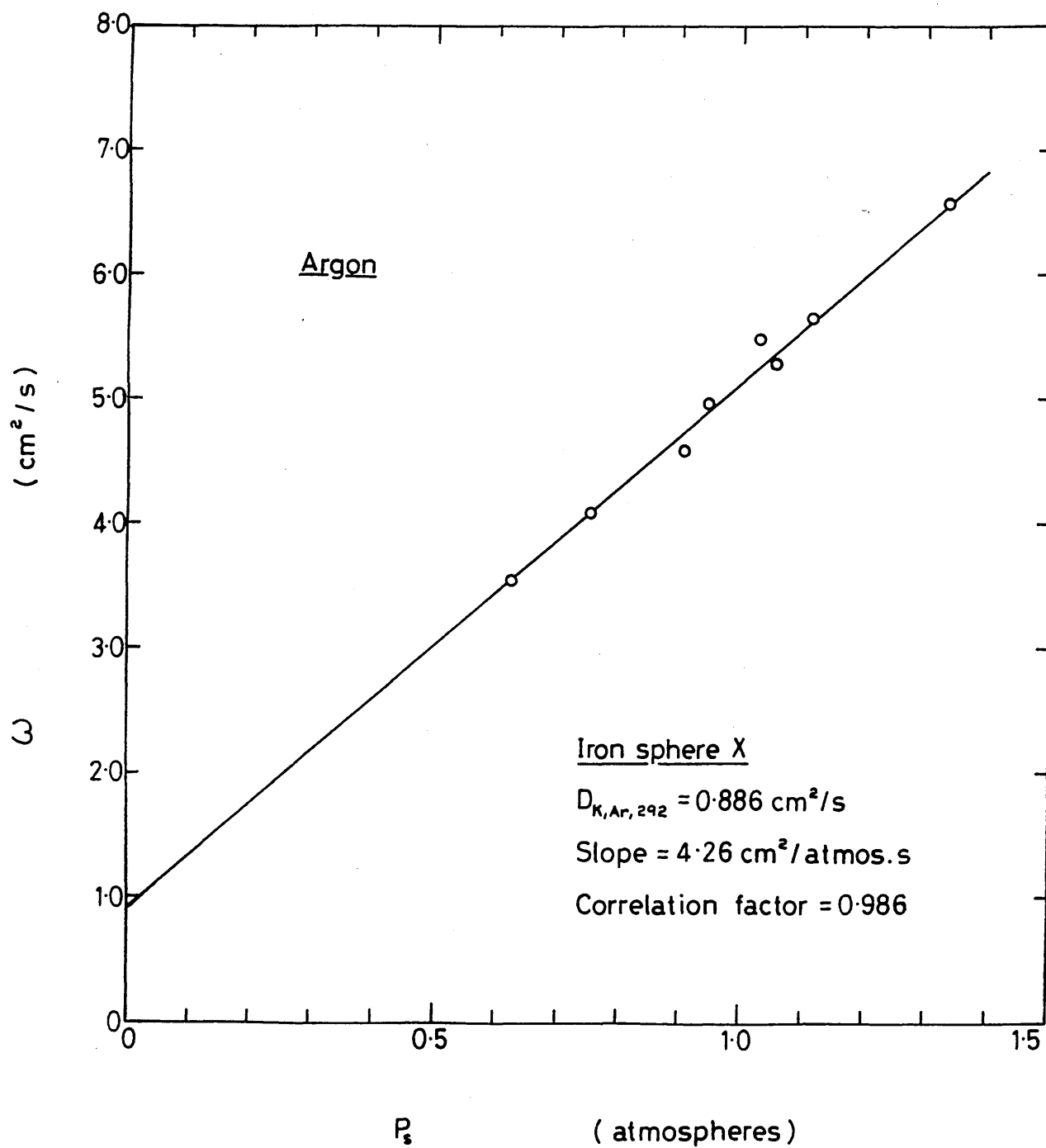
TABLE No.5.31   Permeability Data for Argon through
                 Iron reduced sphere X at 291 K

Barometric pressure = 1.01 (atm)
Shape factor   = 10.63 (cm)

No Reading	$\Delta p/$ (atm)	$p_i/$ (atm)	$p_s/$ (atm)	$\dot{n}/$ (μmol.s^{-1})	$\omega/$ (cm^2.s^{-1})
1.	0.0401	1.3190	1.340	117.20	6.59
2.	0.0326	1.1100	1.128	81.40	5.63
3.	0.0326	1.0370	1.055	76.73	5.30
4.	0.0233	1.0150	1.028	56.96	5.50
5.	0.0250	0.9280	0.940	55.37	4.98
6.	0.0401	0.8820	0.902	81.48	4.57
7.	0.0367	0.7389	0.752	66.45	4.07
8.	0.0367	0.5950	0.628	57.75	3.54

$D_{K,Ar}$ = 0.886 (cm^2.s^{-1})

Slope = $^{Bo}/\mu_{Ar}$ = 4.260 (cm^2.s^{-1}.atm^{-1})

Correlation factor = 0.986

Figure 5·32 : The permeability of argon through sphere X at 898K.

$S = 10·63\,cm$; $\gamma = 58·94\%$

Argon

ω (cm^2/s)

Iron sphere X

$D_{K,Ar,898} = 1·51\,cm^2/s$

Slope $= 2·39\,cm^2/atmos.s$

Correlation factor $= 0·958$
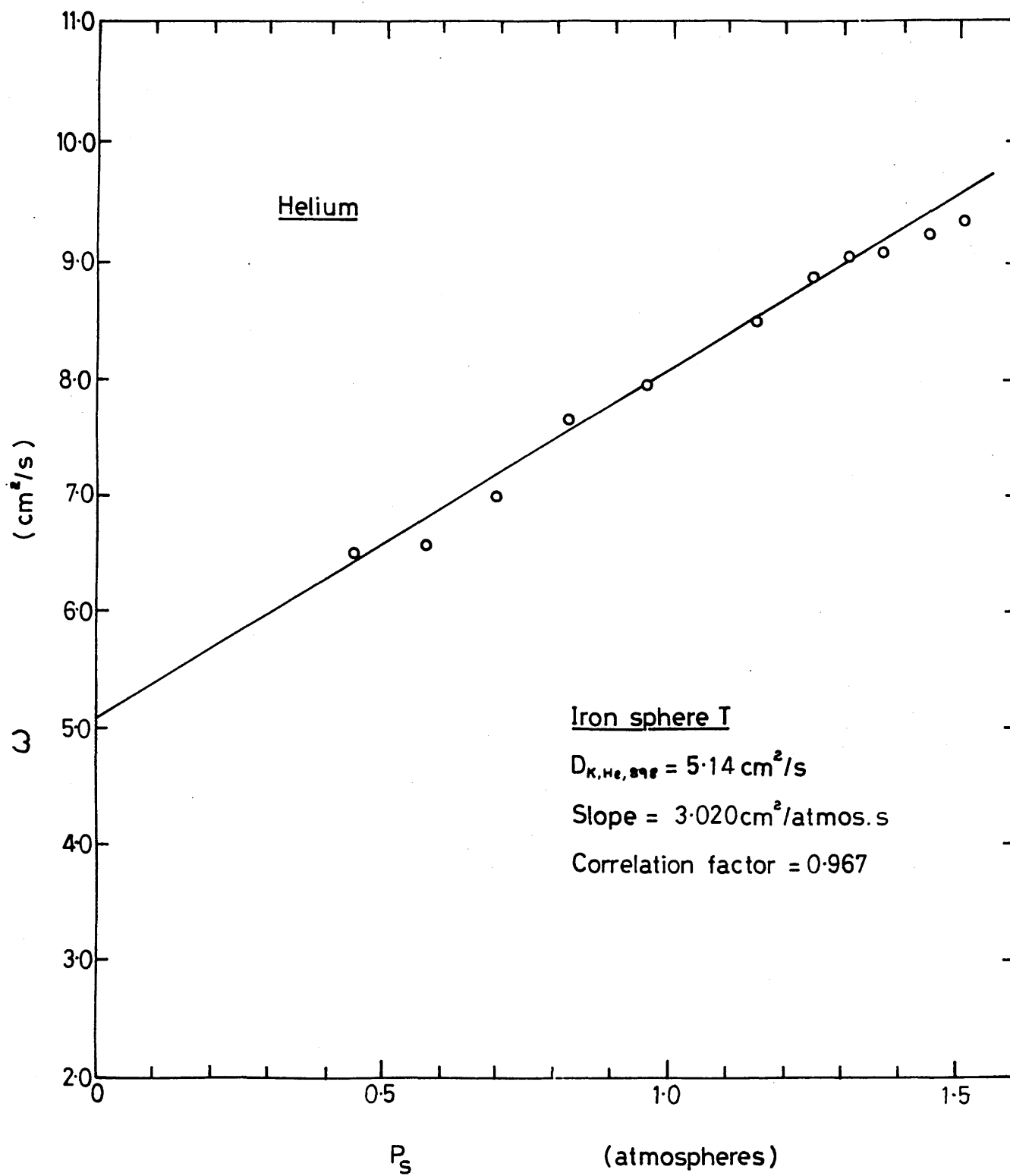
P_s (atmospheres)

TABLE No.5.32   Permeability Data for Argon through
                  Iron reduced sphere X at 898 K

Barometric pressure = 1.01 (atm)
Shape factor   = 10.63 (cm)

No Reading	$\Delta p/$ (atm)	$p_i /$ (atm)	$p_s/$ (atm)	$\dot{n}/$ ($\mu mol.s^{-1}$)	$\omega /$ ($cm^2.s^{-1}$)
1.	0.1437	1.278	1.349	96.00	4.67
2.	0.1870	1.036	1.129	107.60	3.98
3.	0.1737	1.041	1.127	107.60	4.29
4.	0.1737	1.034	1.120	110.70	4.42
5.	0.1437	0.845	0.916	79.11	3.81
6.	0.1570	0.790	0.868	81.48	3.59
7.	0.1738	0.687	0.774	81.48	3.25

$D_{K,Ar} = 1.51$ ($cm^2.s^{-1}$)

Slope $= {}^{Bo}/\mu_{Ar} = 2.39$ ($cm^2.s^{-1}.atm^{-1}$)

Correlation factor = 0.958

Figure 5·33 : The permeability of argon through sphere D at 898 K.

$S = 12·53$ cm ; $\gamma = 58·12$ %

Argon

Iron sphere D

$D_{K,Ar,898} = 1·36$ cm^2/s

Slope = 2·28 cm^2/atmos.s

Correlation factor = 0·9944

$\frac{P}{S}$ (atmospheres)
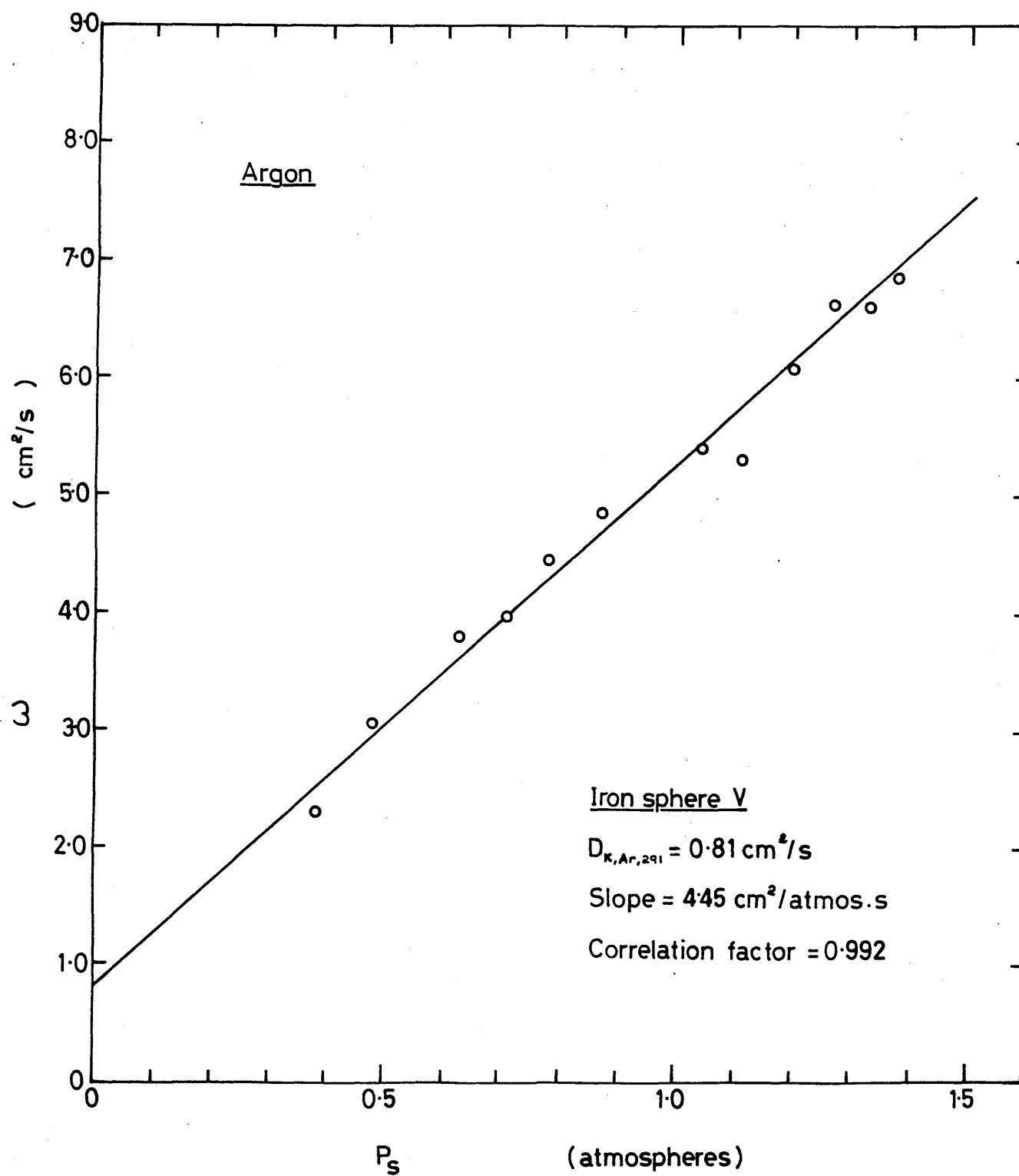
ω

(cm^2/s)

249

TABLE No.5.33.   **Permeability Data for Argon through
Iron reduced sphere D at 898 K**

Barometric pressure = 1.023 (atm)
Shape factor   = 12.53 (cm)

No Reading	$\Delta p/$ (atm)	$p_{orifice}/$ (atm)	$p_i/$ (atm)	$p_s/$ (atm)	$\dot{n}/$ (μmol.s^{-1})	$\omega/$ (cm^2.s^{-1})
1.	0.1213	1.028	1.053	1.113	82.5	3.99
2.	0.1549	1.054	1.090	1.167	105.5	4.00
3.	0.0970	1.174	1.198	1.246	69.0	4.18
4.	0.1310	1.237	1.262	1.327	96.0	4.31
5.	0.1347	1.376	1.400	1.467	107.5	4.69
6.	0.1078	0.874	0.922	0.976	68.0	3.71
7.	0.1280	0.815	0.857	0.915	74.6	3.43
8.	0.1250	0.663	0.704	0.767	66.3	3.11
9.	0.1347	0.475	0.517	0.585	60.0	2.62

$D_{K,Ar}$ = 1.36 (cm^2.s^{-1})

Slope = 2.28 (cm^2.s^{-1}.atm^{-1}) = $B_\circ/\mu_{Ar}$

Correlation factor = 0.9944

Figure 5·34 : The permeability of nitrogen through sphere A1 at 291 K
after sintering for 5 hours at 1373 K.

$S = 12·25$ cm ; $\delta = 57·53$ %

Nitrogen

Iron sphere A1

$D_{K,N_2,291} = 1·592$ cm^2/ s

Slope $= 8·251$ cm^2/ atmos.s

Correlation factor $= 0·995$

P_S (atmospheres)

TABLE No.5.34   Permeability Data for Nitrogen through
                       Sintered Iron sphere Al at 291 K

Barometric pressure = 0.967 (atm)
Shape factor   = 12.25 (cm)

No Reading	$\Delta P/$ (atm)	$P_{orifice}/$ (atm)	$P_i/$ (atm)	$P_s/$ (atm)	$\dot{n}/$ ($\mu mol.s^{-1}$)	$\omega/$ ($cm^2.s^{-1}$)
1.	0.0167	1.028	1.036	1.045	88.15	10.29
2.	0.0200	1.110	1.113	1.123	111.90	10.91
3.	0.0150	1.251	1.272	1.280	96.20	12.50
4.	0.0167	1.358	1.369	1.378	107.90	12.60
5.	0.0150	1.438	1.442	1.450	107.00	13.90
6.	0.0150	0.826	0.834	0.842	64.80	8.42
7.	0.0167	0.559	0.602	0.611	54.40	6.35
8.	0.0133	0.442	0.478	0.485	39.20	5.75
9.	0.0167	0.290	0.316	0.325	38.40	4.48

D_{K,N_2} = 1.592 ($cm^2.s^{-1}$)

Slope = B_o/μ_{N_2} = 8.251 ($cm^2.s^{-1}.atm^{-1}$)

Correlation factor = 0.995

Figure 5·35 : The permeability of argon through sphere A1 at 291K after sintering for 5 hours at 1373 K.

$S = 12·25\,cm$; $\delta = 57·53\,\%$

Argon

Iron sphere A1

$D_{K,Ar,291} = 1·258\ cm^2/s$

Slope $= 7·41\ cm^2/atmos.s$

Correlation factor $= 0·995$

P_S (atmospheres)

TABLE No.5.35   Permeability Data for Argon through
                     Sintered Iron sphere A1 at 291 K

Barometric pressure = 0.987 (atm)
Shape factor   = 12.25 (cm)

No Reading	$\Delta p/$ (atm)	$P_{orifice}/$ (atm)	$p_i/$ (atm)	$p_s/$ (atm)	$\dot{n}/$ (μmol.s^{-1})	$\omega /$ (cm^2.s^{-1})
1.	0.0167	0.989	0.997	1.005	76.5	8.20
2.	0.0134	1.184	1.187	1.194	69.5	10.14
3.	0.0167	1.329	1.332	1.341	93.5	10.90
4.	0.0134	0.812	0.809	0.816	53.5	7.80
5.	0.0234	0.619	0.639	0.650	70.5	5.87
6.	0.0234	0.454	0.472	0.483	55.0	4.62

$D_{K,Ar}$ = 1.258 (cm^2.s^{-1})

Slope = B_o/μ_{Ar} = 7.41 (cm^2.s^{-1}.atm^{-1})

Correlation factor = 0.9948

Figure 5·36 : The permeability of argon through sphere A1 at 898 K

after sintering for 5 hours at 1373 K.

$S = 12·25\,cm$; $\gamma = 57·53\,\%$

Argon

Iron sphere A1

$D_{K,Ar,898} = 2·22\ cm^2/s$

Slope = $3·54\ cm^2/atmos.s$

Correlation factor = $0·993$

$\frac{P}{S}$ (atmospheres)

TABLE No.5.36   Permeability Data for Argon through
                      Sintered Iron reduced sphere Al at 898 K

Barometric pressure =   0.982 (atm)
Shape factor   =   12.25 (cm)

No Reading	$\Delta P/$ (atm)	$P_{orifice}/$ (atm)	$P_i/$ (atm)	$P_s/$ (atm)	$\dot{n}/$ (μmol.s^{-1})	$\omega/$ (cm^2.s^{-1})
1.	0.0969	0.987	1.008	1.046	96.65	6.00
2.	0.0467	1.102	1.105	1.128	48.10	6.20
3.	0.0584	1.185	1.195	1.224	63.30	6.52
4.	0.0836	1.296	1.298	1.370	101.70	7.32
5.	0.0935	1.383	1.393	1.440	113.5	7.30
6.	0.0969	0.827	0.837	0.886	84.10	5.22
7.	0.1036	0.697	0.713	0.765	87.00	5.05
8.	0.0935	0.595	0.603	0.650	74.30	4.78
9.	0.1069	0.399	0.421	0.475	68.20	3.84

$D_{K,Ar}$ = 2.22 (cm^2.s^{-1})

Slope = B_o/μ_{Ar} = 3.54 (cm^2.s^{-1}atm^{-1})

Correlation factor = 0.993

Figure 5·37 : The permeability of nitrogen through sphere B1 at 291 K after sintering for 5 hours at 1373 K.

$S = 11·462$ cm ; $\gamma = 57·08$ %

Nitrogen

Iron sphere B1

$D_{K,N_2,291} = 1·63$ cm^2/s

Slope = 9·159 cm^2/atmos.s

Correlation factor = 0·995

P_s (atmospheres)
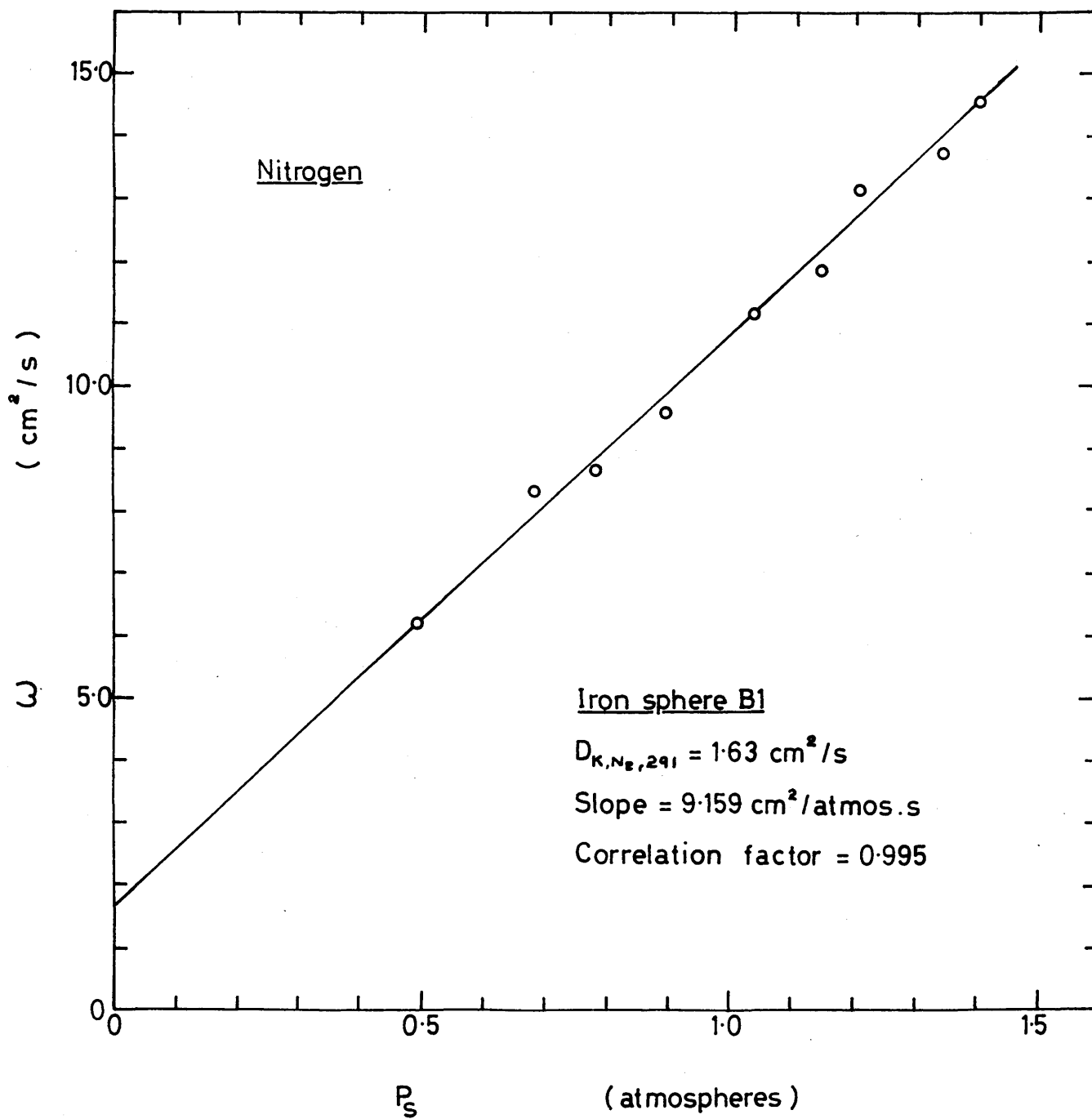
TABLE No.5.37   Permeability Data for Nitrogen through
                 sintered Iron sphere Bl at 291 K

Barometric pressure = 0.999 (atm)
Shape factor   = 11.462 (cm)

No Reading	$\Delta p/$ (atm)	$p_{orifice}/$ (atm)	$p_i/$ (atm)	$p_s/$ (atm)	$\dot{n}/$ ($\mu mol.s^{-1}$)	$\omega/$ ($cm^2.s^{-1}$)
1.	0.0254	1.008	1.019	1.031	136.0	11.19
2.	0.0183	1.129	1.136	1.146	103.7	11.85
3.	0.0234	1.185	1.196	1.207	146.8	13.12
4.	0.0134	1.326	1.329	1.336	87.8	13.70
5.	0.0150	0.854	0.885	0.892	68.5	9.56
6.	0.0200	0.763	0.780	0.790	82.8	8.65
7.	0.0234	0.660	0.679	0.690	93.0	8.30
8.	0.0234	0.471	0.491	0.503	69.0	6.17

$D_{K,N_2} = 1.63$ $(cm^2.s^{-1})$

Slope $= B_o/\mu_{N_2} = 9.159$ $(cm^2.s^{-1}.atm^{-1})$

Correlation factor = 0.9945

Figure 5·38 : The permeability of argon through sphere B1 at 291 K
after sintering for 5 hours at 1373 K.

$S = 11·462$ cm ; $\delta = 57·08\%$

Argon

Iron sphere B1

$D_{K, Ar, 291} = 1·189$ cm^2/ s

Slope = 8·18 cm^2/atmos.s

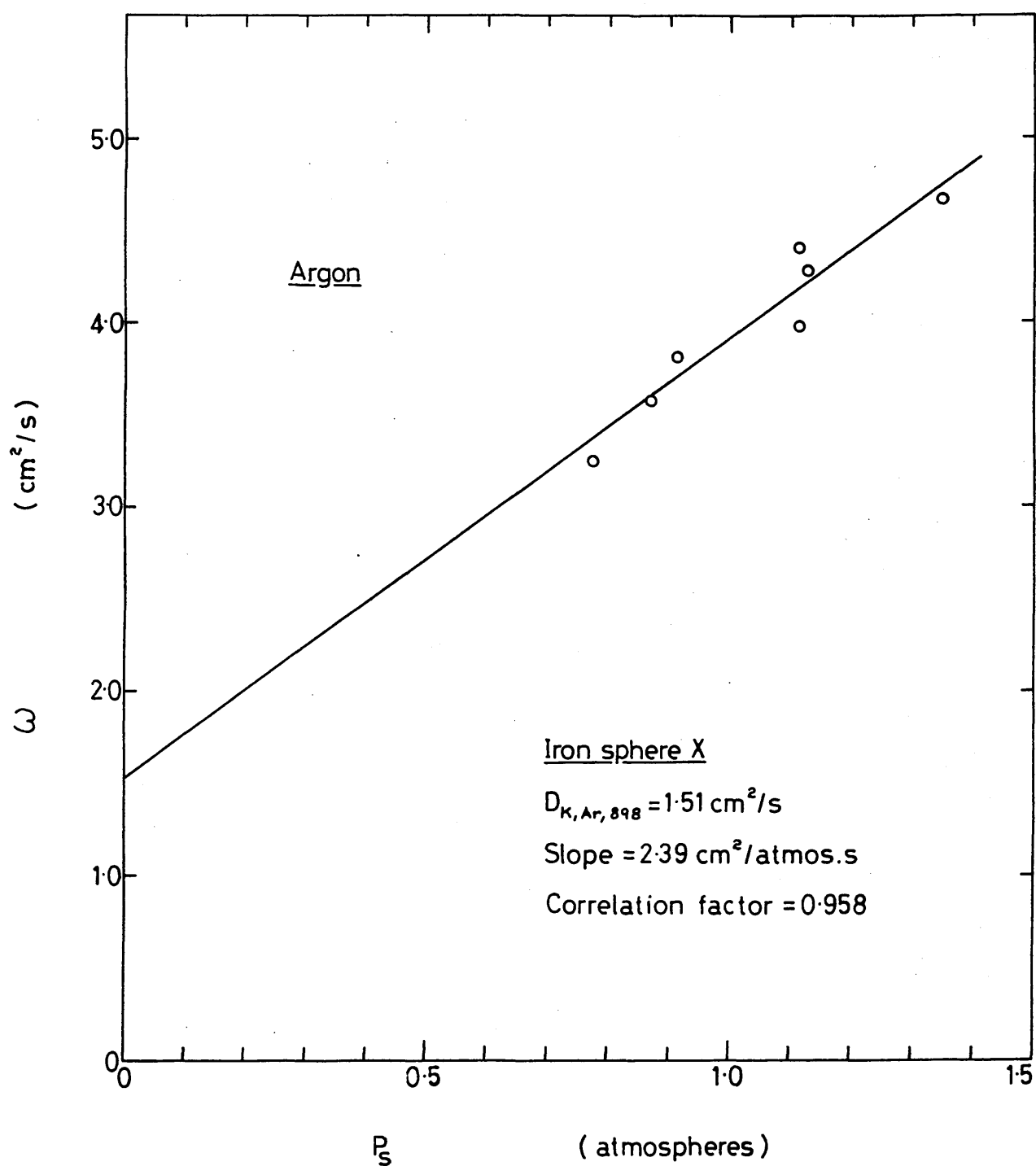Correlation factor = 0·990
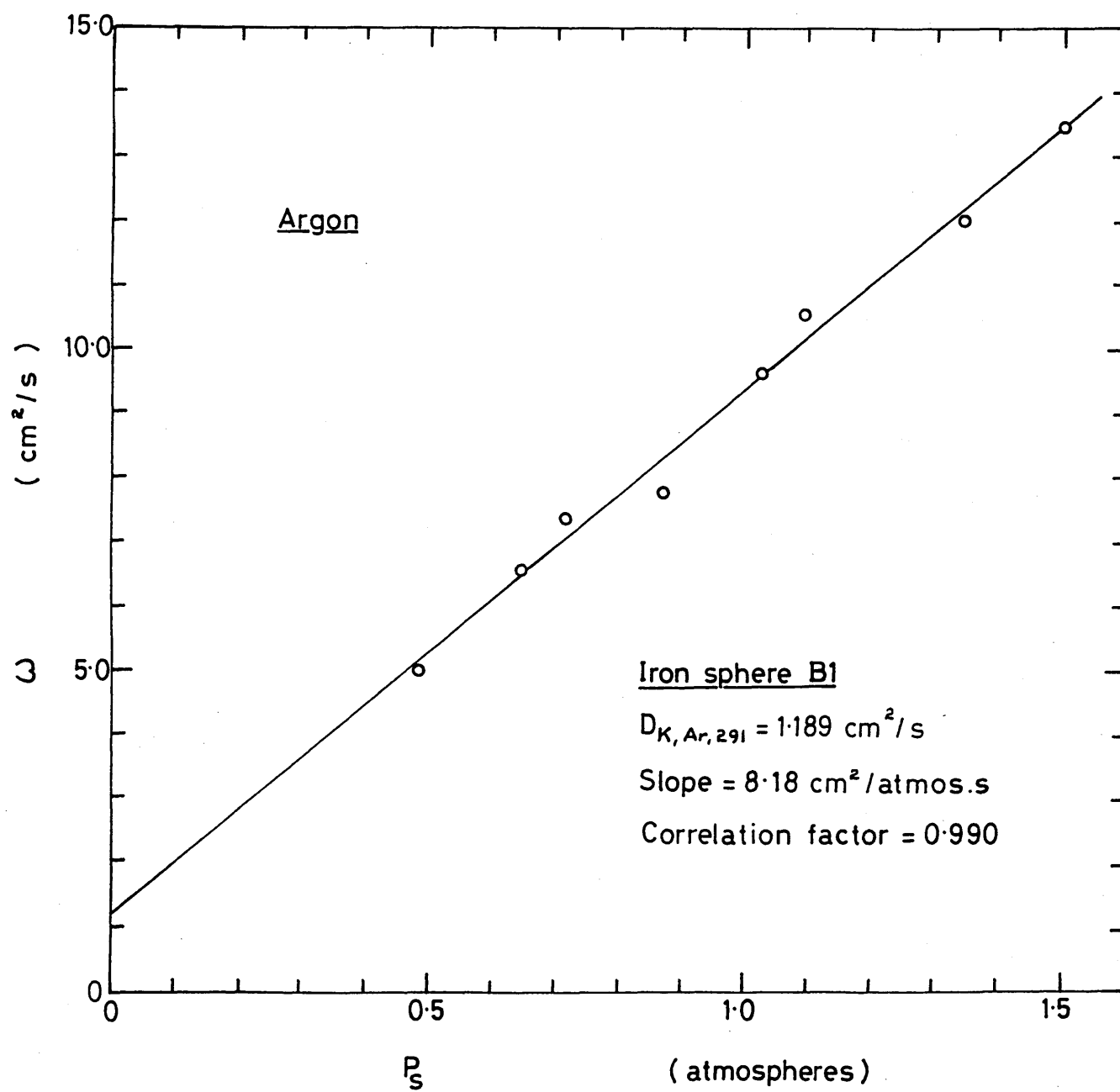
TABLE No.5.38   Permeability Data for Argon through
                     Sintered Iron reduced sphere B1 at 291 K

Barometric pressure = 0.999 (atm)
Shape factor   = 11.462 (cm)

No Reading	$\Delta p/$ (atm)	$p_{orifice}/$ (atm)	$p_i/$ (atm)	$p_s/$ (atm)	$\dot{n}/$ ($\mu mol.s^{-1}$)	$\omega/$ ($cm^2.s^{-1}$)
1.	0.2330	1.005	1.015	1.026	108.00	9.63
2.	0.0133	1.087	1.089	1.095	67.13	10.55
3.	0.0167	1.325	1.333	1.341	96.60	11.96
4.	0.0234	0.846	0.865	0.872	86.80	7.75
5.	0.0167	0.693	0.704	0.714	58.70	7.35
6.	0.0200	0.613	0.644	0.644	63.00	6.58
7.	0.0300	0.445	0.471	0.486	71.70	4.98

$D_{Ar,K} = 1.189$ $(cm^2.s^{-1})$

Slope $= B_o/\mu_{Ar} = 8.18$ $(cm^2.s^{-1}.atm^{-1})$

Correlation factor = 0.990

Figure 5·39 : The permeability of argon through sphere B1 at 898 K

after sintering for 5 hours at 1373 K.

$S = 11·462$ cm ; $\gamma = 57·08$ %

Argon

Iron sphere B1

$D_{K, Ar, 898} = 2·003$ cm^2/s

Slope = $4·022$ cm^2/atmos.s

Correlation factor = $0·9865$
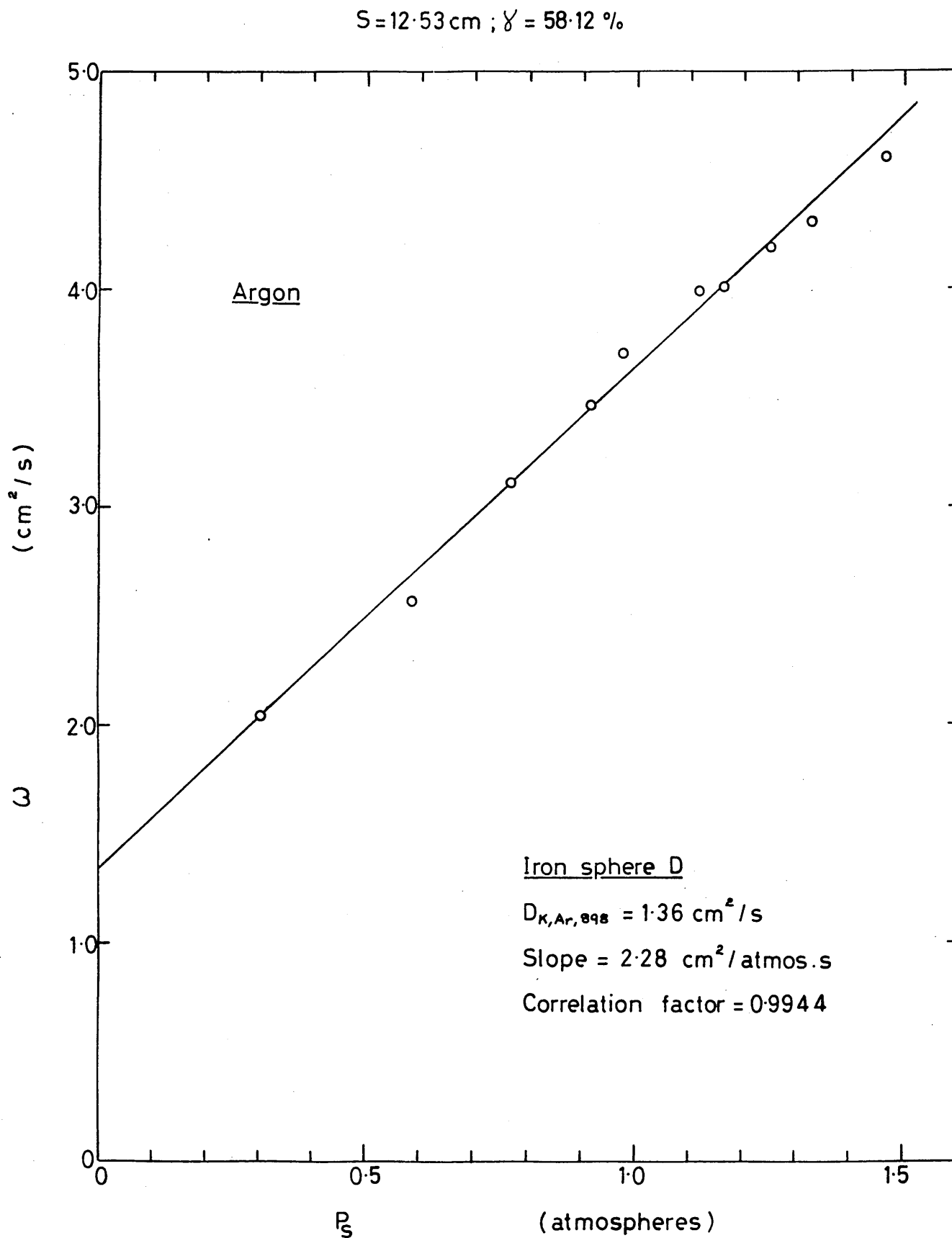
P_S (atmospheres)
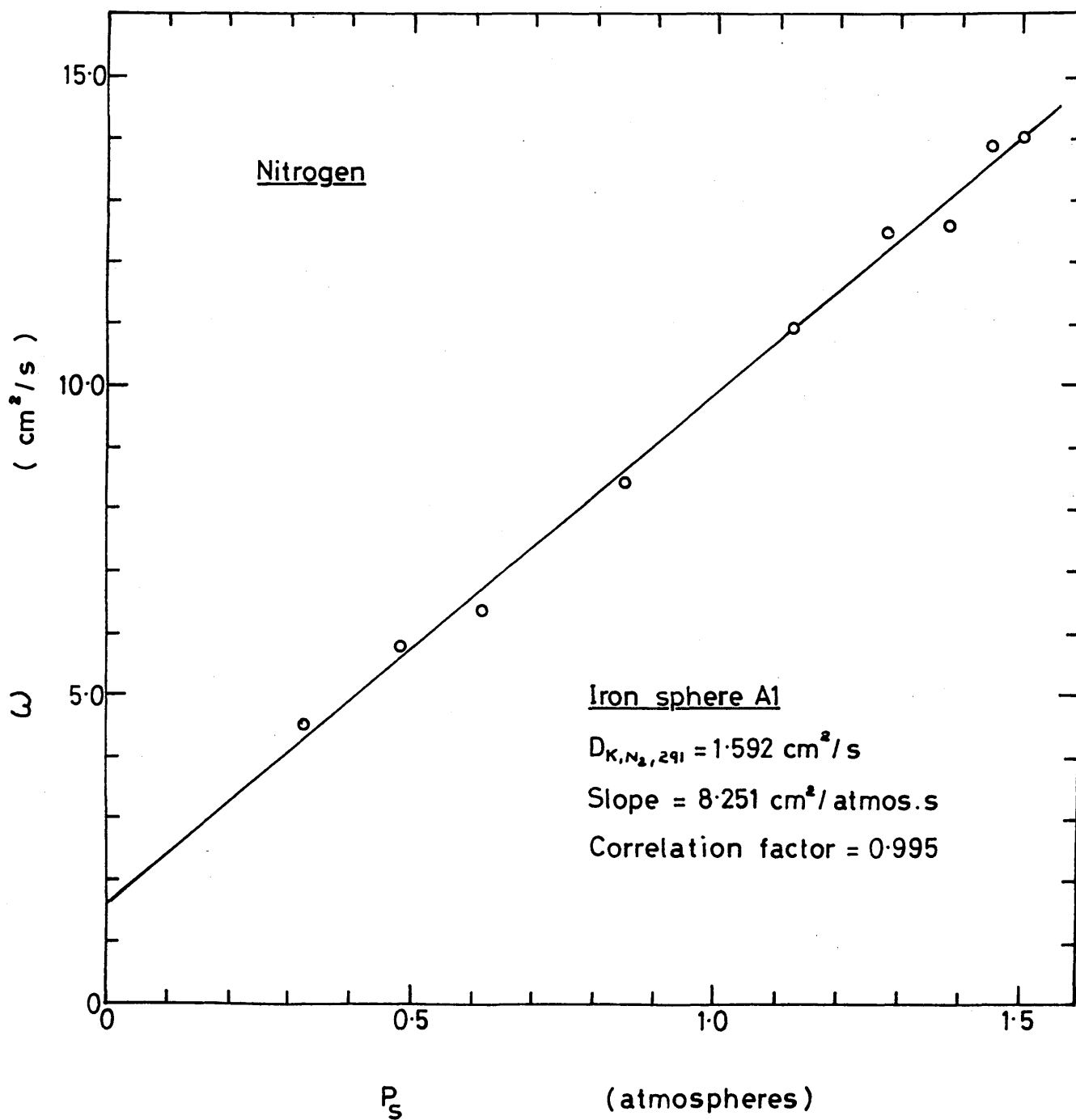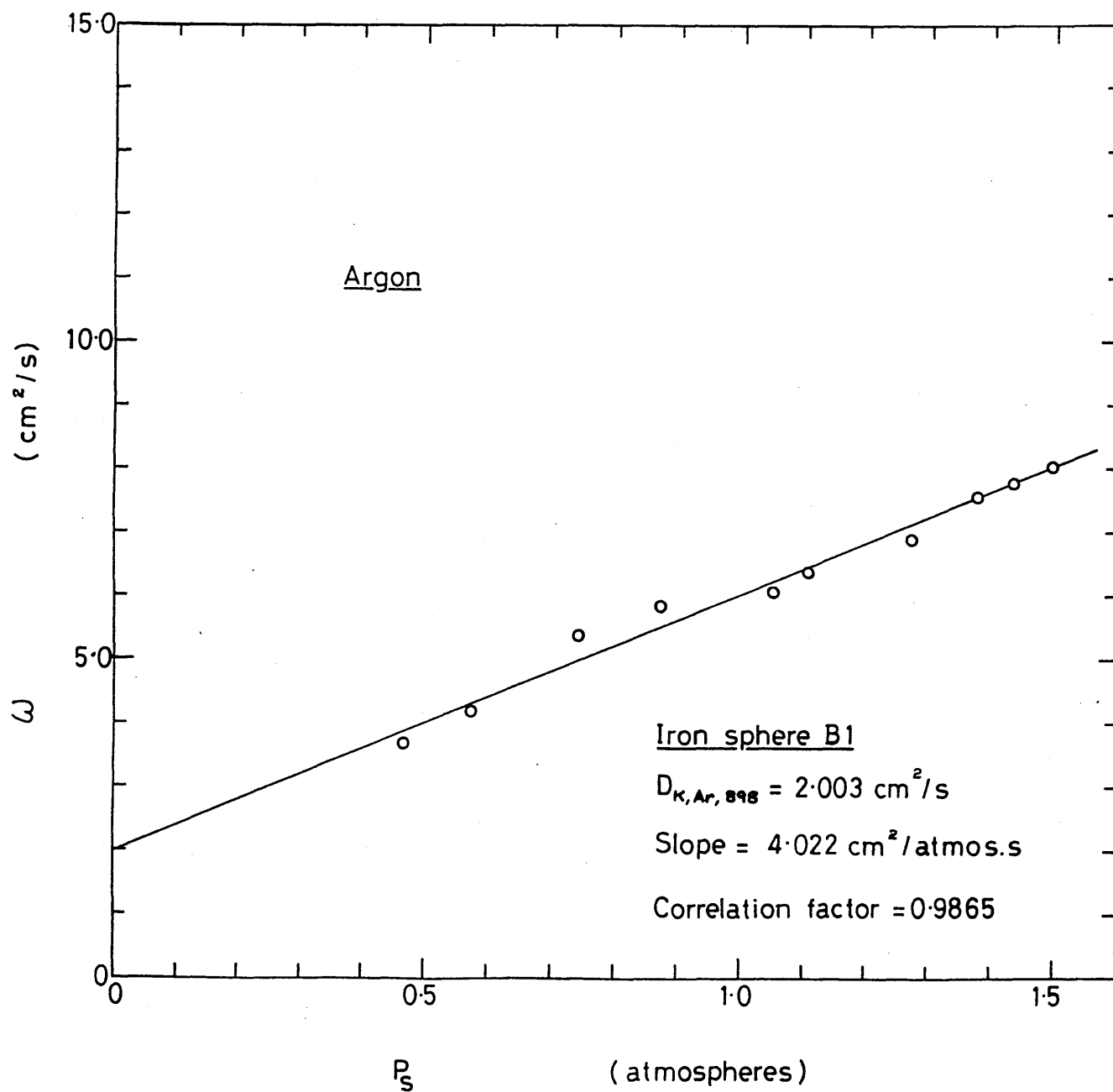
TABLE No.5.39   Permeability Data for Argon through
                 sintered iron reduced sphere B1 at 898 K

Barometric pressure = 0.990 (atm)
Shape factor   = 11.672 (cm)

No Reading	$\Delta p/$ (atm)	$P_{orifice}$ /(atm)	$p_i/$ (atm)	$p_s/$ (atm)	$\dot{n}/$ (μmol.s^{-1})	$\omega/$ (cm^2.s^{-1})
1.	0.0668	0.994	1.019	1.052	64.20	6.08
2.	0.0300	1.090	1.095	1.110	30.20	6.37
3.	0.0367	1.222	1.259	1.277	40.00	6.90
4.	0.0500	1.345	1.353	1.378	60.00	7.58
5.	0.0535	1.400	1.410	1.436	65.90	7.80
6.	0.0468	0.828	0.845	0.868	43.25	5.85
7.	0.0568	0.696	0.718	0.746	48.30	5.38
8.	0.0468	0.529	0.556	0.577	30.80	4.17
9.	0.0635	0.404	0.440	0.471	36.70	3.66

$D_{K,Ar}$ = 2.003 (cm^2.s^{-1})

Slope = B_o/μ_{Ar} = 4.002 (cm^2.s^{-1}.atm^{-1})

Correlation factor = 0.9865

Figure 5·40 : The permeability of argon through sphere C1 at 291 K after sintering for 5 hours at 1373 K.

$S = 15·99$ cm ; $\gamma = 57·27\%$

Argon

Iron sphere C1

$D_{K,Ar,291} = 1·226$ cm^2/s

Slope = $8·62$ cm^2/atmos.s

Correlation factor = $0·992$

ω (cm^2/s)

P_s (atmospheres)
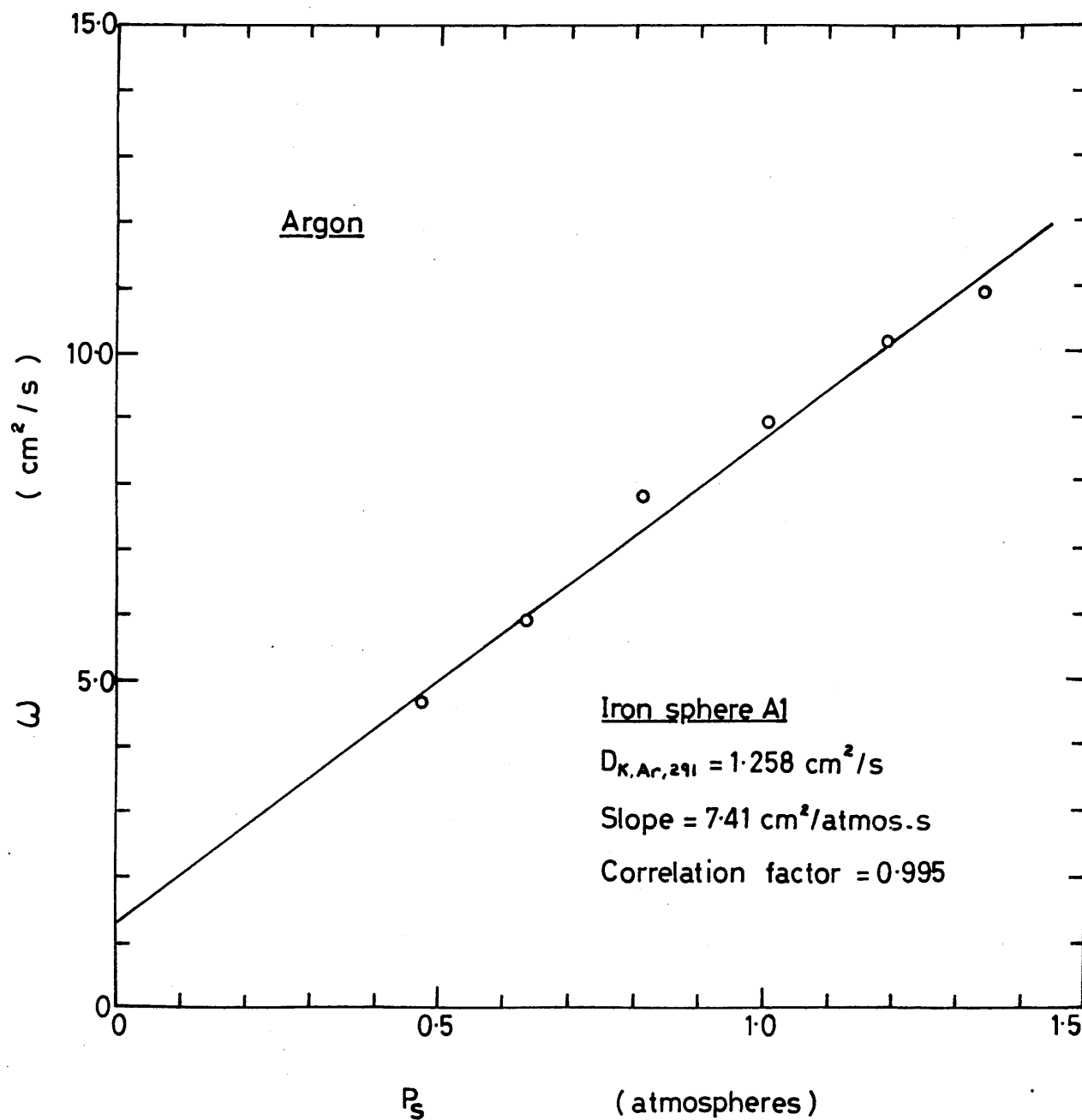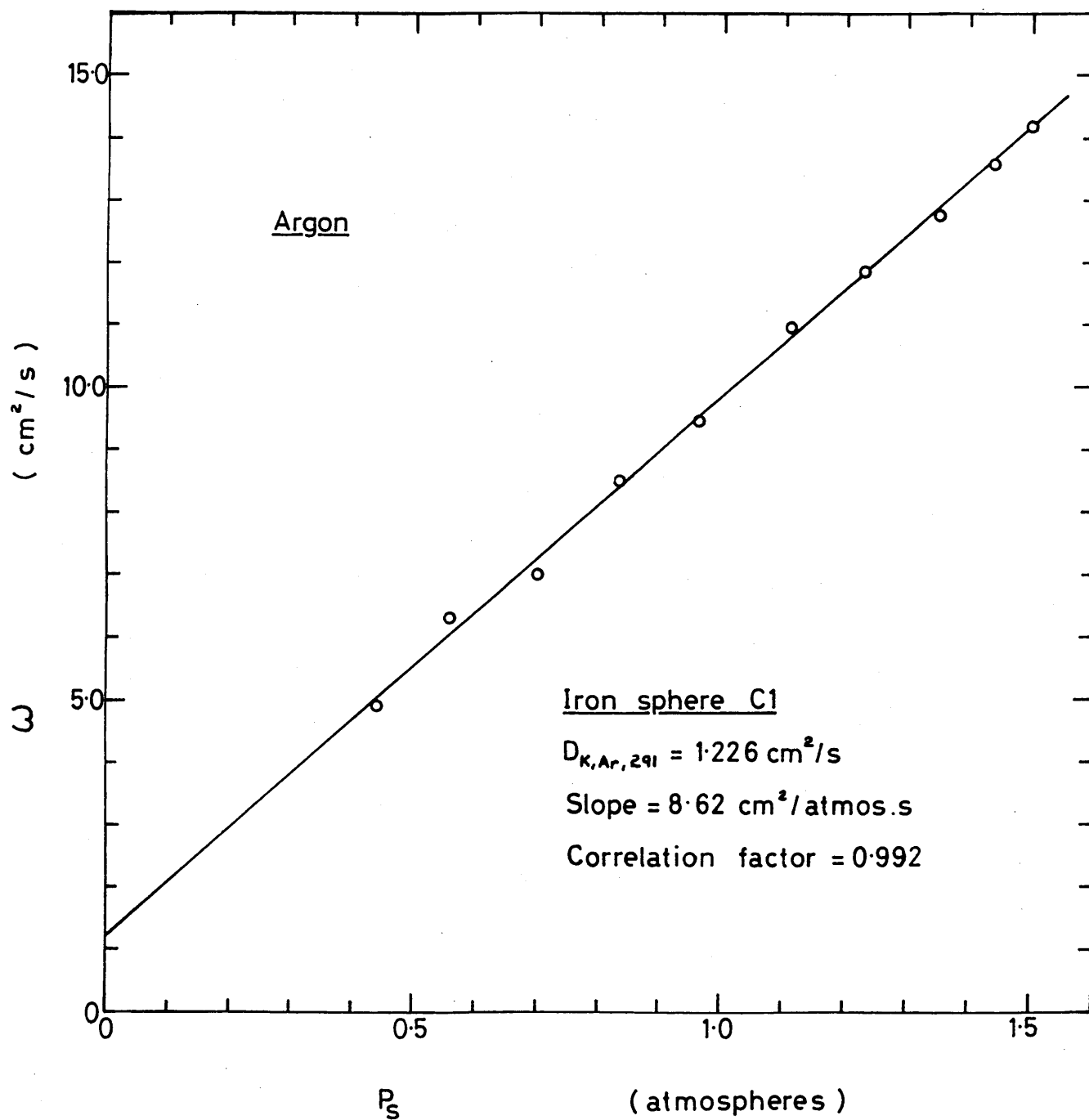
TABLE No.5.40   Permeability Data for Argon through
                Sintered Iron sphere Cl at 291 K

Barometric pressure = 0.971 (atm)
Shape factor   = 15.99 (cm)

No Reading	$\Delta p/$ (atm)	$p_{orifice}/$ (atm)	$p_i/$ (atm)	$p_s/$ (atm)	$\dot{n}/$ (μmol.s^{-1})	$\omega/$ (cm^2.s^{-1})
1.	0.0167	1.080	1.089	1.110	123.20	11.02
2.	0.0133	1.210	1.228	1.235	106.00	11.90
3.	0.0133	1.305	1.353	1.360	114.00	12.81
4.	0.0167	0.398	1.423	1.432	152.00	13.59
5.	0.0116	0.948	0.954	0.963	73.70	9.49
6.	0.0116	0.779	0.820	0.835	66.25	8.53
7.	0.0167	0.632	0.691	0.700	78.50	7.02
8.	0.0200	0.498	0.551	0.561	84.40	6.30
9.	0.0167	0.367	0.433	0.442	55.00	4.92

$D_{Ar,K} = 1.226$ (cm^2.s^{-1})

Slope $= B_o/\mu_{Ar} = 8.62$ (cm^2.s^{-1}.atm^{-1})

Correlation factor = 0.992

Figure 5·41 : The permeability of nitrogen through sphere C1 at 291 K after sintering for 5 hours at 1373 K.

$S = 15\cdot99$ cm ; $\gamma = 57\cdot27\%$

Nitrogen

Iron sphere C1

$D_{K,N_2,291} = 1\cdot57$ cm^2/s

Slope = $9\cdot70$ cm^2/atmos.s

Correlation factor = $0\cdot999$
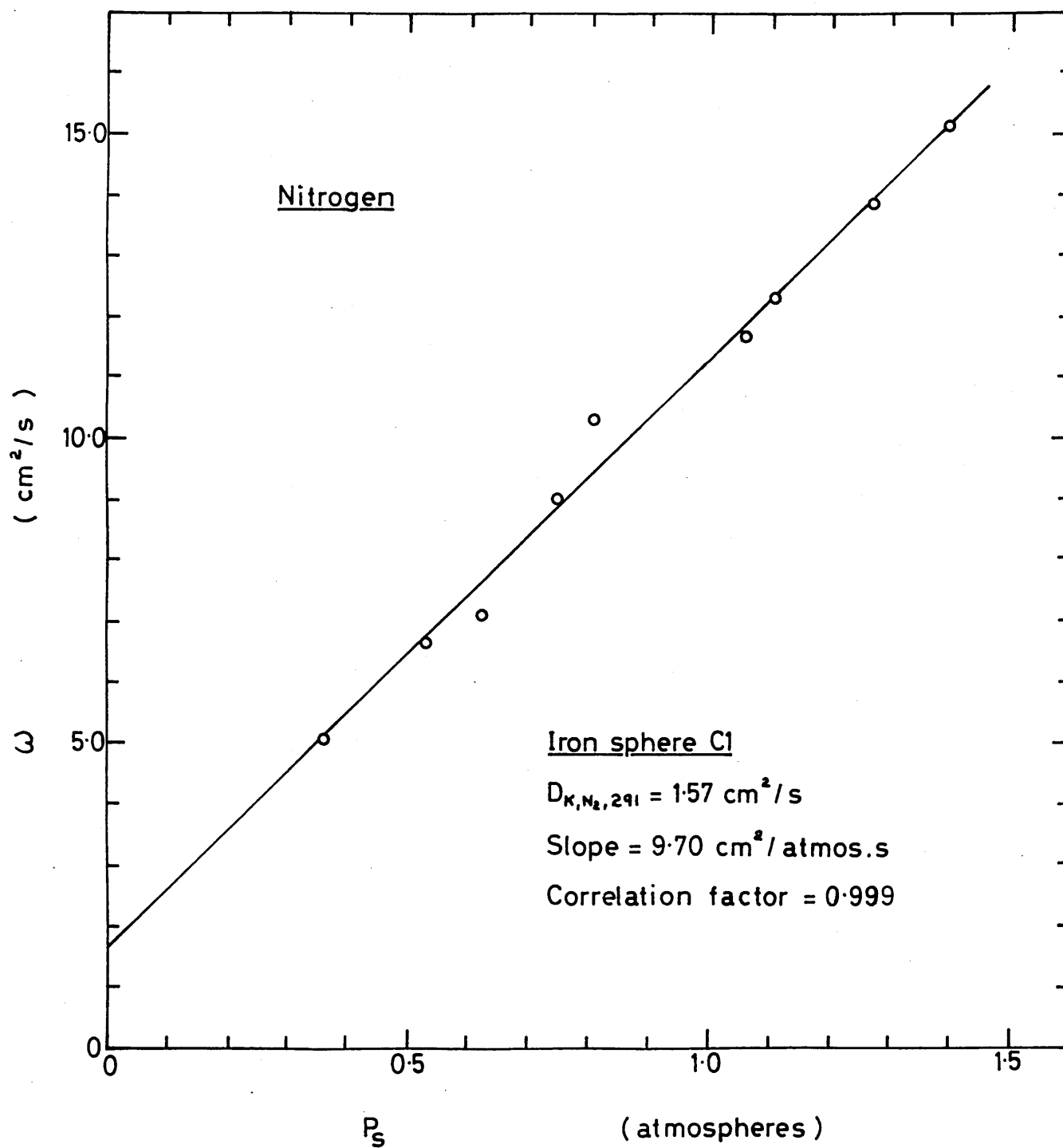
TABLE No.5.41   Permeability Data for Nitrogen through
                  Sintered Iron sphere Cl at 291 K

Barometric pressure = 0.971 (atm)
Shape factor   = 15.99 (cm)

No Reading	$\Delta p /$ (atm)	$P_{orifice} /$ (atm)	$p_i /$ (atm)	$p_s /$ (atm)	$\dot{n} /$ (μmol.s^{-1})	$\omega /$ (cm^2.s^{-1})
1.	0.0150	0.976	0.987	0.994	115.00	11.44
2.	0.0134	1.046	1.054	1.061	104.50	11.68
3.	0.0067	1.099	1.108	1.110	55.00	12.29
4.	0.0134	1.269	1.271	1.278	124.00	13.86
5.	0.0116	0.785	0.800	0.806	80.00	10.29
6.	0.0134	0.601	0.616	0.623	63.50	7.09
7.	0.0150	0.501	0.519	0.527	67.00	6.67
8.	0.0167	0.327	0.352	0.361	56.5	5.05

$D_{K,N_2} = 1.57$ (cm^2.s^{-1})

Slope = $^{B}o /_{\mu N_2}$ = 9.70 (cm^2.s^{-1}.atm^{-1})

Correlation factor = 0.999

Figure 5·42: The permeability of argon through sphere C1 at 898 K after sintering for 5 hours at 1373 K.
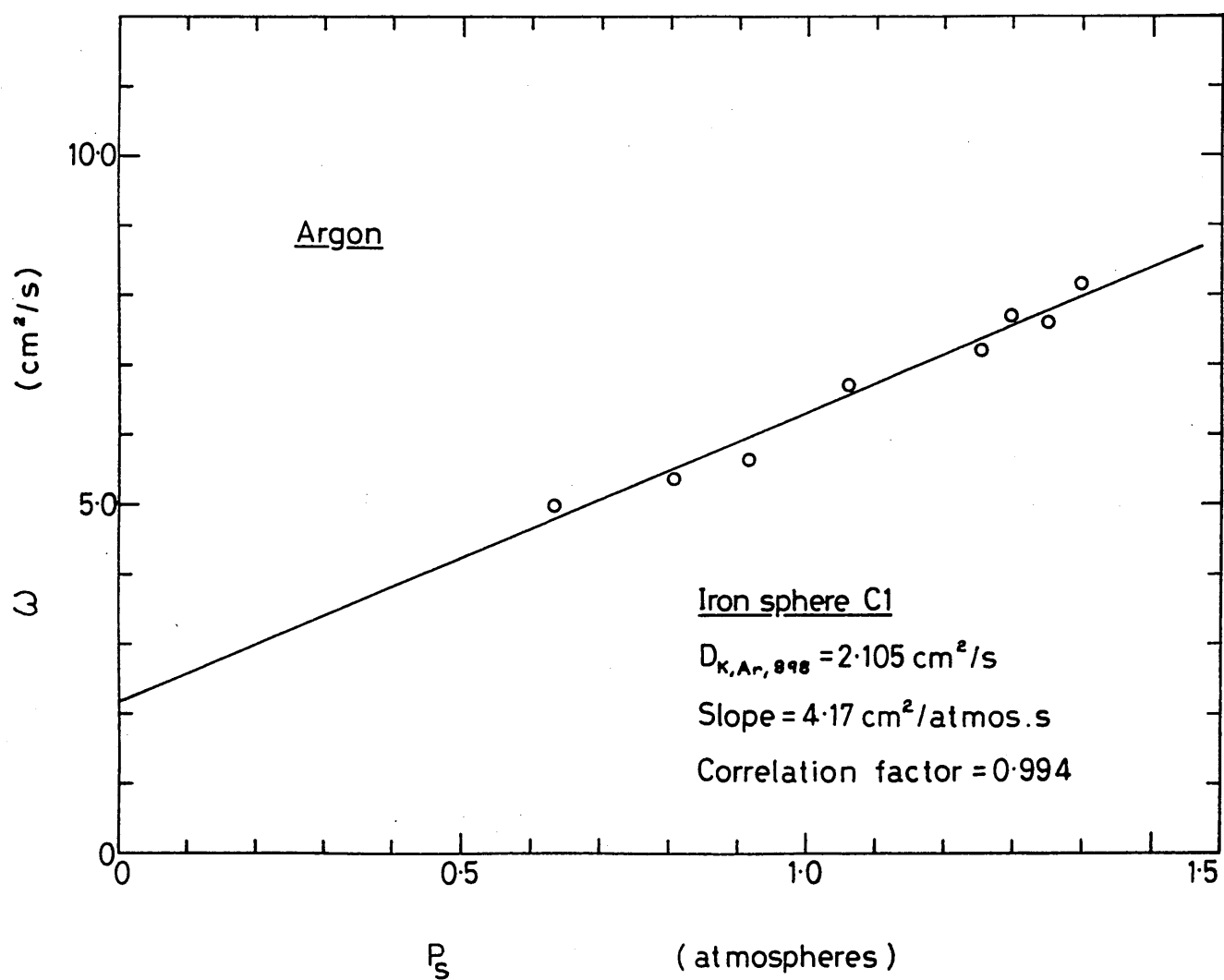
$S = 15.99$ cm ; $\delta = 57.27\%$

Argon
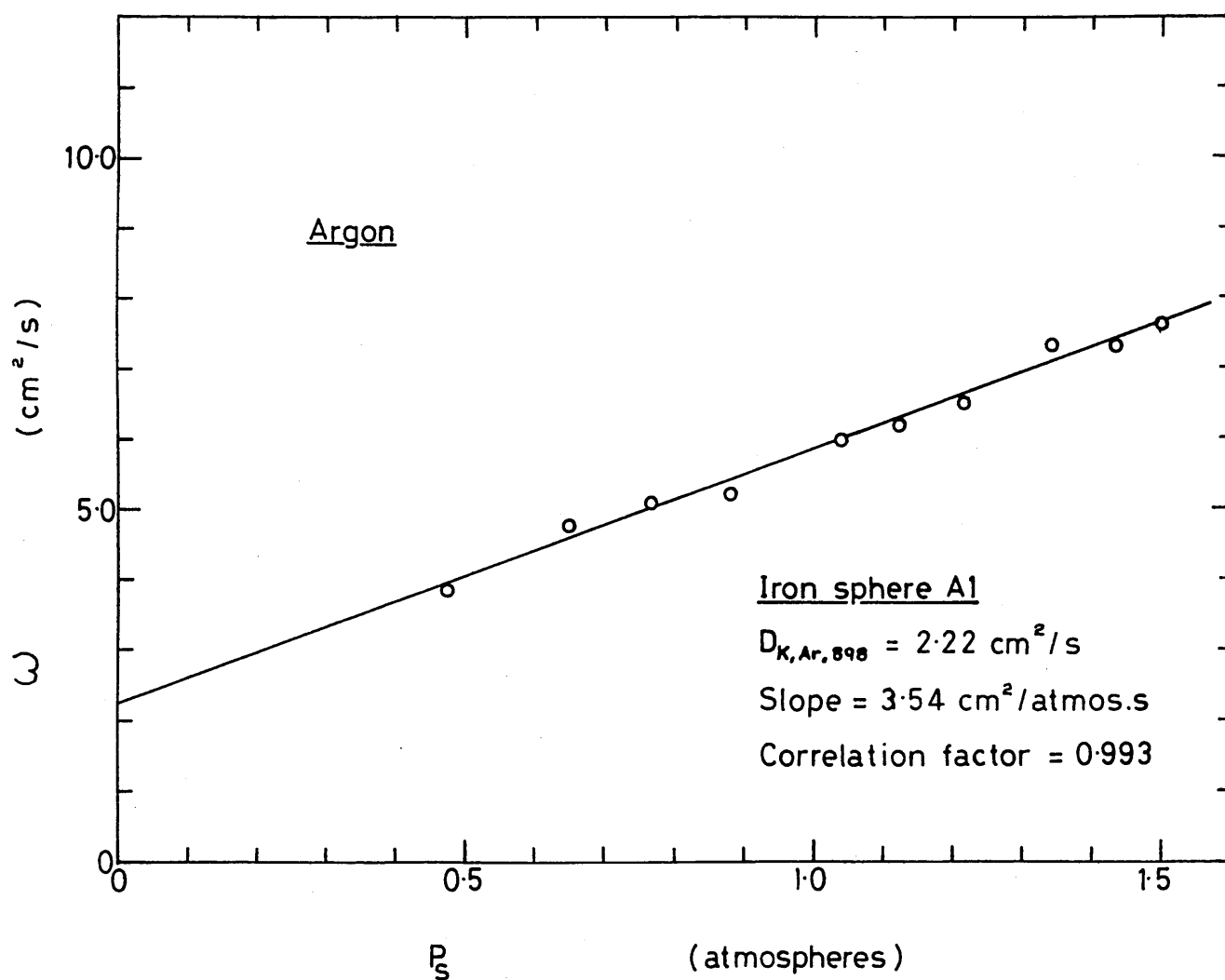
Iron sphere C1

$D_{K, Ar, 898} = 2.105$ cm^2/s

Slope $= 4.17$ cm^2/atmos.s

Correlation factor $= 0.994$

Barometric pressure = 0.982 (atm)
Shape factor   = 15.99 (cm)

No Reading	Δp/ (atm)	$p_{orifice}$/ (atm)	p_i/ (atm)	p_s/ (atm)	$\dot{n}$/ (μmol.s^{-1})	ω/ (cm^2.s^{-1})
1.	0.0734	0.992	1.022	1.059	106.70	6.70
2.	0.0333	1.228	1.236	1.252	52.00	7.20
3.	0.0500	1.249	1.266	1.291	82.30	7.59
4.	0.0567	1.307	1.323	1.357	93.50	7.60
5.	0.0634	1.350	1.369	1.400	114.30	8.31
6.	0.0835	0.827	0.872	0.913	101.50	5.60
7.	0.0333	0.734	0.795	0.811	38.90	5.39
8.	0.0567	0.567	0.621	0.637	61.50	5.00

$D_{K,Ar}$ = 2.105 (cm^2.s^{-1})

Slope = B_o/μ_{Ar} = 4.17 (cm^2.s^{-1}.atm^{-1})

Correlation factor = 0.994

5.4 MEASUREMENT OF EFFECTIVE BINARY DIFFUSION COEFFICIENTS

5.4.1 Introduction To Method of Determination

Equation (3.59) defines the effective binary diffusion coefficient as:-

$$D_{AB,eff} = C_o \, D_{AB} \tag{5.4.1}$$

where D_{AB} is the free gas binary diffusion coefficient which can be calculated from the Chapman Enskog theory[89] or from the correlation by Fuller, Schettler and Giddings [87]. C_o is the ratio of the porosity, γ , to the tortuosity, T. C_o can only be calculated from the results of an isobaric diffusion experiment using equation (3.61). As indicated in Section 4.4.2, the isobaric experiments were carried out in this work using a hollow spherical shell as the diffusion cell. Seven different diffusion cells have been constructed. Four spheres W, X, Y and Z, were made by reducing sintered hematite, sphere Z being subsequently further sintered before measurements were made, and three spheres 71, 72 and 73, were made by decomposing sintered calcium carbonate. Measurements were made on sphere Y before and after it was sintered and on spheres W, X, Y and Z at 292 K and at 898 K.

The calculations from the experimental results were carried out in terms of mole fractions in the gas phase, defined as:-

$$C_A^* = p_A/p_T \tag{5.4.2}$$

so that equation (3.61) for C_O, expressed in terms of helium, becomes:-

$$C_O = \frac{\dot{N}_{He}\ R\theta(\mathcal{K} - 1)}{\mathcal{K}\ D_{He/Ar}S_P T Ln\left\{\dfrac{\mathcal{K} - \delta_{He}(\mathcal{K} - 1)[C^*_{He}]^o_s}{\mathcal{K} - \delta_{He}(\mathcal{K} - 1)[C^*_{He}]^i_s}\right\}} \qquad (5.4.3)$$

where the suffix 's' refers to conditions at the surface, and the superfices 'i' and 'o' refer respectively to the inner and outer surfaces of the spherical shell.

As indicated in Section 3.2.4, equation (5.4.3) is not explicit in C_O since δ_{He} is a function of C_O as indicated in equation (3.62). In terms of helium, this equation becomes:-

$$\delta_{He} = \left\{1 + \frac{C_O\ D_{He/Ar}}{D_{He,K}}\right\}^{-1} \qquad (5.4.4)$$

The solution of equations (5.4.3) and (5.4.4) requires an iterative procedure and this was carried out as described in Section 5.4.5.

Thus calculation of C_O requires the determination of values of the variables listed below. The section of the thesis specified against each variable in the list is the section where the method used to calculate values of that variable is presented. The variables involved are:-

(i)   The Knudsen diffusion coefficient for helium, $D_{He,K}$ – see
         Sections 5.3 and 5.4.4

(ii)   The diffusive flux of helium through the spherical shell –
         see Section 5.4.2.

270

(iii) The ratio, χ , of the Knudsen diffusion coefficient for helium to the Knudsen diffusion coefficient for argon - see Section 5.4.2

(iv) The binary diffusion coefficient for helium argon mixtures - see Appendix 1 .

(v) The mole fractions of helium in the gas phase at the surface either side of the spherical shell - see Section 5.4.3

(vi) The shape factor of the spherical shell - see Section 5.3.1.

As indicated above, Sections 5.4.2 to 5.4.4 are concerned with the calculation of certain of the above variables. Section 5.4.5 then describes the calculation of C_O, and presents the measured and calculated values of the relevant variables.

5.4.2 The Diffusive Fluxes Of Helium And Argon And The Knudsen Diffusion Coefficient ratio

The molar fluxes of gases counter diffusing through the spherical shell may be obtained from simple mass balances for the system. For example, the helium flux, N_{He}, may be obtained by multiplying its mole fraction in the external exit gas stream by the molar flow rate of the external exit gas stream:-

$$\dot{N}_{He} = \dot{G}^O_e \, [C^*_{He}]^O_e \qquad\qquad (5.4.5)$$

Additionally, the molar diffusive flux of helium may be

271

obtained from corresponding values for the internal exit gas stream:-

$$\dot{N}_{He} = \dot{G}_i^i - \dot{G}_e^i [C_{He}^*]_e^i \qquad (5.4.6)$$

where the input gas is pure helium.

In a similar way, the flux of argon can be determined from the composition and flow rate of the internal exit gas stream:-

$$\dot{N}_{Ar} = \dot{G}_e^i [C_{Ar}^*]_e^i \qquad (5.4.7)$$

The exit compositions were determined using the gas chromatograph as described in Section 4.4.3. Figure 5.43 shows the calibration curve that was obtained as outlined in that section.

Table 5.43 shows twin values of the helium flux, calculated after equations (5.4.5) and (5.4.6), and values of the argon flux calculated after equation (5.4.7). Results are presented for all the different spheres for which isobaric measurements were carried out. The two values of each helium flux show close agreement - providing to some degree an independent check on the flow measurements and chromatograph calibration. Equation (5.4.6), however, involves the difference between two experimentally determined quantities and is therefore likely to be subject to a greater proportional error than equation (5.4.5). For this reason, helium diffusion fluxes calculated as shown by equation (5.4.5) were used in the calculations of values of C_o.

As shown in equation (3.53), the flux ratio under isobaric

Figure 5·43 : The calibration curves for the chromatograph.
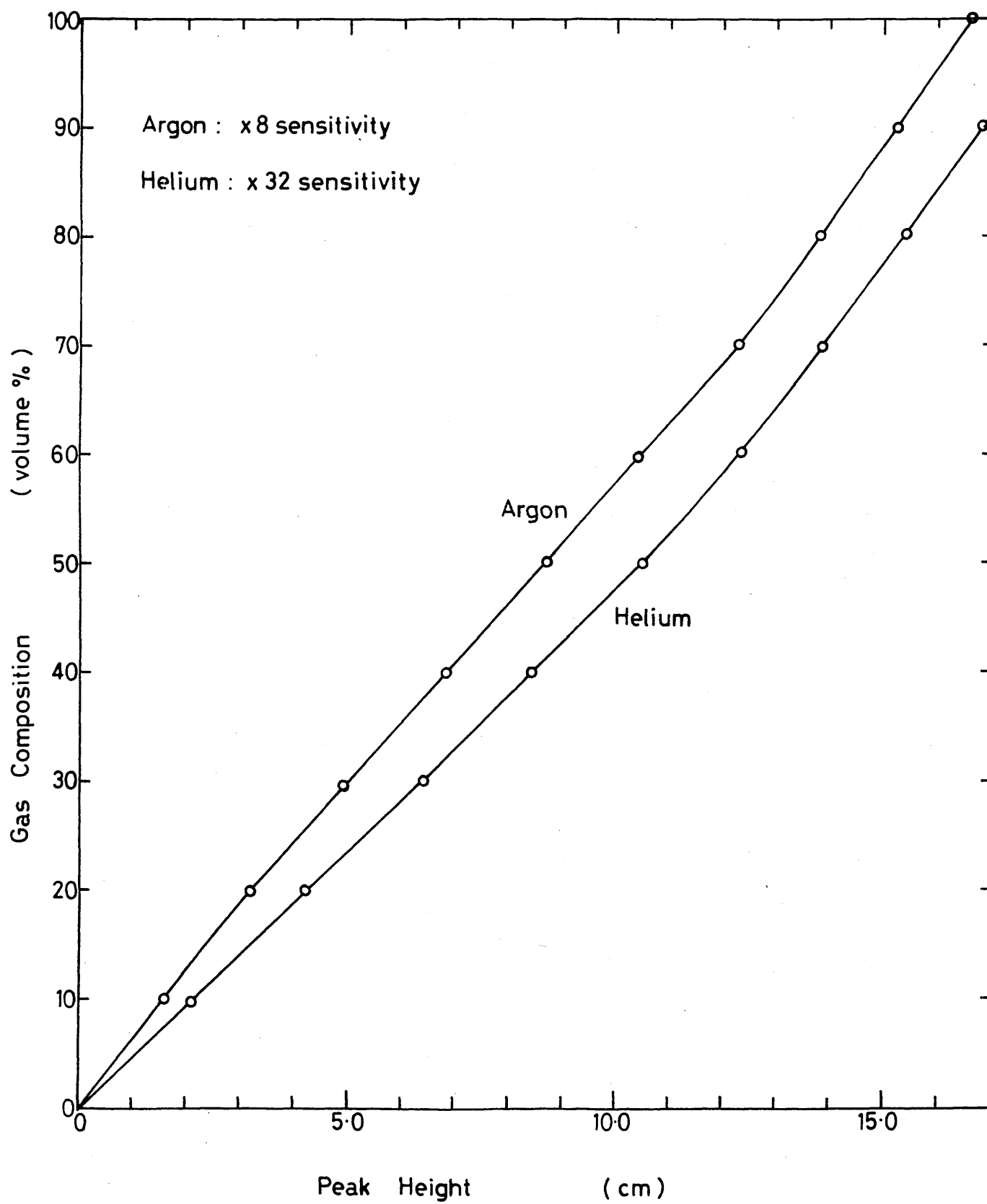
Table 5.43   The diffusion fluxes of helium and argon for
                              isobaric experiments

	Sphere	T	EXP FLUX Ar/	EXP FLUX He$_1$/ (5.4.5)	FLUX He$_2$/ (5.4.6)	β_{exp}
		K	(μmol.s^{-1})	(μmol.s^{-1})	(μmol.s^{-1})	
Reduced Iron	X	292	12.00	36.13	36.20	0.332
		898	18.52	54.95	58.13	0.337
	W	292	19.37	52.80	52.70	0.367
		898	26.19	67.23	68.30	0.389
	Y	292	15.65	38.24	40.07	0.409
		898	21.15	62.22	64.58	0.340
Sintered Iron	Y	292	19.75	58.72	58.75	0.335
	Z	292	21.06	56.78	56.76	0.370
		829	28.38	80.20	89.30	0.357
CaO	71		24.20	72.53	72.60	0.334
	72	292	22.14	62.20	61.14	0.356
	73		25.01	72.50	71.31	0.345

conditions should be equal to the reciprocal of the ratio of

the Knudsen diffusion coefficients. For the counter diffusion

of helium through argon, this relationship should give a

value of β = 0.316 but the experimentally determined

values of the flux ratio presented in Table 5.43 have an average

value of 0.356. However, since the derivation of equation

(5.4.3) depends upon the validity of the theoretical

relationship, the theoretical value of χ (3.43) has been used

in calculating C_o. The implications of doing this will be

considered in the discussion chapter.

5.4.3 The Mole Fractions Of Helium In the Gas Phase At The Internal And External Surfaces Of The Spherical Shell

5.4.3.1 Overall Equations

The mole fractions of the gas phase components at the inner

and outer surfaces of the spherical diffusion shell cannot

be measured directly in the experiments. The values that

can be determined are for the bulk gas phases. Gas enters

the inner cavity through the narrow annular exit from the

diffusion shaft with high momentum so that the inner cavity

can be considered to be perfectly stirred. The bulk gas

composition within the cavity is thus the same as that

leaving the cavity and it is this composition that is

measured directly using the gas chromatograph (see

Section 4.4). The composition of the gas stream flowing

past the outside of the spherical shell varies across the

sphere. Thus the bulk gas composition is taken to be the

average between the input concentration – pure argon – and

the output concentration measured by the chromatograph.

These bulk compositions may be used, as the bases for calculating the surface gas compositions. The relationship between bulk and surface gas compositions has already been discussed in Section 3.4, in which equation (3.65) relates the surface and bulk partial pressures of helium. In terms of mole fractions and with the helium flux taken as positive, the relationship for the internal surface is:-

$$[C*_{He}]^i_s = \frac{1 - \left\{1 - (1-\beta)[C*_{He}]^i_b \exp(\dot{N}_{He}(1-\beta)R\theta/p^i_T \alpha^i A^i)\right\}}{1-\beta} \quad (5.4.8)$$

where $A^i = 4\pi r^{i2} - 2 A_S$, A_S being the cross-sectional area of the diffusion and total pressure shafts (the factor 2 was omitted for the measurements on lime since a separate total pressure shaft was not used in the lime experiments) Similar equations exist for the outer surface of the sphere, the superfix 'i' being replaced by the superfix 'o' and the sign of the flux reversed.

The internal and external mass transfer coefficients appearing in the equations were determined as discussed in the next sub-sections.

5.4.3.2 The External Mass Transfer Coefficient

Campbell[50] has investigated the effect of flow rate on the mass transfer coefficient for flow of gas over the outside of a sphere placed centrally within a tube under geometric

276

conditions indentical to those used in this work. The

dimensionless correlation that he obtained is:-

$$Sh = 2.0 + 2.33\ Re^{0.3385}Sc^{1/3} \qquad (5.4.9)$$

where:-

$$Sh = \frac{\alpha^{o}d^{o}}{D_{He/Ar}} \qquad (5.4.10)$$

$$Sc = \frac{\mu_{Ar}}{\rho_{Ar}D_{He/Ar}} \qquad (5.4.11)$$

$$Re = \frac{\rho_{Ar}\ u\ d^{o}}{\mu_{Ar}} \qquad (5.4.12)$$

where u is the approach velocity of the gas down the tube,

and which is equal to the volumetric gas flow rate divided

by the cross sectional area of the tube.

Equation (5.4.9) has been used in this work to calculate the

external mass transfer coefficient to the spherical shell.

The viscosity of pure argon has been used in the calculations

since, although the boundary layer around the sphere contains

small concentrations of helium, the viscosities of argon and

helium are so similar that the viscosity of argon is relatively

insensitive to small concentrations of helium.

5.4.3.3 Internal Mass Transfer Coefficient

Although the geometry of the diffusion shaft used in this

work was similar to that used by Campbell, it was not

precisely the same so that the correlation he obtained for

the internal mass transfer coefficient could not be assumed

to apply.   Hence, special mass transfer measurements were
undertaken using naphthalene, as described in Section 4.4.5.
The internal mass transfer coefficient was determined from
the results of these experiments using the equation:-

$$\propto_N = \frac{\dot{n}_N \, R \, T}{A^i \, \Delta p_N} \qquad (5.4.13)$$

where the suffix 'N' refers to naphthalene, and $\dot{n}_N$ is the molar
evaporation rate. Δp_N is the difference between the
equilibrium sublimation pressure of naphthalene and its partial
pressure in the bulk gas phase within the spherical cavity.
This partial pressure was found to be negligible in the
experiments and was therefore taken as zero.   The value of
the equilibrium sublimation pressure was taken as that given by
the following equation[103]-

$$Log \left\{ \frac{[p_N]_{es}}{1 \, Atm} \right\} = 11.55 - \frac{3765}{T/K} \qquad (5.4.14)$$

The results of the naphthalene evaporation experiments are
presented in Table 5.44 and the calculated mass transfer
coefficients plotted against the volumetric air flow rate into
the central cavity in Figure 5.44. This figure shows that the
mass transfer coefficient values are most simply correlated by
a straight line giving a positive intercept on the mass transfer
coefficient axis suggesting a dimensionless correlation of the
form:-

$$Sh^i = A + B \, Re \, Sc^{1/3} \qquad (5.4.15)$$

where the Schmidt number exponent has been assumed to be 1/3 in

Table 5.44   Results from measurement of the mass transfer
                    coefficient in naphthalene-air system

Sample No.	$\dot{n}/$ mol.s^{-1}	$T/$ K	V.P/ atm	$\alpha/$ cm.s^{-1}	$\dot{V}/$ cm^3.s^{-1}
1.	3.65×10^{-9}	291.7	5.780×10^{-5}	0.332	2.29
2.	5.35×10^{-9}	290.4	5.060×10^{-5}	0.554	2.62
3.	8.01×10^{-9}	291.8	5.841×10^{-5}	0.7235	5.08
4.	8.96×10^{-9}	291.4	5.605×10^{-5}	0.842	5.24
1.	1.16×10^{-8}	292.8	6.207×10^{-5}	0.992	7.00
2.	1.17×10^{-8}	293.0	6.590×10^{-5}	0.943	7.00
2.	1.04×10^{-8}	290.8	5.270×10^{-5}	1.036	8.19
3.	1.24×10^{-8}	292.8	6.207×10^{-5}	1.057	8.19
1.	1.90×10^{-9}	293.9	7.290×10^{-5}	1.370	8.52
4.	1.19×10^{-8}	290.6	5.160×10^{-5}	1.210	10.81
5.	1.46×10^{-8}	290.7	5.220×10^{-5}	1.469	10.81
6.	2.38×10^{-8}	292.8	6.460×10^{-5}	1.949	14.74
7.	2.58×10^{-8}	293.0	6.590×10^{-5}	2.070	14.74
5.	1.75×10^{-8}	290.8	5.270×10^{-5}	1.751	13.10

Figure 5·44: The effect of air flow rate on the internal convective mass transfer coefficient obtained from naphthalene sublimation experiments .
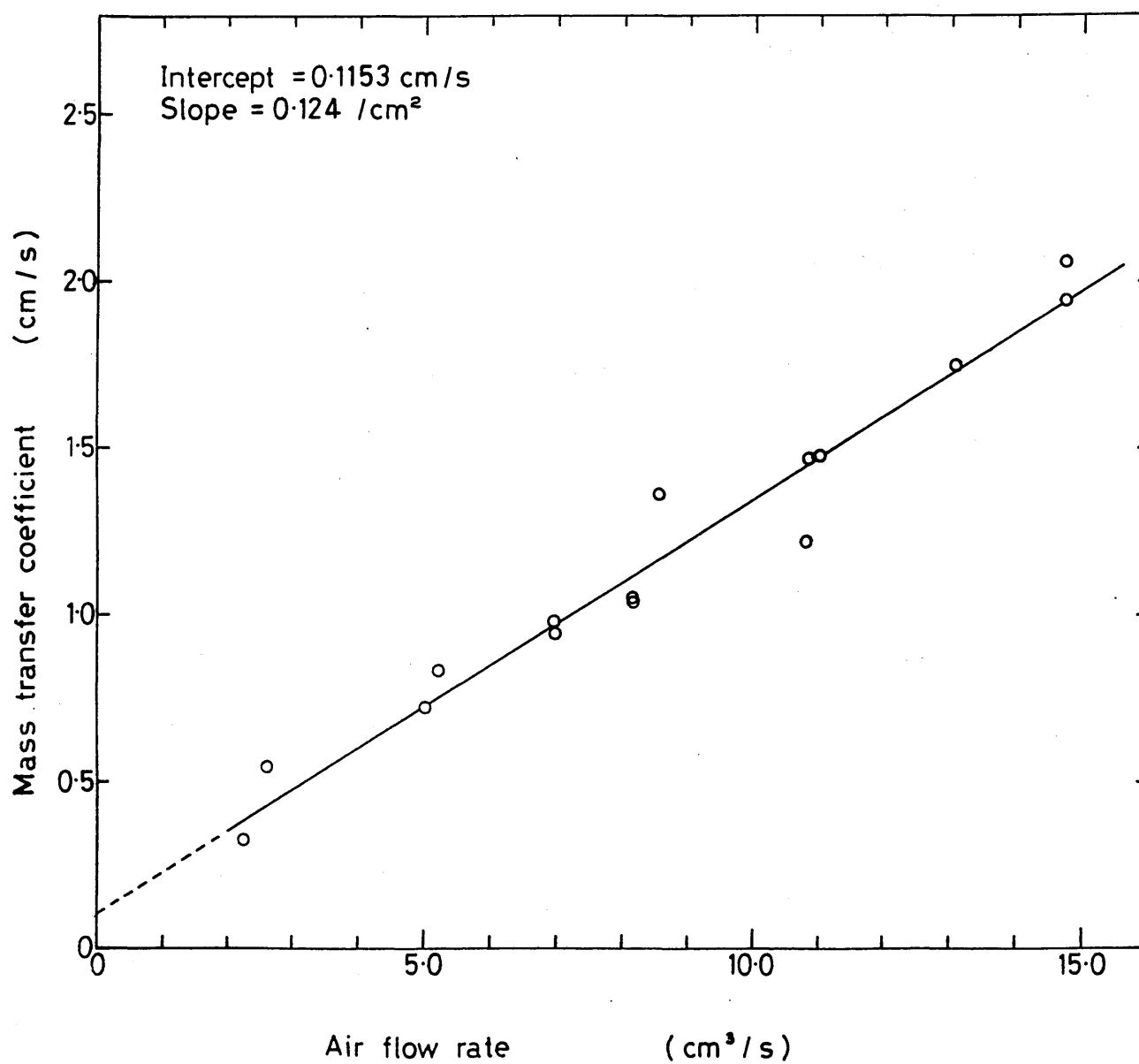
view of the almost universal adoption of this value under turbulent flow conditions (The definition of the Chilton-Colburn j-factor for mass transfer[89], for example, is based on this exponent value)

Applying equation (5.4.15) shows that the value of the intercept in Figure 5.44 is $A.D_{N-Air}/d$, where d is the characteristic linear dimension of the system - taken as the internal diameter of the spherical cavity.   At room temperature, the binary diffusion coefficient, D_{N-Air}, is 0.0611 cm^2s^{-1} [69] giving A the value 2.36.   The value of B can then be determined from the plot of $Log[(Sh^i-2.36)/Sc^{1/3}]$ against Re shown in Figure 5.45, the data on which this figure is based being shown in Table 5.45.   The figure gives an intercept of 0.2758 and a slope of 0.9928 giving rise to the following equation:-

$$Sh^i = 2.36 + 0.2758\ Re^{0.9928}\ Sc^{1/3}, \qquad (5.4.16)$$

for the determination of the internal mass transfer coefficient.

The density and viscosity used to evaluate the Reynolds number in equation (5.4.16) are obviously those applying within the central cavity of the diffusion sphere, but the momentum input that stirs the gas within this cavity is provided by the input gas stream.   This produces no problem in the naphthalene evaporation experiments where air is the input gas and the central cavity contains vanishingly small concentrations of naphthalene vapour since, under these conditions, the densities of the input gas stream and the bulk gas phase

Figure 5·45 : Graphical presentation of the Sherwood-Schmidt-Reynolds number relationship for mass transfer from the internal surface of the spherical shell.

intercept = 0·2758
slope = 0·9928

$\therefore$ Sh = 2·359 + 0·2758 Re$^{0.9928}$ Sc$^{1/3}$

$\log_{10}$ Re

$\log_{10} \dfrac{Sh - 2·359}{Sc^{1/3}}$
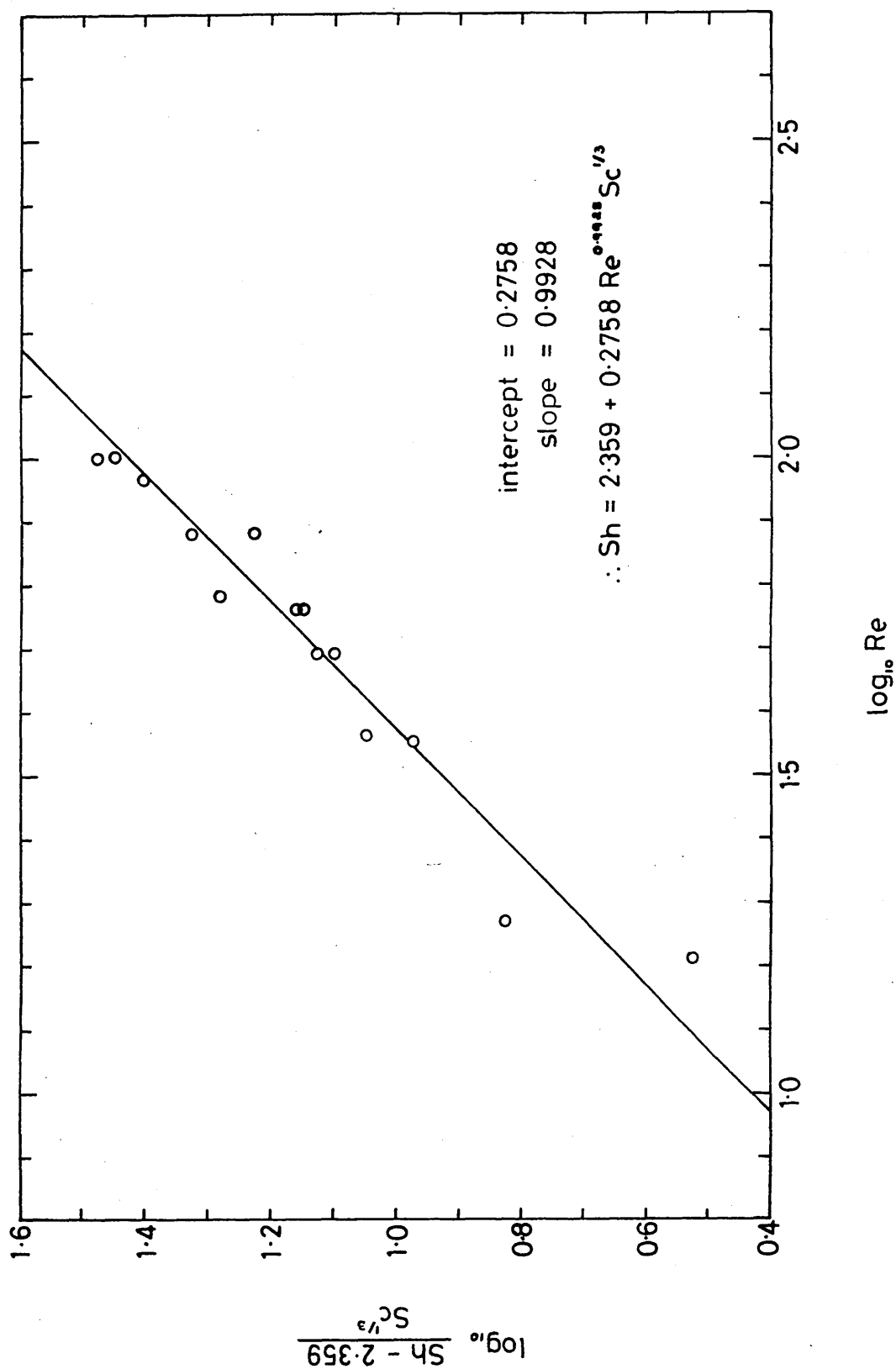
Table 5.45   Results from measurement of the internal mass transfer coefficient in naphthalene-air system

α /(cm.s^{-1})	0.33	0.55	0.72	0.84	0.99	0.94	1.04	1.06	1.37	1.21	1.47	1.75	1.95	2.07
$\dot{V}$ /(cm^3.s^{-1})	2.29	2.62	5.08	5.24	7.00	7.00	8.19	8.19	8.52	10.81	10.81	13.10	14.74	14.7
$v = \dfrac{\dot{V}}{A_{across\ cavity}}$ /(cm.s^{-1})	1.86	2.13	4.14	4.27	5.70	5.70	6.67	6.67	6.94	8.81	8.81	10.67	12.01	12.0
Re	16.31	18.66	36.19	37.33	49.87	49.87	58.35	58.35	60.70	77.02	77.02	93.33	105.00	105.0
log Re	1.21	1.27	1.56	1.57	1.70	1.70	1.77	1.77	1.78	1.89	1.89	1.97	2.02	2.0
$Sh = \dfrac{\alpha.d}{D_{naph-air}}$	6.79	11.33	14.81	17.22	20.29	19.29	21.19	21.62	28.02	26.75	30.05	35.82	39.87	42.3
$\dfrac{Sh - 2.359}{Sc^{1/3}}$	3.35	6.78	9.41	11.23	13.55	12.80	14.23	14.56	19.40	16.92	20.93	25.29	28.35	30.2
$\log \dfrac{Sh - 2.359}{Sc^{1/3}}$	0.53	0.83	0.97	1.05	1.13	1.11	1.15	1.16	1.29	1.23	1.32	1.40	1.45	1.4

$r_i = 0.625$ cm

$A = 1.227$ cm^2

$Sc^{1/3} = 1.323$

$\mu_{air} = 1.747.10^{-4}$ g.cm^{-1}s^{-1}

$\rho_{air} = 1.22.10^{-3}$ g .cm^{-3}

$D_{naph-air} = 0.0611$ cm^2.s^{-1}

$Sc = 2.33$

within the cavity are virtually identical. Thus the linear
velocity of the input gas stream adequately specifies the
input stirring momentum.

This state of affairs does not apply, however, in the diffusion
experiments themselves. Here, the input gas is pure helium
but the internal cavity contains a mixture of argon and
helium and the densities of the two can be very different.
The linear velocity of the input gas stream is no longer an
adequate description of the input momentum. However, an
effective linear velocity can be defined at which gas of
composition identical to that in the central cavity would
carry down the diffusion shaft a momentum flux equal to that
actually carried by the input helium. This effective
velocity is obviously related to the actual velocity, u, by
the equality:-

$$\rho_{He-Ar} \cdot u^2_{eff} \quad = \quad \rho_{He} \, u^2 \tag{5.4.17}$$

The effective Reynolds number in the central cavity for the
diffusion experiments is thus:-

$$Re \quad = \quad \frac{\rho_{He-Ar} \cdot u_{eff} \cdot d^i}{\mu_{He-Ar}} \quad = \quad \frac{\sqrt{\rho_{He-Ar} \cdot \rho_{He}} \cdot u \cdot d^i}{\mu_{He-Ar}} \tag{5.4.18}$$

where the suffix 'He-Ar' refers to the gas composition in the
central cavity (equal to the exit gas composition from the
central cavity).

Thus internal mass transfer coefficients in the diffusion
experiments were calculated from the input helium velocity down
the diffusion shaft, and the exit gas composition using
equations (5.4.16) and (5.4.18).

284

5.4.3.4 Comparison Of Bulk And Surface Mole Fractions

The internal and external mass transfer coefficients and the surface gas compostions calculated for each set of results are presented in the complete tabulations in Section 5.4.5.   In order to show more conveniently the effect of the mass transfer processes either side of the spherical shell, however, the measured bulk gas compositions and the calculated surface gas compositions have been extracted into Table 5.46 below.   They show that, for the diffusion experiments on the porous iron spheres W, X and Y, the difference between the bulk gas helium partial pressures is 10 to 15% greater than the difference between the surface partial pressures.   For the experiments on the sintered iron spheres Y and Z, the bulk pressure difference is 18 to 20% higher than the surface pressure difference, and, for the lime spheres 71, 72 and 73, the bulk pressure difference is 20 to 25% greater than the surface pressure difference.

Table 5.46   Bulk and surface partial pressure of helium

Sphere	Mole fractions of helium			
	External		Internal	
	Bulk	Surface	Bulk	Surface
W, 292K	0.1470	0.1943	0.8960	0.8564
W, 898K	0.1912	0.2211	0.7523	0.7162
X, 292K	0.1216	0.1542	0.7880	0.8242
X, 898K	0.1623	0.1859	0.6754	0.7430
Y, 292K	0.1029	0.1374	0.9320	0.8903
Y, 898K	0.1720	0.2021	0.7760	0.7296
Y,sin,292K	0.2020	0.2589	0.9140	0.8621
Z,sin,292K	0.2050	0.2590	0.9110	0.8625
Z,sin,898K	0.2065	0.2420	0.7340	0.6806
71, 292K	0.2160	0.2867	0.8670	0.8006
72, 292K	0.1915	0.2535	0.8920	0.8370
73, 292K	0.1945	0.2648	0.8600	0.7949

5.4.4 The Knudsen Diffusion Coefficient for Helium

The Knudsen diffusion coefficient for helium must be known before the effective helium-argon diffusion coefficient can be calculated from the helium flux measured in the isobaric experiments. The determination of Knudsen diffusion coefficients from permeability measurements has already been described in Sections 5.3.1, 5.3.2 and 5.3.3.

The measurements reported in these sections include full permeability results for spheres X and 71 which were obtained prior to their use in the isobaric experiments. For the remaining spheres used in the isobaric experiments, spot argon permeability measurements were made at 1.1 atmospheres to check that Knudsen diffusion and permeability through the spheres could be described in terms of the parameters determined in the full permeability investigations. Table 5.47B shows these spot permeability measurements and Table 5.47A shows permeability values at 1.1 atmospheres that were measured as part of the full permeability measurement investigations. Table 5.47B also specifies the permeability sphere, from Table 5.47A whose permeability at 1.1 atmospheres most closely matches the spot permeability measured for each sphere used in the isobaric experiments. The A_O value determined for that permeability sphere is the value used to determine the helium Knudsen diffusion coefficient to be used in calculating the effective binary diffusion coefficient from the results of the isobaric diffusion measurements.

286

Table 5.47A   Permeability Values at 1.1 atm $[(\omega/(cm^2 \cdot s^{-1}))]$

PERMEABILITY EXPERIMENTS

REDUCED IRON		SINTERED IRON		CaO	
292 K	898 K	292 K	898 K	292 K	1230 K
Sphere R 6.278	Sphere R 3.502	Sphere A 9.410	Sphere A 6.110	Sphere No.60 0.93	Sphere No.60 0.643
Sphere T 6.168	Sphere T 3.438	Sphere B 10.187	Sphere B 6.424	Sphere No.59 0.97	Sphere No.59 0.671
Sphere V 5.705	Sphere V 3.014	Sphere C 10.708	Sphere C 7.132	Sphere No.58 1.20	Sphere No.58 0.702
Sphere Q 6.027	Sphere Q 3.353			Sphere No.62 1.58	Sphere No.62 0.920
Sphere X 5.572	Sphere X 4.150			Sphere No.71 1.90	

Table 5.47B   Binary Diffusion Experiments

REDUCED IRON		SINTERED IRON		CaO
292 K	898 K	292 K	898 K	292 K
Sphere Y 6.140 (≡ to T)	Sphere Y 3.240 (≡ to T)	Sphere Y 9.240 (≡ to A1)	—	Sphere No.71 1.890 (measured)
Sphere X 5.572 (measured)	Sphere X 4.150 (measured)	Sphere Z 9.590 (≡ to A1)	Sphere Z 6.380 (≡ to B1)	Sphere No.72 2.080 (≡ to 71)
Sphere W 6.120 (≡ to T)	Sphere W 3.260 (≡ to T)		—	Sphere No.73 1.740 (≡ to 71)

However, for spheres X and 71 the A_O values have been measured directly, as indicated in Table 5.47B.

5.4.5 Calculation of C_O

Once all the relevant data had been obtained, as described in Sections 5.4.1 to 5.4.4, from the experimental measurements carried out as described in Section 4.4.4, it was possible to calculate the values of C_O by solving equations (5.4.3) and (5.4.4) iteratively. A computer programme written in MBASIC and called ISORT.BAS was written to carry out these computations using a Shelton Sig/net microcomputer. The programme is listed in Appendix 3. The programme contains an iterative loop in which an estimated value of C_O is used to determine $\hat{\delta}_{He}$ from equation (5.4.4) so that this value can be used in equation (5.4.3) to obtain a better estimate of C_O. Iteration commences with the value $C_O = 0.4$ and is continued until the difference between two consecutive estimates of C_O is less than .01% of the current estimate. The starting value of 0.4 is used because it corresponds roughly to $\Upsilon = \sqrt{2}$, ie to the theoretical value of Υ for an unconsolidated porous solid.

The input data for the computer programme is listed below in terms of the mathematical symbol used in the theoretical developments and the variable name used in the computer programme. Values of this data, as calculated from the experimental results, are then shown in Table 5.48 - for the

reduced iron spheres, Table 5.49 – for the sintered iron spheres, and Table 5.50 for the decomposed calcium carbonate spheres. The headings used in these tables are the variable names used in the computer programme and the values in the tables are expressed in the units specified in brackets after each variable name.

The input data is:-

(i)   The temperature of the system, θ – T (K)

(ii)   The total pressure in the system, P_T – PS (atm)

(iii)   The mole fraction of helium in the bulk gas outside the spherical diffusion cell, $[C^*_{He}]^o_b$ – CHEOB

(iv)   The mole fraction of helium in the bulk gas stream leaving the inner spherical cavity, $[C^*_{He}]^i_b$ – CHEIB

(v)   The volumetric flow rate of the external argon stream – FLAO $(cm^3.s^{-1})$ (this was obtained from the exit molar flow using the Gas Laws)

(vi)   The total molar flux of helium through the spherical shell $\dot{N}_{He}$ – FLUXHE $(\mu mol.s^{-1})$

(vii)   The shape factor for the spherical shell, S – S (cm)

(iix)   The outer radius of the sphere, r^o – RADO (cm)

(ix)   The internal radius of the spherical shell, r^i – RADI (cm)

(x)   The Knudsen diffusion coefficient for helium, $D_{He,K}$ – DHEK $(cm^2.s^{-1})$

(xi)   The ratio of the argon flux to the helium flux, β – BETA

(xii)   The volumetric flow rate of the internal helium stream – FLHEI $(cm^3.s^{-1})$

Table 5.48   Experimental Data Obtained from Isobaric Experiments on Reduced Iron Spheres

Sphere	T	Ps	CHEOB	CHEIB	FLAO	FLHEI	FLUXHE	BETA	S	RADO	RADI	DHEK
X γ=0.5894	292	1.095	0.1216	0.8740	2.61	2.72	36.13	0.332	10.63	1.325	0.550	2.800
	898	1.112	0.1623	0.7880	8.60	8.40	54.95	0.337	10.63	1.325	0.550	4.800
Y γ=0.5912	292	1.116	0.1029	0.9320	3.46	5.47	38.24	0.409	14.16	1.198	0.594	2.94
	898	1.109	0.1720	0.7760	8.44	8.53	62.22	0.340	14.16	1.198	0.594	5.14
W γ=0.5845	292	1.122	0.1470	0.8960	3.12	4.69	52.80	0.367	16.39	1.270	0.670	2.94
	898	1.115	0.1912	0.7523	8.82	9.80	67.23	0.389	16.39	1.270	0.670	5.14

Table 5.49 Experimental Data Obtained from Isobaric
Experiments on Reduced Iron Spheres after sintering

Sphere	T	Ps	CHEOB	CHEIB	FLAO	FLHEI	FLUXHE	BETA	S	RADO	RADI	DHEK
Y γ=0.5729	292	1.138	0.2020	0.9140	2.30	5.66	58.72×10^{-6}	0.335	14.16	1.198	0.594	3.81
Z	292	1.122	0.2050	0.9110	2.50	7.03	56.78×10^{-6}	0.369	14.90	1.210	0.612	3.31
γ=0.5692	898	1.108	0.2065	0.7340	8.29	11.34	76.4×10^{-6}	0.357	14.90	1.210	0.612	6.33

Table 5.50   Experimental Data Obtained from Isobaric Experiments on Lime Spheres at 292K

Sphere	PS	CHEOB	CHEIB	FLAO	FLHEI	FLUXHE	BETA	S	RADO	RADI	DHEK
71 $\gamma=0.5877$	1.098	0.2160	0.8670	2.61	5.03	72.53	0.334	18.10	1.162	0.650	0.73
72 $\gamma=0.5732$	1.101	0.1915	0.8920	2.66	5.33	62.20	0.356	16.87	1.160	0.636	0.73
73 $\gamma=0.5904$	1.100	0.1945	0.8600	3.13	5.16	72.50	0.345	19.80	1.158	0.675	0.73

The values of the variables listed in Tables 5.48 to 5.50 were fed into the computer programme for each sphere in turn and the the computer programme run. The programme computed the mass transfer coefficients and then the surface concentrations. After the iterative solution of equations (5.4.3) and (5.4.4), the programme provided values of the output variables listed below. The values obtained are presented in Table 5.51 for the reduced iron spheres, in Table 5.52 for the sintered iron spheres and in Table 5.53 for the decomposed calcium carbonate spheres.

The output variables are:-

(i) The total molar concentration in the system, C_T - CT $(mol.cm^{-3})$

(ii) The binary molecular diffusion coefficient, D_{He-Ar} - DHA$(cm^2.s^{-1})$ (calculated from the correlation by Fuller, Schettler and Giddings[87])

(iii) The mass transfer coefficient of the external surface of the sphere, $\propto^o$ - ALFAO $(cm.s^{-1})$

(iv) The mass transfer coefficient at the internal surface of the sphere, $\propto^i$ - ALFAI $(cm.s^{-1})$

(v) The mole fraction of helium in the gas mixture at the external surface of the sphere, $[C^*_{He}]^o_s$ - CHEOS

(vi) The mole fraction of helium in the gas mixture at the internal surface of the sphere, $[C^*_{He}]^i_s$ - CHEIS

(vii) The effective molecular diffusion coefficient through the porous shell, $D_{He-Ar,eff}$ - DHEEFF $(cm^2.s^{-1})$

Table 5.51   Computed Data For Isobaric Experiments on Reduced Iron Speres

Sphere	T	CO	DHEEFF	DHA	CT	ALFAO	CHEOS	ALFAI	CHEIS
X	292	0.1150	0.072	0.642	4.569×10^{-5}	1.029	0.1542	2.197	0.8242
X	898	0.1040	0.428	4.521	1.509×10^{-5}	6.371	0.1859	12.880	0.7430
Y	292	0.0770	0.047	0.631	4.657×10^{-5}	1.264	0.1374	2.028	0.8903
Y	898	0.0913	0.383	4.533	1.505×10^{-5}	6.933	0.2021	11.825	0.7296
W	292	0.1054	0.064	0.627	4.680×10^{-5}	1.079	0.1943	2.347	0.8564
W	898	0.0906	0.378	4.508	1.513×10^{-5}	6.529	0.2211	12.606	0.7152

Table 5.52   Computed Data for Isobaric Experiments
              on Sintered Iron Spheres

Sphere	T	CO	DHEEFF	DHA	CT	ALFAO	CHEOS	ALFAI	CHEIS
Y	292	0.1445	0.0873	0.6185	4.749×10^{-5}	1.0594	0.2589	2.5548	0.8621
Z	292	0.1323	0.0812	0.6270	4.682×10^{-5}	1.0710	0.2590	2.5017	0.8625
	898	0.1318	0.5460	4.5370	1.503×10^{-5}	6.8610	0.2420	12.487	0.6806

Table 5.53   Computed Data for Isobaric Experiments on Lime Spheres At 292 K

Sphere	CO	DHEEFF	DHA	CT	ALFAO	CHEOS	ALFAI	CHEIS
71	0.2135	0.115	0.641	4.582×10^{-5}	1.143	0.2867	2.259	0.8006
72	0.1615	0.090	0.639	4.594×10^{-5}	1.147	0.2535	2.335	0.8370
73	0.1832	0.101	0.640	4.590×10^{-5}	1.176	0.2648	2.127	0.7949

5.5   RESULTS FOR THE NON-ISOBARIC DIFFUSION EXPERIMENTS

In order to test the validity of the Dusty Gas Model for
binary gas mixtures as described in Section 3.2 and in
particular the validity of the solutions to equations (3.46),
(3.50) and (3.52), it is necessary to have experimental data
for diffusion under non-isobaric conditions. The series of
counter current diffusion experiments described in Section
4.4.4 were therefore carried out on the spheres for which
the isobaric diffusion results listed in Section 5.4 had
been obtained, the only difference being that the pressure
drop across the spherical shell was maintained at a constant
non-zero value. The experimental data obtained in these
experiments are listed in Tables 5.54 to 5.65.

The computer solution to the Dusty Gas Model equations for
non isobaric diffusion in binary gas mixtures is outlined in
Section 3.4.2 and the FORTRAN programme that carried out the
computations is listed in Appendix 4. Variables involved in
this programme that had already been used in analysing the
isobaric results were given the same names in the FORTRAN
programme as they had in the isobaric MBASIC programme. In
addition, since total partial pressures were involved in the
computations, certain additional variables were involved as
listed below. The experimentally measured values of all the
variables involved are presented in the tables listed under
their computer name. Each table presents data obtained on
an individual sphere in order of increasing pressure

difference. As before, the units in which the data

presented are those specified in the lists in this and the

previous section.

The additional variables involved are:-

  (i)   The partial pressure of helium in the external

     bulk gas phase $[P_{He}]_{b,2}$ - PHEO (atm)

  (ii)   The partial pressure of helium in the internal

     bulk gas phase $[P_{He}]_{b,1}$ - PHE1 (atm)

  (iii)   The total pressure in the gas phase outside the

     sphere, $[P_T]$ - PTOO (atm)

  (iv)   The total pressure in the gas phase inside the

     sphere, $[P_T]_1$ - PTOI (atm)

In addition to the variables measured in the non-isobaric

experiments, the computer solution to the theoretical

equations involved the diffusion properties of each sphere

that had been obtained from analysis of the permeability

and isobaric diffusion experiments. The relevant values are

also listed in the tables under their computer name. The

only new variable name is for:-

   The average slope of the permability versus temperature

   curve, B_o/μ - BOVMU ($cm^2.s^{-1}atm^{-1}$)

The values of this variable used in the computer programme

have been calculated for the gas mixture of average composition in each experiment from the helium permeability results using the relation:-

$$\left[\frac{B_o}{\mu_{gas}}\right]_{prog} = \left[\frac{B_o}{\mu_{He}}\right]_{perm} \quad X \quad \frac{\mu_{He}}{\mu_{gas}} \qquad (5.4.19)$$

Table 5.54   Experimental Data Obtained During Non-Isobaric Experiments on Sphere X at 292 K

RUN	p ($10^{-3} \cdot$atm)	BETA	FLUXHE 10^6	PHEO	PHEI	PTOO	PTOI	S	RADO	RADI	FLAO	FLHEI	DHEEFF	DHEK	CO	BOVMU
													DIFFUSION		PROPERTIES	
2	10	1.459	23.27	0.10381	0.8981	1.100	1.090	10.63	1.325	0.550	3.230	3.630	0.072	2.80	0.1150	5.49
3	18	4.380	12.35	0.07611	0.8287	1.104	1.086	10.63	1.325	0.550	3.200	3.760	0.072	2.80	0.1150	5.49
4	24	9.330	8.27	0.05463	0.7865	1.107	1.083	10.63	1.325	0.550	4.820	3.180	0.072	2.80	0.1150	5.49

Table 5.55 Experimental Data Obtained in Non-Isobaric Experiments on Reduced Iron Sphere X at 898 K

RUN	p $(10^{-3} \cdot atm)$	BETA	FLUXHE 10^6	PHEO	PHEI	PIOO	PIOI	S	RADO	RADI	FLAO	FLHEI	DHEEFF	DHEK	CO	BOVM
					EXPERIMENTAL DATA								DIFFUSION		PROPERTIES	
2	18	0.568	46.10	0.16815	0.8502	1.121	1.103	10.63	1.325	0.550	8.75	9.00	0.428	4.80	0.1040	3.59
3	46	0.960	35.86	0.15072	0.8014	1.129	1.083	10.63	1.325	0.550	8.64	11.41	0.428	4.80	0.1040	3.59
4	55	1.350	28.80	0.13273	0.7869	1.133	1.078	10.63	1.325	0.550	8.67	9.16	0.428	4.80	0.1040	3.59
5	85	2.850	18.00	0.10109	0.7322	1.154	1.069	10.63	1.325	0.550	8.08	9.63	0.428	4.80	0.1040	3.59

Table 5.56 Experimental Data Obtained During Non-Isobaric
Experiments on Reduced Iron Sphere Y at 292 K

RUN	p (10^{-3}·atm)	BETA	FLUXHE 10^6	PHEO	PHEI	PTOO	PTOI	S	RADO	RADI	FLAO	FLHEI	DHEEFF	DHEK	CO	BOVM
						EXPERIMENTAL DATA							DIFFUSION		PROPERTIES	
2	12	1.282	22.60	0.09116	0.9965	1.122	1.170	14.16	1.198	0.594	3.44	5.49	0.047	2.94	0.077	5.95
3	20	3.540	13.94	0.08467	0.9329	1.126	1.106	14.16	1.198	0.594	3.15	5.62	0.047	2.94	0.077	5.95
4	24	7.800	10.00	0.07690	0.8676	1.128	1.104	14.16	1.198	0.594	3.83	5.66	0.047	2.94	0.077	5.45

Table 5.57   Experimental Data Obtained In Non-Isobaric Experiments on Reduced Iron Sphere Y at 898 K

RUN	p $(10^{-3} \cdot$atm$)$	BETA	FLUXHE 10^6	PHEO	PHEI	PTOO	PTOI	S	RADO	RADI	FLAO	FLHEI	DHEEFF	DHEK	CO	BOV
					EXPERIMENTAL DATA								DIFFUSION		PROPERTIES	
2	24	0.778	52.83	0.17319	0.8172	1.121	1.097	14.16	1.198	0.594	10.67	11.40	0.383	5.14	0.0913	3.0:
3	40	1.200	40.00	0.15072	0.7296	1.129	1.089	14.16	1.198	0.594	10.57	9.81	0.383	5.14	0.0913	3.0:
4	68	2.800	24.02	0.12516	0.6450	1.143	1.075	14.16	1.198	0.594	10.53	7.87	0.383	5.14	0.0913	3.0:
5	92	6.400	15.61	0.11720	0.5889	1.155	1.063	14.16	1.198	0.594	10.16	9.80	0.383	5.14	0.0913	3.0:

Table 5.58   Experimental Data Obtained in Non-Isobaric Experiments
on Reduced Iron Sphere W at 292 K

				EXPERIMENTAL DATA									DIFFUSION PROPERTIES			
RUN	p (10⁻³·atm)	BETA	FLUXHE 10⁶	PHEO	PHEI	PTOO	PTOI	S	RADO	RADI	FLAO	FLHEI	DHEEFF	DHEK	CO	BOVN
2	8	1.174	34.13	0.12667	0.9413	1.126	1.118	16.39	1.270	0.670	3.43	5.22	0.064	2.94	0.1054	5.9
3	16	2.990	21.07	0.10170	0.8700	1.130	1.114	16.39	1.270	0.670	3.63	5.02	0.064	2.94	0.1054	5.9

304

Table 5.59   Experimental Data Obtained in Non-Isobaric Experiments on Reduced Iron Sphere W at 898 K

| | | | | E X P E R I M E N T A L   D A T A | | | | | | | | | | DIFFUSION | PROPERTIES | |
RUN	p $(10^{-3} \cdot$atm$)$	BETA	FLUXHE 10^6	PHEO	PHEI	PTOO	PTOI	S	RADO	RADI	FLAC	FLHEI	DHEEFF	DHEK	CO	BOV
2	16	0.567	57.65	0.20231	0.8235	1.123	1.107	16.39	1.270	0.670	10.60	8.41	0.378	5.14	0.0906	3.0
3	33	1.065	43.20	0.18784	0.7758	1.134	1.096	16.39	1.270	0.670	10.41	8.59	0.378	5.14	0.0906	3.0
4	45	1.350	37.90	0.18476	0.7751	1.137	1.092	16.39	1.270	0.670	10.38	8.25	0.378	5.14	0.0906	3.0
5	56	2.840	22.78	0.18167	0.7710	1.148	1.082	16.39	1.270	0.670	10.28	6.85	0.378	5.14	0.0906	3.0

Table 5.60 Experimental Data Obtained in Non-Isobaric Experiments on Sintered Iron Sphere Y at 292 K

RUN	p $(10^{-3} \cdot \text{atm})$	BETA	FLUXHE 10^6	PHEO	PHEI	PTOO	PTOI	S	RADO	RADI	FLAO	FLHEI	DHEEFF	DHEK	CO	BOVN
2	4	0.679	49.80	0.21888	1.0269	1.140	1.136	14.16	1.198	0.594	2.98	7.16	0.087	3.81	0.1445	8.29
3	8	1.166	37.86	0.19471	0.9967	1.142	1.134	14.16	1.198	0.594	2.95	7.17	0.087	3.81	0.1445	8.29
4	14	2.940	22.79	0.15456	0.9352	1.145	1.131	14.16	1.198	0.594	2.91	7.03	0.087	3.81	0.1445	8.29
5	16	5.670	15.40	0.12558	0.8805	1.146	1.130	14.16	1.198	0.594	2.81	7.05	0.087	3.81	0.1445	8.29

EXPERIMENTAL DATA — DIFFUSION — PROPERTIES

Table 5.61   Experimental Data Obtained During Non-Isobaric Experiments on Sintered Iron Sphere Z at 292 K

RUN	p (10^-3·atm)		EXPERIMENTAL DATA											DIFFUSION		PROPERTIES	
		BETA	FLUXHE 10^6	PHEO	PHEI	PTOO	PTOI	S	RADO	RADI	FLAO	FLHEI	DHEEFF	DHEK	CO	BOV
2	5	0.949	40.30	0.20250	0.9892	1.125	1.119	14.90	1.210	0.612	2.340	7.10	0.081	3.81	0.1323	8.2
3	9	1.960	26.60	0.17187	0.9572	1.127	1.117	14.90	1.210	0.612	2.400	7.28	0.081	3.81	0.1323	8.2
4	14	3.730	20.00	0.16935	0.9054	1.129	1.115	14.90	1.210	0.612	2.560	7.37	0.081	3.81	0.1323	8.2

Table 5.62   Experimental Data Obtained in Non-Isobaric Experiments on Sintered Iron Sphere Z at 898 K

RUN	p (10⁻³·atm)	BETA	FLUXHE 10^6	PHEO	PHEI	PTOO	PTOI	S	RADO	RADI	FLAO	FLHEI	DHEEFF	DHEK	CO	BOV
						EXPERIMENTAL DATA								DIFFUSION PROPERTIES		
2	24	0.839	57.64	0.21448	0.7782	1.120	1.096	14.90	1.210	0.612	9.61	11.51	0.546	6.33	0.1318	5.01
3	38	1.369	44.24	0.20173	0.7514	1.127	1.089	14.90	1.210	0.612	9.31	11.94	0.546	6.33	0.1318	5.01
4	44	1.898	36.73	0.19323	0.7287	1.130	1.086	14.90	1.210	0.612	9.26	12.04	0.546	6.33	0.1318	5.01
5	56	3.100	25.90	0.16915	0.6512	1.136	1.080	14.90	1.210	0.612	8.67	10.57	0.546	6.33	0.1318	5.01

Table 5.63   Experimental Data Obtained in Non-Isobaric Experiments on Calcium Oxide Sphere No. 71 at 292 K

RUN	p (10⁻³·atm)	BETA	FLUXHE 10⁶	EXPERIMENTAL DATA									DIFFUSION PROPERTIES			
				PHEO	PHEI	PTOO	PTOI	S	RADO	RADI	FLAO	FLHEI	DHEEFF	DHEK	CO	BOV
2	8	0.518	67.37	0.23803	0.9484	1.102	1.094	18.10	1.162	0.650	3.11	5.73	0.115	0.730	0.2135	1.7
3	20	0.704	55.89	0.22320	0.9291	1.108	1.088	18.10	1.162	0.650	3.04	5.88	0.115	0.730	0.2135	1.7
4	28	0.987	48.31	0.21180	0.9052	1.112	1.084	18.10	1.162	0.650	3.04	6.12	0.115	0.730	0.2135	1.7
5	39	1.593	38.00	0.19422	0.9011	1.118	1.079	18.10	1.162	0.650	3.04	6.12	0.115	0.730	0.2135	1.7
6	48	2.050	32.23	0.18790	0.8549	1.122	1.074	18.10	1.162	0.650	3.02	6.22	0.115	0.730	0.2135	1.7
7	52	4.540	19.33	0.15520	0.7975	1.129	1.067	18.10	1.162	0.650	2.98	6.19	0.115	0.730	0.2135	1.7

Table 5.64 Experimental Data Obtained in Non-Isobaric Experiments on Calcium Oxide Sphere No. 72 at 292 K

| | | | | | EXPERIMENTAL DATA | | | | | | | | DIFFUSION | | PROPERTIES | |
RUN	p (10⁻³·atm)	BETA	FLUXHE 10⁶	PHEO	PHEI	PTOO	PTOI	S	RADO	RADI	FLAO	FLHEI	DHEEFF	DHEK	CO	BO
2	6.0	0.468	55.16	0.20200	0.9673	1.104	1.098	16.87	1.162	0.636	3.10	4.77	0.090	0.730	0.1615	1.7
3	16.0	0.667	45.85	0.19075	0.9432	1.109	1.093	16.87	1.162	0.636	3.09	4.67	0.090	0.730	0.1615	1.7
4	26.0	0.997	37.54	0.17267	0.9171	1.114	1.088	16.87	1.162	0.636	3.05	4.75	0.090	0.730	0.1615	1.7
5	50.0	2.850	19.53	0.14356	0.8662	1.126	1.076	16.87	1.162	0.636	3.00	4.94	0.090	0.730	0.615	1.7

Table 5.65   Experimental Data Obtained in Non-Isobaric Experiments on Calcium Oxide Sphere No. 73 at 292 K

RUN	p (10⁻³·atm)	BETA	FLUXHE 10⁶	PHEO	PHEI	PTOO	PTOI	S	RADO	RADI	FLAO	FLHEI	DHEEFF	DHEK	CO	BO
2	13	0.616	60.02	0.19742	0.9148	1.106	1.093	19.80	1.158	0.675	3.21	5.40	0.101	0.73	0.1832	1.
3	23	0.873	52.00	0.17776	0.8954	1.111	1.088	19.80	1.158	0.675	3.24	5.90	0.101	0.73	0.1832	1.7
4	32	1.356	39.10	0.16517	0.8672	1.116	1.084	19.80	1.158	0.675	3.26	5.04	0.101	0.73	0.1832	1.7
5	74	7.910	13.32	0.09209	0.7207	1.137	1.063	19.80	1.158	0.675	3.31	5.68	0.101	0.73	0.1832	1.7

p in units of 10^{-3}·atm; FLUXHE in units of 10^{6}.

EXPERIMENTAL DATA   DIFFUSION   PROPERTIES

6.1 OVERVIEW OF THE WORK CARRIED OUT

The experimental technique developed by Campbell[50] for measuring gas permeabilities and diffusivities through porous material has been refined. The technique involves the manufacture of a spherical shell of the porous material under investigation and its study in an apparatus that can maintain gases of known composition at known pressures within the shell and outside it, at the same time as determining the diffusion and flow fluxes across the shell.

The technique has been used to carry out the measurement strategy developed by Mason et alia[83] from the predictions of the Dusty Gas Model. This strategy involves the measurement of gas permeabilities at a range of different total pressures and the measurement of one effective binary diffusion coefficient under isobaric conditions. The Dusty Gas Model indicates that three parameters, namely A_O, B_O and C_O, can be calculated from the results of these experiments. Two of them, A_O and B_O, are determined from the permeability measurements and are related to Knudsen diffusion behaviour and viscous flow of gases through the media. The third parameter, C_O, related to molecular diffusion through the solid, may be calculated from the results of the isobaric binary diffusion experiments together with the Knudsen parameter.

This experimental strategy has been carried out using argon and helium in porous iron produced by the reduction of sintered

hematite compacts, in porous iron compacts produced by the further sintering of such compacts after reduction and in compacts of porous lime produced by decomposing calcium carbonate. Measurements have been carried out at several different temperatures between 25°C and 950°C. Some room temperature results have also been obtained using nitrogen. In addition, to these experiments, the diffusive flow of helium and argon through the materials has been studied under non-isobaric conditions. The results obtained represent the most comprehensive experimental study of the Dusty Gas Model that has been carried out to date.

The Dusty Gas Model itself has been restated in a more direct form and generalised equations presented which, for the first time, incorporate viscous flow terms in the diffusion equations for multi-component gas mixtures. A coherent method of solution has also been developed for these equations for binary gas mixtures within porous solids of any geometric shape and this method has been applied to a number of different situations.

6.2. ASSESSMENT OF ERRORS IN THE EXPERIMENTAL WORK

The experimental technique was successfully extended to a wider range of materials and to higher temperatures than those involved in Campbell's work. Measurements made on individual spheres showed a high degree of reproducibility as can be seen from the high correlation factors obtained for the straight line relationships linking individual permeability measurements to the total system pressure - see Figures 5.8 to 5.42. Further internal evidence for the accuracy of the experimental work is provided by the isobaric diffusion measurements where separate mass balances allowed two independent assessments to be made of the diffusion fluxes through the porous spherical shells. Twin values of the helium flux are shown in Table 5.43 and their mean ratio is 1.02 with a standard deviation of 0.04. Since the calculation of these mass balances involves gas flow rates determined from the reading of four orifice meters and gas compositions determined using gas chromatography, 4% is a satisfactorily low standard deviation to have achieved.

The scales on the orifice meters were calibrated in 2 mm intervals and could be read to $\pm$ 20% of this interval. The heights of manometric fluid to be read were of the order of 4 cm giving a reading error of the order of $\pm$ 1%. This error is involved in both the calibration of the meters and their use to determine experimental gas flow rates and so the gas flow rate error is of the order of $\pm$ 2%.

The Wosthoff pump used in calibrating the gas chromatograph

has a stated accuracy of $\pm$ 0.1% and the error associated

with the sampling valve on the chromatograph is of the same

order. The largest error involved in the gas chromatography

would be associated with the measurement of peak height.

Peak heights varying between 5 and 15 cm were measured and

could be read to an accuracy of about 0.5 mm giving a

maximum error of 1%. Since the two mass balances referred

to above involved the determination of four gas flows and

two gas compositions, it can be seen that the standard

deviation is some 30% of the aggregated maximum reading

error - the type of relationship that would be expected.

The determination of permeability values involved

measurement of the gas flow through and the pressure

difference across the porous shell as well as determination

of its shape factor. All the permeability determinations

carried out on a given sphere would involve the same shape

factor, so that their relative errors would be independent

of the error in the shape factor and would only involve the

errors in the pressure difference and the flow rate. The

minimum pressure differences involved was about 2 cm of

mercury and could be read to an accuracy of 0.5 mm, ie to an

accuracy of $\pm$2.5%. Including the effect of the error in the

flow rate discussed above, we can see that the maximum

relative error in permeability measurements on a given

sphere would be of the order of 4.5%, which is in keeping

with the data shown on Figures 5.8 to 5.42.

The slope of the lines in these figures provides the value of

315

B_o. It is shown in Appendix 5 that the standard deviation of the slope, m, is related to the correlation coefficient, R, by the equation:-

$$\frac{S_e(m)}{m} = \sqrt{\frac{1/R^2 - 1}{n}} \qquad (6.1)$$

Values of the correlation coefficient are shown in Tables 5.5 to 5.42 to vary in the range 0.99 to 0.94 with an average at about 0.97, there being some 10 readings in each table. Thus the standard deviation of the slopes in these figures is about 8%.

Calculation of the shape factor involved determination of the inner and outer radii of the porous shell. The outer radius was measured directly and the inner radius was determined as the difference between the outer radius and the measured shell thickness. The measurements were carried out using a micrometer, a number of different measurements being made in different directions and the mean and standard deviation determined. A typical value for the mean outer diameter was 2.15 cm with a standard deviation of 0.020 cm, and for the mean thickness, 0.67 cm with a standard deviation of 0.029 cm. Thus the percentage error in the outer radius is about 1% and that in the thickness is about 4%. Variations in the shell thickness were principally due to difficulties in placing the Wood's metal sphere precisely in the centre of the Gelflex cavity during the manufacture of the original compacts. Thus the centres of the inner and outer surfaces of the porous spherical shell were not precisely coincident

so that the shell thickness varied. The effect that this would have on errors in the calculated shape factor values is difficult to determine since the effect of the thicker portions of the shell would tend to compensate effects due to the thinner regions. The most straightforward way to estimate the error in the shape factor is to consider its evaluation as involving the determination of the mean area of the shell and its mean thickness, the error in the mean area being twice that involved in determining the outer radius. This would suggest that the error in determining the shape factor is about $\pm 6\%$.

The value of the Knudsen diffusion coefficient for one sphere can be regarded as one value of the permeability for that sphere. However, the evaluation of the permeability as a property of the porous material from which the sphere is made does involve the value of the shape factor of that sphere. Thus the error in the Knudsen diffusion coefficients through the porous materials will be of the order of the sum of the errors in the shape factor and in the permeability ie it will be about $\pm 10\%$. The significance of this figure will be considered further in Section 6.4 of the discussion.

Similarly, the calculation of values of B_o for a given material involves an error arising from the determination of the slope of the line, together with an error arising from

317

the determination of the shape factor. Thus we can see that the error in the values of B_O will be of the order of 14%.

Determination of the values of C_O in the isobaric diffusion experiments involves measurement of four flow rates and two gas compositions and, in addition, it involves the determination of the surface gas compositions from the mass transfer processes inside and outside the sphere. Data presented in Section 5.4.3.4 show that the partial pressure differences across the gas phase boundary layers amount to some 20% of the partial pressure differences between the surface gas compositions inside and outside the sphere, with the difference being relatively greater for the experiments involving lime. The lime shells were thinner than the iron shells with a correspondingly bigger shape factor. Thus the diffusion fluxes through the lime shells were greater than through the iron shells and, although the internal gas flow rate was greater in the lime experiments, the resulting increase in the mass transfer coefficient was insufficient to allow for the overall greater mass transfer flux without increasing the proportional partial pressure difference across the boundary layer. The lime shell thickness was thinner than the iron shell thickness because the decomposition of calcium carbonate results in a larger decrease in volume than that associated with the reduction of hematite.

Thus we can see that the mass transfer processes correspond to a significant proportion of the differences in partial

318

pressure measured between the inner and outer gas compositions and ignoring the effect of these processes would produce a major error. Although the convection mass transfer resistances could not be measured directly in this work, the analogy technique that was used does not produce too great an error. Individual mass transfer coefficients in the naphthalene experiments are shown in Figure 5.44 and it can be seen that their mean error from the lines drawn in that figure is better than 5%. If, however, we take this as the error involved in assessing the total of the partial pressure drops across the two gas phase 'boundary layers', we can see that this would produce a further error of 1% in the difference between the surface partial pressures either side of the spherical shell. Thus the error involved in measuring these partial pressure differences is 3%, 2% being the error involved in determining the two bulk phase partial pressures using the gas chromatograph.

Determination of values of C_O entails determining this partial pressure difference, the diffusive flux through the spherical compact and the shape factor of the spherical shell. The diffusive flux is calculated by multiplying one gas flow rate by the corresponding gas composition, the error in both these readings being 1%, as has already been discussed. Thus the error involved in determining the diffusive flux is about 2% (this gives an error in β of about 4%, incidently). The error in determining the shape factor has already been established as being about 6%.

319

In addition to these errors, some error will ensue in the determination of C_0 from the involvement of $\hat{\delta}_A$ in the calculation of C_0 from the experimental results. The influence of this error is extremely difficult to assess since the involvement of $\hat{\delta}_A$ arises in the iterative calculation process. However, the values of $\hat{\delta}_A$ found in this work are of the order of 0.9, the departure from unity being due to the value of the Knudsen diffusion coefficient. Since we have already assessed the error in the Knudsen diffusion coefficient as being about 10%, the error in $\hat{\delta}_A$ would be about 1%. However, the effect of this error in this work will probably be somewhat greater since values of the Knudsen diffusion coefficient used in the calculation of C_0 were not always available for the sphere on which the isobaric experiments had been carried out. The variability introduced by this fact would probably result in an error of some 2 to 3%. Accumulating these different errors together suggest that the error in determining the values of C_0 is of the order of 14%.

A further potential source of error has been considered. As will be discussed subsequently, the flux ratio measured in the isobaric experiments is not precisely equal to the theoretical ratio that was used in deriving equation (3.61) – the equation from which C_0 was calculated from the experimental results. The error that might result from this discrepancy was examined by analysing one set of experimental results using the theoretical value of β and

then the most extreme experimental value. Values of the

surface concentrations, the effective binary diffusion

coefficient and C_O calculated using the two values are shown

in Table 6.1. The table shows that the two values

effectively give the same computed values of the variables

so that no sensible error is likely to occur from

differences between the theoretical and experimental values

of β .

Table 6.1   The effect of β values on the analysis of
            the isobaric results for iron sphere Y at 292 K

	$\beta = 0.3160$	$\beta = 0.409$
$[C^*_{He}]^o_s$	0.1374	0.1400
$[C^*_{He}]^i_s$	0.8903	0.8902
C_O	0.0770	0.0772
$D_{AB,eff}$	0.0485	0.0487

The only errors that remain to be discussed are those

involved in the non-isobaric experiments. Three

measurements were made in these experiments, the diffusive

flux of each gas through the porous shell and the pressure

drop across it. The error in the diffusion flows has

already been assessed as 1%. The pressure drop was read on

a water manometer which could be read to 0.5 mm, the minimum

pressure drop in the experiments being 4 cm of water. Thus

the error in measuring the pressure drop is also about 1%.

The significance of these errors will be discussed in a

subsequent section.

6.3. THE EXPERIMENTAL DETERMINATION OF GAS DIFFUSION AND FLOW PARAMETERS IN POROUS MATERIAL

The assessment of errors discussed in the previous section shows that the experimental methods used in this work for studying gas permeation and isobaric binary diffusion through porous solids are capable of providing tolerably accurate values for the parameters that control the diffusion and flow of gases through porous media. The experimental work, together with the theoretical development presented in Chapter 3, show that measurement of binary diffusion fluxes alone does not provide unambiguous values of effective diffusion coefficients. As equations (3.61) and (3.62) show, the results of isobaric diffusion experiments cannot be analysed unless a value of the Knudsen diffusion coefficient is available for the calculation of δ_A. The Knudsen coefficient can only be measured directly by extrapolating permeability data down to zero system pressure, but relatively few workers[8, 33, 34, 48, 49, 50, 51] have undertaken the necessary permeability studies at the same time as their isobaric diffusion experiments. Only can these studies be considered as full experimental investigations of the diffusion and flow of gases in porous solids, since it is only the permeability experiments that allow B_O to be measured as well as the effective molecular and the Knudsen diffusion coefficients. An alternate technique for studying diffusion has been used[3,13,29,35] in which binary isobaric diffusion experiments have been

carried out at a number of different total pressures, this technique allowing A_O and C_O to be determined but not B_O. One investigation[11] that partly falls into this category, although an approximate equation was used to determine the effective diffusion coefficient, was carried out on porous iron produced by the reduction of hematite and will be discussed in greater detail later.

The majority of other workers have carried out isobaric diffusion measurements at one pressure only and without the necessary supporting permeability studies from which to determine the Knudsen diffusion coefficient, so that question marks must be placed against the values that they have obtained for C_O, or its equivalent.

The most credible of these values have been obtained by those authors[15,16,17,24,30,52,53,55,82] who have properly used equation (3.61) to analyse their results and have then estimated the Knudsen diffusion coefficient by applying the capillary pore model to specific surface areas measured by the B.E.T. adsorption technique or to mean pore radii determined by mercury porosimetry. Some other investigators have used equation (3.61) with $\hat{\delta}_A$ set equal to 1, assuming that the Knudsen diffusion coefficient is at least two orders of magnitude greater than the molecular diffusion coefficient as a result of the way the porous material was constructed[28,32].

Some of the earliest workers[31, 92, 93, 94] effectively
assumed that isobaric diffusion is synonimous with equi-
molar counter diffusion. The equation that they used to
analyse their experimental results was an integrated form of
equation (3.41) with the fluxes of A and B set equal and
opposite, this integrated form involving a linear driving
force rather than the logarithmic driving force that must
always appear with non-equimolar counter diffusion in binary
gas mixtures. The results of these earlier experiments
cannot be related to the bulk of more up to date work. It
is surprising, however, that so few of these more recent
investigators have combined permeability determinations with
binary diffusion experiments, since the permeability
determinations involved are no more difficult than the far
less reliable experimental strategies that are involved in
determining the Knudsen diffusion coefficient from specific
surface areas measured by the B.E.T. technique or pore sizes
measured by mercury porosimetry.

A further potential source of error that must be considered
when evaluating measurements of diffusion parameters in
porous solids is that due to the effects of mass transfer.
Campbell[50] used the technique employed in this work to
determine the actual contribution made by mass transfer and
found a similar large effect. On the other hand,
Turkdogan[13], by demonstrating that the diffusion
coefficients that he determined were independent of the
length of the specimen, showed that mass transfer had no

influence on his results . Virtually all the other investigators have used the bulk gas compositions either side of the diffusion path in analysing their results, implicitly assuming that the design of their diffusion cells was such that mass transfer effects presented no contribution to the overall transfer resistances between the bulk gas phases either side of their cell.

It is unfortunate that so few investigators have examined the validity of this assumption. A number of authors[12, 62], for example, have shown that similar assumptions made about kinetic investigations of gas solid reactions have been erroneous. It is possible, of course, that mass transfer processes in this work make an unusually high proportional contribution to the bulk phase partial pressure difference across the diffusion cell, but the contribution is such that to have ignored mass transfer effects would have produced major errors in the values reported.

6.4. THE VALIDITY OF THE DUSTY GAS MODEL

It is a basic premise of the Dusty Gas Model that the characteristics of the porous solid that control the diffusion and flow of gases through it can be specified in terms of phenomenological constants that are independent of the gases involved and of the temperature and total pressure at which the diffusion and flow processes take place - in other words that these characteristics are properties of the porous solid itself. Thus, once values of these parameters

have been determined for a certain porous material, the
Dusty Gas Model allows predictions to be made of diffusive
flow of any system of gases through the porous material
under a very wide range of conditions. In this work, the
characteristics are designated in terms of three parameters
- defined as A_O, the Knudsen diffusion parameter, B_O, the
viscous flow parameter and C_O, the molecular diffusion
parameter.

Although it is generally acknowledged that the parameters A_O
and B_O are independent of gas type[5] only very few tests
have been made on the wider validity of the model. Mason et
alia[20,32,33] carried out permeability, isobaric and non-
isobaric experiments in high and low permeability graphite
and showed that accurate predictions could be made of the
non-isobaric behaviour from the A_O, B_O and C_O values
determined from the permeability and isobaric diffusion
measurements. The results that they report suggested,
however, that A_O values determined for argon at 25°C were
slightly lower than those determined for helium. They also
report some limited isobaric diffusion measurements at 100°C
which showed that the value of the molecular diffusion
parameter, C_O, was constant over that limited temperature
range.

The work of Bradshaw and his coworkers[44] can only be
regarded as a partial test of the general validity of the
model. They measured hydrogen permeabilities in magnetite
produced by the reduction of hematite, reporting values for

326

A_O and B_O, and carried out diffusion experiments under conditions approximating to isobaric using nitrogen/carbon dioxide mixtures, allowing them to calculate values for C_O. These values were then used to estimate effective carbon monoxide and carbon dioxide diffusion coefficients at the elevated temperatures at which they carried out the reduction of the hematite. They showed that these estimated values were in keeping with the reaction model that they had proposed involving chemical rate constants that they had measured in independent kinetic experiments. They did not, however, measure effective diffusion coefficients at the high temperatures directly, so their results are no more than a partial test of the validity of the Dusty Gas Model.

In addition they carried out room temperature permeability measurements on hydrogen, helium and carbon dioxide as well as the room temperature diffusion measurements on binary carbon dioxide/nitrogen mixtures. Mean A_O and $B_O X10^{10}/cm^2$ values calculated from the results that they present graphically for each of the three gases are respectively 0.192 and 7.64 (hydrogen), 0.182 and 7.45 (helium) and 0.190 and 7.36 (carbon dioxide). The scatter of their B_O values was considerably greater than the scatter of the A_O values. The standard deviation for the B_O values was 91% of the mean value, for A_O it was 25% but the scatter was principally due to variation from pellet to pellet and not from gas to gas. However, their results do support the general conclusion that A_O and B_O values are independent of the permeating gas.

In the present work, permeability experiments have been carried out on helium and argon at high and low temperatures with a limited number of addition^{al} room temperature experiments on nitrogen. In addition, truly isobaric diffusion measurements have been made on helium/argon mixtures also at both high and low temperatures.

The measured permeability of the samples vary with the total pressure in accordance with equation (3.25) and in all cases a high degree of correlation with the straight line relationship was obtained. Knudsen diffusion coefficients and B_o/μ values obtained from the intercepts and slopes are shown in Tables 6.2, 6.3 and 6.4 for porous reduced iron, porous reduced iron that has been sintered and for lime. Values of the effective binary diffusion coefficients determined for the same three materials in the isobaric diffusion experiments are shown in Table 6.5.

The A_o, B_o and C_o values computed from these results for the three different materials have then been brought together in Tables 6.6, 6.7 and 6.8.

Table 6.2 Results from permeability measurements on reduced iron spheres

SPHERE	T (K)	PERMEABILITY EXPERIMENT			
		ARGON		HELIUM	
		$D_K/$ $(cm^2.s^{-1})$	$B_o/\mu/$ $(cm^2.s^{-1}.atm^{-1})$	$D_K/$ $(cm^2.s^{-1})$	$B_o/\mu/$ $(cm^2.s^{-1}.atm^{-1})$
Q	291	0.892	4.670	2.960	5.320
γ=0.5988 S=15.87(cm)	898	1.340	1.830	4.810	2.750
R	291	0.954	4.840	2.940	5.790
γ=0.6034 S=13.24(cm)	898	1.397	1.915	4.930	2.890
T	291	0.910	4.780	2.970	6.790
γ=0.6026 S=12.53(cm)	898	1.150	2.080	5.140	3.020
V	291	0.810	4.450	—	—
γ=0.6004 S=12.73(cm)	898	1.250	1.603	5.280	2.470
D*	291	—	—	—	—
γ=0.5812 S=12.60(cm)	898	1.360	2.280	—	—
X**	291	0.886	4.260	—	—
γ= 0.5894 S=10.63(cm)	898	1.510	2.390	—	—

* Sphere D was kept 5 hours at 825°C after reduction before permeability measurements were performed at 625°C.

** For sphere X both permeability and isobaric experiments were carried out.

329

Table 6.3   Results from permeability experiments on
            sintered iron spheres

| SPHERE | T (K) | PERMEABILITY EXPERIMENT | | | |
| | | ARGON | | NITROGEN | |
		$D_K/$ $(cm^2.s^{-1})$	$B_0/\mu/$ $(cm^2.s^{-1}.atm^{-1})$	$D_K/$ $(cm^2.s^{-1})$	$B_0/\mu/$ $(cm^2.s^{-1}.atm^{-1})$
A1	291	1.258	7.410	1.592	8.251
S=12.25(cm) γ=0.5753	898	2.220	3.540	–	–
B1	291	1.189	8.180	1.630	9.159
S=11.462(cm) γ=0.5708	898	2.003	4.022	–	–
C1	291	1.226	8.620	1.570	9.700
S=15.99(cm) γ=0.5727	898	2.150	4.170	–	–

Table 6.4 Results from permeability measurements on
          CaO spheres

SPHERE	T (K)	PERMEABILITY EXPERIMENT			
		ARGON		HELIUM	
		$D_K/$ $(cm^2.s^{-1})$	$B_o/\mu/$ $(cm^2.s^{-1}.atm^{-1})$	$D_K/$ $(cm^2.s^{-1})$	$B_o/\mu/$ $(cm^2.s^{-1}.atm^{-1})$
58	441	–	–	0.639	0.7890
γ=0.4618 S=14.02(cm)	1230	0.3397	0.3302	1.091	0.4130
59		–	–	–	–
γ=0.4572 S=13.88(cm)	1230	0.3962	0.2490	1.2639	0.3280
60	413	–	–	0.7695	0.7800
γ=0.4793 S=16.92(cm)	1230	0.3820	0.2377	1.3469	0.3531
62 γ=0.5680 S=19.48(cm)	1230	0.4420	0.4340	1.4190	0.5850
71[*] γ=0.5877 S=18.10(cm)	292	0.2308	1.5800	–	–

[*] The experiments for sphere 71 were carried out together
     with the diffusion experiments.

Table 6.5   Effective binary diffusion coefficients determined
from the isobaric diffusion experiments

MATERIAL	SPHERE	$T/$ (K)	$P/$ (atm)	$D_{He-Ar}/$ ($cm^2.s^{-1}$)	C_o	$D_{He-Ar,eff}/$ ($cm^2.s^{-1}$)
Reduced Iron	X	292	1.092	0.642	0.1150	0.074
	X	898	1.112	4.521	0.1040	0.470
	Y	292	1.116	0.631	0.0770	0.049
	Y	898	1.109	4.533	0.0913	0.414
	W	292	1.122	0.627	0.1054	0.067
	W	898	1.115	4.508	0.0906	0.408
Sintered Iron	Y	292	1.138	0.618	0.1445	0.089
	Z	292	1.122	0.627	0.1323	0.083
	Z	898	1.108	4.537	0.1318	0.598
Lime	71	292	1.098	0.641	0.2135	0.137
	72	292	1.101	0.639	0.1615	0.103
	73	292	1.100	0.640	0.1832	0.117

Table 6.6 Diffusion and flow parameters for the porous reduced iron spheres

SPHERE	T	PERMEABILITY EXPERIMENTS				ISOBARIC EXPERIMENTS
		Argon		Helium		Ar-He
		$A_o/*$	$B_o/$ (cm^2)	$A_o/*$	$B_o/$ (cm^2)	Co
Q $\gamma=0.5988$ S=15.87(cm)	291	0.3291	1.00×10^{-9}	0.3464	1.02×10^{-9}	
	898	0.2826	$0.91 x^{-10}$	0.3210	1.09×10^{-9}	
R $\gamma=0.6034$ S=13.24(cm)	291	0.3528	1.04×10^{-9}	0.3441	1.10×10^{-9}	
	898	0.2946	0.95×10^{-9}	0.3290	1.15×10^{-9}	
T $\gamma=0.6026$ S=12.53(cm)	291	0.3365	1.03×10^{-9}	0.3476	1.28×10^{-9}	
	898	0.2425	1.03×10^{-9}	0.3430	1.20×10^{-9}	
V $\gamma=0.6004$ S=12.73(cm)	291	0.2995	0.90×10^{-9}	-	-	
	898	0.2634	0.80×10^{-9}	0.3523	0.98×10^{-9}	
D $\gamma=0.5812$ S=12.60(cm)	898	0.2868	1.13×10^{-9}	-	-	
X $\gamma=0.5894$ S=10.63(cm)	291	0.3276	0.92×10^{-9}	-	-	0.1150
	898	0.3184	1.18×10^{-9}	-	-	0.1040
Y $\gamma= 0.5912$ S=14.16(cm)	291	-	-	-	-	0.0770
	898	-	-	-	-	0.0913
W $\gamma=0.5845$ S=16.39(cm)	291	-	-	-	-	0.1054
	898	-	-	-	-	0.0906

$*cm^2.s^{-1}(g.mol^{-1}.K^{-1})^{0.5}$

Table 6.7   Diffusion and flow parameters for the porous sintered iron

| SPHERE | T | PERMEABILITY EXPERIMENTS | | | | ISOBARIC EXPERIMENTS |
| | | Argon | | Nitrogen | | Ar-He |
		$A_o/{}^*$	$B_o/$ (cm^2)	$A_o/{}^*$	$B_o/$ (cm^2)	Co
A1	291	0.4660	1.59×10^{-9}	0.4938	1.36×10^{-9}	–
$\gamma = 0.5753$ S=12.25(cm)	898	0.4682	1.75×10^{-9}	–		–
B1	291	0.4405	1.75×10^{-9}	0.5060	1.52×10^{-9}	–
$\gamma = 0.5708$ S=11.46(cm)	898	0.4224	1.90×10^{-9}	–	–	–
C1	291	0.4542	1.85×10^{-9}	0.4870	1.62×10^{-9}	–
$\gamma = 0.5727$ S=15.99(cm)	898	0.4440	2.07×10^{-9}	–	–	–
Y $\gamma = 0.5729$ S=14.16(cm)	292	–	–	–	–	0.1445
Z	292	–	–	–	–	0.1323
$\gamma = 0.5692$ S=14.90(cm)	898	–	–	–	–	0.1318

* $cm^2 . s^{-1} (g.mol^{-1} . K^{-1})^{0.5}$

334

Table 6.8   Diffusion and flow parameters for the porous lime

| SPHERE | T | PERMEABILITY EXPERIMENTS | | | | ISOBARIC EXPERIMENTS |
| | | Argon | | Helium | | Ar-He |
		$A_o/*$	$B_o/$ (cm^2)	$A_o/*$	$B_o/$ (cm^2)	Co
58 $\gamma=0.4618$ $S=14.02(cm)$	441	–	–	0.0608	2.00×10^{-9}	–
	1230	–	–	0.0622	2.00×10^{-10}	–
59 $\gamma=0.4572$ $S=13.88(cm)$	1230	0.0713	1.51×10^{-10}	0.0721	1.59×10^{-10}	–
60 $\gamma=0.0.4793$ $S=16.92(cm)$	413	–	–	0.0610	1.88×10^{-10}	–
	1230	0.0688	1.45×10^{-10}	0.0768	1.71×10^{-10}	–
62 $\gamma=0.5680$ $S=19.48(cm)$	1230	0.0796	2.64×10^{-10}	0.0809	2.83×10^{-10}	–
71 $\gamma=0.5877$ $S=18.10(cm)$	292	0.0853	3.38×10^{-10}	–	–	0.2135
72 $\gamma=0.5732$ $S=16.87(cm)$	292	–	–	–	–	0.1615
73 $\gamma=0.5904$ $S=19.80(cm)$	292	–	–	–	–	0.1832

* $cm^2.s^{-1}(g.mol^{-1}.K^{-1})^{0.5}$

335

For the basic assumption underlying the Dusty Gas Model to be valid, the values appearing in these tables for any given material should be the same, independent of the temperature at which they were determined and independent of the gases that were involved. As the tables show, the values are not all precisely the same and, of course, the errors involved in their determination would ensure that this would be the case. To examine the validity of the Dusty Gas Model, then, we have to determine whether the scatter of the values in Tables 6.6, 6.7 and 6.8 arises because of random error or because of some systematic error.

We can carry out this examination in two ways. In the first place, we can assume that all the values of any one parameter for any one material do, in fact, belong to a single population of values, determine the standard deviation of that population and compare that with the assessment of errors made in Section 6.2. Table 6.9 contains the mean values of the three parameters for the three different materials together with the standard deviations of those means expressed as absolute values, and as percentages of the means. The data for the lime spheres has been grouped into two bands for two different mean porosities.

The table shows that the percentage standard deviation for the value of A_o varies between 4% and 10%, which compares with the value of 10% assessed in Section 6.2 in the light of a critical appraisal of the method of measurement.

Similarly, we find that the standard deviation of B_O, shown in Table 6.9, varies between 11% and 13%, compared with the error of 14% assessed in Section 6.2. Finally, the table shows that the deviation for C_O varies in the range from 1% to 14%, compared with an assessed error of 14%.

The assessment of errors carried out in Section 6.2 is not a precise procedure but we can see that the assessed errors and the standard deviations are very close. This clearly suggests that variations in the measured values of the parameters are, in fact, due to random experimental error, not due to any systematic error which might suggest that the theory is invalid.

The second approach that we can adopt formally questions whether or not all the values of one of the parameters measured for a given material come from the same population. Each set of values determined for a given gas or for a given temperature constitute a sample which might or might not come from the same population. If they do, variations between their separate means will arise due to sampling errors alone. If they do not, these variations will be greater than could be reasonably expected to arise from random sampling variations. Whether or not this is the case can be tested using the F-test.

Appendix 6 outlines the F-test as well as the supporting L-test. The L-test examines whether or not a series of samples of values of a variable come from normal populations with the

Table 6.9   Mean values and standard deviations for the diffusion and flow parameters of the materials studied

Material	$A_o/cm^2.s^{-1}(g.mol^{-1}.K^{-1})0.5$				$B_o \times 10^{+9}/[cm^2]$			C_o		
	*	Mean	S D	%	Mean	S D	%	Mean	S D	%
Reduced iron $\gamma = 0.59$	18	0.3176	0.0324	10	1.040	0.120	11	0.0970	0.013	14
Sintered Fe $\gamma = 0.57$	9	0.4668	0.0241	5	1.710	0.210	12	0.1362	0.007	1
Lime $\gamma = 0.46$	7	0.0676	0.0063	9	0.173	0.023	13	-	-	-
Lime $\gamma = 0.57$	3	0.0819	0.0029	4	0.295	0.038	13	0.1861	0.026	14

* number of samples
S D = Standard Deviation

same variance. If the L-test shows that this is likely to be the case, the F-test examines whether or not differences between the means of the samples is likely to arise from sampling variation or from some non-random cause.

Tables 6.10 and 6.11 show the analysis of the variance of the experimental values of A_O, B_O and C_O using the F-and L-tests. The results for A_O and B_O for each material have been separated into sets depending on the gas and temperature for which the measurements were made and then, at least for porous and sintered iron, into sets depending on the sphere for which the measurement was made. C_O values measured for porous iron have been similarly treated, except that they are only a function of temperature and they were not analysed by sphere.

Where the calculated value of F shown in the tables for a group of sets is greater than its value tabulated for a specified level of significance, the chance that the differences between the means of the sets in the group would arise from sampling error is equal to or less than the specified level of significance. Table 6.9 shows that the results obtained for A_O in porous iron analysed by gas and temperature appear to exhibit a variation that is significant. Examination of the data shows that the A_O values obtained for argon at 898K are some 16% below the average of the remaining values, and that the value of F calculated from this group of sets of values falls beyond the 1% significance level. If the analysis is repeated with

339

Table 6.10   Analysis of variance of diffusion and flow parameters for porous iron

Value	Criteria	A_0 (i)	A_0 (ii)	$B_0 \times 10^9$	C_0	Sph.	A_0	$B_0 \times 10^9$
		Analysis by Gas and/or Temperature				Analysis by Sphere		
n(1)	Ar/	5	5	5	3		4	4
mean (1)	292 K	0.329	0.392	0.978	9.9×10^{-2}	Q	0.319	0.99
S D (1)		1.9×10^{-2}	1.9×10^{-2}	6.4×10^{-2}	2.0×10^{-2}		2.7×10^{-2}	20×10^{-2}
n (2)	Ar/	6	–	6	3		4	4
mean (2)	898 K	0.282	–	1.00	9.5×10^{-2}	R	0.330	1.07
S D (2)		2.6×10^{-2}	–	14×10^{-2}	0.7×10^{-2}		2.6×10^{-2}	8.7×10^{-2}
n (3)	He/	3	3	3	–		4	4
mean (3)	292 K	0.346	0.346	1.133	–	T	0.317	1.03
S D (3)		0.2×10^{-2}	0.2×10^{-2}	13×10^{-2}	–		5.0×10^{-2}	8.9×10^{-2}
n (4)	He/	4	4	4	–		3	3
mean (4)	898 K	0.336	0.336	1.105	–	V	0.305	1.05
S D (4)		1.4×10^{-2}	1.4×10^{-2}	9.5×10^{-2}	–		4.4×10^{-2}	10×10^{-2}
n (5)		–	–	–	–		2	2
mean (5)				–		X	0.308	1.05
S D (5)		–	–	–	–		2.9×10^{-2}	18×10^{-2}
F (5%)		3.34	4.26	3.34	7.71		3.26	3.26
F (1%)		5.56	8.02	5.56	21.2		5.41	5.41
F (calc)		7.84	1.00	1.65	0.06		1.24	1.09
L (Tab)		0.585	0.470	0.585	0.311		0.492	0.492
L (Calc)		0.380	0.351	0.848	0.624		0.860	0.770

(Symbols and units as per Table 6.11)

Table 6.11   Analysis of variance of diffusion and flow parameters for sintered iron

Value	Criteria	A_o/* (i)	A_o/* (ii)	$B_o \times 10^9$ / (cm^2)	Sph.	A_o/*	$B_o \times 10^9$ / (cm^2)
n(1)	Ar/	3	3	3		3	3
mean (1)	292 K	0.452	0.452	1.73	A1	0.476	1.56
S D (1)		1.3×10^{-2}	1.3×10^{-2}	0.13		1.5×10^{-2}	0.20
n (2)	Ar/	3	3	3		3	3
mean (2)	898 K	0.445	0.445	1.90	B1	0.456	1.72
S D (2)		2.3×10^{-2}	2.3×10^{-2}	0.16		4.4×10^{-2}	0.19
n (3)	N_2/	3	–	3		3	3
mean (3)	292 K	0.496	–	1.50	C1	0.462	1.84
S D (3)		1.0×10^{-2}	–	0.13		2.2×10^{-2}	0.23
F (5%)		5.14	7.71	5.14		5.14	5.14
F (1%)		10.92	21.20	10.92		10.92	10.92
F (Calc)		7.73	0.15	4.13		0.348	1.384
L (Tab)		0.304	0.311	0.304		0.304	0.304
L (Calc)		0.780	0.857	0.980		0.675	0.987

* $cm^2 . s^{-1} (g.mol^{-1} K^{-1})^{0.5}$ SD = Standard Deviation

Table 6.12   Analysis of variance of diffusion and flow parameters of lime spheres

Value	Criteria	$A_O/*$	$B_O \times 10^9/(cm^2)$
		Analysed by gas and temperature	
n (1)	Ar/	2	2
Mean (1)	1230 K	0.070	1.48
SD (1)		1.3×10^{-3}	4.2×10^{-2}
n (2)		3	3
Mean (2)	He/	0.070	1.76
SD (2)	1230 K	7.5×10^{-3}	21×10^{-2}
n (3)		2	2
Mean (3)	He/420 K	0.061	1.94
SD (3)		0.1×10^{-3}	8.5×10^{-2}
F (5%)	−	6.94	6.94
F (1%)	−	18.00	18.00
F (calc.)	−	4.74	0.44
L (Tab)	−	0.14	0.14
L (calc.)	−	0.06	0.466

$* \; cm^2.s^{-1}(g.mol^{-1}.K^{-1})^{0.5}$

SD = Standard Deviation

this set of values ommitted (analysis A_O(ii)), the F test falls well inside the 5% significance level showing that the variation between the means in this restricted group is most likely to have arisen from random error only.

However, clear conclusions about the two groups of sets is open to some question because the computed values, of L fall below the relevant tabulated value suggesting that the sets in these two groups are not samples from normal distributions with the same variance. Examination of the standard deviations listed in the table shows that the odd variance is possessed by the set of values measured using helium at 292 K, and that this set produces an unfavourable L-test for both groups of A_O values. A further factor to be borne in mind, moreover, is that the tabulated values of L are for sets which all contain the same number of values.

A similar situation is generated by the A_O values measured in sintered iron for which the values measured for nitrogen at 292 K verge on being significantly different from the other values, although here the computed value of F falls between the 1% and 5% levels of significance. The L-test here is favourable.

The remaining values all appear to be well behaved, and do not show any significant variation. Whenever values are analysed by the sphere on which the measurements were made, computed values of F are well below the 5% significance level showing that differences between the behaviour of

different spheres arise solely due to random variation.
The values of C_O measured at 292 K and 898 K in porous iron
(Table 6.9) are particularly interesting, since the low
value of F shows that the variation of C_O with temperature
is much less than the variation with sample. This
represents a particularly crucial test of the validity of
the Dusty Gas Model since no other determinations of the
binary diffusion parameter have been made over such a wide
temperature range in material that exhibits mixed Knudsen
and molecular diffusion. When it is remembered that this
parameter is calculated from the experimental results using
equation (3.61), the constancy of the C_O value is a powerful
confirmation of the assumptions upon which that equation is
based. This is particularly true of the Bosanquet
interpolation formula, since the values determined from the
experimental results show that the contribution made by
Knudsen diffusion to the overall diffusion of argon at room
temperature is 8%, whereas it is 24% at the higher
temperature. In spite of this change in the relative roles
of Knudsen and molecular diffusion, the effective
diffusivity determined by the Bosanquet interpolation
formula properly accounts for the diffusion processes at the
two temperatures. The effective diffusion coefficient for
argon over this temperature range varies with the 1.48 power
of the absolute temperature whereas, of course, the
contributing Knudsen and molecular diffusion coefficients
vary, respectively, with the 0.5 and 1.75 powers of the
absolute temperature.

344

A further test of the validity of the Dusty Gas Model is provided by the measured values of the flux ratio, β — equal to the flux of argon during the isobaric experiments divided by the flux of helium. These values are presented in Tables 5.48, 5.49 and 5.50 and have been determined at both high and low temperatures and at least at room temperature for all three different materials. The mean of the room temperature values is 0.355 with a standard deviation of 0.026, the corresponding values for the high temperature measurements being 0.354 and 0.024. At room temperature, the means for the three different materials are 0.372, 0.352, and 0.345.

Comparison of the high and low temperature values shows that L- and F-tests are not necessary to conclude that the measured values of β are not a function of temperature. The situation is a little less clear for the different materials. However, treating the values measured for the three types of material as different sets of data results in a calculated value of L of 0.652, against the relevant tabulated value of 0.304, and a calculated value of F of 0.655. Thus we can conclude that the differences between the means arise from random variation and not from any systematic difference between the three different classes of materials.

The results obtained for the flux ratio under isobaric conditions thus show that it is not a function of the material being used nor is it a function of temperature.

345

This fact is also a confirmation of the Dusty Gas Model which predicts that the value of the isobaric flux ratio is constant and independent of the relative importances of Knudsen and molecular diffusion. The constancy of the flux ratio determined experimentally in this work is a direct confirmation of this, since the relative importances of the two types of diffusion vary with the experimental temperature as well as from material to material.However, the actual magnitude of the experimental flux ratio is not precisely the value predicted by the Dusty Gas Model, since the model predicts that it should be the ratio of the Knudsen diffusion coefficients - equal, therefore, to the square root of the inverse ratio of the molecular masses. The flux ratio for argon and helium should thus be 0.316 so that the experimentally determined values are 12% greater than the theoretical values. Discrepancies from the theoretical ratio have been reported by other authors, although not in the same sense. Mason et al[20] reports the flux ratio to be 8% less than the theoretical value and Rothfeld[29] reports flux ratios that are 19% below the theoretical value. Neither of these authors offer explanations for these discrepancies, the only suggestion that has been offered for similar effects is the influence of surface diffusion which is not included in the Dusty Gas Model. The values measured in this work do not really support this explanation since it appears unlikely that similarity would exist between surface diffusion effects in

porous lime and porous iron.

Values of the flux ratio are, of course, sensitive to
pressure differences across the diffusion cell. The non-
isobaric results, discussed later in this section, suggest
that a 12% increase in the flux ratio would result if the
pressure outside the sphere were on average some 1.5 cm of
water higher than the pressure inside the sphere. Great
care had been taken in the experiments to ensure that
isobaric conditions were achieved by using a differential
manometer containing paraffin, which maintained an accuracy
much better than the equivalent of 1.5 cm of water. In any
case, any inaccuracy in maintaining truly isobaric
conditions would cause random and not systematic errors.

However, it could be that a systematic error might be built
into the design of the apparatus, since the highly dynamic
flow conditions maintained in the inner cavity of the sphere
could produce higher pressure at the mouth of the pressure
probe than on the true inner surface of the sphere.
Maintaining the indicated pressure difference as zero would
then produce a slightly lower pressure at the surface within
the cavity and could thus result in a higher value of beta.
It is unlikely, however, that pressure variations as high as
1.5 cm of water could be produced within the cavity,
although the pressure on the pressure probe in the iron
experiments - opposite the inlet gas flow - might be greater
than that on the probe in the lime experiments - contained
within the inlet probe. β values measured in the lime

347

experiments are slightly below those in the iron
experiments, although the differences have been shown not to
be significant. No theoretical explanation can be advanced,
however, for the high values of β , so that some
experimental anomaly remains the most likely explanation.

One other anomaly remains in the experimental results, and
this is the experimental values of A_O for argon at high
temperatures. As explained previously, this value is
significantly lower than the other measurements - argon at
room temperature and helium at high and low temperatures.
No theoretical explanation can be advanced for this
discrepancy and an experimental anomaly associated with this
set of measurements remains the most likely explanation.
This view is strengthened by one direct measurement of A_O
for the high temperature diffusion of argon that was made
during the subsequent isobaric experiments. The value
obtained was 0.318 which was significantly higher than that
of the mean of the previous set - 0.282 - and closer to the
means of the other results. Further confirmation for the
anomalous nature of the high temperature argon results is
provided by the measured values of the flux ratio that has
been discussed above. The flux ratio is theoretically equal
to the ratio of the Knudsen diffusion coefficient for argon
to the Knudsen diffusion coefficient for helium. If the
value of A_O for argon were, in fact, lower than the value
for helium, the diffusion coefficient ratio would be smaller
than the square root of the inverse molecular mass ratio.

As we have seen, the measured ratios were some 12% bigger that this square root, which suggests that the low value of A_O for argon at high temperatures is not the true value.

Thus the diffusion property values measured in this work support the validity of the assumptions upon which the Dusty Gas Model in its phenomenological form has been based. A further test that was carried out of the model is provided by the non-isobaric experiments in which the measured values of A_O, B_O and C_O were used to predict diffusion behaviour in the presence of a bulk pressure gradient. Experiments and predictions were carried out at low and at room temperature for porous and sintered iron and at high temperature for lime. The experimental results and the theoretical predictions are shown in Figures 6.1 to 6.12 plotted against increasing values of β. It can be seen that good agreement was obtained between the experimental points and the theoretical predictions, although the difference between the theoretical and experimental values for the pressure difference is somewhat greater than the error that has been assessed for the measurement of the pressure difference in Section 6.2. However, the theoretical curves depend upon the values of the parameters A_O, B_O and C_O which each have their associated error. The differences between the experimental points and the theoretical curves in the figures are within the experimental errors that have been previously assessed. The agreement shown for the total pressure drop across the porous solid is the more significant

Figure 6·1 : The comparison between the calculated and experimentally obtained results for iron sphere X at 292 K under non-isobaric conditions.

Figure 6·2 : The comparison between the calculated and experimentally obtained results for iron sphere X at 898 K under non-isobaric conditions.

Figure 6·3 : The comparison between the calculated and experimentally obtained results for iron sphere Y at 292 K under non-isobaric conditions.

Figure 6·4 : The comparison between the calculated and experimentally obtained results for iron sphere Y at 898 K under non-isobaric conditions.

Figure 6·5 : The comparison between the calculated and experimentally
obtained results for iron sphere W at 292 K under
non-isobaric conditions.

Figure 6·6 : The comparison between the calculated and experimentally obtained results for iron sphere W at 898 K under non-isobaric conditions.

Figure 6·7 : The comparison between the calculated and experimentally obtained results for sintered iron sphere Y at 292 K under non-isobaric conditions.
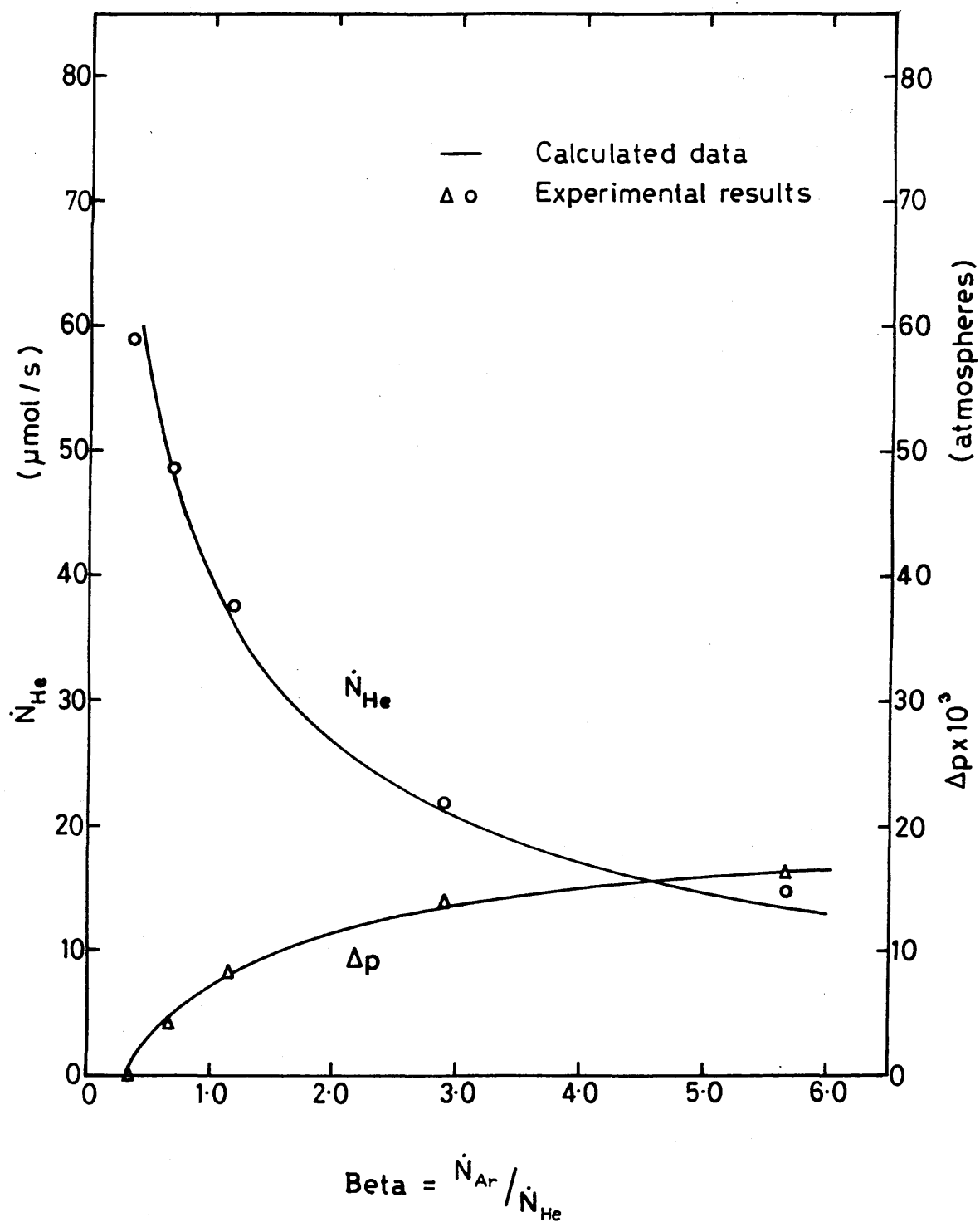
Figure 6·8 : The comparison between the calculated and experimentally obtained results for sintered iron sphere Z at 292K under non-isobaric conditions.
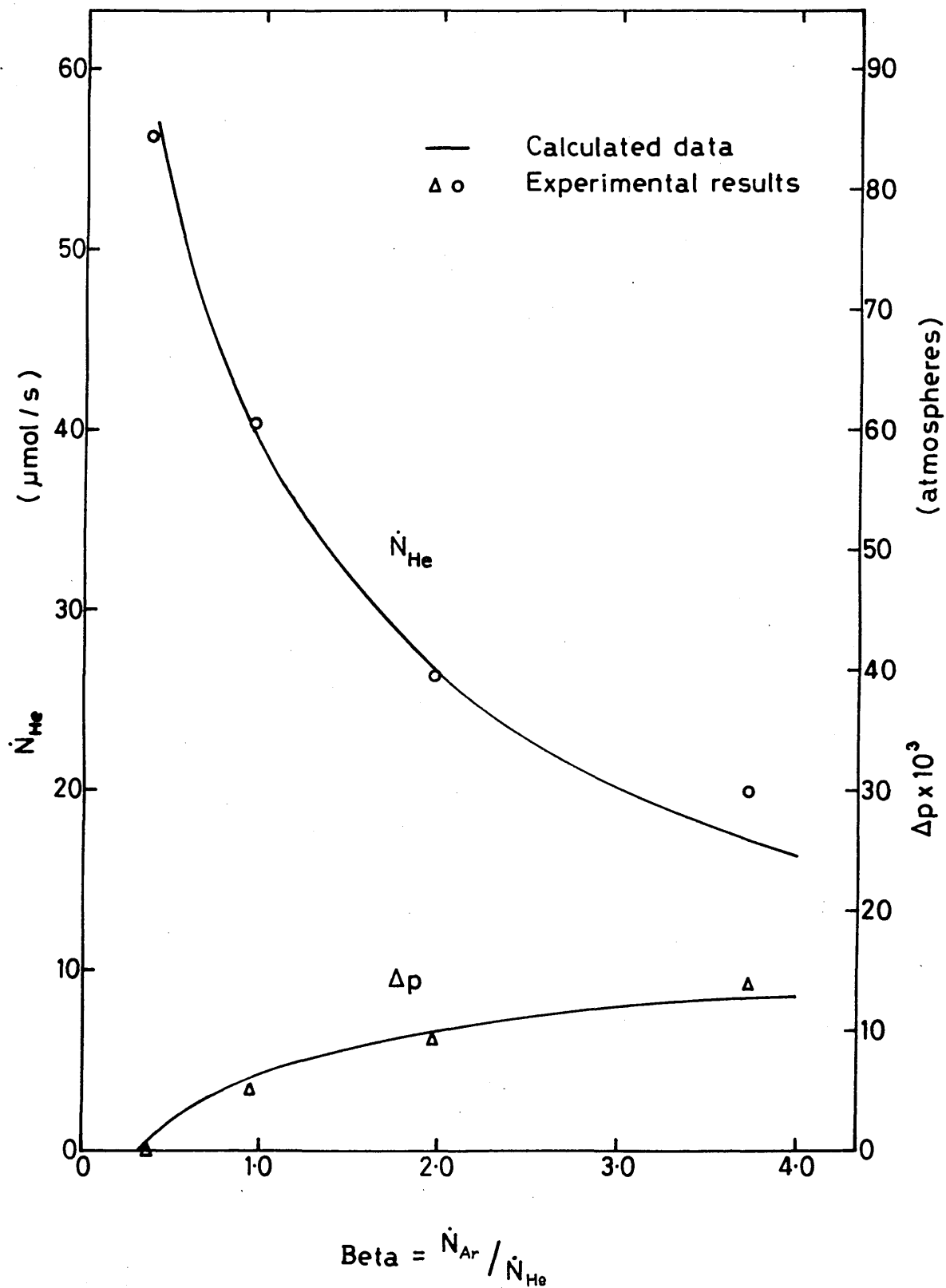
Figure 6·9 : The comparison between the calculated and experimentally obtained results for sintered iron sphere Z at 898K under non-isobaric conditions.

$Beta = \dot{N}_{Ar} / \dot{N}_{He}$
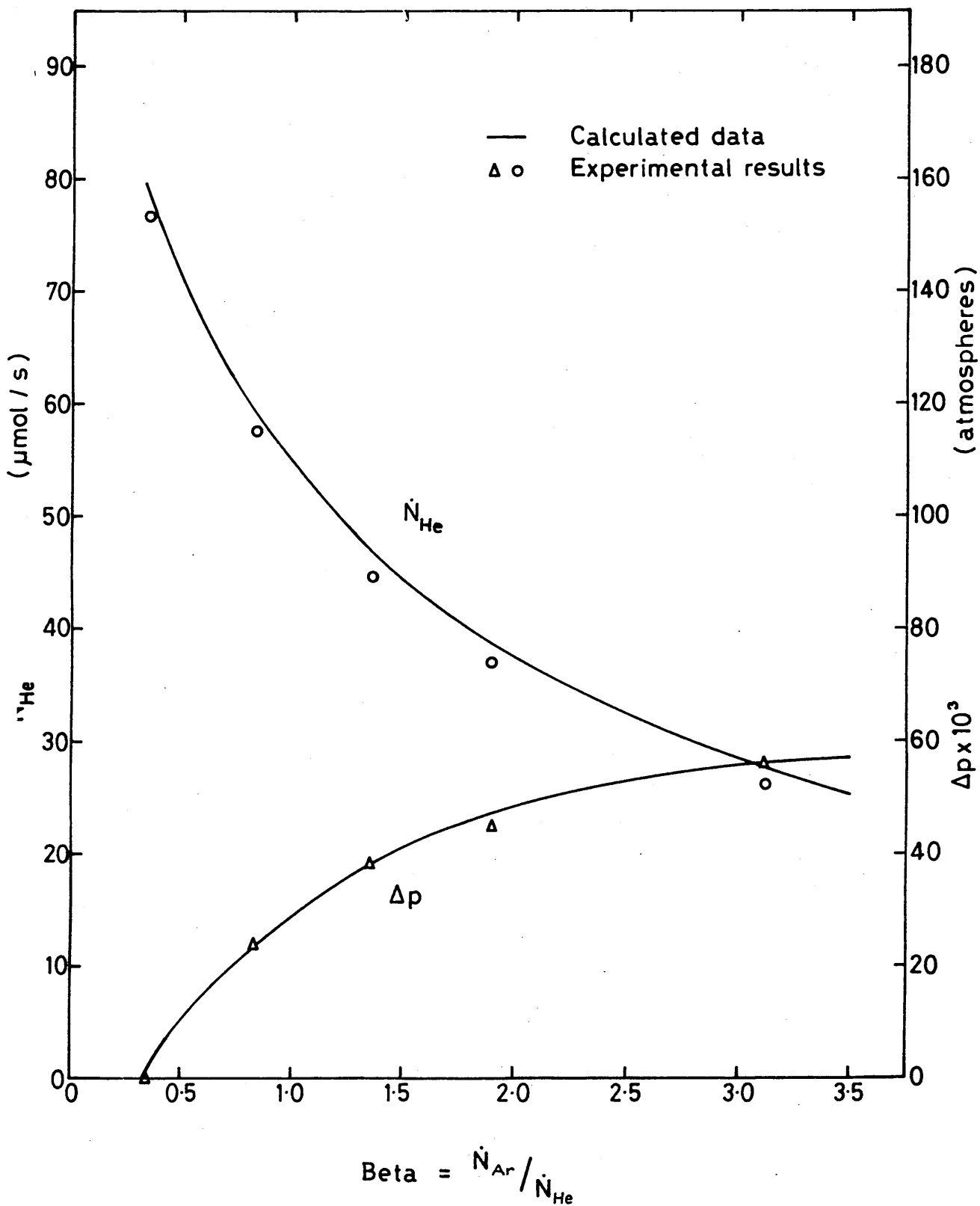
Figure 6·10: The comparison between the calculated and experimentally obtained results for lime sphere 71 at 292 K under non-isobaric conditions.
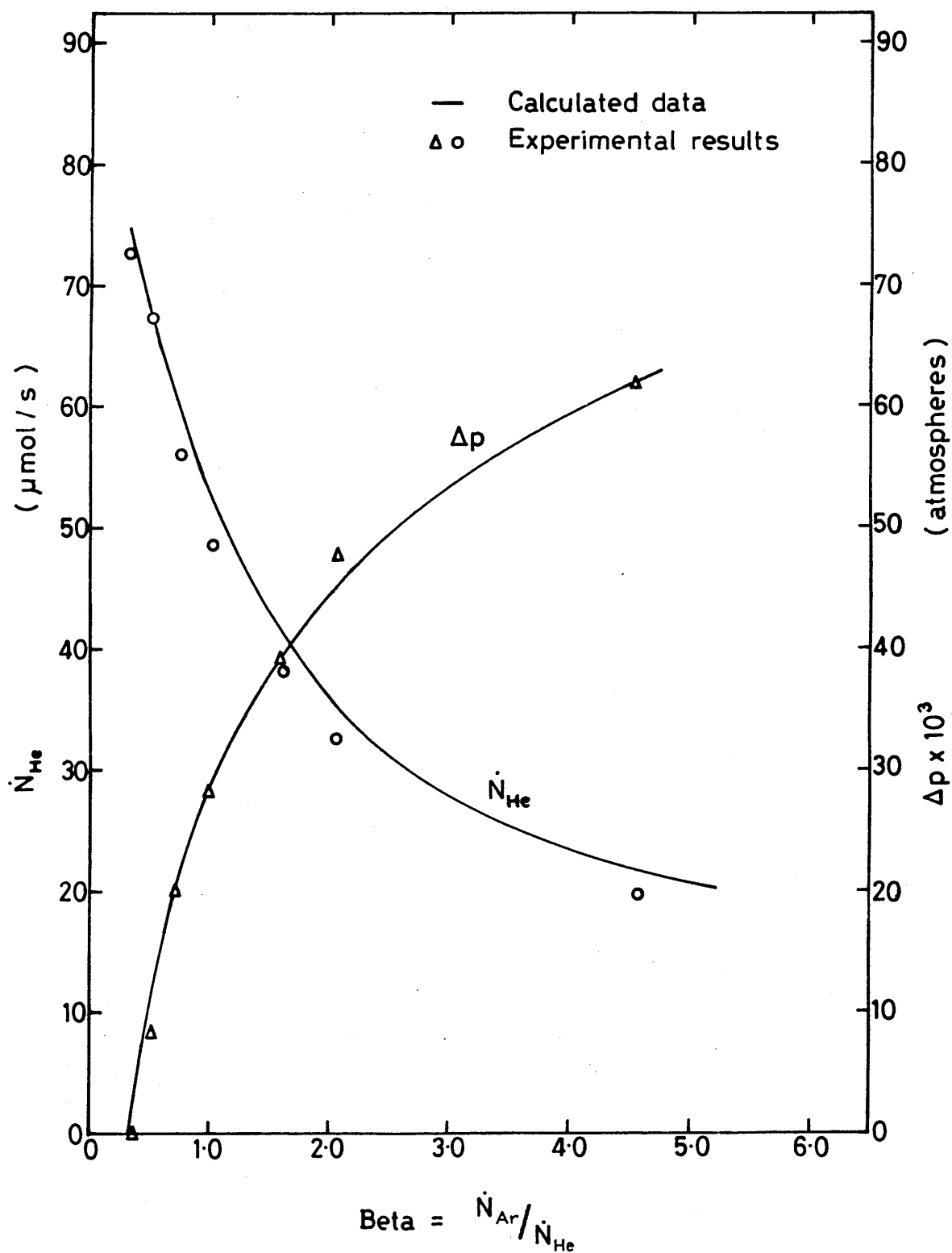
Figure 6·11 : The comparison between the calculated and experimentally obtained results for lime sphere 72 at 292 K under non-isobaric conditions.
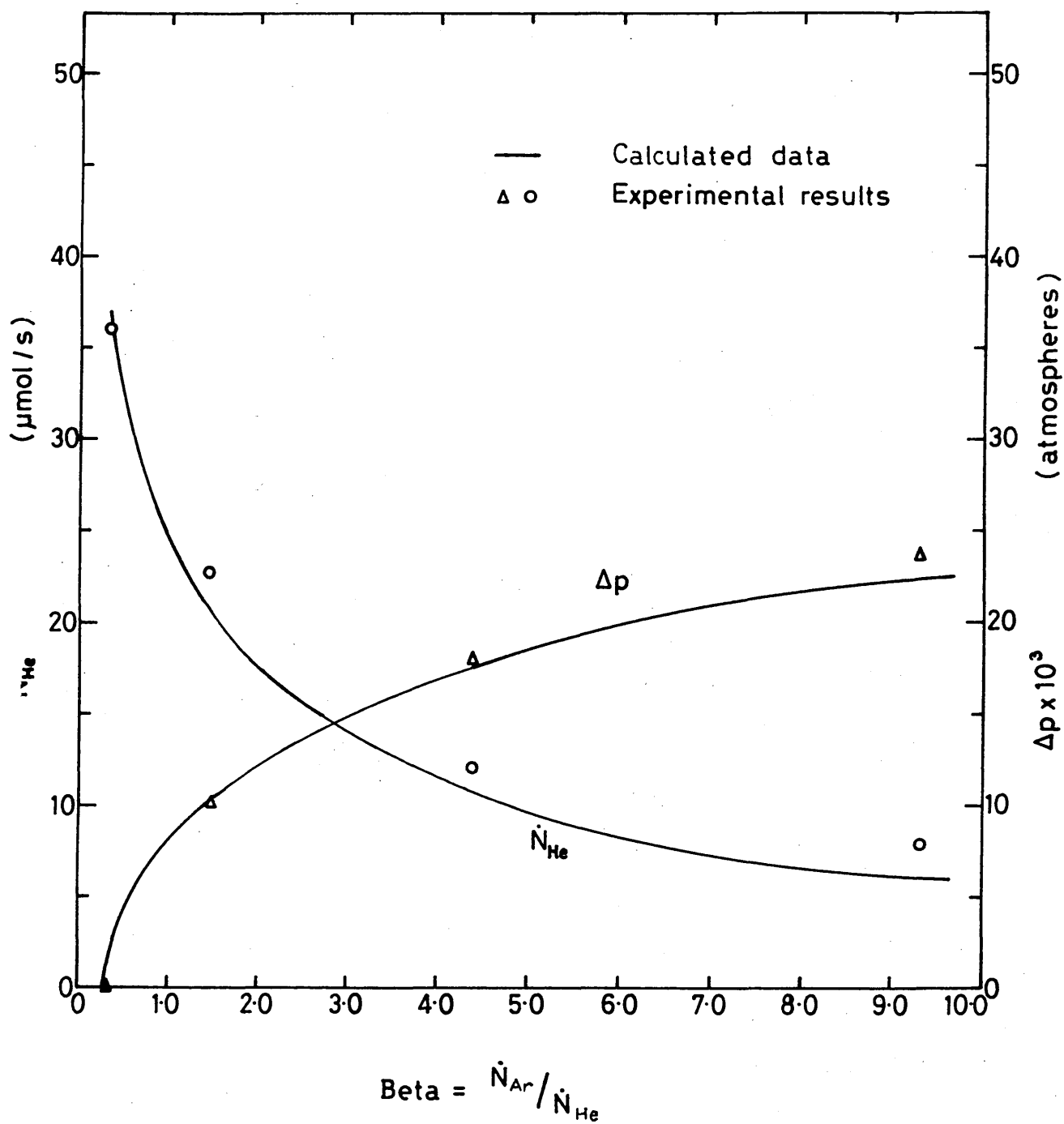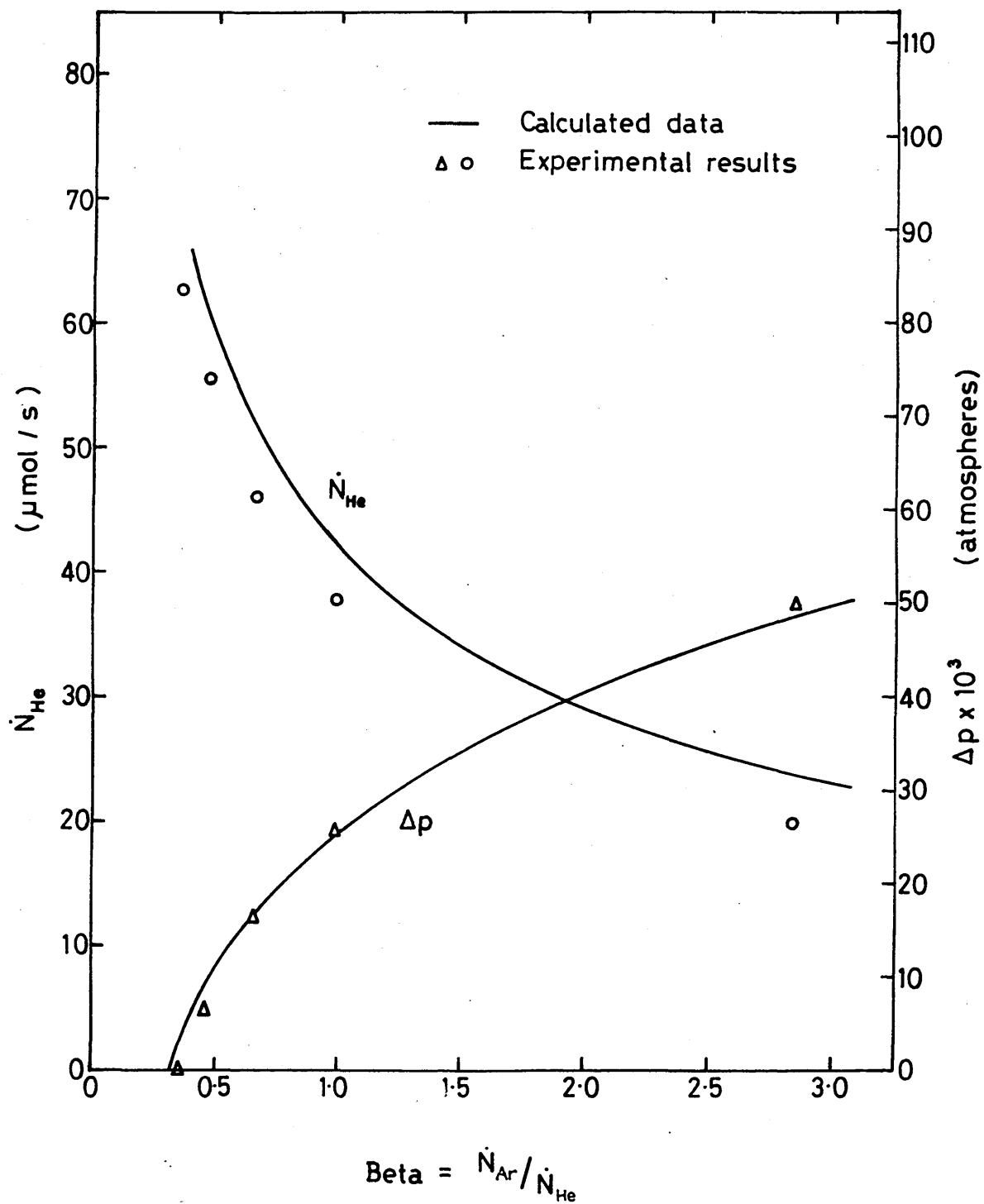
Figure 6·12 : The comparison between the calculated and experimentally
obtained results for lime sphere 73 at 292 K under
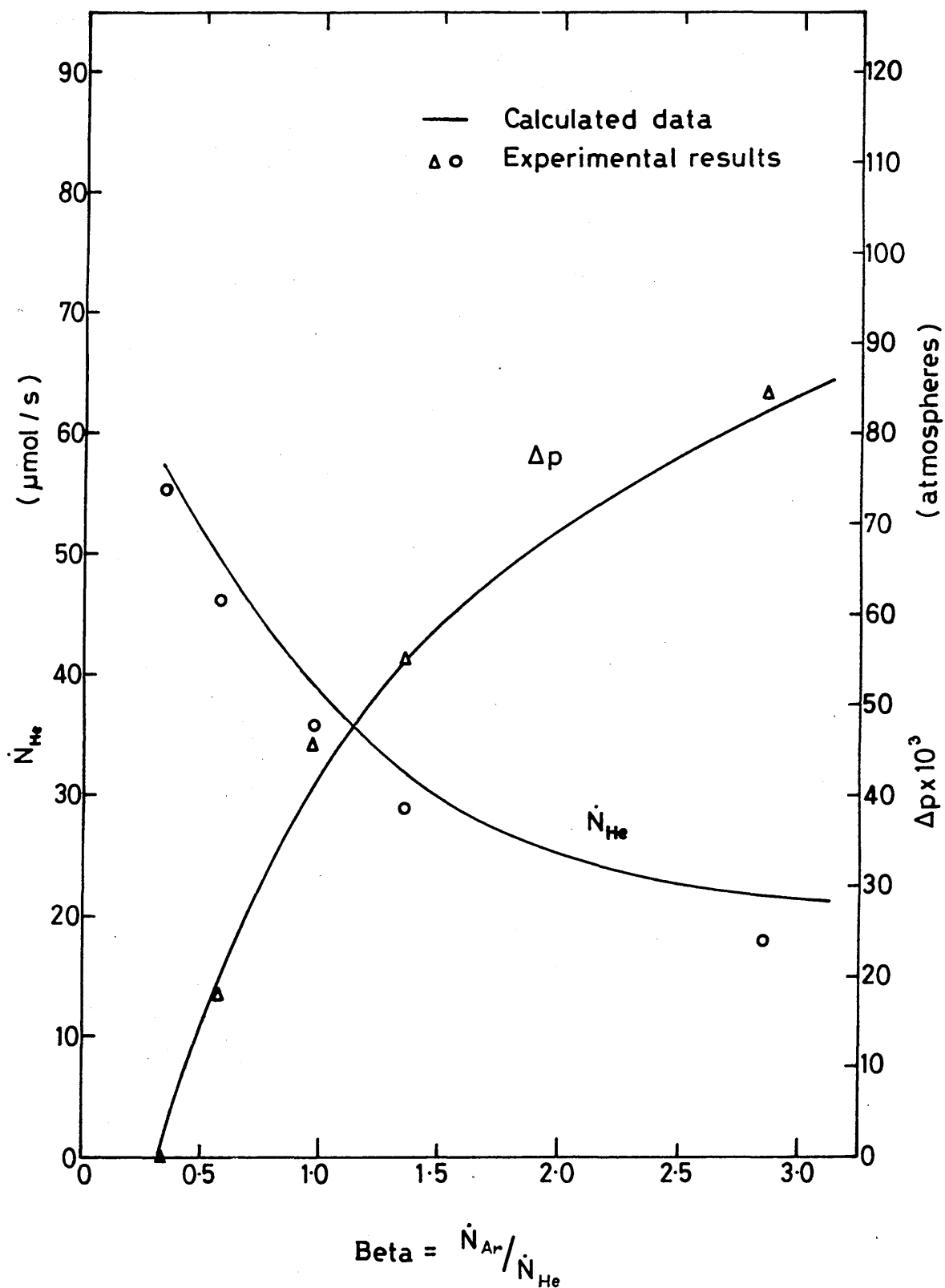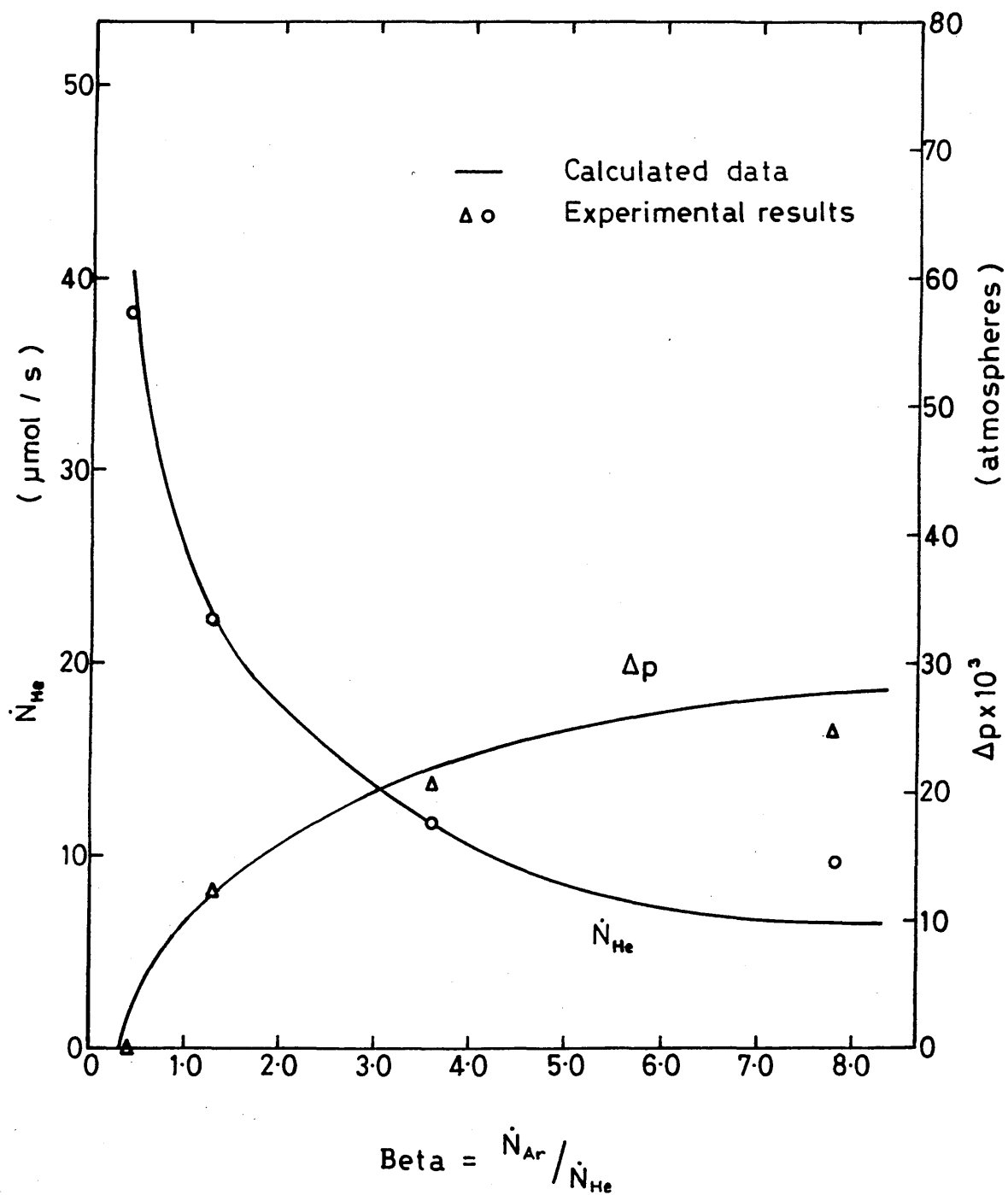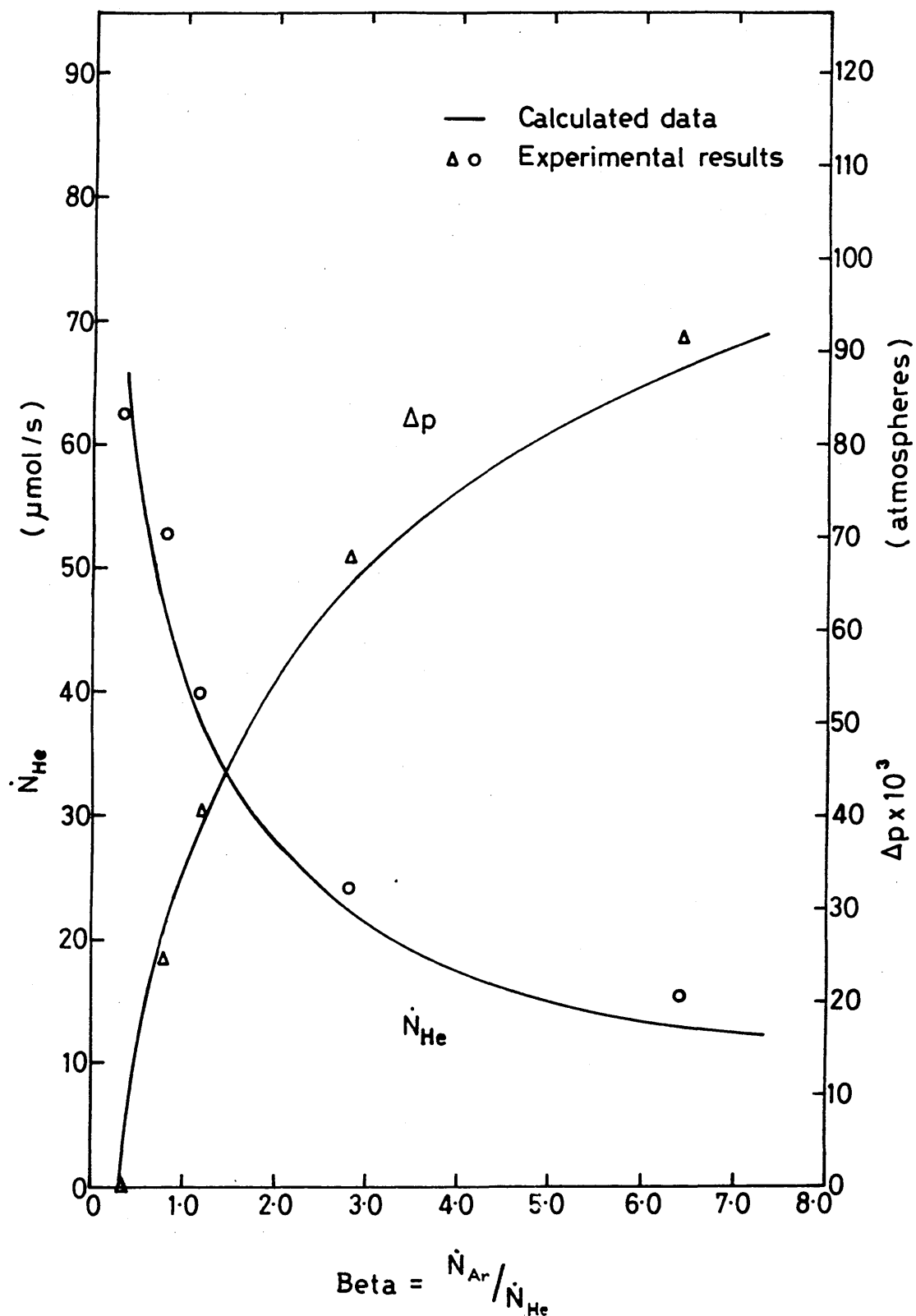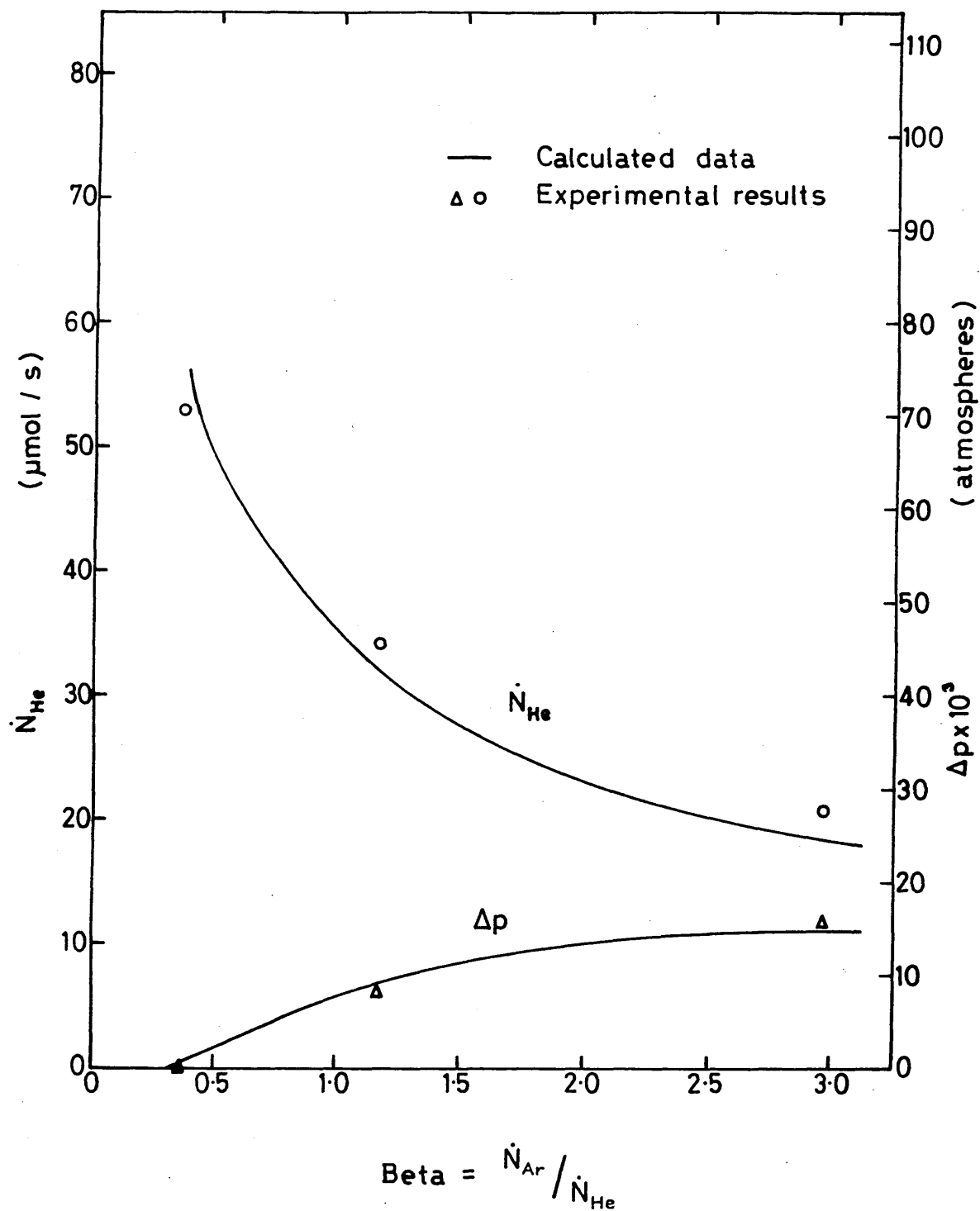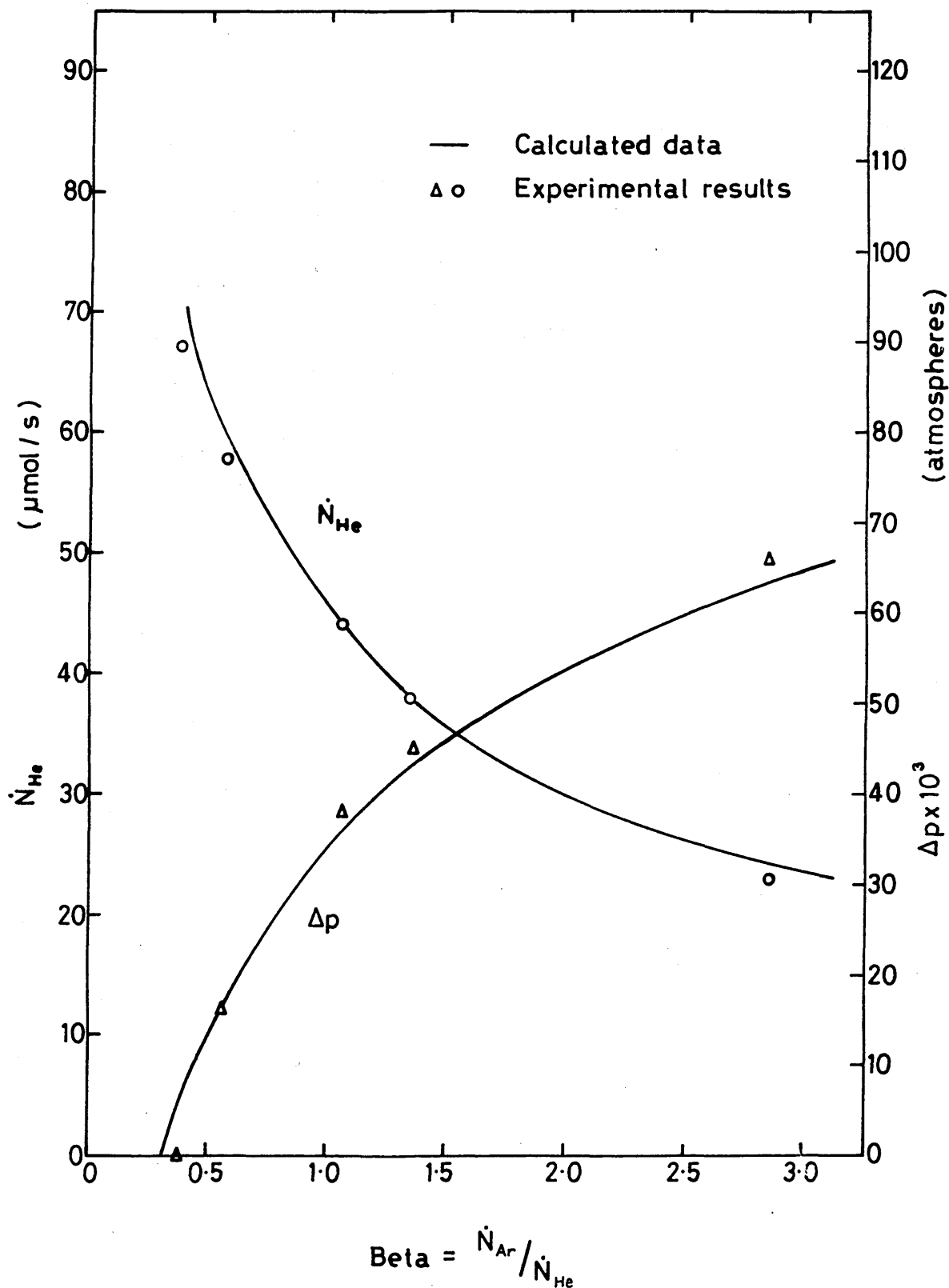non-isobaric conditions.
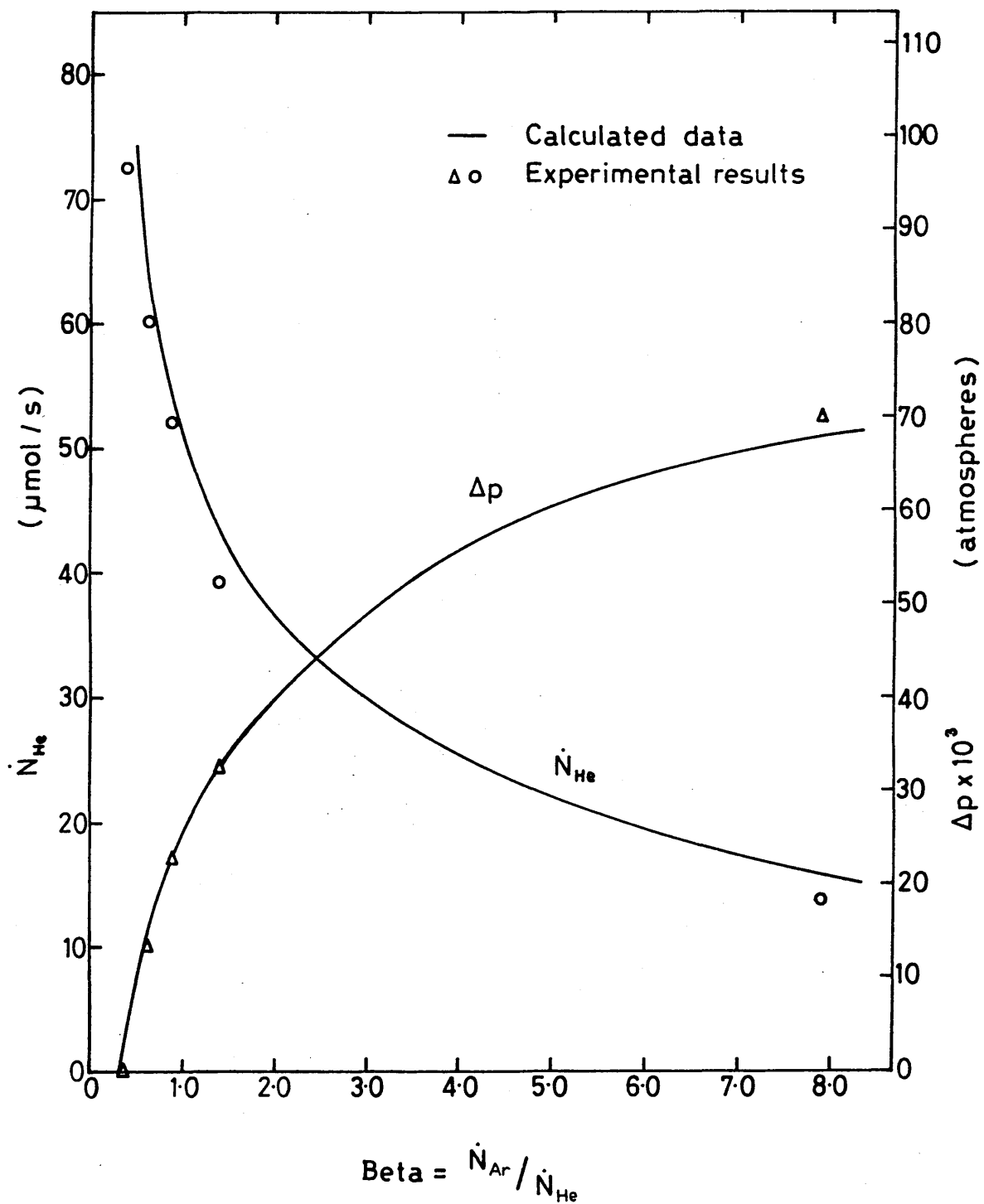
because this variable is particularly sensitive to errors in the parameters.

The agreement achieved is strong support for the Dusty Gas Model because no disposable parameters have been used in determining the theoretical curves and, as has already been shown, the phenomenological parameters, A_o, B_o and C_o, are properties solely of the porous solid in question. Thus the agreement shows that measurements made at one temperature using one gas system can be used to make accurate predictions at a different temperature and for a different gas system.

6.5 RELATIONSHIP BETWEEN THE PHENOMENOLOGICAL CONSTANTS AND STRUCTURAL MODELS FOR DIFFUSION AND FLOW OF GASES IN POROUS MATERIALS

Section 2.2 of the thesis discusses the structural models that have been used to predict diffusion and flow in porous media – an approach that differs fundamentally from the Dusty Gas Model since the latter relies entirely on the direct measurement of diffusion and flow rates. As discussed in Section 3.4, the Dusty Gas Model generates three phenomenological parameters from these measurements that fully characterise the diffusion and flow of gases through the solid. It is interesting to compare these two different approaches by comparing the parameters developed by the Dusty Gas Model with the parameters generated by the structural models.

362

The most commonly used structural model is the random

orientated single sized pore model described in Section

2.2.2. Equation (2.19) in that Section describes the flow

of a gas through the porous solid in terms of that model,

and comparison between this equation and equations (3.24),

(3.57) and (2.2) shows that:-

$$A_O = 2/3 \ (\gamma/\tau)(8R/\pi)^{1/2} \ r \qquad (6.2)$$

where f and δ are both taken as unity and r is the

equivalent capillary radius.

and that:-

$$B_O = \frac{\gamma r^2}{8\tau} \qquad (6.3)$$

Evaluating equation (6.2) gives:-

$$A_O = 9700 \ (\gamma/\tau) \ r \quad cm.s^{-1}(g.mole^{-1}K^{-1})^{1/2} \qquad (6.4)$$

Comparison between equation (3.8) and (3.59) shows that the

molecular diffusion parameter, C_O is related to the

tortuosity and permeability in the single sized pore model

by the equation:-

$$C_O = \frac{\gamma}{\tau} \qquad (6.5)$$

No measurements of pore size have been made in this work so

that the validity of these equations cannot be examined

separately. Indeed, the Dusty Gas Model has been developed

to circumnavigate the experimental and theoretical

uncertainties associated with the measurement of pore sizes

and their use to evaluate diffusion coefficients. However,

it is interesting to examine the collective validity of the

equations by examining their ability to predict one of the three diffusion parameters from the other two. In effect this is equivalent to saying that the equivalent pore radius for diffusion and flow cannot be measured directly - it can only be deduced by studing diffusion and flow.

Eliminating γ, τ and r by combining equations (6.3), (6.4) and (6.5) gives:-

$$C_O = \frac{A_O{}^2}{7.53 \times 10^8 \, B_O} \tag{6.6}$$

Thus it is possible to calculate values of C_O using this equation and compare them with the experimentally measured values. This comparison is carried out in Table 6.13 which shows the experimentally measured values of A_O, B_O and C_O together with the value of C_O calcuated according to equation (6.6). The seventh column shows the equation value divided by the measured value and shows ratios that are, in the main, remarkably close to 1. Two values are significantly less than one, however, but these are both for material that combines a low Knudsen diffusion coefficient with an appreciably higher value of the porosity. If, for the moment, we set these two values aside, the mean of the remaining ratios is 1.02 with a standard deviation of 0.24.

Considering the range of different materials involved, it is surprising that equation (6.6), based on the random oriented single sized pore model, allows such close prediction of the molecular diffusion parameter, C_O. Since equation (6.6) was based on the assumption that the value of the term δ in

364

equation (2.20) was unity, the agreement between the calculated and the experimental values of C_O is strong confirmation that this is the appropriate value for $\hat{\delta}$ in porous materials. The confirmation is strengthened when the results shown in the table are compared with the results obtained by Hewitt[8] who carried out a similar calculation but with $\hat{\delta}$ taken as its value for slip flow in a capillary, ie 0.59. The values for C_O that he calculated were some 3 times his measured values.

We have, so far, set aside consideration of the two materials with low Knudsen diffusion coefficients. In order for these materials to have such low Knudsen diffusion coefficients whilst their porosities are relatively high, they must have large specific surface area. This can only be the case if the porous materials themselves, are composed of large numbers of fine crystallites. In such a structure, the length of individual pores would be very similar to their diameters, a structure quite different from that existing in the other materials. The microstructure of the porous iron obtained by the hydrogen reduction of hematite in this work, and shown in Plate 6·1 , suggests, for example, that the length of individual pores is very much greater than their width. This type of structure approximates to the assemblage of capillaries upon which the random orientation single sized pore model has been based, incorporating as it does Knudsen's equation[1] for the diffusion of a gas along a long capillary.

Plate 6.1: The structure of porous iron produced
by reducing hematite in hydrogen at
825°C.

Plate 6.2: The structure of porous iron produced
by reducing hematite in hydrogen at
825°C followed by sintering at 1100°C
for five hours in hydrogen.
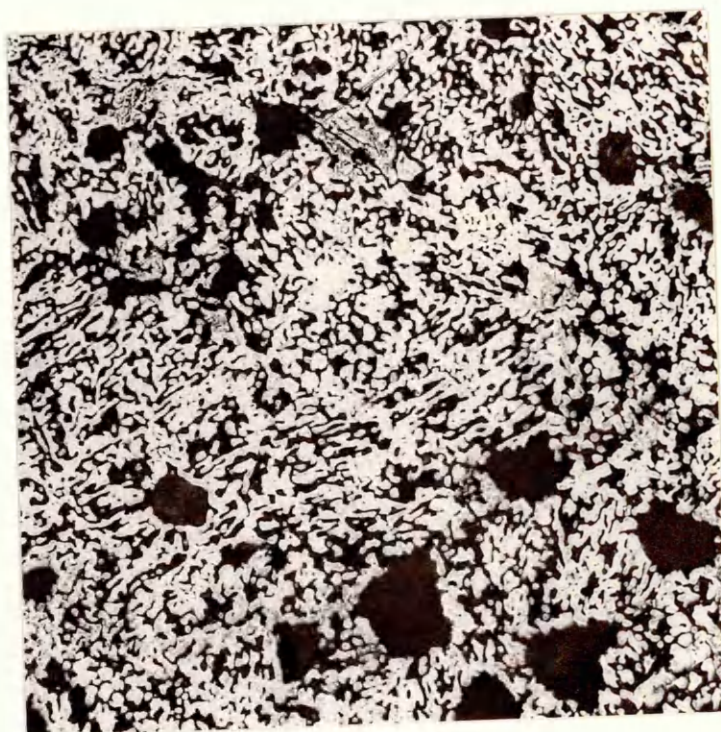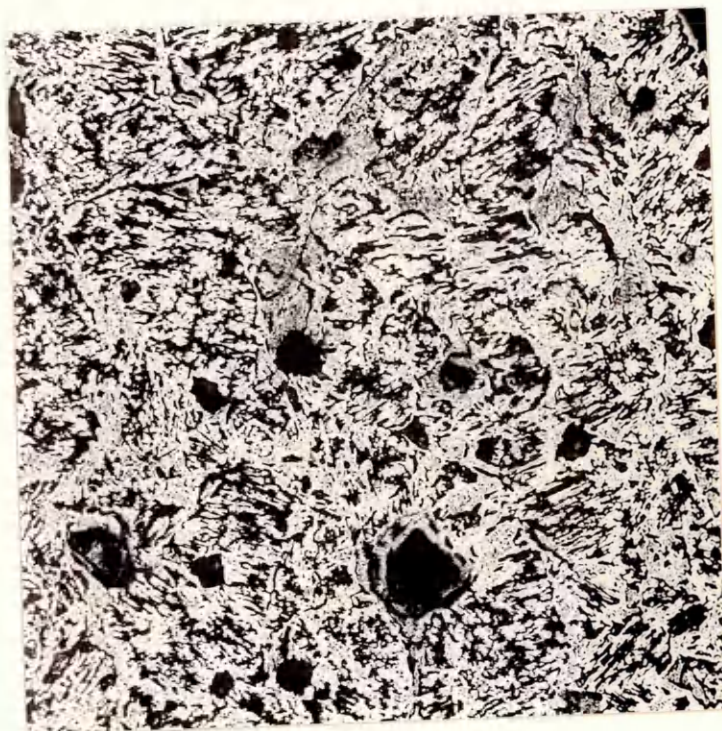
Knudsen also considered the diffusion of a gas along a short capillary, obtaining the following expression for the Knudsen diffusion coefficient in the capillary:-

$$[D_{K,A}]_r = 2/3 \ (r/k_1) \ (8RT/\pi \ M_A)^{1/2} \qquad (6.7)$$

which would give:-

$$A_o = 2/3 \ (\gamma/k_1 T)(8R/\pi)^{1/2} \ r \qquad (6.8)$$

in a porous material consisting of bundles of short capillaries.

The parameter k_1 is related to the aspect ratio of the capillary by the equation:-

$$k_1 = 1 + (8/3)(r/L) \qquad (6.9)$$

where L is the length of the capillary.

If A_o is evaluated using equation (6.8), equation (6.6) for C_o becomes:-

$$C_o = \frac{A_o{}^2 \ k_1^2}{7.53 \times 10^8 \ B_o} \qquad (6.10)$$

This then is the relationship between the three parameters for a structure consisting of short capillaries.

Equation (6.9) shows that, for a capillary as long as it is wide, the value of k_1 is 2.33. Applying this value to the C_o values for lime and for nickel reduced at 800°C, increases their calculated C_o values to 0.130, and 0.24 respectively, and the calculated to measured C_o ratios to 0.87 and 1.6. These latter two values are more in agreement with the other values obtained, suggesting that a short capillary pore model is more in keeping with the diffusion nature of these materials.

368

This analysis is somewhat speculative because detailed
structural analyses were not carried out in this work,
indeed such analyses are outside the scope of an
investigation into the Dusty Gas Model. However, the
improved agreement obtained when a short capillary model was
used to explain the diffusion parameter values in the lime
and the nickel reduced at $800^{\circ}C$, does suggest that the
aspect ratio of the typical capillaries in a porous material
might play a significant role in determining the Knudsen
diffusion coefficient in that material. Certainly much of
the variation shown in Table 6.13 could be explained by
aspect ratios that vary upwards from the value of one that
appears to apply in the low Knudsen coefficient materials.

Although a detailed structural analysis is outside the scope
of this work, pore size measurements on the materials
studied have been reported in the literature and it is
therefore interesting to use the random orientated single
size pore model to determine average pore sizes from the
phenomenological parameters determined in the work.

Substituting into equation (6.2) from equation (6.5) and
rearranging gives:-

$$r = \frac{3\ A_o}{2\ C_o}\ (8R/\pi)^{-1/2} \qquad\qquad (6.11)$$

and this equation provides one estimate of the pore size. A
second estimate of the pore size is provided by combining
equations (6.3) and (6.5) to give:-

able 6.13   Parameter relationship generated by the single pore model

aterial	γ	Experimental			Eqn.(6.6)	Eq / /Exp	Source
		$A_o/*$	$B_o \times 10^{10}/**$	C_o	C_o		
orous Iron ed:825°C	0.59	0.318	10.5	0.097	0.128	1.32	Present Work
intered ron ed:825°C	0.57	0.465	18.0	0.136	0.151	1.11	
ime	0.57	0.082	3.06	0.186	0.030	0.16	
ematite	0.30	0.192	7.64	0.085	0.064	0.75	Bradshaw[44]
agnetite ed:700°C	0.32	0.306	14.10	0.111	0.088	0.79	
raphite	0.21	0.033	1.93	0.0085	0.0074	0.87	Truitt[32]
ickel d:250°C	0.64	0.750	1.65	0.395	0.453	1.14	
ickel d:350°C	0.62	0.368	4.20	0.306	0.428	1.40	
ickel d:450°C	0.60	0.448	7.36	0.332	0.362	1.09	Campbell[50]
ickel d:650°C	0.38	0.050	0.51	0.093	0.065	0.69	
ickel d:750°C	0.47	0.250	3.60	0.220	0.230	1.04	
ickel d:800°C	0.41	0.109	2.80	0.193	0.056	0.29	
raphite	–	0.093	7.92	0.0086	0.015	1.68	Hewitt[8]

$^2.s^{-1}(g.mol^{-1}.K^{-1})^{0.5}$

^{2}

$$r = \sqrt{\frac{8\ B_O}{C_O}} \qquad\qquad (6.12)$$

Values of r determined by these two equations are shown in Table (6.14) and they will be discussed in the next section.

Table 6.14   Mean pore radii inferred from diffusion and flow parameters

Material	$r_O/\mu m$	
	Eq. (6.11)	Eq. (6.12)
Reduced Iron	3.36	2.94
Sintered Iron	3.57	3.34
Porous Lime	0.456	1.14

As explained in Chapter 2, the single size pore model is merely the simplest model that has been used in attempts to predict diffusion coefficients in porous materials. The distributed size pore model has been used almost as extensively as the single size pore model. The range of pore sizes as determined by mercury porosimetry provides the base of the model, the porous material being considered to consist of a bunch of different sizes capillaries, the relative number coinciding with the volume fraction of the pores of different sizes. Equation (2-21) gives the diffusion flux through the porous material that results from this model.

Since pore sizes have not been determined in this work, no examination of the validity of this model can be carried

371

out. However, it is interesting to compare the form of

equation (2-21) with the corresponding equation generated by

the Dusty Gas Model. If the value of β is substituted

into equation (3.40) the resulting equation gives:-

$$\dot{N}_A'' = \frac{D_{A,eff}}{[1 - C_A^*(1-\beta)\delta_A]} \frac{\nabla p_A}{RT} \qquad (6.13)$$

Substituting for the values of $D_{A,eff}$ and δ_A and further

rearranging gives:-

$$\dot{N}''_A = \left\{ \frac{1 - C_A^*(1-\beta)}{D_{AB,eff}} + \frac{1}{D_{A,K}} \right\}^{-1} \frac{\nabla p_A}{RT} \qquad (6.14)$$

This is, of course, of very similar form to equation (2.21)

and that equation can be placed in the form of equation

(6.14) by the choice of a suitable effective average radius

with which to calculate the Knudsen diffusion coefficient

using equation (2.2). Thus the distributed pore model and

the Dusty Gas Model can describe binary diffusion by equations

of the same form, but the two equations do not necessarily

behave in the same way. As pointed out by Satterfield and

Caddle[15], the effective average radius as generated by the

distributed pore model, is a function of operating

conditions. Thus, if this model were the correct represen-

tation of diffusion in porous media, the Knudsen diffusion

coefficient to be used in equation (6.14) would be a

function of operating conditions. The most significant

variation that would be predicted in this way by the

distributed pore model and not by the Dusty Gas Model or,

indeed, by the single sized pore model, is that the

372

effective Knudsen diffusion coefficient to be used in

equation (6.14) would be a function of total pressure and of

temperature.

Binary diffusion measurements have only been carried out at

one pressure in this work so that it is only the variation

with temperature than can be examined here. As is shown by

the C_O values in Table 6.5 there is no evidence to support

a variation of binary diffusion behaviour with temperature

and it would appear that the Dusty Gas Model must provide a

better representation of diffusion behaviour than the dis-

tributed pore model. A number of other workers have carried

out experiments at different pressures over a range of

several atmospheres and their conclusions show considerable

variation. Some[eg 16] claim that the distributed pore

model provides the more accurate representation of the way

in which diffusion varies with pressure. On the other hand,

other workers[eg.30] claim that the single sized pore model

gives a better representation of the variation of diffusion

rates with pressure than the distributed pore size model.

Since the form of the equations generated by the distributed

pore model and the Dusty Gas Model are the same*, this

conclusion would also apply to the Dusty Gas Model.

Whichever model is the more accurate, it cannot be denied

---

*FOOTNOTE Although the forms of equation are the same, the
parameters in them are measured in different ways.
Parameters in the Dusty Gas Model are measured directly,
whereas parameters in the single pore size model are
calcuated from estimated pore sizes.

that the distributed pore size model is considerably more
difficult to apply, and certainly not significantly more
accurate over moderate pressure ranges. Only if diffusion
data at very high presure is to be estimated from data
measured at moderate pressures, would it be necessary to
face up to deciding between the distributed pore size model
and the other models. For all other diffusion problems, the
easiest approach to use is provided by the Dusty Gas Model
incorporating, as it does, the results of direct measure-
ments of flow and diffusion. Certainly, for problems
involving diffusion of more than two gaseous species, by far
the easiest formalism to use is that provided by the Dusty
Gas Model.

6.6 RELEVANCE OF THE DUSTY GAS MODEL TO METALLURGICAL PROCESSING

6.6.1 Diffusion during the reduction of hematite

The mathematical methods developed in this work allow a
fuller treatment to be developed for the diffusion of gases
in porous materials than has been applied hitherto to the
analysis of metallurgical processes. It is now generally
agreed, for example, that diffusion of reactant and product
gases in the porous iron product layers play a rate
controlling role in the reduction of hematite iron ores.
Previous treatments for this diffusion process have normally
assumed the diffusion process to be molecular diffusion[eg 42]
or mixed Knudsen and molecular diffusion[eg 43, 64] but the
effect of the mechanically driven flow has not been included.

374

The experimental results obtained in this work allow the importance of this flow to be assessed.

This has been done by calculating the data shown in Table 6.15 using equation (3.75). Data in the first row has been calculated using the values of A_O, B_O and C_O obtained in this work for the iron produced by the reduction of sintered hematite at 825^OC. The fifth column in the table represents the value of $t^* \cdot p_T/RT\ C_p$ calculated from the equation. As can be seen, no attempt has been made to calculate an absolute reduction time since we are merely interested in relative times.

The sixth, seventh and eighth columns in the table show values of the total pressure at the reaction front in the hematite particle, the partial pressure there and the value of the hypothetical pressure function. The model used for the reaction is described in Section 3.4.3.

Table 6.15   Pressures and dimensionless times for the reduction of hematite

Row No.	A_O/#	$B_O \times 10^{10}$/(cm^2)	C_O	$\dfrac{t^* p_T}{RTC_p}$	p_T/ atm	p_{H2}/ atm	ψ_{H2}/ atm
1	0.3180	10.5	0.0972	16.7	1.036	0.640	0.659
2	∞	10.5	0.0972	13.5	1.000	0.618	0.618
3	0.3180	0	0.0972	16.7	1.067	0.659	0.658
4	0.3180	∞	0.0972	16.7	1.000	0.618	0.659
5	0.0859	10.5	0.2840	16.5	1.060	0.654	0.765
6	0.0859	0	0.2840	16.8	1.250	0.771	0.771
7	0.0859	∞	0.2840	17.7	1.000	0.618	0.767
8	0.1160	10.5	0.2840	13.6	1.067	0.660	0.755
9	0.4650	19.0	0.1360	11.9	1.032	0.637	0.657

cm$^2 \cdot$s^{-1}(g.mol^{-1}.K^{-1})$^{0.5}$

The first line in the table thus shows that use of the data measured in this work predicts a total pressure at the reduction front of 1.036 atmospheres, a hydrogen partial pressure of 0.648 atmospheres, and a value for the hypothetical pressure function of 0.659 atmospheres. This total pressure agrees quite well with the work of McKewan[42] who reported that the largest pressure difference that he measured across porous iron during the counter diffusion of hydrogen and water was 0.04 atm. This result is directly comparable with the prediction made in this work because the total pressure is obtained by integrating equation (3.46) and is thus independent of the shape factor of the diffusion path.

The second line in the table has been obtained to examine what happens when Knudsen diffusion is ignored. This examination has been carried out by making A_0 equal to ∞ since the form of the Bosanquet interpolation formula, equation (3.30), makes the effective diffusion coefficient equal to the molecular diffusion coefficient under these conditions.

The table shows that the reduction time is decreased by 20% when the effect of Knudsen is ignored and that the reaction front pressure is reduced to one atmosphere giving no pressure gradient across the iron layer. There is thus no mechanically driven flow and molecular diffusion is the only transport mechanism involved. As a result, the hypothetical pressure function is equal to the partial pressure of

hydrogen, as shown by the two final columns.

This result is illuminating since it shows that   it is the existence of Knudsen diffusion that creates the mechanically driven flow. The influence of Knudsen diffusion, especially when the molecular masses of the gas species differ considerably, causes the effective diffusion coefficients of the two gases to differ significantly. Under equimolar counter flow, then, the total pressure cannot remain constant throughout the diffusion path and a total pressure gradient is established. The effect of the mechanically flow is to 'relax' the effect of this chemically established pressure gradient as can be seen from the third line in the table. B_O has been set equal to zero in this line thus arresting all mechanically driven flow and this increases the total pressure at the reaction front to 1.067 atmospheres. It does not, however, change the reduction time compared with the first line in the table because the partial pressure of hydrogen at the reaction front is also increased. This latter increase compensates for the absence of the mechanically driven flow in integration of equation (3.52) so that the same value of $[\psi_{H_2}]$ is predicted at the reaction front whatever the value of B_O. That this is so is further demonstrated by the fourth line in the table where the value of B_O has been set equal to ∞ removing any ability the porous structure might have to resist a mechanically driven flow. No total pressure gradient can then be sustained within the porous

structure, and the total pressure at the reaction front is 1 Atm, the partial pressure of hydrogen is correspondingly decreased but the value of [ψ_{H_2}] at the reaction front and the reduction time are not changed.

The above analysis based on the data determined in this work shows that the reduction time is not affected by the mechanically driven flow since the same reduction time is predicted whatever the value of B_o. It would appear, therefore, that a model based solely on molecular and Knudsen diffusion would adequately predict reaction rates and that the influence of the mechanically driven flow can be ignored. The Knudsen component in the diffusion process cannot be ignored. Moreover, the mechanically driven flow cannot be ignored if the total pressure at the reaction front is to be predicted. It is not clear, however, how general these conclusions are, and the work of Turkdogan provides an alternate set of data against which to test them.

As described in the literature survey, Turkdogan obtained diffusion coefficients by analysing the reaction curves of single ore particles and by measuring the rates at which gases diffused through an iron plug formed by the previous reduction of hematite. These latter experiments were carried out at 600°C using hydrogen and water vapour and at room temperature using carbon dioxide and helium, in both cases over the pressure range from 0.1 to 10 atm. In both types of measurement, Turkdogan obtained an

effective diffusion coefficient computed by analysing his experiments as if they were taking place under isobaric conditions. He then used the Bosanquet interpolation formula to separate molecular and Knudsen coefficients from the effective coefficients he had obtained assuming that one Knudsen coefficient applied to both gases in the binary mixtures involved in his experiments. This latter assumption is of course invalid since, in both gas mixtures, the Knudsen coefficients differ by a factor of 3 or more. It is consequently difficult to decide what value of A_o relates to the Knudsen diffusion coefficients that Turkdogan has reported.

He presents a table in which Knudsen and molecular diffusion coefficients are listed for the helium/carbon dioxide measurements. Since these values arose by analysing the experimental results in terms of a single effective gas diffusivity and since these results would be dominated by the slowest gas, the Knudsen coefficient in the table might be thought to be that for carbon dioxide. Such an analysis would provide the highest possible value of A_o and this is found to be 0.116 in the standard units used in this thesis. Turkdogan, on the other hand, analysed his Knudsen coefficient in terms of a gas of molecular mass equal to the average of the molecular mass of helium and carbon dioxide. This gives an A_o value of 0.086 in the same units. Both values are, of course, considerably below the values obtained in this work but are compensated for by higher

values of the effective molecular diffusion coefficients.
The values reported by Turkdogan correspond to a value of
0.284 for C_O and to an effective diffusion coefficient for
his average hydrogen/water vapour gas of 0.9 cm^2s^{-1} in iron
produced by reduction at 825°C. Corresponding values
obtained from the data obtained in this work would be 0.75cm^2s^{-1}
for hydrogen and 0.63 cm^2s^{-1} for water vapour.

Thus Turkdogan's analysis of his results suggests that the
balance between the relative importances of Knudsen and
molecular diffusion is weighted more towards Knudsen
diffusion and his data can therefore be used to further
examine the influence of mechanically driven flows. This is
done in the 5th, 6th and 7th rows in Table 6.15.
Calculations upon which the 5th row is based have been
carried out using Turkdogan's data, analysed in terms of the
average molecular weight gas, together with the flow
parameter B_O determined in this work. It is interesting to
note that the reduction time predicted in this way from
Turkdogan's data is virtually identical to that predicted
from the data obtained in this work but that the total
pressure at the reaction front is predicted to be 1.060 atm.
B_O has been put equal to zero for the data in the 6th row
and this produces an insignificant change in the reduction
time but increases the reaction front total pressure to 1.25
atmospheres. Similarly, putting B_O equal to ∞ for the 7th
row has a negligible effect on the reduction time and, as
before, reduces the total pressure at the reaction front to

1 atm. Thus we can see even when the Knudsen diffusion
coefficient is of considerable importance, the mechanically
driven flow does not influence the total reduction time, it
merely determines the actual values of the pressures at the
reaction front.

Thus the role played by mechanically driven flows will only
be important when the total and actual partial pressures at
the reaction front are important. Mechanically driven flows
need only be considered in the reduction mechanism of
hematite, therefore, if some form of surface reaction at the
reaction front contributes to the overall mechanism of
reduction. This is because the kinetics of such a reaction
would be dependent upon actual gas pressures at the reaction
front and these, as we have seen, are substantially
influenced by the resistance of the product layers to
mechanically driven flows. However, if the reduction is
solely determined by diffusion processes, the mechanically
driven flows can be omitted from a reaction model. Such an
omission would be compensated for by exagerated values of
the reaction front pressures.

It was noted above that Turkdogan's data, together with the
flow data determined in this work, predicts a total reaction
front pressure of 1.06 atm. Turkdogan does not present
actual measurements of total pressure but quotes the
pressures measured by McKewan, not exceeding 1.04 atm, as
support for his use of an isobaric analysis. The value
calculated from his work is higher than the value measured

by McKewan, and predicted from the parameters measured in this work, because Turkdogan's results place a higher relative weighting on the importance of Knudsen diffusion. The high pressure predicted casts some doubt on the correctness of this weighting, and this is further reinforced by the 8th row in Table 6.15 showing data calculated using the highest possible value of A_O that is compatible with Turkdogan's analysis. Even here, a reaction front pressure of 1.066 atm is predicted.

Reaction front pressures more in keeping with those measured by McKewan would be predicted if the balance between Knudsen and molecular diffusion were closer to that found in this work. They would also be predicted, of course, if a value of B_O higher than the value determined from this work were used in the analysis. Such a value might be compatible with Turkdogan's analysis of his results since he reports a porosity of 0.68 for his reduced iron compared with a value of 0.59 for this work. Since the value of B_O is strongly dependent upon porosity, see equation (3.18), it is possible that the iron produced by Turkdogan gives much lower Knudsen diffusion coefficients at the same time as higher bulk flows. It is also possible, however, that the relatively greater importance he attributes to Knudsen diffusion is an artifact of his analysis of the effective diffusion coefficients he measured at different pressures in terms of the Knudsen diffusion of an average gas.

There is some independent evidence in Turkdogan's work,

382

however, that the porous iron he investigated did have the low Knudsen diffusion coefficients that he quotes. He made independent measurement of the pore sizes be mercury porosimetry and by B.E.T. As the diffusion relevant pore size, he took the pore radius that corresponded to the point of inflexion of the porosimetry curve, obtaining a value of 0.35 μm for iron reduced at 825°C. The value calculated from his B.E.T. surface area measurement is 0.58 μm and both values are considerably below the values shown in table (6.14) calculated by applying the random orientated single sized pore model to the results measured in this work. Warner[12] also measured pore sizes directly obtaining values in the range 0.4 to 1.0 μm for iron produced by reduction at 850°C. He points out however, that the diffusion relevant pore size will probably be greater than that measured by mercury porosimetry since the latter technique tends to measure the size of restrictions in the pores. It is unlikely, however, that the irons investigated in each reaction will have the same pore size - a range of pore sizes, and therefore a range of balances between Knudsen and molecular diffusion, is the most likely situation.

The values of A_o, B_o and C_o obtained by Bradshaw and Unal for magnetite produced by the reduction of hematite in carbon monoxide are interesting in this context. In the units used in this thesis, they were 0.330, 1.14 X 10^{-9}, and 0.15, respectively, values that show a weighting between Knudsen and molecular diffusion very close to that

determined in this work. That this type of weighting is found in the two investigations that directly measured molecular and Knudsen diffusion is quite significant, even though Bradshaw and Unal's results are for porous magnetite. Edstrom[71] points out that the most significant structural changes during the reduction of hematite to iron occur during the hematite to magnetite stage so it might be inferred that the structure of the porous iron finally produced would bear strong similarity to that of the intermediate magnetite. However, Bradshaw and Unal carried out their reductions in carbon monoxide, and no comparative study has yet been carried out on the diffusion properties of porous iron produced by reduction in hydrogen and by reduction in carbon monoxide. Thus little can be learnt from direct comparison of the numerical values obtained in this work and those obtained by Bradshaw and Unal, although the relative weightings are more comparable.

6.6.2 Effect of sintering

No previous investigation has been reported on the effect of sintering on the diffusion of gases through porous iron. It might be thought that sintering would decrease the diffusion rates and it is therefore perhaps surprising that the sintering processes carried out in this work at 1100°C for 5 hours resulted in an increase in the values of all three parameters. The effect that these changes have on the reduction rate is shown in the last row of Table 6.15. The data in this row corresponds to that determined in the

sintered iron, the actual values of A_O, B_O and C_O being

shown in Table 6.9. The calculated data in this last row

shows that the reduction time would be decreased by 30% were

it to be controlled by diffusion and flow through porous

iron with the same structure as that produced by sintering

at 1100°C for 5 hours. This is a very severe sintering

process quite clearly far more severe than any sintering

that could occur during the reduction of an ore particle.

It can thus be concluded that sintering of the porous

product iron layer would have a negligible effect during the

reduction of hematite particles.

It is interesting, nevertheless, to examine the cause of

this increase in diffusion rates brought about by sintering.

Plate 6.2 shows the microstructure of the porous iron layer

after sintering and is to be compared with Plate 6.1 which

shows the original microstructure of the reduced iron.

Plate 6.2 shows that the porosity of the iron has been

little affected by sintering - the measured porosity showed

a 2% change (see Section 6.4) - but that the shape of the

flow channels has been considerably affected. As might be

expected, the profile of the channels has been 'rounded' as

the sintering process has filled in re-entrant and acute

angles. Thus the diffusion paths have been straightened and

the proportion of dead space in the structure has been

reduced. Expressing the value of C_O as the ratio of the

porosity to the tortuosity shows that the change in the

effective molecular diffusion coefficient brought about by

sintering suggests a change in tortuosity from 6.1 to 4.2. The application of this change to the value of Knudsen diffusion coefficient A_O measured for the reduced iron would predict a value of 0.462 for A_O in the sintered iron. The fact that the value measured in the sintered iron was 0.465 suggests that the sintering process had virtually no effect on the pore size, and this is confirmed by calculations carried out in Section 6.5 and the pore sizes shown in Table 6.13. In particular, the pore sizes calculated from equation (6.11) show virtually no change on sintering.

6.6.3 The decomposition of calcium carbonate

The decomposition of calcium carbonate is a process in which the value of β is zero. Thus it provides a further test of the importance of mechanically driven flows on gas solid reactions. Equation (3.78) has been derived for the dimensionless time of decomposition when the reaction front temperature remains constant and the first row in Table 6.16 shows values of the dimensionless time calculated using the values of A_O, B_O and C_O measured in this work for lime whose porosity is about 50% and assuming that the interface temperature is 850°C.

The effect of the mechanically driven flow on the kinetics of this reaction is investigated in the same way as for the reduction of hematite in that reaction front pressures and dimensionless decomposition times have been calculated for values of B_O effectively infinite and effectively zero.

386

The resulting values are shown in rows 2 and 3 of Table 6.16 and demonstrate that mechanically driven flows play a more important role in the decomposition of calcium carbonate than they do in the reduction of hematite. The dimensionless reaction time is increased by some 10% when the value of B_O is zero, stopping all mechanically driven flows, and decreased by about the same amount when the value of B_O is made infinite - allowing completely free movement of bulk gas flows through the porous structure.

Table 6.16 Pressures and dimensionless times for the decomposition of calcium carbonate

Row No.	A_O/#	$B_O \times 10^{10}$/(cm^2)	C_O	$\dfrac{t^* p_T}{RTC_p}$	p_T/ atm	p_{CO2}/ atm	ψ_{CO2}/ atm
1	0.061	2.0	0.186	3.21	1.11	0.441	0.541
2	0.061	0	0.186	3.51	1.24	0.441	0.492
3	0.061	∞	0.186	2.91	1.00	0.441	0.595

#cm^2.s^{-1}(g.mol^{-1}.K^{-1})$^{0.5}$

The greater effect of the mechanically driven flow arises in this reaction because the transport of carbon dioxide through the porous lime away from the reaction front is brought about partly by diffusion through the inert gas - air or nitrogen in this case - and partly through permeation down a bulk pressure gradient.

As stated in the theoretical section, Hills[70] had investigated the decomposition of calcium carbonate but had analysed the diffusion process as if it were solely Knudsen diffusion. The measurements made in this work suggest,

however, that molecular and Knudsen diffusion play more or less equal parts in the transport of carbon dioxide through the porous lime product layer. The A_o and C_o values shown in Table 6.16 give an effective Knudsen diffusion coefficient for carbon dioxide in the porous lime at 850°C of 0.323 cm^2s^{-1} and an effective binary molecular diffusion coefficient for a carbon dioxide/air mixture of 0.303 cm^2/s^{-1}.

Using the Bosanquet interpolation formula, these values would give an effective diffusion coefficient for carbon dioxide of 0.156 cm^2s^1 which is well within the range of values determined by Hills and his coworkers[45]. However, the values determined by Hills from the kinetics of decomposition of spherical particles must also have be influenced by the bulk flow process, and it is for this reason that equation (3.77) has been derived for an equivalent pseudo Knudsen diffusion coefficient. The value determined from the data in the first line of Table (6.16) using this equation is 0.191 cm^2s^{-1} and this is somewhat above the values determined by Hills. However, the highest furnace temperature at which Hills studied the decomposition was 900°C and he showed the pseudo diffusion coefficient to increase with temperature, so that the value calculated from equation (3.77) is not outside reasonable agreement with the findings of Hills.

The choice of reaction front temperature is, however, crucial to this agreement since the decomposition pressure increases rapidly with the temperature. Thus, had a

temperature higher than 850°C been chosen, the higher decomposition pressure would allow a higher total pressure to be built up at the reaction front thereby increasing the mechanically driven flow. This would result in an increased rate of decomposition, an increased difference in ψ_{CO_2} and hence an increased value of the pseudo diffusion coefficient. The value of 850°C has been chosen since, at a furnace temperature of 900°C, Hills showed the reaction interface to be some 70°C below the furnace temperature and he also showed that this temperature difference increased very rapidly with furnace temperature. Thus a difference of 100°C is not an unreasonable figure for a furnace temperature of 950°C.

A full investigation of the relationship between the values of A_o, B_o and C_o determined in this work and the findings of Hills would require the incorporation of the Dusty Gas Equations into a heat and mass transfer model for the reaction. The development of such a model is beyond the scope of this thesis. However, the pseudo diffusion coefficients determined from the results of this work are not sufficiently far from the values determined by Hills to invalidate the model that he proposed for the decomposition reaction, especially when differences due to the different source of the carbonate are taken into account.

CHAPTER 7 – <u>CONCLUSIONS AND FURTHER WORK</u>

7. 1. CONCLUSIONS

1. A previously developed experimental method for studying diffusion and flow in porous media has been refined and used to study the diffusion of gases in iron produced by the reduction of hematite, in iron produced by the sintering of such iron, and in lime produced by the decomposition of calcium carbonate.

2. The Dusty Gas Model has been re-stated in its phenomenological form and used to develop equations for the flow of a single gas through a porous media and for the diffusion of binary gases in the presence of a total pressure gradient.

3. Basic equations developed from the Dusty Gas Model have been used to analyse the results of pure gas permeability experiments and binary gas isobaric diffusion experiments carried out using the experimental method. The analysis results in three phenomenological parameters that fully characterise the diffusion and flow properties of any given porous solid, differentiating between Knudsen and molecular diffusion and mechanically driven bulk flow. The parameters determined have been shown to be independent of temperature and of gas type within the limits of experimental error. One set of results, for the Knudsen diffusion of argon in porous iron at high temperature, however, deviates from the other results

in porous iron by a factor slightly greater than can be accounted for by random variation. This variation is thought to be due to some experimental artifact.

4. Equations developed from the Dusty Gas Model have been used to predict diffusion rates under non-isobaric conditions and the results compared with experimental measurements. Good agreement was obtained which, with the constancy of the experimental values of the phenomenological parameters, has been taken to confirm the accuracy of the Dusty Gas Model, at least for making predictions at moderate pressures.

5. A survey has been carried out of the structural models that have been proposed for the prediction of diffusion and flow in porous media. The models have all been shown to contain at least one adjustable parameter that can only be determined by making diffusion measurements. They would seem to offer little advantage over the Dusty Gas Model, although this work has shown that a relationship between the phenomenological parameters provided by the single size random capillary pore model applies fairly accurately as long as Knudsen diffusion is of relatively little importance. When Knudsen diffusion is of importance, the pores in the solid seem to behave as short Knudsen capillaries, rather than the long straight capillaries on which the single size random pore model is based.

6. The non-isobaric equations generated by the Dusty Gas
    Model have been used to determine relative reduction
    rates of hematite and these have shown that Knudsen
    diffusion must be included in any analysis of the
    mechanism of gas/solid reactions. Mechanically driven
    gas flows, on the other hand, are only important if
    actual pressures at the reaction front are important.
    Virtually the same reduction times are predicted with
    and without inclusion of the mechanically driven flow.

7. The non-isobaric equations have also been used to
    analyse diffusion during the decomposition of calcium
    carbonate. This analysis has shown that previous work
    on the mechanism of the reaction is in error in that it
    assumed the diffusion process to be wholly Knudsen in
    nature. A mixed diffusion model is in operation, but
    the reaction times generated using the data obtained in
    this work are not significantly different from those
    obtained previously.

7.2 FURTHER WORK

The work has shown that Knudsen diffusion is of relatively
little importance in porous iron produced by the reduction
of hematite, at least when the reduction is carried out at
$825^{O}C$. Iron reduced at lower temperatures has been shown to
have a much greater surface area, so that a study similar to
this one on iron reduced at a lower temperature, say $600^{O}C$,
would show whether   Knudsen diffusion would play the more
important role that might be expected.

The reduction in this work has been carried out in pure hydrogen, and the proposed work at $600^{\circ}C$ would also be, but microphotographs of porous irons have shown the structure of to be coarser when the iron is reduced in carbon monoxide. The diffusion and flow parameters could thus have higher values in iron reduced in CO that in H_2 and experiments could usefully be carried out to discover whether or not this is so.

Such an investigation would be of great relevance to the direct reduction process since differing amounts of CO and H_2 in natural gas reformed in different ways could result in different structures and thus in different diffusion rates. The importance of such differences should be explored in further theoretical work in which the Dusty Gas Model is applied to the four component gas mixture involved in direct reduction and reduction rates are predicted in reducing gases of different hydrogen to carbon ratios.

Further theoretical work could be done on the decomposition of calcium carbonate to modify the apparently successful previous heat and mass transfer model to include the true mixed diffusion and flow process that occurs in the lime rather than Knudsen diffusion alone.

REFERENCES

1. Knudsen M, - Ann. Phys, $\underline{28}$, 75, (1909).

2. Bosanquet C H - British Report BR507, (1944).

3. Scott D S and Dullien F A L - A.I.Ch.E. $\underline{8}$, 113, (1962).

4. Scott D S and Dullien F A L - ibid, 293, (1962).

5. Carman P C - Flow of gases through porous media, Butterworth, London Scientific Publications, (1956)

6. Wakao N, Otani S and Smith J M - A.I.Ch E. $\underline{11}$ (3), 435, (1965).

7. Wheeler A - Catalysis, $\underline{2}$, (105), 479 (1955).

8. Hewitt F G and Morgan J R - Progress in Applied Mat.Res. $\underline{5}$, 165, (1964).

9. Hutcheon J M, Longstaff B and Warner R K - Ind. Carbon and Graphite Conference in London, 24-26 Sept. 1957, Soc. of Chemical Industry, 259, (1958).

10. Wyllie M R J and Rose W D - Nature, $\underline{165}$, 972, (1950).

11. Turkdogan E T, Olsson R G and Vinters J V - Metallurgical Transactions $\underline{2}$, 3189, (1971).

12. Warner N A - Transactions Met.Soc.AIME $\underline{230}$, 171, (1964).

13. Turkdogan E T, Olsson R G and Vinters J V - Carbon, $\underline{8}$, 545, Pergamon Press (1970).

14. Johnson M and Stewart W - Journal of Catalysis, $\underline{4}$, 248, (1965).

15. Satterfield C N and Caddle P J - Ind.Eng.Chem.Fundam, $\underline{7}$, 202 (1968).

16. Brown L F, Haynes H W and Manogue W H - Journal of Catalysis, $\underline{14}$, 220 (1969).

17. Wakao N and Smith J M - Chem.Eng.Sc, $\underline{17}$, 825, (1962).

18. Satterfield C N - Mass Transfer in Heterogeneous Catalysis, MIT Press, Cambridge, Massachussetts (1970).

19. Derjaguin B and Bakanov S P - Sov.Phys. Doklady, $\underline{2}$, 326, (1957).

20. Evans R B, Watson G M and Mason E A - The Journal of Chemical Physics, $\underline{35}$, (6), 2076, (1961).

21. Mason E A and Marrero T R - Advances in Atomic and Molecular Physics, $\underline{6}$, 200, (1970).

22. Dye R F and Dallavalle J M - Ind. and Eng.Chem, $\underline{50}$ (8), 1195, (1962).

23. Ney E P and Armistead F C - Phys. Rev. $\underline{71}$, 14, (1947).

24. Greco G - Ingeneria Quimica Italiana, $\underline{8}$, (10), 225, (1972).

25. Hoogshagen J - Ind. Eng.Chem, $\underline{47}$, 906, (1955).

26. Wicke E and Kallenbach R - Kolloid Z, $\underline{97}$, p135, (1941).

27. Weller K R, Stenhouse N S and Watts H - Canadian J. of Chem. $\underline{52}$, 2684, (1974).

28. Scott D S and Cox K E - The Canadian J. of Chem.Eng. 201, (1960)

29. Rothfeld L B - A.I.Ch.J, $\underline{9}$, 19, (1963).

30. Kadlec B, Hudgins R R and Silveston P L - Chemical Eng. Sci $\underline{28}$, 935, (1973).

31. Hoogshagen J and Bokhoven C - Journal of Chem.Phys. $\underline{21}$, (1), (1953).

32. Evans R B, Watson G M and Truitt J - Journal of Chem and Eng. Data $\underline{6}$, (4), 522 (1961).

33. Evans R B, Watson G M and Truitt J - Journal of Applied Physics $\underline{33}$, (9), 2682, (1962).

34. Asaeda M, Watanable J, Matono Y, Kojima K and Toei R - Journal of Chem. Eng. of Japan, $\underline{14}$, (1), 13, (1981).

35. Remick RR and Geankopolis C J - Ind.Eng.Chem.Fundam. $\underline{12}$, (2), (1973).

36. Davis B R and Scott D S - Symposium on Fundamentals of Heat and Mass Transfer, 58th Annual Meeting, American Inst. of Chem.Eng., Philadelphia (1965).

37. Schneider P and Smith J M - A.I.Ch.E.J. $\underline{14}$, 762 (1968).

38. Rosental A L. Zenkovski S M and Feodorov. - Zhurnal Prikladnoi Khimu, $\underline{47}$, (10), 2183 (1947), (translated).

39. Dogu G and Smith J M - A.I.Ch.E.J, $\underline{21}$, 58 (1975).

40. Moffat A J - Journal of Catalysis 54, 107 (1978).

41. Watanable J, Asaeda M and Kitamoto M - Journal of Chem.Eng. of Japan, 14, (1981).

42. Olsson R G and McKewan W M - Tran.Met.Soc.AIME, 236, 1518 (1966).

43. Turkdogan E T and Vinters J V - Metallurgical Trans. 2, 3175 (1971).

44. Bradshaw A V and Unal V -Private Communication, Paper to be published (see reference 105).

45. Campbell F R, Hills A W D and Paulin A - Chem.Eng.Sci. 25 , 929 (1970).

46. Schneider P, Chem.Eng.Sci. 33, 1311 (1978).

47. Reshetov V A - Russian Journal of Phys.Chem. 44, (12), 1740, 1960.

48. Hawtin P, Dawson R W and Roberts J - Trans.Instn.Chem Engrs., 47, T109, (1969).

49. Paulin A - PhD Thesis, London University, (1968).

50. Campbell F R, PhD Thesis, London University, (1971).

51. Partridge B A and Wall G P, Process Technology Division, Atomic Energy Research Establishment, Harwell, Berkshire, (1972).

52. Kim KK, Smith J M - Diffusion in Nickel Oxide Pellets, A.I.Ch.E Journal, 20, 670 (1974).

53. Ray H S - J.App.Chem. Biotechnol 26, 436 (1976).

54. Matyas A G and Bradshaw A V - Iron and Steelmaking 1, 180 (1974).

55. Szekely J and Evans J W - Metallurgical Trans, 2, 1699 (1971).

56. Bogdandy L and Engell H J - The Reduction of iron Ores, Berlin, Springer Verlag, (1970).

57. Szekely J, Evans J W and Sohn H Y - Gas Solid Reactions, Academic Press, NY (1976).

58. Quets J M, Wadsworth M E, Lewis T R - Trans. TMS AIME, 218, 545 (1960).

59. McKewan W M - Trans AIME, 212, 791 (1958).

60. Themelis N J and Gauvin W H - Trans.Canad.Inst.Min.& Met. 55, 444 (1962).

61. Kawasaki E, Sanscrainte J and Walsh J T - A.I.Ch.E Journal 48 (1962).

62. Hills A W D - Heterogeneous Kinetics at Elevated Temperatures, Plenum Press, 449 (1970).

63. Yagi T and Ono Y - Trans. ISI Journal, 8, 378 (1968).

64. Spittzer H, Manning F S and Philbrook W O - Trans. AIME 236, 1175 (1966).

65. Tien R H and Turkdogan E T - Metallurgical Transactions 3, 2039, (1972).

66. Szekely J and Evans J W - Metallurgical Transactions 2, 1691 (1971).

67. Szekely J , Lin C I and Sohn H Y - Chemical Engn.Sci., 28, 1975, (1973).

68. Bradshaw A V and Matyas A G - Metallurgical Transactions B, 7B, 81 (1976).

69. Sadrashemi F - PhD Thesis, London University, (1977).

70. Hills A W D - Chem.Eng.Sci, 23, 287 (1968).

71. Edstrom J O - Journal of The Iron and Steel Inst, 289, (1953).

72. Thomas C G, Hamilton J D and Bowling M Mc G - The Australian Inst. of Min. and Metall. Newcastle and District Branch, Pellets and Granules Symposium, 95, (1974).

73. Bowling M McG and Carter N B - Australian-Japan Extractive Metallurgy Symposium, Sydney, Australia, 133, (1980).

74. Thomas C G, Gray C H, Bowling M McG and Armstrong G J - Australas, Inst.Min.Metall. Conf - Western Australia, 533 (1973).

75. Urich D M and Tsu-Ming Han - Agglomeration (ed. W A Knepper), 669, (1962).

76. Fitton J T and Goldwin D C - J. Iron and Steel Institute, 204, 452 (1966).

77. Sasaki M, Nakazawa T and Kondo S - Trans. Iron and Steel Inst. of Japan 8 (3), 146 (1968).

78. Hamilton J D G – Trans. Inst. Min. Metall. (Sect. C Mineral Processing Extr. Metall) C 30, (1976).

79. Steenks A, Koopmans K, Hakvoort G and Reijen L L – Delft Progress Report 5, 292 (1980).

80. Seth B B L and Ross H U – Canadian Metallurgy Quarterly, 2 (1) (1963).

81. Strangway P K and Ross H U – Candadian Metallurgy Quarterly, 4 (4), (1965).

82. Maxwell J C cited by Reference No. 21.

83. Evans R B, Watson G M and Mason E A – The Journal of Chemical Physics, 36 (7), 1894, (1962).

84. Mason E A, Malinauskas A P and Evans R B – The Journal of Chemical Physics, 46, (8), 3199 (1967).

85. Bird R B, Stewart W E and Lightfoot E N – Transport Phenomena, Wiley, N.Y., (1960).

86. Hirschfelder J O, Curtis C F and Bird R B – Molecular Theory of Gases and Liquids, Wiley, N.Y., (1956).

87. Fuller E N, Schettler P D and Giddings J C – Ind. Eng. Chem. 58, (5), (1966).

88. Turkdogan E T and Vinters J V – Met. Trans. 3, 1561, (1972).

89. Geiger G H and Poirier D R – Transport Phenomena in Metallurgy, Addison Wesley Publishing Co., (1973).

90. Youngquist G R – Ind. Engng. Chem. 62, 52, (1970).

91. McKewan W M – Trans. TMS AIME, 218, 2-6 (1960) – Steelmaking, The Chipman Conference, 141, MIT Press.

92. Weisz P P – Z. Phys.Chem, 11, (1), (1957).

93. Walker P L. Rusinko J and Kaats E – Nature, 176, 1167, (1955).

94. Walker P L and Rusinko J – Journal Phys. Chem. 59, 241, (1955).

95. NEL Report – Ministry of Technology, Report 197, (1965).

96. Proc. Inst. Mech. Engrs., 169, (4), 107, (1955).

97. Metal Treatment – 29 (198), 97, (1962).

98. Becker S I and Mollick L - Trans. Amer. Soc. Mech. Engrs., _82_, (2), 136 (1960).

99. Morgan R A P - Sheet Metal Ind., _38_ (406), 99.

100. Butterworth G - Private Communication, Sheffield City Polytechnic, (1979).

101. Bradshaw A V - Trans. A.I.M.M.E., _79_, C281, (1970).

102. Low Melting Point Alloys - Metals Handbook, 74, (1948).

103. Harrington M J - PhD Thesis, Sheffield Polytechnic, (1972).

104. Hills A W D - Private Communication, Sheffield City Polytechnic, (1982).

105. Unal V - Ph.D Thesis, London University, (1975)

106. Beale C O, Appleby J E, Butterfield P and Young P A - I.S.I. Special Report 78,50, (1964).

107. Mickley H S, Sherwood T K and Reed C E - Applied Mathematics in Chemical Engineering, Mc. Graw Hill Book Co, (1957)

108. Neville A M and Kenedy J B - Basic Statistical Method for Engineers and Scientists, Intertext Student Book, (1964)

109. Hills A W D - Direct Reduction Course, Central University of Caracas, Venezuela, (1976).

Appendix 1

THE CALCULATION OF THE DIFFUSION COEFFICIENTS IN BINARY GAS MIXTURES

Although the most accurate method of estimating binary molar diffusion coefficients is the theoretical equation[86], based on the modern kinetic theory of gases and the Lenard-Jones expression for intermolecular forces:

$$D_{AB} = \frac{0.001858 \; T^{3/2} [(M_A + M_B)/M_A M_B]^{1/2}}{P \sigma^2_{AB} \Omega_D} \; , \qquad (a)$$

where,

T = absolute temperature

M_A and M_B = molecular masses of the two species

P = total pressure

Ω_D = collision integral as function of KT/Σ

Σ, σ = force constants in the Lenard-Jones potential

K = Boltzman constant,

a much simpler expression has been developed by Fuller et al[87]. Their equation,

$$D_{AB} = \frac{1.10^{-3} \cdot T^{1.75}}{P(v_A^{1/3} + v_B^{1/3})^2} \sqrt{\frac{1}{M_A} + \frac{1}{M_B}} \; , \qquad (b)$$

where v_A and v_B represents the diffusion volumes given for simple molecules, avoids the necessity of evaluating the collision integral Ω_D. They predicted binary diffusion coefficients, D_{AB}, to within 10% of the measured values 92.6% of the time. The equation (b) was used in the present work to calculate binary diffusion coefficients for the gas pair of interest at different temperatures. The characteristics of the gases employed are presented in the

Table below together with the correspondent values of the diffusion coefficients.

GAS PAIR AB	T/ (T)	$v_A/$ (**)	$v_B/$ (**)	$M_A/$ ($g.mol^{-1}$)	$M_B/$ ($g.mol^{-1}$)	$D_{AB}*/$ ($cm^2.s^{-1}$)
Ar-He	292	16.1	2.88	39.94	4.00	0.694
	898					4.96
Ar-CO_2	1223	16.1	26.9	39.94	44.00	1.81
CO_2-Air	1223	26.9	20.1	44.00	28.0	1.87
H_2-H_2O	1073	7.07	12.7	2.00	12	8.45
H_e-CO_2	293	2.88	26.9	4.00	44	0.555

* The values for D_{AB} in this table were calculated for 1 atm pressure, although in calculating the results from isobaric and non isobaric experiments the effect of total pressure in the system was taken into account.

** Arbitrary units

Appendix 2

THE CALCULATION OF THE VISCOSITIES OF GASES STUDIED

The viscosity of a single, nonpolar gas at low pressures is given by the equation developed by Chapman and Enskog[86] using the Lenard-Jones potential:

$$\mu = 2.67 \cdot 10^{-5} \frac{\sqrt{M_T} T}{\sigma^2 \Omega_n} \tag{a}$$

where μ = viscosity [g/cm.s]

T = temperature, [K]

σ = characteristic diameter of a molecule [$\overset{o}{A}$]

Ω_n = collision integral which is a function of the dimensionless temperature parameter $K_B T/\Sigma$

K_B = Boltzman constant , $\left[erg.K^{-1}.mol^{-1} \right]$

Σ = force constant in the Lenard-Jones potential function

In order to determine the viscosity of a gas using equation (a) appropriate values of Σ/K_B, Ω_n and σ may be obtained from tabulated data[89].

Viscosity values for the gases used in the present work together with the values of the pertinent parameters are presented in the following Table.

Gas	T / [K]	σ / [A]	Σ/K_B [K]	M / [g.mol^{-1}]	μ / [g.cm^{-1}s^{-1}]
Ar	.292	3.418	124.0	39.944	2.160
	898				5.014
	1230				6.137
He	292	2.576	10.2	4.0	1.927
	413				2.435
	441				2.561
	898				4.022
	1230				4.896
N$_2$	292	3.681	91.5	28.0	1.688
H$_2$	292	2.915	38.0	2	0.882

APPENDIX 3: MBASIC programme to compute C_o from the isobaric diffusion experiments.

```
 500 REM PROGRAMME "ISORT" TO CALCULATE CO AND DHEEFF FROM ISOBARIC EXPERIMENTS
 510 REM
 520 REM
 960 LPRINT "EXPERIMENTAL DATA"
 965 LPRINT
 980 LPRINT "  RUN   PRESS   RE   RI    S    CHOB   CHIB   FLUXH    DKH "
1000 PRINT "TYPE OPEN @I@,1,@EXPRESN.DTA@ , WHERE @ REPRESENTS INVERTED COMMAS"
1001 PRINT "                             AND N REPRESENTS THE CHANGING DIGIT"
1002 PRINT "THEN TYPE CONT"
1003 STOP
1100 REM CHOB=HELIUM MOLAR FRACTION OUTSIDE BULK
1110 REM CHIB=HELIUM MOLAR FRACTION INSIDE BULK
1120 REM CAIB=ARGON MOLAR FRACTION INSIDE BULK
1130 REM CAOB=ARGON MOLAR FRACTION OUTSIDE BULK
1140 REM "VISA" AND "VISH" ARE VISCOSITIES OF ARGON AAND HELIUM RESPECTIVELY
1150 REM "FLHI" AND "FLAO" ARE VOLUMETRIC FLOW RATES OF HELIUM AND ARGON
1160 REM RESPECTIVELY
1170 REM DKH=HELIUM KNUDSEN DIFFUSION COEFFICIENT
1180 REM "RI" AND "RE" ARE THE INTERNAL AND EXTERNAL RADII OF THE SPHERE
1190 REM S=SHAPE FACTOR
1200 REM KA=RATIO OF THE KNUDSEN DIFFUSION COEFICIENNT OF HELIUM AND ARGON
1400 DIM FLUXH(20), PS(20), T(20), CHOB(20), CHIB(20), CAOB(20), CAIB(20),
VISA(20), VISH(20), FLIH(20), FLAO(20), DKH(20), RI(20), RE(20), S(20),KA(20)
1500 IF EOF(1) GOTO 20200
1510 INPUT #1,N,FLUXH(N),PS(N),T(N),CHOB(N),CHIB(N),CAOB(N),CAIB(N),
VISA(N),VISH(N),FLHI(N),FLAO(NN),DKH(N),RI(N),RE(N),S(N),KA(N)
1520 LPRINT USING "##.### ";N,PS(N),RE(N),RI(N),S(N),CHOB(N),CHIB(N),
FLUXH(N),DKH(N)
2010 K = N
2015 REM DHA=MOLECULAR DIFF.COEFF.OF AR-HE
2020 DHA = T(K)@1.75*3.4127E-05/PS(K)
```

A3-1

```
2030 REM CT=TOTAL MOLAR CONCENTRATION
2035 REM BETA =FLUX OF AR/FLUX OF HE
2040 CT=PS(K)/(82.0594*T(K))
2050 BETA=.409
2052 TEBA=1-BETA
2055 AK=KA(K)-1
2058 REM ROA AND ROH ARE DENSITIES OF AR AND HE RESPECTIVELY
2060 ROA=.4868*PS(K)/T(K)
2080 ROH=.04878*PS(K)/T(K)
2090 REM RYO=REYNOLDS NUMBER OUTSIDE SPHERE
2100  RYO=ROA*FLAO(K)*2*RE(K)/(12.57*VISA(K)*.0001)
2118 REM SCHO=SCHMIDT NUMBER OUTSIDE SPHERE
2120 SCHO=VISA(K)*.0001/(ROA*DHA)
2130 REM ALFAO=EXTERNAL MASS TRANSFER COEFFICIENT
2140 ALFAO=DHA*(2+2.33*RYO@.3385*SCHO@.33)/(2*RE(K))
2150 REM AREAO=EXTERNAL AREA OF THE SPHERE-(CROSS SECTIONAL AREAA OF THE
DIFFUSION SHAFT + CROSS SECTIONAL AREA OF THE PRESSURE PROBE
2160 AREAO=4*3.14159*RE(K)@2-.772
2170 REM CHOS= EXTERNAL MOLAR FRACTION OF HE AT SURFACE
2180 CHOS=(1-(1-TEBA*CHOB(K)/2)*EXP(-FLUXH(K)*.000001*TEBA/(CT*ALFAO*AREAO)))/TEBA
2200 ROAH=CHIB(K)*ROH+CAIB(K)*ROA
2218 REM RYI=REYNOLDS NUMBER INSIDE SSPHERE
2220 RYI=((ROAH*ROH)@.5*FLHI(K)*2)/(3.14159*RI(K)*VISH(K)*.0001)
2238 REM SCHI=SCHMIDT NUMBER INSIDE SPHERE
2240 SCHI=VISH(K)*.0001/(ROH*DHA)
2245 RY2=RYI@.9928
2250 SHI2=SCHI@.33
2258 REM ALFAI=INTERNAL MASS TRANSFER COEFFICIENT
2260 ALFAI=DHA*(2.359+.2758*RY2*SHI2)/(2*RI(K))
2270 REM AREAI=INTERNAL AREA OF THE SPHERE-(CROSS SECTIONAL AREAS OF
THE DIFFUSION SHAFT AND THE PRESSURE PROBE)
2280 AREAI=4*3.14159*RI(K)@2-.772
2285 REM CHIS=INTERNAL CONCENTRATION OF HE AT SURFACE
```

```
2300 CHIS=(1-(1-TEBA*CHIB(K))*EXP(FLUXH(K)*.000001*TEBA/(CT*ALFAI*AREAI)))/TEBA
2320 CO=.45
2340 DELTA=1/(1+CO*DHA/DKH(K))
2342 Z=(FLUXH(K)*.000001*T(K)*82.0594*AK)
2344 X=(KA(K)*DHA*S(K)*PS(K))
2346 W=LOG((KA(K)-AK*CHOS*DELTA)/(KA(K)-AK*CHIS*DELTA))
2358 REM CO=RATIO OF POROSITY TO TORTUOSITY FACTOR

2360 COC=Z/(X*W)
2380 PRINT CO, COC
2400 IF (ABS(CO - COC) > ABS(.0001*COC)) THEN GOTO 2500
2405 GOTO 2900
2500 CO = COC
2520 GOTO 2340
2900 DHEFF=1/(1/(COC*DHA)+1/DKH(K))
2950 LPRINT "DHEFF=";DHEFF
3000 LPRINT "CO = ";COC
3001 LPRINT "DHA=";DHA
3002 LPRINT "ALFAO=";ALFAO
3003 LPRINT "ALFAI=";ALLFAI
3004 LPRINT "CT=";CT
3005 LPRINT "CHOS=";CHOS
3006 LPRINT "CHIS=";CHIS
3007 LPRINT "RY2=";RY2
3008 LPRINT "SHI2=";SHI2
3009 LPRINT "ROA=";ROA
3010 LPRINT "ROH=";ROH
3011 LPRINT "ROAH=";ROAH
3012 LPRINT "AK=";AK
3013 LPRINT "Z=";Z
3014 LPRINT "X=";X
3015 LPRINT "W=";W
3050 GOTO 15000
```

APPENDIX 4: FORTRAN PROGRAMM TO COMPUTE THE NON-ISOBARIC DIFFUSION
RATES.

This programme solves equations (3.46) and (3.52) for the conditions
applying in the non-isobaric diffusion experiments. The integration is
carried out using a Runge-Kutta technique, the separate estimates of the
gradient being called for and averaged by the subroutine 'STEP4' which
is called by the main programme 'NNISOB'. 'STEP4' calls for a further
subroutine named 'DIFREL' which calculates the actual values of the
differentials from equations (3.46) and (3.52).

The differential interval is split into 25 steps and 'STEP4' called
to advance the integration over each step. An iteration procedure is
involved as described in Chapter 3, the differences between the bulk and
surface partial pressures inside and outside the sphere being calculated
in function statements 'FHEO(ND)' and 'FHEI(ND)'. Integration is first
carried out between the bulk phase partial pressures and the flux
determined in this way used in the function statements to determine
first estimates of the surface partial pressures. Integration is then
repeated between these two pressures and the iteration loop repeated
until the flux changes by less than a thousandth of its value between
two iterations (see the statement after statement 102).

Before computation begins, the experimental data is read from the disc
file 'EXPRIMNT.DTA' where it had previously been written using
"DATASTAR".

The listings of the main programme and the two sub-programmes are
presented below.

```
        PROGRAM NNISOB
C PROGRAMME TO COMPUTE NON-ISOBARIC FLUX AND NON-ISOBARIC TOTAL PRESSURE
C DROP FROM EXPERIMENTALLY DETERMINED INTERNAL AND EXTERNAL BULK GAS
C COMPOSTIONS, ISOBARICALLY DETERMINED EFFECTIVE DIFFUSION COEFFICIENT
C AND DHEK AND BO/MU DETERMINED FROM PERMEABILITY MEASUREMENTS.
C
C THE DIFFERENTIAL EXPRESSIONS USED (AS CALLED BY STEP4) ARE THOSE
C DEVELOPED BY THE FINAL MASON AND EVANS DUSTY GAS MODEL.
C
C THIS PROGRAMME CALCULATES DELTA FROM THE GIVEN VALUE OF DHE,EFF AND
C NOT FROM DHE,K
C
        DIMENSION PHE(2),PTOT(2),CAPFI(2),BLAN(2)
        REAL NDOTHE(2),ND,KSI,NDOTA
        EXTERNAL DIFREL
        COMMON DHEEFF,BETA,AKAPP,DHEK,DELTA,BOOVMU,KSI
        OFHEO(ND) = PTOO*(1.0-(1.0-(1.0-BETA)*PHEO/PTOO)*EXP(ND*(BETA-1.0)
        1*82.06*THETA/(PTOO*ALFAO*AO)))/(1.0-BETA)
        OFHEI(ND) = PTOI*(1.0-(1.0-(1.0-BETA)*PHEI/PTOI)*EXP(ND*(1.0-BETA)
        1*82.06*THETA/(PTOI*ALFAI*AI)))/(1.0-BETA)
        CALL OPEN (6,'EXPRIMNTDTA',0)
49      OREAD (6,2,END=50) IS,IRUN,DHE,BT,AK,DKHE,CO,BM,PHEO,PHEI,PTOO,
        1       PTOI, S, THETA,RADO, RADI,FLAO,FLHEI,VISA,VISH
2       OFORMAT (I1,1X,I2,1X,2(F5.3,1X),2(F4.2,1X),F6.4,1X,F5.3,1X,F7.5,1X,
        1          F6.4,1X,2(F5.3,1X),F5.2,1X,F4.0,1X,2(F5.3,1X),F4.2,1X,
```

```
    2        F5.2,2(1X,E11.4))
     DHEEFF = DHE
     BETA = BT
     AKAPP = AK
     DHEK = DKHE
     BOOVMU = BM
    OWRITE(2,3) IS,IRUN,DHE,BT,AK,DKHE,CO,BM,PHEO,PHEI,PTOO,
    1      PTOI, S, THETA,RADO, RADI,FLAO,FLHEI,VISA,VISH
  3  OFORMAT (10X,38HNON-ISO-BARIC EXPERIMENT ON SPHERE NO , I1,
     119H, EXPERIMENT NUMBER ,I3//10X,48HCALCULATIONS USING MASON & EVAN
     2S DUSTY GAS MODEL,18H DELTA FROM DHEEFF/
     210X,8HDHEEFF = ,F5.3,15H CM2/S, BETA =
     3,F5.3,10H, KAPPA = ,F5.3/10X,6HDHEK = ,F5.3, 16H CM2/S, CZERO =
     4,F6.4,10H, BO/MU = ,F5.3,12H CM2/(S.ATM)/10X,6HPHEO = ,F7.5,4H ATM
     58H, PHEI = ,F6.4,13H ATM, PTOO = ,F5.3,4H ATM/10X,8H PTOI = ,F5.3,
     610H ATM, S = ,F5.2,13H CM, THETA = ,F4.0,11H K, RADO = ,F5.3,3H CM
     7/10X,7HRADI = ,F5.3,12H CM, FLAO = ,F5.2,16H CM3/S, FLHEI = ,
     8F6.3,6H CM3/S/10X,7HVISA = ,E11.4,19H GM/(CM.S), VISH = ,E11.4,
     911H GM/(CM.S) /)
     KSI = DHEK/BOOVMU
     DHA = THETA**1.75*3.4127E-05/(PTOO+PTOI)*2
     DELTA = DHEEFF/(CO*DHA)
     ROA = .4868*PTOO/THETA
     SCHMDO = VISA/(ROA*DHA)
     RENO = ROA*FLAO*2*RADO/(12.57*VISA)
     ALFAO = DHA*(2+2.33*RENO**.3385*SCHMDO**.33)/(2*RADO)
     AO = 12.566*RADO**2-0.772
     ROHE = .04878*PTOI/THETA
     ROAHE = ROA*(PHEI/PTOI) + ROHE*(1-PHEI/PTOI)
     SCHMDI = VISH/(ROHE*DHA)
     RENI = SQRT(ROAHE*ROHE)*FLHEI*2/(3.14*RADI*VISH)
     ALFAI = DHA*(2.359+0.2758*RENI**0.9928*SCHMDI**0.33)/(2*RADI)
     AI = 12.566*RADI**2-.772
     DELPEX = PTOO - PTOI
    OWRITE(2,100) KSI,DHA,DELTA,ROA,SCHMDO,RENO,ALFAO,AO,ROHE,
    1ROAHE,SCHMDI,RENI,ALFAI,AI,DELPEX
100  OFORMAT(10X,17HCALCULATED DATA:-/10X,6HKSI = ,F4.3,8H; DHA = ,F6.4
     1,7H CM2/S;,9H DELTA = ,F6.4,/10X,15HDENSITY OF A = ,E9.4,
     27H G/CM3;,9H SC(O) = ,F5.3,9H; RE(O) = ,F6.3/10X,10HALFA(O) = ,
     3F5.3,14H CM/S; A(O) = ,F5.2,22H CM2; DENSITY OF HE = ,E9.4,
     46H G/CM3/10X,24HHARMONIC MEAN DENSITY = ,E11.4,16H G/CM3; SC(I)
     5 = ,F5.3/10X,10H; RE(I) = ,F6.3,12H; ALFA(I) = ,F6.3,
     614H CM/S; A(I) = ,F5.2,5H CM2./10X,21HEXPERIMENTAL DELPT = ,E11.4/
     7/10X,39HDATA FOR INTERMEDIATE ITERATION STEPS:-)
     PHEIN = PHEI
     NDOTHE(1) = 0
     J=0
     PHE(1) = PHEO
 22  NDOTHE(2) = NDOTHE(1)
     PTOT(1) = PTOO
     CAPFI(1) = PHE(1)
     BLAN(1) = 0.0
     HSTEP = (PHEIN - PHE(1))/25
     DO 20 I = 1,26
     CALL STEP4(PTOT,CAPFI,PHE,BLAN,HSTEP,1,DIFREL)
```

```
      PHE(1) = PHE(2)
      PTOT(1) = PTOT(2)
      CAPFI(1) = CAPFI(2)
20    BLAN(1) = BLAN(2)
      NDOTHE(1) = S*DHEEFF/(82.06*THETA)*(CAPFI(1)-PHEO)
      J=J+1
      PHE(1) = FHEO(NDOTHE(1))
      PHEIN = FHEI(NDOTHE(1))
      WRITE(2,102) NDOTHE(1),J,PHE(1),PHEIN
102   FORMAT (15X,E11.4,I5,2(5X,E11.4))
      IF (ABS(NDOTHE(1)-NDOTHE(2)).GT.ABS(0.001*NDOTHE(1))) GO TO 22
      DELPTH = PTOO - PTOT(1)
      NDOTA = -BETA*NDOTHE(1)
      WRITE (2,12) PHEIN,DELPTH,PTOT(1),CAPFI(2),NDOTHE(1),NDOTA
12    0FORMAT (/19X,20HCALCULATED RESULTS:-/
     110X,31HINTERNAL SURFACE A PRESSURE = ,F6.4,15HTHEORY DELPT = ,
     2E11.4/
     210X,26HINTERNAL TOTAL PRESSURE = ,F6.4,15H   FI INSIDE = ,F6.4/
     310X,27HTOTAL MOLAR FLOWS: OF A = ,E11.4,10H,  OF B = ,E11.4////)
      GO TO 49
50    ENDFILE 6
      END


      SUBROUTINE STEP4(Y,Z,U,V,H,N,DIFFUN)
C RUNGE-KUTTA SUBPROGRAM THAT INTEGRATES 4 SIMULTANEOUS DIFFERENTIAL
C EQUATIONS OVER AN INTEGRATION STEP H, SET BY THE CALLING PROGRAM
C THE DUMMY VARIABLE N IS THE POSITION IN ONE DIMENSIONAL ARRAYS FROM
C WHICH THE SUBPROGRAM READS THE INITIAL VALUES, RETURNING THE FINAL
C VALUES TO POSITIONS N+1.    SHOULD THE DIFFERENTIAL EXPRESSIONS
C INVOLVE X,  ONE VARIABLE MUST BE X.
C
C NB NB
C
C STEP4 REQUIRES A FURTHER SUBROUTINE TO CALCULATE
C THE DIFFERENTIALS.   THE DUMMY NAME OF THIS FUNCTION IS 'DIFFUN'
C AND ITS ACTUAL NAME MUST BE PROVIDED AS ONE OF THE ARGUMENTS
C SPECIFIED WHEN STEP4 IS CALLED BY THE CALLING PRGRAMME.
C IF THE EXPRESSIONS FOR THE DIFFERENTIALS INVOLVE X, IT MUST BE
C INCLUDED AS ONE OF THE 4 VARIABLES AND ITS DIFFERENTIAL MUST BE
C INCLUDED IN THE DIFFUN SUBROUTINE AND PUT EQUAL TO 1.   IN THIS CASE
C STEP4 CAN ONLY INTEGRATE THREE EQUATIONS FOR THREE DEPENDENT VARIABLES
C
      DIMENSION Y(3), Z(3), U(3), V(3), YINC(5), ZINC(5), UINC(5),
     1      VINC(5)
      YA    = Y(N)
      ZA    = Z(N)
      UA    = U(N)
      VA    = V(N)
      DO 100 J = 1,4
      CALL DIFFUN(YA,ZA,UA,VA,ADY,ADZ,ADU,ADV)
      YINC(J)  = H*ADY
      ZINC(J)  = H*ADZ
      UINC(J)  = H*ADU
      VINC(J)  = H*ADV
      IF (J-3) 101,102,100
```

```
101    YA     =   Y(N) + 0.5*YINC(J)
       ZA     =   Z(N) + 0.5*ZINC(J)
       UA     =   U(N) + 0.5*UINC(J)
       VA     =   V(N) + 0.5*VINC(J)
       GO TO 100
102    YA     =   Y(N) + YINC(J)
       ZA     =   Z(N) + ZINC(J)
       UA.    =   U(N) + UINC(J)
       VA     =   V(N) + VINC(J)
100    CONTINUE
       Y(N+1) = Y(N) + (YINC(1)+2.0*YINC(2)+2.0*YINC(3)+YINC(4))/6
       Z(N+1) = Z(N) + (ZINC(1)+2.0*ZINC(2)+2.0*ZINC(3)+ZINC(4))/6
       U(N+1) = U(N) + (UINC(1)+2.0*UINC(2)+2.0*UINC(3)+UINC(4))/6
       V(N+1) = V(N) + (VINC(1)+2.0*VINC(2)+2.0*VINC(3)+VINC(4))/6
       RETURN
       END


       SUBROUTINE DIFREL(PT,FI,PHE,BL,DPT,DFI,DPHE,DBL)
C SUBROUTINE TO CALCULATE THE DIFFERENTIALS FOR PHE AND FI FOR NON-
C EQUIMOLAR COUNTER NON-ISOBARIC DIFFUSION THROUGH A POROUS SOLID IN
C WHICH KNUDSEN AND MOLECULAR DIFFUSION AND VISCOUS FLOW ALL
C CONTRIBUTE TO THE TRANSPORT PROCESS.
C
C PROGRAM USES THE FINAL MASON & EVANS DUSTY GAS MODEL
C
       REAL KSI
       COMMON DHEFF,BETA,AKAPP,DHEK,DELTA,BOOVMU,KSI
       ODPT = PT*(1-BETA*AKAPP)*(1-DELTA)/(((1+PHE/KSI+AKAPP*(PT-PHE)/KSI)*
      1    (PT-PHE*DELTA*(1-BETA)) - PHE*PT*(1-DELTA)*(1-BETA*AKAPP)/KSI)
       ODFI = 1/(1 - PHE*(1-BETA)*DELTA/PT - (1-DELTA)*(1-BETA*AKAPP)*PHE/
      1      (KSI+PHE+AKAPP*(PT-PHE)))
       DPHE = 1.0
       DBL = 0
       RETURN
       END
```

Appendix 5

REGRESSION ANALYSIS USING THE LEAST SQUARES METHOD

The principle underlying the fitting of the best line to a set of data is that of the least squares. This states that if y is a linear function of an independent variable x, the most probable position of a line, $Y = a + mx$, is such that the sum of squares of deviations of all points (x_i, y_i) from the line is a minimum; the deviations are measured in the direction of the y-axis. It should be stressed that the underlying assumption is that x is either free from error (being assigned) or subject to negligible error only, while y is the observed or measured quantity subject to errors which have to be minimised by the method of least squares. The observed quantity y is thus a random value from the population of values of y corresponding to a given x. Thus the best fitting line through the data is the line which makes the sum of the squares of deviation of the measured y values from the predicted Y values a minimum. This sum of squares is:

$$\sum_i^{n_i} (Y_i - y_i)^2 = \sum_i^{n_i} [a + m(x_i - \bar{x}) - y_i]^2 \tag{1}$$

The sum of squares is a function of the constants a and m and it will be a minimum when:

$$\frac{\partial}{\partial a} \left(\sum_i^{n_i} (Y_i - y_i)^2 \right) = 0 \tag{2}$$

$$\frac{\partial}{\partial m} \left(\sum_i^{n_i} (Y_i - y_i)^2 \right) = 0 \tag{3}$$

where n_i is the number of observations.

When the indicated differentiations are carried out and the

resulting expression solved for a and m, there results:

$$a = \text{intercept} = \frac{\sum\limits^{ni} x^2_i \sum\limits^{ni} y_i - \sum\limits^{ni} x_i \sum\limits^{ni} x_i y_i}{n_i \sum\limits^{ni} x^2_i - (\sum x_i)^2} \qquad (4)$$

$$m = \text{slope} = \frac{n_i \sum\limits^{ni} x_i y_i - \sum\limits^{ni} x_i \sum\limits^{ni} y_i}{n_i \sum x_i^2 - (\sum x_i)^2} \qquad (5)$$

Hence the equation to the line of best fit can be written as:

$$Y = \frac{\sum\limits^{ni} x_i^2 \sum\limits^{ni} y_i - \sum\limits^{ni} x_i \sum\limits^{ni} x_i y_i}{n_i \sum x_i^2 - (\sum x_i)^2} + \frac{n_i \sum\limits^{ni} x_i y_i - \sum\limits^{ni} x_i \sum\limits^{ni} y_i}{n_i \sum x_i^2 - (\sum x_i)^2} x \qquad (6)$$

and is known as the line of regression of y on x.

The operation of fitting the best line is normally followed by a test of the degree of closeness to a straight line, since although it is possible to fit a straight line relation to a number of observations it does not mean that the physical data really follow a straight line.

The degree of closeness to a straight line is measured by the correlation coefficient, R, which is defined as:

$$R = \frac{\text{covariance of } x_i \text{ and } y_i}{(S_e(x) = \text{standard deviation of } x_i)(S_e(y) = \text{standard deviation of } y_i)} \qquad (7)$$

The covariance of x_i and y_i is a measure of the variation of the products of x_i and y_i. Therefore R is equal to:

$$R = \frac{\{\sum\limits^{ni} x_i y_i - (\sum\limits^{ni} x_i)(\sum\limits^{ni} y_i)/n_i\}(n_i - 1)}{\sqrt{\dfrac{\sum\limits^{ni} x_i^2 - (\sum\limits^{ni} x_i)^2/(n_i-1)}{n_i - 1}} \cdot \sqrt{\dfrac{\sum\limits^{ni} y_i^2 - (\sum\limits^{ni} y_i)^2/(n_i-1)}{n_i - 1}}} \qquad (8)$$

The $(n_i - 1)$ terms all divide out and this then is reduced to:

A5-2

$$R = \frac{\overset{ni}{\sum} x_i y_i - (\overset{ni}{\sum} x_i)(\overset{ni}{\sum} y_i)/n_i}{\sqrt{\overset{ni}{\sum} x_i^2 - (\sum x_i)^2/n_i} \cdot \sqrt{\overset{ni}{\sum} y_i^2 - (\sum y_i)^2/n_i}} \qquad (9)$$

Observing the similarity with equation (5) for the slope m, R can be expressed as:

$$R = \frac{m \, S_e(x_i)}{S_e(y_i)} \qquad (10)$$

Values of R = $\pm$1 indicate a perfect linear correlation.

Relationship between the standard deviation of the slope m and the correlation coefficient

Both the values of a and m calculated from equations (4) and (5) respectively, are subject to error, this error being a direct consequence of the error in the measured value of y. Estimates of the error variance of a and m are readily evaluated:

$$S_e^2(a) = S_e^2(\bar{y}) = \frac{S_e^2(y_i)}{n_i} \qquad (11)$$

and

$$S_e^2(m) = \frac{S_e^2(y_i)}{(x_i - \bar{x})^2} \qquad (12)$$

where $S_e^2(y_i)$ is the variance of estimate equal to:

$$S_e^2(y_i) = \frac{\overset{ni}{\sum}(Y_i - y_i)^2}{n_i - 2} \qquad (13)$$

The (n_i-2) degrees of freedom result from the use of the two quantities, a and m, which are calculated from the data. Therefore if we substitute equation (13) into (12) the following results: (14)

$$S_e^2(m) = \frac{\sum\limits^{ni}(Y_i - y_i)^2}{(n_i - 2)\sum\limits (x_i - \bar{x})^2} \qquad (14).$$

The mean square deviation $\sum\limits^{ni}(x_i - x)^2$ is related to the variance of x_i as follows:

$$\sum\limits^{ni}(x_i - \bar{x})^2 = n_i S_e^2(x_i) \qquad (15)$$

By substituting equation (15) and equation (1), equation (14) becomes:

$$S_e^2(m) = \frac{\sum\limits^{ni}[a + m(x_i - \bar{x}) - y_i]^2}{n_i(n_i - 2)S_e^2(x_i)} \qquad (16)$$

But $a = \bar{y}$ from equation (11), and hence equation (16) can be written as:

$$S_e^2(m) = \frac{\sum\limits^{ni}[m(x_i - \bar{x}) - (y_i - \bar{y})]^2}{n_i(n_i - 2)S_e^2(x_i)} \qquad (17)$$

After some algebraic manipulation and bearing in mind that $\sum(x - \bar{x}) = 0$, equation (17) becomes:

$$S_e^2(m) = \frac{n_i S_e^2(y_i) - m^2 n_i S_e^2(x_i)}{n_i(n_i - 2)S_e^2(x_i)} \qquad (18)$$

In $n_i \gg 2$ equation (18) can be rearranged:

$$S_e^2(m) = \frac{S_e^2(y_i)}{n_i^2 S_e^2(x_i)} - \frac{m^2}{n_i} \qquad (19)$$

Substituting equation (16) in (19) and further rearrangement gives:

$$S_e^2(m) = \frac{m^2}{n_i}\left(\frac{1}{R^2} - 1\right) \qquad (20)$$

Therefore the standard deviation becomes:

$$\frac{S_e(m)}{m} = \sqrt{\frac{1/R^2 - 1}{n_i}} \qquad (21)$$

A5-4

Appendix 6

THE COMPARISON OF VARIANCES AND THEIR PROPERTIES – THE L-TEST AND F-TEST

The L-Test

It is often important to know with some degree of certainty whether the standard deviations of two or more samples are the same, ie they do not differ significantly. This is achieved by the L-test.

A calculation is carried out to determine the probability that the samples represent normal populations exhibiting the same population variances but without regard to the population means. This test was devised by Neyman and Pearson[107], who defined the quantity L as equal to:

$$L = \frac{n_i (S_1^2 . S_2^2 .... S_i^2)^{1/n_i}}{\Sigma S_i^2} \qquad (1)$$

n_i represents the number of sample sets, each set containing the same number of entries, $(n_k)_i$.

The calculated value of L is compared with a tabulated value of L associated with a 5% probability and if it is bigger than the tabulated value of L it is reasonable to conclude that the populations represented by the samples have the same variance. If the L test is affirmative, the probability that the population means are equal may be ascertained using the F-test.

The F-Test

The F-test assesses whether two sets of data come from the same population. The basis for the F-test, lies in making two independent estimates of the variance of the population.

One estimate comes from the variance of the means $S^2_{m,p}$, which is determined by dividing the sum of the squares of the deviations of the sample means, $\bar{x}_i$, from the mean of all the values, $\bar{x}_p$, by the number of samples, n_i, less 1 (one degree of freedom lost in determining the overall mean)

$$S^2_{m,p} = \frac{\overset{ni}{\Sigma}(\bar{x}_i - \bar{x}_p)^2}{n_i - 1} \tag{2}$$

This variance of the means becomes an estimate of the variance of the population, S_p^2, since it is multiplied by the average number of readings in the samples, n_k,

$$S_p^2 = S^2_{m,p} \times n_{k,i} \tag{3}$$

The second estimate of the variance of the population, S_e^2, is generated by adding the sums of the squares of the deviations within each sample $\overset{n_i}{\Sigma}\,\overset{n_{i,k}}{\Sigma}(x_{i,k} - \bar{x}_i)^2$ and dividing by the total number of readings, $\Sigma n_{k,i}$, less the number of samples, n_i,

$$S_e^2 = \frac{\overset{n_i}{\Sigma}\,\overset{n_{i,k}}{\Sigma}(x_{i,k} - \bar{x}_i)^2}{\Sigma n_{k_i} - n_i} \tag{4}$$

The degree of freedom associated with S_e^2 is the total number of measurements in all samples less the number of samples.

The variable F is the number generated by dividing the first variance estimate, S_p^2, by the second variance estimate, S_e^2.

$$F = \frac{S_p^2}{S_e^2} \tag{5}$$

Values of F are tabulated[108] for 1% and 5% levels of significance. If the value computed from the results exceeds the tabulated value, the variance between the sample means

A6-2

can be said, to the given level of significance, to be unlikely to have arisen from random variations.

APPENDIX 7: FORTRAN PROGRAMS TO COMPUTE DIMENSIONLESS REACTION TIMES FOR
THE REDUCTION OF HEMATITE AND THE DECOMPOSITION OF CALCIUM CARBONATE

Fortran programmes were written to solve equations (3.46) and (3.52) for
the reduction of hematite - called 'SFERED' - and for the decomposition
of calcium carbonate - called 'CACO3D'. The listings of these
programmes are presented in this appendix. As with the programme
'NNISOB' described in Appendix 4, the solution involves the Runge-Kutta
scheme managed by the subroutine 'STEP4' which in turn calls a further
subroutine to calculate the differentials. In the case of these gas-
solid reactions, this latter subroutine is called 'DIFHRD' and differs
from the subroutine used in the non-isobaric calculations in that it
allows for viscosity variations along the diffusion path.

No iterations are required in these solutions, although the programme
'SFERED' involves a trial and error approach to the remote boundary
condition since that condition involves an equilibrium equation linking
the dependent and independent variables.

For both programmes, data is entered via further subroutines named
'DATUM' and 'DATM2', the use of such subroutines avoiding the detailed
accuracy needed for disc data files without requiring the entire main
programme to be recompiled for each data change.

The listings of the programmes are presented below, with the exception
of 'STEP4' which is listed in Appendix 4.

```
        PROGRAM SFERED
C PROGRAMME TO COMPUTE THE REDUCTION TIME FOR SPHERICAL PARTICLE OF
C HEMATITE ASSUMING THAT THE REACTION IS CONTROLLED BY DIFFUSION
C WITH THE REACTION FRONT EQUILIBRIUM BEING THAT FOR FE/FEO
C
C THREE DIFFERENT TIMES ARE COMPUTED, ONE FOR THE FULL DUSTY GAS MODEL,
C ONE FOR THE DUSTY GAS MODEL WITH KNUDSEN AND MOLECULAR DIFFUSION ONLY
C AND ONE WITH MOLECULAR DIFFUSION ONLY
C
C THE DIFFUSION DATA IS THAT DETERMINED IN THIS WORK
C
C GAS 'A' IS TAKEN AS HYDROGEN, GAS 'B' AS WATER VAPOUR
C
      REAL ND,KSI,KEQ
      DIMENSION PA(2), PTOT(2), CAPFI(2), BLAN(2)
      EXTERNAL DIFHRD
      COMMON DAEFF,BETA,AKAPP,DAK,DELTA,BOVDAK,VISCA,VISCB
      CALL DATUM(AO,BO,CO,PAOUT,THETA)
C EQULILIBRIUM CONSTANT FROM HILLS DIRECT REDUCTION COURSE (109)
      KEQ = EXP(-1805/(THETA+273)+1.203)
C BINARY GAS DIFFUSION COEFFICIENT FROM FULLER ET ALIA (87 )
      DAB = (THETA+273.)**1.75*4.122E-05/PAOUT
      DABEFF = CO*DAB
      DAK = AO*((THETA + 273.)/2)**.5
      BOVDAK = BO/DAK
      BETA = 1.0
      AKAPP = 3.
      DAEFF = 1.0/(1.0/DAK + 1.0/DABEFF)
```

A7-1

```
C VISCOSITIES OF GASES IN ATM.S - 1 ATM.S = 1.014E6 POISE
C FROM GEIGER AND POIRIER (89 )
      VISCA = 2.0E-10
      VISCB = 3.8E-10
      DELTA = DAEFF/DABEFF
C REDUCTION IS TAKING PLACE IN PURE HYDROGEN AT 1 ATM PRESSURE
      PA(1) = PAOUT
      PTOT(1) = PAOUT
      CAPFI(1) = PA(1)
      BLAN(1) = 0.0
      HSTEP = - PA(1)/50
23    WRITE(1,1111) CAPFI(1)
1111  FORMAT(' ABOUT TO CALL STEP4',E10.3)
      CALL STEP4(PTOT,CAPFI,PA,BLAN,HSTEP,1,DIFHRD)
      PREV = PA(1)
      PTEST = PTOT(2)/(KEQ + 1)
      IF (PA(2) .GT. PTEST) GO TO 24
      IF (ABS(PA(2)-PTEST) .LT. ABS(PA(2)*1E-4)) GO TO 25
      HSTEP = HSTEP/2.
      GO TO 23
24    PA(1) = PA(2)
      PTOT(1) = PTOT(2)
      CAPFI(1) = CAPFI(2)
      BLAN(1) = BLAN(2)
      GO TO 23
25    TSTAR = 1/(2.*DELTA*(PAOUT - CAPFI(2)))/CO
      OWRITE(2,100) PAOUT, AO, BO, CO, THETA, KEQ, DABEFF, DAK, DAEFF,
     2 DELTA, VISCA, VISCB, TSTAR
100   OFORMAT(1H0,'REDUCTION OF SPHERES OF HEMATITE CALCULATED BY THE DUS
     1TY GAS MODEL',//'REDUCTION ATMOSPHERE IS PURE HYDROGEN AT ',
     2F3.1,' ATM',/' WITH THE FOLLOWING PROPERTY VALUES: AO = ',E10.3
     3', BO = ',E10.3,', CO = ',F6.4,/'THE REDUCTION TEMPERATURE IS TAKE
     4N AS ',F5.1,' GIVING KEQ AS ',F5.3,/
     5' AND DABEFF = ',F6.4,', DAK = ',E11.4,', DAEFF = ',F6.4,
     6' AND DELTA = ',F6.4,//'VISCOSITIES TAKEN AS - HYDROGEN: ',E10.4,
     7'WATER VAPOUR: ',E10.4//
     8'THE DIMENSIONLESS TIME TO COMPLETE REDUCTION (OVER R*THETA*CP) ='
     9,1X,E11.5)
      WRITE(2,101) PTOT(2),PA(2),CAPFI(2)
101   FORMAT('WHEN PT, PA, AND CAPFI ARE, RESEPECTIVELY, ',3(F6.4,1X))
      END



      SUBROUTINE DATUM(AO,BO,CO,PAOUT,THETA)
      AO = 0.465
      BO = 1.9E-9
      CO = 0.136
      THETA = 800.
      PAOUT = 1.0
      RETURN
      END
```

```
      SUBROUTINE DIFHRD(PT,FI,PA,BL,DPT,DFI,DPA,DBL)
C
      REAL KSI
      COMMON DAEFF,BETA,AKAPP,DAK,DELTA,BOVDAK,VISCA,VISCB
      KSI = (PA*VISCA + (PT - PA)*VISCB)/(PT*BOVDAK)
      ODPT = PT*(1.0-BETA*AKAPP)*(1.0-DELTA)/((1.0+PA/KSI+AKAPP*(PT
     1 -PA)/KSI)*(PT-PA*DELTA*(1.0-BETA)) - PA*PT*(1.0-DELTA)*(1.0
     2 -BETA*AKAPP)/KSI)
      ODFI = 1.0/(1.0 - PA*(1.0-BETA)*DELTA/PT - (1.0-DELTA)*(1.0
     1 -BETA*AKAPP)*PA/(KSI+PA+AKAPP*(PT-PA)))
      DPA = 1.0
      DBL = 0
      RETURN
      END


      PROGRAM CACO3D
C PROGRAMME TO COMPUTE THE DECOMPOSITION TIME FOR SPHERICAL PARTICLE OF
C CACOS ASSUMING THAT THE REACTION IS CONTROLLED BY DIFFUSION
C WITH THE CO2 PRESSURE AT THE REACTION SURFACE BEING THE EQUILIBRIUM
C DECOMPOSITION PRESSURE.  AN ISOTHERMAL MODEL IS USED AND THE PROPERTY
C VALUES TAKEN TO BE THOSE DETERMINED BY MARIANA AT 950 C
C
C THE DUSTY GAS MODEL IS USED WITH AO, BO AND CO INCLUDED
C
C
      REAL ND,KSI,KEQ
      DIMENSION PA(2), PTOT(2), CAPFI(2), BLAN(2)
      EXTERNAL DIFHRD
      COMMON DAEFF,BETA,AKAPP,DAK,DELTA,BOVDAK,VISCA,VISCB
      CALL DATM2(AO,BO,CO,PAOUT,THETA)
C EQULILIBRIUM CONSTANT FROM HILLS MEASURED DATA
      KEQ = EXP(16.6-19560.0/(THETA+273.))
      DAB = (THETA+273.)**1.75*7.467E-06/PAOUT
      DABEFF  = CO*DAB
C GAS A IS TAKEN AS CO2
      DAK = AO*((THETA + 273.)/40)**.5
      WRITE(2,2) KEQ, AO, BO, CO, DABEFF, DAK
2     OFORMAT(' EQUILIBRIUM PRESSURE IS ',E10.3,' ATM, AO = ',E10.3/
     1' BO = ',E10.3,', CO = ',E10.3,', DABEFF = ',E10.3,'AND DAK = ',
     2E10.3//)
      BOVDAK = BO/DAK
      BETA = 0.
C AKAPP IS DKA/DKB = SQRT(MB/MA)
      AKAPP = 0.837
      DAEFF = 1.0/(1.0/DAK + 1.0/DABEFF)
C VISCOSITIES OF GASES IN ATM.S - 1 ATM.S = 1.014E6 POISE
      VISCA = 4.2E-10
      VISCB = 4.2E-10
      DELTA = DAEFF/DABEFF
C DECOMPOSITION IS TAKING PLACE IN AIR AT THE TOTAL PRESSURE SPECIFIED
C IN DATUM, THE AIR CONTAINING NO CO2
      PA(1) = 0.0
      PTOT(1) = PAOUT
      CAPFI(1) = PA(1)
```

```
      BLAN(1) = 0.0
      HSTEP = KEQ/50
      DO 23 I=1,50
      WRITE(1,1111) CAPFI(1)
1111  FORMAT(' ABOUT TO CALL STEP4',E10.3)
      CALL STEP4(PTOT,CAPFI,PA,BLAN,HSTEP,1,DIFHRD)
      PA(1) = PA(2)
      PTOT(1) = PTOT(2)
      CAPFI(1) = CAPFI(2)
23    BLAN(1) = BLAN(2)
      TSTAR = 1/(6.0*DELTA*CAPFI(2)*CO)
      DKHILL = DAEFF*CAPFI(2)/KEQ
      WRITE(2,10)THETA,PAOUT,TSTAR,PTOT(2),PA(2),CAPFI(2),DKHILL
10    OFORMAT(1H1,'THE DECOMPOSITION OF CACO3 AT ',F5.0,' DEG IN AIR AT '
     1,F3.1, ' ATM'//' THE DIMENSIONLESS TIME FOR THE COMPLETE DECOMPOSI
     2TION OF A SPHERE IS ',E10.3/' WHEN THE TOTAL PRESSURE AT THE REACT
     3ION FRONT IS ',F5.3,' ATM '/' THE CO2 PARTIAL PRESSURE IS ',F5.3,
     4' AND CAPFI IS ',F5.3,//
     4' THE VALUE OF HILLS DIFFUSION COEFFICIENT THAT WOULD HAVE GIVEN T
     5HE SAME TIME IS '/E10.3)
      END


      SUBROUTINE DATM2(AO,BO,CO,PAOUT,THETA)
      AO = 0.061
      BO = 0.2E16
      CO = 0.1861
      THETA = 850.
      PAOUT = 1.0
      RETURN
      END
```

CASE STUDY ON DIRECT REDUCTION

Examine the effect of changing the rate of production on the conversion costs per tonne of iron processed through a continuous counter flow direct reduction reactor.

You may make the following assumptions:-

1. The reduction gas behaves as if it were pure hydrogen although it is produced by the steam reforming of natural gas.

2. The process gas is hydrogen containing 5% water vapour by volume on entry to the reactor. Its temperature on entry is 950°C, having been heated by a natural gas recuperator whose thermal efficiency is 50%.

3. The reactor is to be operated to produce 95% metallisation of the product.

4. The reduction reactions in the hematite pellet occur in such a way that the layers of intermediate oxides, magnetite and wustite, are infinitely thin.

5. The reduction reactions are transport controlled, the diffusion and flow processes in the porous iron occuring under infinitely viscous conditions.

6. Temperature differences in the reactor between the solid and the gas phase are negligibly small.

7. The thermal capacity of the gas stream is constant and equal to 32 $J.mol_G^{-1}K^{-1}$.

8. The thermal capacity of the solid stream is constant and equal to 52 $J.mol_{Fe}^{-1}K^{-1}$

SOLUTION TO CASE STUDY

Theoretical Considerations

The principle of the continuous shaft gas reduction process is the countercurrent flow of solid iron oxide materials and hot reducing gas. The solids moving downwards through the shaft are heated and gradually reduced by the hot reducing gas which flows upwards and is oxidised by removing oxygen from the iron oxide material.

The principal tool for analysing the reduction process of the iron oxide by the reducing gas in a reactor is the conservation equations applied over a differential control volume within the shaft.

Gas Stream Oxygen Balance

Considering a differential slice of height dx across the reactor as the control volume, we can draw up an oxygen balance on the gas stream within that volume to give:-

$$\dot{G}_G'' \frac{d\eta_O}{dx} = \dot{n}_O''{}' \qquad\qquad (A8-1)$$

where $\dot{G}_G''$ = is the molar flow of all gas species through unit area of the shaft

η_O = the degree of oxidation of the gases ie the mole fraction of all the oxidised gas species - CO_2 and/or H_2O

$\dot{n}_O''{}'$ = the rate of reaction in the shaft per unit area of reactor volume

Heat Balance

The heat balance is more complicated than the mass balance in that more terms are involved. We will consider each term separately:-

The heat entering the control volume = $\dot{G}_{Fe}'' T_{x+dx} C_{Fe} + \dot{G}_G'' T_x C_G$

and leaving the control volume = $\dot{G}_{Fe}'' T_x C_{Fe} + \dot{G}_G'' T_{x+dx} C_G$

Where T = the temperature at the specified height in the shaft, the solid and gas temperatures being assumed equal.

C_{Fe} = the heat capacity of the solid stream per unit mole of elemental iron

C_G = the heat capacity of the gas stream per unit mole of all gas species

$\dot{G}_{Fe}''$ = the molar flow rate of elemental iron through unit area of the shaft.

The heat absorbed by the reaction = $\Delta H_O \dot{n}_O''{}' dx$

Where ΔH_O is the overall heat of reaction per mole of atomic oxygen removed from the solid stream - assumed to be that for the reduction of hematite to iron.

Thus the heat balance gives:-

$$(\dot{G}''_G C_G - \dot{G}''_{Fe} C_{Fe}) \frac{dT}{dx} = - \Delta H_O n''_O{}' \qquad \text{(A8-2)}$$

or

$$\dot{G}''_G (C_G - C_{Fe}/\Gamma) \frac{dT}{dx} = - \Delta H_O n''_O{}' \qquad \text{(A8-3)}$$

Where Γ represents the total molar gas flow per unit mole of elemental iron processed.

Dividing equation (A8-3) by equation (A8-1) and rearranging gives:-

$$\frac{dT}{d\eta_O} = \frac{\Delta H_O}{C_G - C_{Fe}/\Gamma} \qquad \text{(A8-4)}$$

The initial appraisal is to be carried out with the denominator taken as constant so that the above equation can be integrated from the gas inlet point to any point in the reactor to give:-

$$T = T_{in} - \frac{\Delta H_O}{C_G - C_{Fe}/\Gamma} (\eta_O - \eta_{O,in}) \qquad \text{(A8-5)}$$

Overall Oxygen Balance

The overall oxygen balance within a control volume drawn across the reactor from the gas inlet point to the cross section of the reactor at a specified height can be expressed as:-

moles of transferrable oxygen brought into the reactor by the inlet gas stream + the moles of transferrable oxygen carried in the solid stream across the cross section at the specified height = moles of transferrable oxygen carried by the gas stream across the cross section at the specified height + the moles of transferrable oxygen carried from the reactor due to incomplete metallisation of the solid stream.

This gives:-

$$\dot{G}''_G \eta_{O,in} + 2/3 \cdot \dot{G}''_{Fe} m^* = \dot{G}''_G \eta_O + 2/3 \cdot \dot{G}''_{Fe} (1-f_{Fe}) \qquad \text{(A8-6)}$$
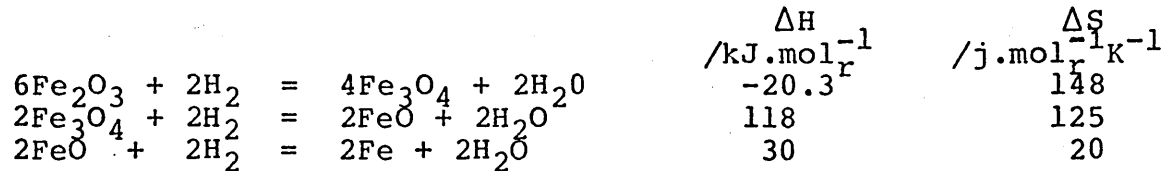
Where f_{Fe} is the degree of metallisation achieved in the reactor, and m^* is the fraction of reaction that has been completed within the solid prior to its reaching the specified height in the reactor.

Rearranging equation (A8-6) and remembering the definition of Γ gives:-

$$3/2 \; \Gamma (\eta_O - \eta_{O,in}) \; = \; m^* - (1-f_{Fe}) \qquad (A8-7)$$

Thermodynamics of the reduction

The reduction of hematite by hydrogen takes place in three stages at temperatures above $560^{\circ}C$. The three reactions and their mean heats and entropies of reaction over the range from 600 to $1000^{\circ}C$ are[1]:-

			ΔH /kJ.mol$_r^{-1}$	ΔS /j.mol$_r^{-1}$K^{-1}
$6Fe_2O_3 + 2H_2$	$=$	$4Fe_3O_4 + 2H_2O$	-20.3	148
$2Fe_3O_4 + 2H_2$	$=$	$2FeO + 2H_2O$	118	125
$2FeO + 2H_2$	$=$	$2Fe + 2H_2O$	30	20

However, in this initial appraisal, we are assuming that the layers of the two intermediate oxide layers are vanishingly thin so that the overall reaction is:-

$Fe_2O_3 + 3H_2 \; = \; 2Fe + 3H_2O$ which gives the value of ΔH_O as 22 kJ.mol$_O^{-1}$.
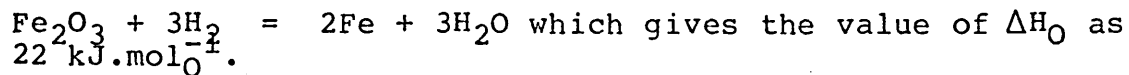
Since the intermediate layers are considered to be infinitely thin, the driving force for diffusion and mass transfer in the reaction of the single pellets in the bed is the difference between the bulk gas phase conditions and conditions in equilibrium with Fe/FeO. Thus it is the bottom values of ΔH and ΔS in the table that are to be used to calculate the equilibrium constant in the reaction rate equations.

Mechanism of the reaction

The stoichiometry of the reduction reaction means that the value of beta to be used in the transport equations developed in the thesis from the Dusty Gas Model is unity. Thus equations (3.46) and (3.52) become:-

$$\frac{dp_T}{dp_A} \; = \; \frac{D_{A,eff}(1 - \mathcal{K})}{D_{A,K} + (B_o/\mu)[\mathcal{K}p_T + \delta_A(1-\mathcal{K})p_A]} \qquad (A8-8)$$

and:-

$$\frac{d\psi}{dp_A} \; = \; \frac{D_{A,K} + (B_o/\mu)[\mathcal{K}p_T + (1-\mathcal{K})p_A]}{D_{A,K} + (B_o/\mu)[\mathcal{K}p_T + \delta_A(1-\mathcal{K})p_A]} \qquad (A8-9)$$

These two equations show that, in general, equi-molar counter diffusion in porous solids will involve viscous flow as well as Knudsen and molecular diffusion. However, the analysis in the thesis also showed that the reduction of hematite could be

analysed without any significant error, if $(^{B}o/\mu)$ is taken to be zero - in value - the infinitely viscous conditions referred to in the case study specifications. Substituting this value into equation (A8-8) and incorporating the definition of $\mathcal{X}$ followed by rearrangement gives:-

$$\frac{dp_T}{dp_A} = 1 - \frac{D_{A,eff}}{D_{B,eff}} \qquad (A8-10)$$

whereas equation (A8-9) shows that $\psi_A = p_A$ whence equation (3.50) shows the flux of A to be given by:-

$$\dot{N}_A = S \frac{D_{A,eff}}{RT} \left\{ [p_A]_s - [p_A]_r \right\} \qquad (A8-11)$$

For the transfer of hydrogen from the bulk gas phase outside a reacting particle to the reaction front, we must sum two resistances together so that we have the following equation for the rate of removal of oxygen from a single particle in the bed:-

$$\dot{n}_O = \frac{C_T \left\{ [p_{H_2}]_G - [p_{H_2}]_R \right\} / p_T}{1/A\alpha_{H_2} + 1/SD_{H_2,eff}} \qquad (A8-12)$$

Where C_T = the total molar concentration in the gas phase,
A = the surface area of the reacting particle
α_{H_2} = the equimolar binary mass transfer coefficient for hydrogen
$D_{H_2,eff}$ = the effective diffusion coefficient of hydrogen in the porous layer iron
S = the shape factor for diffusion through the outer layer of porous iron
p_T = the total pressure
$[p_{H_2}]_G$ = the partial pressure of hydrogen in the gas phase surrounding the pellet
$[p_{H_2}]_R$ = the partial pressure of hydrogen at the reaction front where the total pressure is greater than in the bulk gas phase as shown be equation (A8-10).

$[p_{H_2}]_R$ is to be calculated from equation (A8-10) and the equation for the reaction equilibrium at the reaction front.

Reduction reaction driving force

Integrating equation (A8-10) from the surface of the particle to the reaction front gives:-

$$P_{T,R} - P_{T,o} = \left\{1 - \frac{D_{H_2,eff}}{D_{H_2O,eff}}\right\}\left\{[p_{H_2}]_R - [p_{H_2}]_S\right\} \qquad \text{(A8-13)}$$

Where $p_{T,o}$ is the total pressure in the gas phase surrounding the particle, and the suffices 'R' and 'S' refer respectively to the reaction front and the particle surface.

But equilibrium conditions at the reaction front give:-

$$[p_{H_2O}]_R = k_{eq}[p_{H_2}]_R \qquad \text{(A8-14)}$$

and, since the only gases present at the reaction front are H_2 and H_2O, the combination and rearrangement of the above two equations give:

$$[p_{H_2}]_R - [p_{H_2}]_S = \frac{[p_{H_2}]_R(1+k_{eq}) - P_{T,o}}{1 - D_{H_2,eff}/D_{H_2O,eff}} \qquad \text{(A8-15)}$$

Writing equation (A8-11) for hydrogen, combining it with equation (A8-12), remembering that one mole of H_2 is transferred for each mole of O that reacts and rearranging the resulting equation, gives:-

$$[p_{H_2}]_S - [p_{H_2}]_R = \left\{[p_{H_2}]_G - [p_{H_2}]_R\right\}\left\{\frac{SD_{H_2,eff}}{A\alpha_{H_2}} + 1\right\}^{-1} \qquad \text{(A8-16)}$$

Thus $[p_{H_2}]_S$ can be eliminated between equation (A8-15) and (A8-16) to give:-

$$[p_{H_2}]_G - [p_{H_2}]_R = [p_{H_2}]_G - \frac{P_{T,o} - b[p_{H_2}]_G}{1 + k_{eq} - b} \qquad \text{(A8-17)}$$

where b is given by:-

$$b = \left\{\frac{1}{D_{H_2,eff}} - \frac{1}{D_{H_2O,eff}}\right\}\left\{\frac{S}{A\alpha_{H_2}} + \frac{1}{D_{H_2,eff}}\right\}^{-1} \qquad \text{(A8-18)}$$

Equation (A8-17) expresses the driving force in the bed as a function of the partial pressure of hydrogen. It can also be expressed in terms of the degree of oxidation of the gas phase, η_O, as:-

$$\frac{\Delta p}{P_{T,o}} = \frac{[p_{H_2}]_G - [p_{H_2}]_R}{P_{T,o}} = 1 - \eta_O - \frac{1 - b(1-\eta_O)}{1 + k_{eq} - b} \qquad \text{(A8-19)}$$

Thus the fractional driving force, $\Delta p/P_{T,o}$ can be expressed as a function of η_O, equations (A8-5) and (A8-7) respectively being used to determine how the bed temperature, T, and the fraction of solid reaction

completed, m^*, vary with the degree of oxidation in the gas phase. The fraction of solid reaction completed is necessary for the calculation of $S/A\alpha_{H_2}$ in equation (A8-18) for b. If we assume the pellets are spherical, and that the layers of intermediate oxide are infinitely thin, the shape factor is given by:-

$$S = \frac{4\pi r}{1/r - 1/r_o} \tag{A8-20}$$

where r is the radius of the reaction front within the pellet of outer radius r_o. Using the Sherwood Number, Sh:-

$$S/A\alpha_{H_2} = 2/(Sh.D_{H_2/H_2O}[(1/m^*)^{0.333} - 1]) \tag{A8-21}$$

which can be substituted into equation (A8-18) to allow b to be calculated as a function of m^* and hence, through equation (A8-7), as a function of η_O.

The temperature is required so that the equilibrium constant and the diffusion coefficients can be calculated as functions of η_O also. The equations for these calculations, together with other data are set out in Table (A8-1).

Table A8-1

Variable	Value	Source
K_{eq}	$= \exp(1805/T + 1.2)$	Ref(1)
C_G	$32\ J.mol^{-1}K^{-1}$	"
C_{Fe}	$52\ J.mol^{-1}K^{-1}$ (mean value)	"
$D_{K,A}$	$= A_o\ T/M_A$, in cm^2s^{-1}	Thesis
A_o	$0.317\ cm^2s^{-1}(g.mol^{-1}K^{-1})^{0.5}$	"
$D_{AB,eff}$	$= C_o\ D_{AB}$	"
C_o	0.0972	"
$D_{A,eff}$	$= 1/(1/D_{K,A} + 1/D_{AB,eff})$	"
D_{AB}	$= 4.81 \times 10^{-5}\ T^{1.75}$	Ref(4)
$T_{G,in}$	1223 K	Given
Sh	5.0 (calculated from j-factor from using data presented in Table (A8-3)	ref (4)
$\eta_{O,in}$	0.05	Given

A is H_2 or H_2O, AB is H_2/H_2O

The data and the system of equations has been used in the MBASIC computer programme on page A8-15 to determine how the reduction driving force varies with η_O through the bed for different parametric values of Γ . The values are tabulated on pages A8-16 and A8-17 and plotted in Figure (A8-1) against $3/2\Gamma(\eta_O - \eta_{O,in})$. This ordinate has been chosen to ensure that the entire reduction zone – the region in which m^* varies from 1.0 to 0.05 – is represented by a constant length of ordinate. Thus any value of Γ that gives a curve producing negative values of the driving force would cause iron to be produced from the shaft with a lower degree of metallisation than that specified.

The figure shows that the minimum possible value of Γ is 2.83, and curves are also presented in the figure of $\Gamma = 3$, 3.3, 4 and 5 and these values naturally give positive values of the reduction driving force throughout the bed.

The total rate of reaction in the bed

Combining equations (A8-12) and (A8-19) gives the rate at which a single sphere is reacting in the bed as:-

$$\dot{n}_O = C_T \left\{ \frac{1 - \eta_O - \dfrac{1 - b(1-\eta_O)}{1 + k_{eq} - b}}{{}^1/_{A\alpha_{H_2}} + {}^1/_{SD_{H_2,eff}}} \right\} \qquad (A8-22)$$

If there are v''' particles per unit volume of bed in the reactor, we can say that the rate of reaction per unit volume is given by:-

$$\dot{n}_O''' = v'''.\dot{n}_O \qquad (A8-23)$$

Thus equation (A8-1) becomes:-

$$\dot{G}_G'' \frac{d\eta_O}{dx} = C_T v''' \left\{ \frac{1 - \eta_O - \dfrac{1 - b(1-\eta_O)}{1 + k_{eq} - b}}{{}^1/_{A\alpha_{H_2}} + {}^1/_{SD_{H_2,eff}}} \right\} \qquad (A8-24)$$

Substituting for the surface area of the pellet and for the shape factor of the diffusion zone gives after rearrangement:-

$$\frac{d\eta_O}{dx} = \frac{4\pi r_o^2 v'''}{\dot{G}_G''} \frac{p_T}{RT_{in}} \left\{ \frac{1 - \eta_O - \dfrac{1 - b(1-\eta_O)}{1 + k_{eq} - b}}{{}^1/_{\alpha_{H_2}} + {}^{r_o}/_{D_{H_2,eff}((1/m^*)^{1/3} - 1)}} \right\} \left\{ \frac{T_{in}}{T} \right\}$$

$$. . . . . . (A8-25)$$

Figure A8-1 : The driving force for the reduction of hematite by hydrogen in a shaft reactor.

Inlet temperature of the reactant gas = 950°C.

$\Gamma = 5\cdot 0$

$\Gamma = 4\cdot 0$

$\Gamma = 3\cdot 3$

$\Gamma = 3\cdot 0$

$\Gamma = 2\cdot 83$

$\dfrac{\Delta p}{P_{t,o}}$

$\frac{3}{2}\, \Gamma\,(\eta_o - \eta_{o,in})$

A8-7a
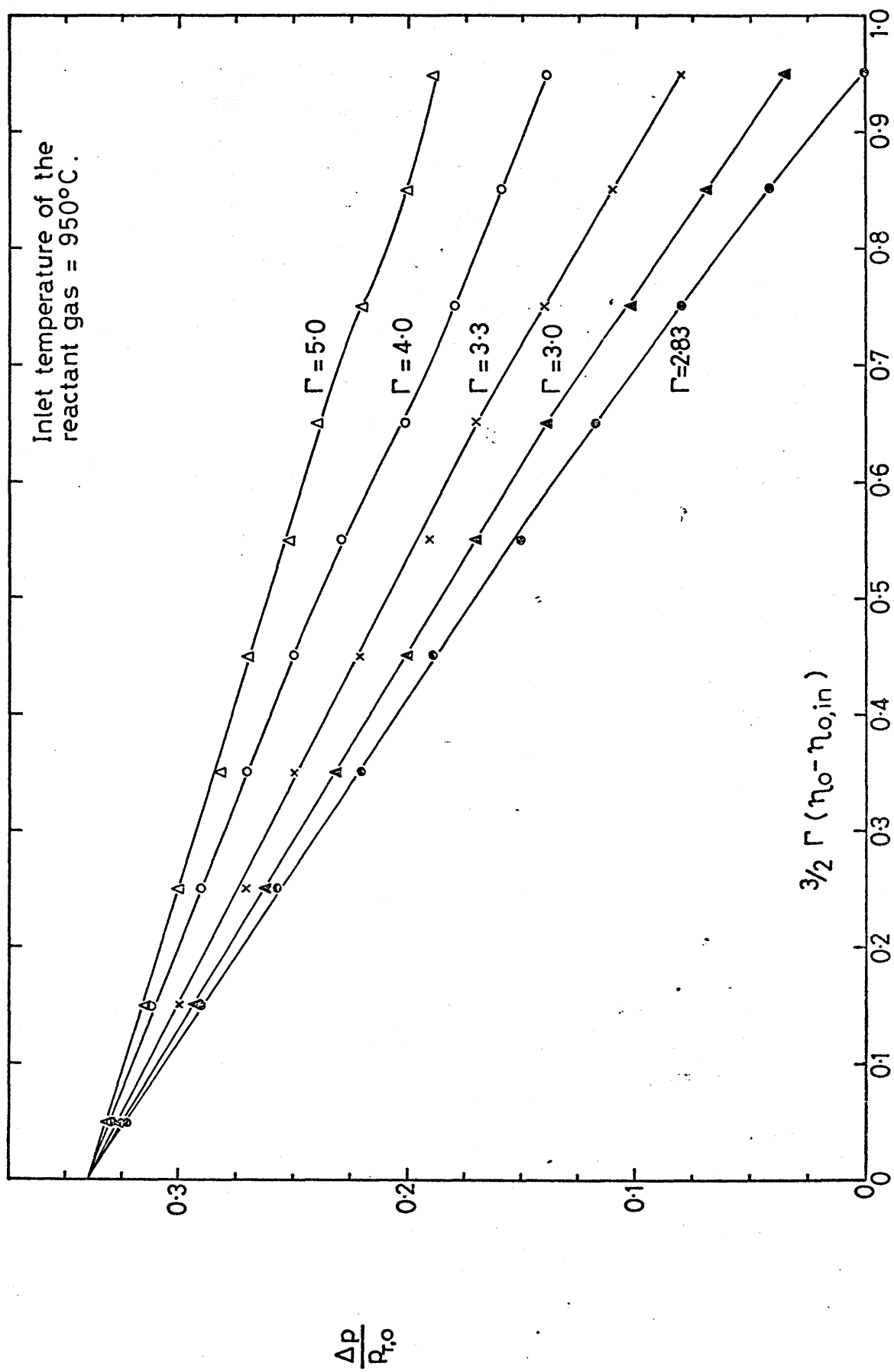
$4\pi r_o^2 . v'''$ is the specific surface area of particles in the bed, S''', and the mass transfer coefficient is related to the Sherwood number so that further rearrangement gives:-

$$\frac{d\eta_O}{dx} \frac{\dot{G}_G'' r_o R T_{in}}{S''' p_T D_{H_2/H_2O}} = \frac{\left\{1 - \eta_O - \dfrac{1 - b(1-\eta_O)}{1 + k_{eq} - b}\right\}}{\dfrac{2}{Sh} + \dfrac{D_{H_2/H_2O}}{D_{H_2,eff}} \left\{\left[\dfrac{1}{m^*}\right]^{1/3} - 1\right\}} \left\{\frac{T_{in}}{T}\right\} \quad \ldots\ldots (A8-26)$$

It is now possible to define a dimensionless bed height x^* given by:-

$$x^* = \frac{S''' p_T (D_{H_2/H_2O})_{in}}{\dot{G}_G'' r_o R T_{in}} x \qquad (A8-27)$$

whence, remembering the temperature variation of the free gas diffusion coefficient shown in Table A8-1, equation (A8-26) can be expressed as:-

$$\frac{d\eta_O}{dx^*} = \frac{\left\{1 - \eta_O - \dfrac{1 - b(1-\eta_O)}{1 + k_{eq} - b}\right\}}{\dfrac{2}{Sh} + \dfrac{D_{H_2/H_2O}}{D_{H_2,eff}} \left\{\left[\dfrac{1}{m^*}\right]^{1/3} - 1\right\}} \left\{\frac{T}{T_{in}}\right\}^{0.75} \qquad (A8-28)$$

So that the dimensionless height of the reduction zone in the reactor can be obtained by quadrature:-

$$L^* = \int_{\eta_{O,in}}^{\eta_{O,out}} \frac{\dfrac{2}{Sh} + \dfrac{D_{H_2/H_2O}}{D_{H_2,eff}} \left\{\left[\dfrac{1}{m^*}\right]^{1/3} - 1\right\}}{\left\{1 - \eta_O - \dfrac{1 - b(1-\eta_O)}{1 + k_{eq} - b}\right\}} \left\{\frac{T_{in}}{T}\right\}^{0.75} d\eta_O \qquad (A8-29)$$

In evaluating this integral, equation (A8-5) is to be used to determine T as a function of η_O, equation (A8-7) for m^*, equation (A8-18) for b and the equations in Table A8-1 for the equilibrium constant and the diffusion coefficients. The upper limit of the integration is the degree of oxidation in the gas phase at the point in the bed where reduction commences. It is given by equation (A8-7) as:-

$$\eta_{O,out} = 2f_{Fe}/3\Gamma + \eta_{O.in} \qquad (A8-30)$$

A computer programme in MBASIC was written (see page A8-18) to evaluate this integral by Simpson's rule for a series of different parametric values of Γ from 2.83 upwards.

Determination of the output from a reactor

Once the value of L* has been determined by quadrature, it can be used to determine the performance of a continuous flow reduction reactor. The maximum possible rate of production is predicted for a given degree of metallisation, a given height of reduction zone and a given value of Γ. The reactor can operate at a slower production rate with the given value of Γ but then not all the reactor volume available for reduction will be utilised. Provided the particular value of Γ in question is greater than 2.83, the reactor can always be operated at such a slower production rate by reducing the value of Γ to ensure that the entire volume of the reduction zone is utilised.

The dimensionless height of the reactor is, of course, a particular value of x*, and equation (A8-27) for this value can be rearranged to give:-

$$\dot{G}''_{Fe} = \frac{S'''p_T(D_{H_2/H_2O})_{in} L}{\Gamma L^* r_o R T_{in}} \qquad (A8-31)$$

where L is the actual height of the reduction zone in the reactor.

The output of the reactor in unit time, $\dot{G}_{Fe}$, can be determined by multiplying equation (A8-31) by the cross sectional area of the reactor:

$$\dot{G}_{Fe} = \pi R_o^2 \dot{G}''_{Fe} = \frac{S'''p_T(D_{H_2/H_2O})_{in} L \pi R_o^2}{\Gamma L^* r_o R T_{in}} \qquad (A8-32)$$

In order to calculate the production rates for different values of L* we need to estimate the values of the following parameters involved in equation (A8-32):-

r_o <u>initial radius of the pellet</u>   When pellets are used as feed materials, a desirable size distribution for a vertical shaft with moving bed was reported[2] as being 85% of pellets with 1.3 cm diameter and 15% of 0.6 cm diameter. Since the mean value for an equivalent diameter is given by:-

$$\bar{d}_e = \frac{1}{\sum\limits_{j=1}^{n} f_j/[d_e]_j} \qquad (A8-33)$$

where f_j is the volume fraction of particle size j and $[d_e]_j$ its respective diameter, the equivalent mean diameter for the above distribution will be 1.1 cm.

S"'   <u>the specific surface area per unit volume of the bed</u> can be expressed as:-

$$S''' = \frac{(1-\gamma)\ 4\pi r_o^2}{4/3\ \pi r_o^3} = \frac{3(1-\gamma)}{r_o} \qquad (A8-34)$$

where γ is the porosity of the bed taken as 0.5.

R_o <u>the radius of the reactor</u>   A review carried out[2] to show the characteristics of the equipment used in shaft direct reduction processes, indicates that the diameter of a moving bed reactor eg. Midrex, varies between 4 and 5.5 m. An intermediate value of 5 m was chosen in the present calculations.

Production rates calculated using equation (A8-32) for different values of Γ are presented in Table A8-2

Table A8-2

Γ	L*	W_{Fe}# t/yr	$[p_{H}]_{out}$ (atm)	$\eta_{o,L}$	U## %	V_G### Nm^3/t_{Fe}
2.83	647	1.40×10^5	0.73	0.27	23.5	1132
3.00	286	3.02×10^5	0.74	0.26	22.0	1200
4.00	165	4.00×10^5	0.79	0.21	17.0	1600
5.00	123	4.20×10^5	0.82	0.18	13.0	2000
6.00	99.3	4.30×10^5	0.84	0.16	11.0	2400
10.0	56.0	4.60×10^5	0.88	0.12	6.00	4000

\# W_{Fe} is expressed by multiplying equation (A8-32) by $31.5 \times M_{Fe}$

\#\#   U = gas utilisation = $\dfrac{\eta_{o,L} - \eta_{o,in}}{1 - \eta_{o,in}}$

\#\#\# V_G = total gas per 1 t of Fe = $400 \times \Gamma$ [Nm^3]

Calculation of the volume of natural gas used to produce 1t of iron

Natural gas is used in the process to heat up the total gas stream through the reactor to the inlet temperature, to provide the top-up H_2 by the reforming reaction and to provide the heat for this reaction.

As a working figure, in this case study, we will assume that the reforming is carried out by steam, one mole of CH_4 providing 2 moles of the reducing gas - hydrogen - and for which the heat of the reaction per mole of reducing gas produced is 113 $kJ.mol^{-1}$ or 5.04 $MJ.Nm^{-3}$ per Nm^3 of the reducing gas.

The top-up gas process volume is equal to :

$$(0.95 - [p_{H_2}]_L)xV_G = (\eta_{O,L} - 0.05)V_G \qquad (A8-35)$$

where 0.95 represents the initial molar fraction of hydrogen in the reactor and $[p_H]_L$ is the molar fraction of the hydrogen leaving the reduction zone of the reactor. Therefore the amount of heat Q_R in $MJ.tonne_{Fe}^{-1}$ required to produce the top up gas, considering an efficiency of the reformer-recuperator of 50%, is equal to:

$$Q_R = \frac{5.04}{0.5}(\eta_{O,L} - 0.05)V_G \qquad (A8-36)$$

where V_G is measured in $Nm^3.tonne_{Fe}^{-1}$.

The volume of natural gas required to produce the top-up gas, N_{TUG}, is equal to:-

$$N_{TUG} = (\eta_{O,L} - 0.05)V_G/2 \qquad (A8-37)$$

The heat required to heat the process gas to the inlet temperature of $950^{O}C$, Q_H, considering that the heating process is 50% efficient, is given by:-

$$Q_H = V_G.C_G.(950 - 30)^{O}C/0.5 = 2.54V_G \qquad (A8-38)$$

when Q_H is measured in $MJ.tonne_{Fe}^{-1}$ and V_G in $Nm^3.tonne_{Fe}^{-1}$.

Considering the calorific power of the natural gas to be 40 $MJ.Nm^{-3}$, the total volume of natural gas required to process 1 tonne of iron is given by:-

$$N_{TOT} = \frac{Q_R + Q_H}{40} + N_{TUG} \qquad (A8-39)$$

Where N_{TOT} and N_{TUG} are measured in $Nm^3.tonne_{Fe}^{-1}$ and Q_R and Q_H are measured in $MJ.tonne_{Fe}^{-1}$.

Table A8-3 presents the calculated values of N_{TOT} for different values of V_G.

V_G /$Nm^3 \cdot t_{Fe}^{-1}$	$n_{O,L}$	N_{TUG} /$Nm^3 \cdot t_{Fe}^{-1}$	Q_R /$MJ \cdot t_{Fe}^{-1}$	Q_H /$MJ \cdot t_{Fe}^{-1}$	$(Q_R+Q_H)/40$ /$Nm^3 \cdot t_{Fe}^{-1}$	N_{TOT} /$Nm^3 \cdot t_{Fe}^{-1}$
1132	0.27	125	2510	2875	135	259
1200	0.26	126	2540	3048	140	266
1600	0.21	128	2580	4064	166	294
2000	0.18	128	2620	5080	193	321
2400	0.16	132	2660	6096	219	351
4000	0.12	140	2822	10000	321	461

Economic Considerations

The analysis of the economics of a shaft direct reduction continuous counter current reactor is shown in Table A8-4. The basic economic data has been taken from an analysis carried out by Lownie[2] of the cost of a direct reduction shaft reactor to be placed in South America. Lownie presents figures for a 400 000 tonne.annum^{-1} plant and presents costs per tonne. His analysis does not allow the effect of different rates of operation to be investigated, so his figures have been used here as a basis of the estimates of fixed costs which, anyway, have been inflated from the 1978 data that he presented. Separate assessments have been made of natural gas costs, two sets of figures being used - one based on UK costs and one on South American. The analysis is carried out to determine the conversion costs of the reactor, ie the costs of converting the pellet feed to iron pellets 95% metallised.

1. Capital cost of plant

The reactor itself is considered to cost some £M35. In order to translate this figure into annual cost to be set against the annual production of the plant, it has been discounted over 15 years at a rate of 10%, this relatively low rate being taken to represent Government support for a major capital venture. This leads to an annual capital charge of £M6.yr^{-1}

2. Fixed running costs

The following have been estimated from Lownie's data:-

Cooling water charges	-	£M0.025.yr^{-1}
Labour	-	£M0.375.yr^{-1}
Supervision	-	£M0.25.yr^{-1}
Maintenance	-	£M1.00.yr^{-1}

3. Total fixed costs   -   £M7.65.yr^{-1}

4. Variable costs

The principal variable cost is for the natural gas required to
heat the process gas and to reform the top-gas. The
quantity of gas required has been calculated in the previous
section of the case study. Two different prices for natural
gas have been used in the economic analysis:-

UK base cost of £0.13.Nm^{-3}

Venezuelan[5] cost of £0.004.Nm^{-3}

The total conversion costs per tonne$_{Fe}$ and the annual
production are shown in Table A8-4 as a function of Γ .

<u>Table A8-4</u> Total Conversion costs/t.$_{Fe}$

Γ	W_{Fe} /t.yr^{-1}	Costs / £.t_{Fe}^{-1}				
		Fixed	Gas UK	Gas Ven	Tot.UK	Tot.Ven
2.83	1.4×10^5	54.6	32.9	10.1	87.5	64.7
3	2.86×10^5	27.4	33.8	10.4	61.2	37.8
4	4×10^5	19.1	37.4	11.5	56.5	30.6
5	4.2×10^5	18.2	40.8	12.6	59.0	30.8
6	4.3×10^5	17.7	44.7	13.7	62.4	31.4
10	4.6×10^5	16.3	58.6	18.0	74.9	34.4

The total conversion costs are shown in Figure A8-2 plotted
against the annual production rate. The two curves for UK and
Venezuelan conditions show that the most cost effective rate
of production in the plant is about 400 000 tonne.yr^{-1} and
that the two different gas prices make little or no difference
to this figure. The curves also show that departures from
this rate of production in either direction result in sharp
increases in conversion costs per tonne.

Figure A8-2 : A comparison of the conversion costs for direct reduced iron in the U.K. and Venezuela .
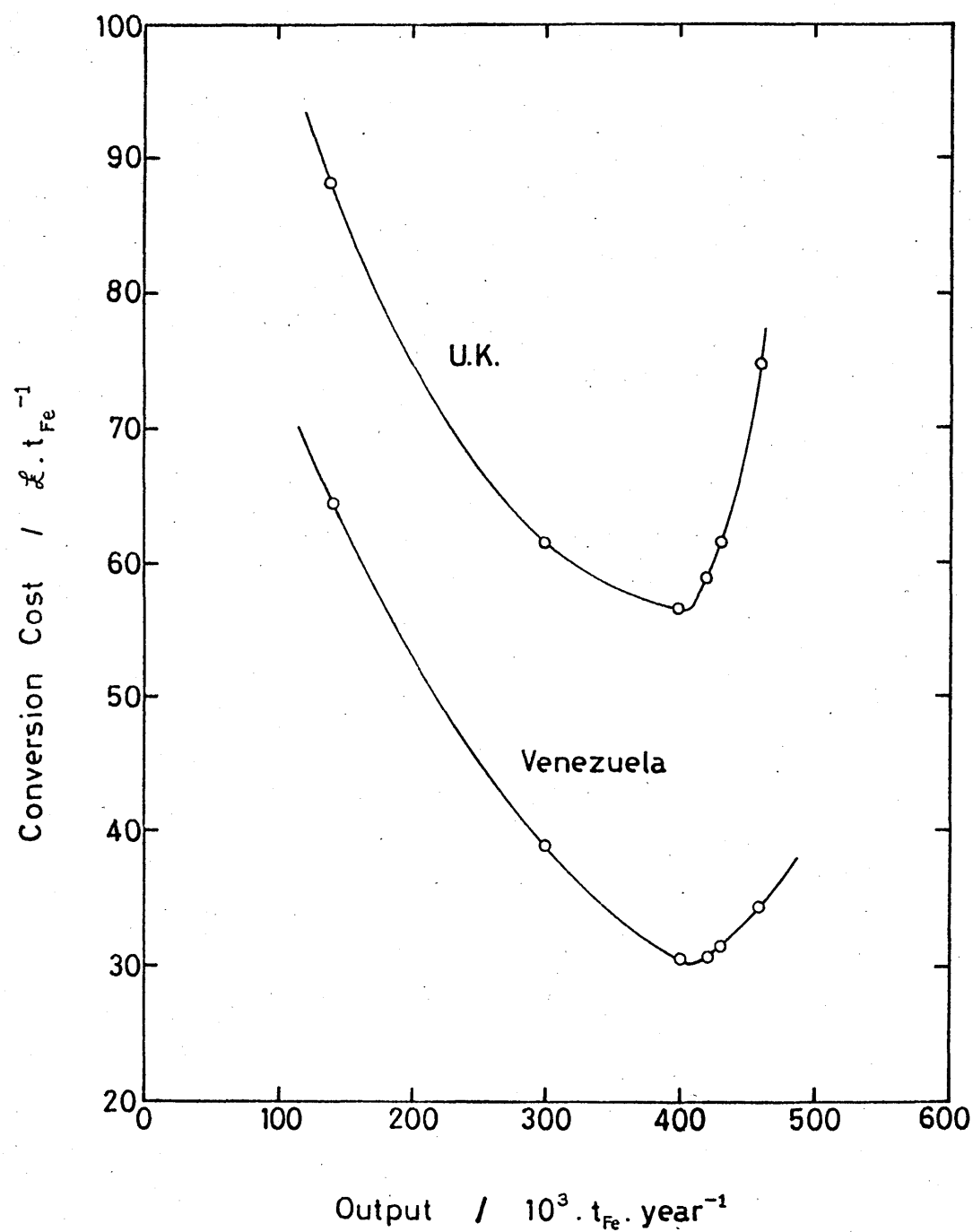
```
3 REM THIS PROGRAMME CALCULATES THE DRIVING FORCE FOR THE REDUCTION
4 REM OF PURE HEMATITE WITH HYDROGEN AS A REDUCTION GAS IN A SHAFT
5 REM REACTOR.
6 REM
7 REM
8 REM THE DUSTY GAS MODEL TOGETHER WITH THE EXPERIMENTAL PARAMETERS
9 REM ARE USED TO OBTAIN AN EQUATION LINKING THE REACTION
10 REM DRIVING FORCE AT ANY HEIGHT IN THE REACTOR TOO THE FRACTION
11 REM MSTAR,OF REMOVABLE OXYGEN REMAINING IN THE ORE AND THE
12 REM EQUILIBRIUM CONSTANT FOR THE REDUCTION.
14 REM
16 REM
50 DELHO = 22000
100 CGH=31
150 CFE=52
200 GAMA=6
250 TGI=1223
300 ETOI=.05
350 FFE=.95
375 CO=.097
400 SH=5
650 LPRINT "ETO","DELPP","PH2","TG","PH2R","KEQH"
700 FOR J=1  TO 10
750 N=J*.1-.05
800 ETO=(2*N/(3*GAMA)+ETOI)
850 MSTAR=1.5*GAMA*(ETO-ETOI)+(1-FFE)
900 TG=TGI-DELHO*(ETO-ETOI)/(CGH-CFE/GAMA)
950 DH2OK=.317*(TG/18)^.5
1000 DH2K=.317*(TG/2)^.5
1050 DH2OH=.0000418*TG^1.75
1075 DH2EF=1/(1/DH2K+1/(DH2OH*CO))
1100 DH2OE=1/(1/DH2OK+1/(DH2OH*CO))
1150 P=DH2EF
11175 S=DH2OE
1200 B = (1/P - 1/S)/(.4/((1/MSTAR)^.333 - 1)/DH2OH + 1/P)
1250 KEQH=1/EXP(1805/TG-1.2)
1300 DELPP=1-ETO-(1-B*(1-ETO))/(1+KEQH-B)
2500 LPRINT ETO,DELPP,1-ETO,TG-273,1-ETO-DELPP,KEQH
2600 NEXT
```

GAMA= 2.83

ETO	DELPP	PH2	TG	PH2R	KEQH
.0617786	.322975	.938222	929.476	.615247	.740026
.0853357	.290627	.914664	888.427	.624038	.701789
.108893	.257777	.891107	847.378	.63333	.662945
.13245	.224164	.86755	806.33	.643386	.623545
.156007	.189672	.843993	765.281	.654321	.583652
.179564	.154219	.820436	724.233	.666217	.543346
.203121	.117734	.796879	683.184	.679145	.502725
.226678	.0801587	.773322	642.136	.693163	.46191
.250236	.0414458	.749764	601.087	.708319	.421046
.273793	1.56307E-03	.726207	560.038	.724644	.380311

GAMA= 3

ETO	DELPP	PH2	TG	PH2R	KEQH
.0611111	.324244	.938889	932.114	.614645	.742462
.0833333	.294567	.916667	896.341	.6221	.70921
.105556	.264588	.894445	860.569	.629857	.675491
.127778	.234065	.872222	824.797	.638157	.641336
.15	.202903	.85	789.024	.647097	.606783
.172222	.171039	.827778	753.252	.6567399	.571879
.194444	.138422	.805556	717.48	.667134	.536682
.216667	.105007	.783333	681.707	.678327	.501259
.238889	.0707548	.761111	645.935	.690356	.465692
.261111	.0356336	.738889	610.163	.703255	.430077

GAMA= 4

ETO	DELPP	PH2	TG	PH2R	KEQH
.0583333	.328668	.941667	939.815	.612999	.749557
.075	.308114	.925	919.444	.616886	.73074
.0916667	.28767	.908333	899.074	.620664	.711767
.108333	.26713	.891667	878.704	.624536	.692641
.125	.246434	.875	858.333	.628566	.673369
.141667	.22555	.858333	837.963	.632783	.653955
.158333	.20446	.841667	817.593	.637207	.634408
.175	.18315	.825	797.222	.64185	.614734
.191667	.161607	.808333	776.852	.646726	.594943
.208333	.139823	.791667	756.482	.651844	.575043

GAMA= 5

ETO	DELPP	PH2	TG	PH2R	KEQH
.0566667	.33092	.943333	942.88	.612414	.752375
.07	.314932	.93	928.641	.615068	.739255
.0833333	.29915	.916667	914.401	.617517	.726057
.0966667	.283378	.903333	900.162	.619956	.712784
.11	.267558	.89	885.922	.622442	.699436
.123333	.251667	.876667	871.683	.625	.686015
.136667	.23569	.863333	857.443	.627644	.672523
.15	.219618	.85	843.204	.630382	.658963
.163333	.203444	.836667	828.964	.633222	.645336
.176667	.187164	.823333	814.725	.636169	.631646

```
3 REM THIS PROGRAMME CALCULATES THE DIMENSIONLESS BED HEIGHT,
4 REM LSTAR, OF THE REDUCTION ZONE IN A SHAFT RECTOR USED FOR
5 REM THE REDUCTION OF HEMATITE BY HYDROGEN.
14 REM THE EVALUATION OF LSTAR ACCORDING TO EQUATION A8-29 IS
15 REM DONE USING SIMPSON'S RULE
16 REM
17 REM
50 DELHO = 22000
100 CGH=31
150 CFE=52
200 INPUT "GAMMA = "",GAMA
220 LPRINT "GAMMA = ";GAMA
250 TGI=1223
300 ETOI=.05
350 FFE=.95
375 CO=.097
400 LPRINT "ETO","DELPP","PH2","TG","PH2R","F"
640 N = 0
650 GOSUB 8000
660 I = F
690 HSTEP = 2*FFE/(30*GAMA)
700 FOR J=1 TO 9
750 N = N + .05
800 GOSUB 8000
850 I = I + 4*F
900 N = N + .05
950 GOSUB 8000
10000 I = I + 2*F
1020 LPRINT ETO,DELPP,1-ETO,TG-273,1-ETO-DELPP,F
1050 NEXT
1100 N = N + .05
1150 GOSUB 8000
1200 I = I + 4*F
1225 LPRINT ETO,DELPP,1-ETO,TG-273,1-ETO-DELPP,F
1250 N = N + .05
1300 GOSUB 8000
1350 I = I + F
1450 LPRINT "LSTAR=";.667*I/GAMA
1500 STOP
8000 ETO=(2*N/(3*GAMA)+ETOI)
8050 MSTAR=1.5*GAMA*(ETO-ETOI)+(1-FFE)
8100 TG=TGI-DELHO*(ETO-ETOI)/(CGH-CFE/GAMA)
8150 DH2OK=.317*(TG/18)^.5
8200 DH2K=.317*(TG/2)^.5
8250 DH2OH=.0000418*TG^1.75
8300 DH2EF=1/(1/DH2K+1/(DH2OH*CO))
8350 DH2OE=1/(1/DH2OK+1/(DH2OH*CO))
8400 P=DH2EF
8450 S=DH2OE
8500 B = (1/P - 1/S)/(.4/((1/MSTAR)^.3333 - 1)/DH2OH + 1/P)
8550 KEQH=1/EXP(1805/TG-1.2)
8600 DELPP=1-ETO-(1-B*(1-ETO))/(1+KEQH-B)
8650 F = (.4 + DH2OH/P*((1/MSTAR)^.333 - 1))*(TGI/TG)^.75/DELPP
8700 RETURN
```

GAMMA = 2.83

ETO	DELPP	PH2	TG	PH2R	F
.0735571	.306831	.926443	908.952	.619612	35.5085
.0971143	.274287	.902886	867.903	.628598	27.5525
.120671	.241075	.879329	826.854	.638254	23.3958
.144229	.207034	.855772	785.806	.648738	20.899
.167786	.17207	.832214	744.757	.660144	19.3903
.191343	.136109	.808657	703.708	.672548	18.6743
.2149	.0990858	.7851	662.66	.686014	18.919
.238457	.0609469	.761543	621.611	.700596	21.2426
.262014	.0216518	.737986	580.562	.716334	35.8328
.273793	1.56295E-03	.726207	560.038	.724644	341.338

LSTAR= 647.13

GAMMA = 3

ETO	DELPP	PH2	TG	PH2R	F
.0722222	.309412	.927778	914.228	.618366	35.1158
.0944445	.279637	.905556	878.455	.625919	26.8709
.116667	.249401	.883333	842.683	.633932	22.4119
.138889	.218568	.861111	806.911	.642543	19.5483
.161111	.187062	.838889	771.138	.651827	17.5434
.183333	.154828	.816667	735.366	.661839	16.0762
.205556	.121817	.794445	699.593	.672628	14.9952
.227778	.0879876	.772222	663.821	.684235	14.2559
.25	.0533046	.75	628.049	.696696	14.0003
.261111	.0356336	.738889	610.163	.703255	14.3298

LSTAR= 286.011

GAMMA = 4

ETO	DELPP	PH2	TG	PH2R	F
.0666667	.318349	.933333	929.63	.614984	33.8608
.0833333	.297897	.916667	909.259	.61877	24.814
.1	.277417	.9	888.889	.622583	19.6426
.116667	.256804	.883333	868.519	.626529	16.0632
.133333	.236017	.866667	848.148	.63065	13.2845
.15	.215032	.85	827.778	.634968	10.9338
.166667	.193833	.833333	807.407	.6395	8.79039
.183333	.172408	.816667	787.037	.644258	6.68945
.2	.150746	.8	766.667	.649254	4.47005
.208333	.139822	.791667	756.482	.651844	3.25528

LSTAR= 165.706

GAMMA = 5

ETO	DELPP	PH2	TG	PH2R	F
.0633333	.322872	.936667	935.761	.613794	33.2825
.0766667	.307034	.923333	921.521	.6163	23.9226
.09	.291267	.91	907.282	.618733	18.5265
.103333	.275476	.896667	893.042	.621191	14.7758
.116667	.259623	.883333	878.803	.623711	11.8715
.13	.24369	.87	864.563	.62631	9.44614
.143333	.227666	.856667	850.324	.629	7.29571
.156667	.211544	.843333	836.084	.631789	5.28861
.17	.195318	.83	821.845	.634682	3.32578
.176667	.187164	.823333	814.725	.636169	2.33355

LSTAR= 123.558

A8-20

GAMMA = 6

ETO	DELPP	PH2	TG	PH2R	F
.0611111	.325678	.938889	939.055	.613211	32.9408
.0722222	.312679	.927778	928.109	.615099	23.4112
.0833333	.29979	.916667	917.164	.616877	17.9069
.0944445	.286916	.905556	906.219	.61864	14.0872
.105556	.274023	.894445	895.274	.620421	11.1472
.116667	.261095	.883333	884.328	.622238	8.71978
.127778	.248122	.872222	873.383	.6241	6.60626
.138889	.235097	.861111	862.438	.626014	4.68458
.15	.222017	.85	851.493	.627983	2.87108
.155556	.215455	.844445	846.02	.628989	1.98447

LSTAR= 99.271

GAMMA = 10

ETO	DELPP	PH2	TG	PH2R	F
.0566667	.330944	.943333	944.315	.61239	32.331
.0633333	.323239	.936667	938.631	.613428	22.5252
.07	.315683	.93	932.946	.614317	16.8672
.0766667	.308184	.923333	927.261	.615149	12.971
.0833333	.30071	.916667	921.576	.615957	10.0165
.09	.293244	.91	915.892	.616756	7.63184
.0966667	.28578	.903333	910.207	.617554	5.61942
.103333	.278311	.896667	904.522	.618356	3.86241
.11	.270835	.89	898.837	.619166	2.28611
.113333	.267093	.886667	895.995	.619574	1.5492

LSTAR= 56.1575

References

1. Hills A W D - "Direct Reduction Course" - Caracas, Venezuela,(1976).
2. Direct Reduced Iron - Technology and Economics of Production and Use - Iron and Steel Society of AIME,(1980).
3. Bird R B,Stewart W E and Lighfoot E N - "Transport Phenomena" ,John Wiley and Sons,(1960)
4. Fuller E N,Schettler P D and Giddings J C - Ind. and Eng.Chem., (1966).
5. Arteaga L - Suitability of the spray steelmaking process as an alternative in the Venezuelan steel industry" - Case Study - Sheffield City Polytechnic ,(1978).